Report of the High-Resolution Ocean Topography Science Working Group Meeting

Edited by

Dudley B. Chelton
College of Oceanic and Atmospheric Sciences
Oregon State University, Corvallis, Oregon

Reference 2001-4
October 2001

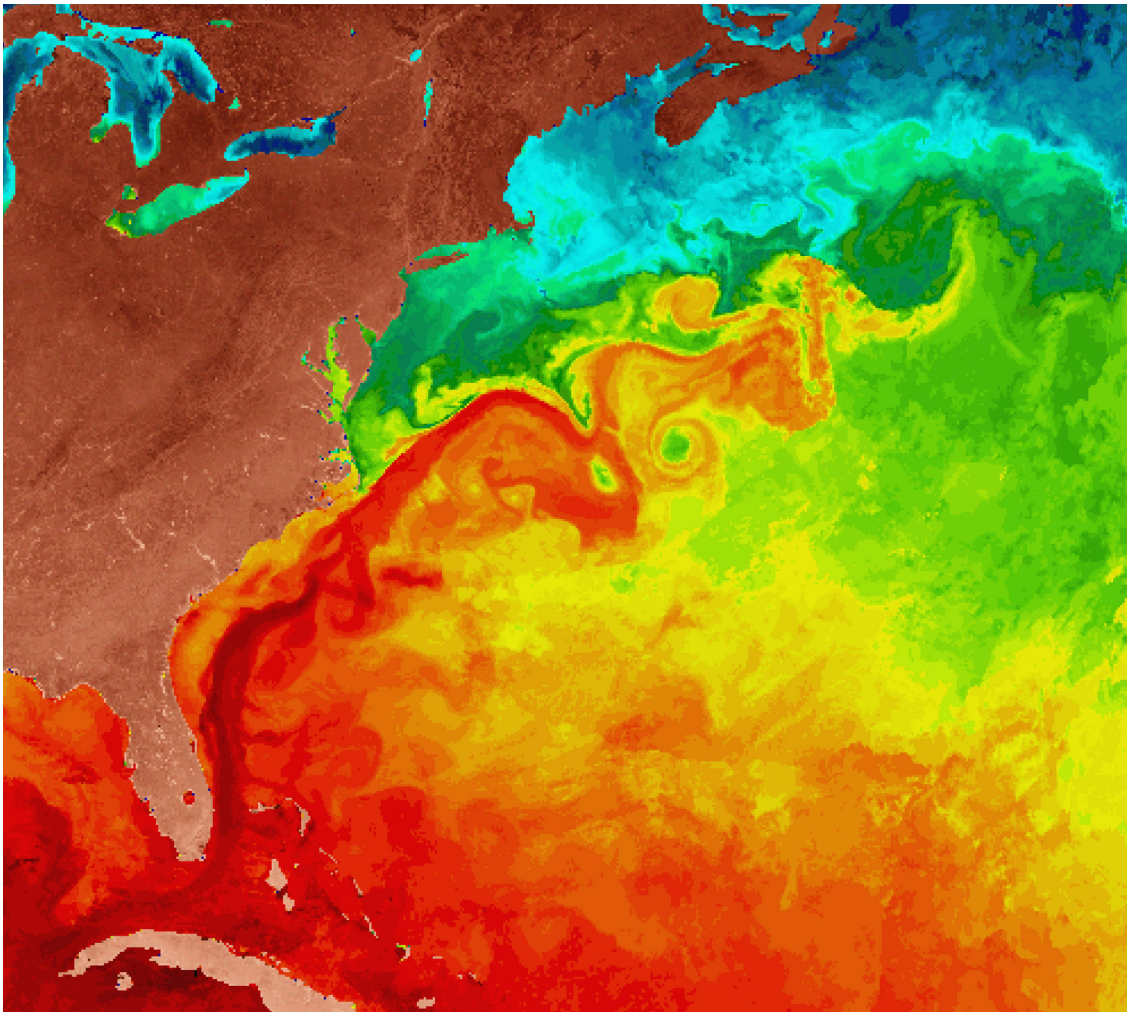

Report of the High-Resolution Ocean Topography Science Working Group Meeting

Convened at the

University of Maryland Conference Center
College Park, Maryland
28-29 March 2001

Edited by

Dudley B. Chelton
College of Oceanic and Atmospheric Sciences
Oregon State University
Corvallis, OR 97331-5501

email: chelton@coas.oregonstate.edu
phone: (541) 737-4017

Reference 2001-4
October 2001

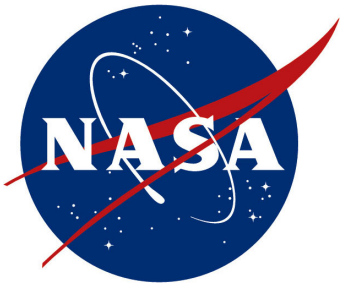

Acknowledgments

We thank Cindy Withrow for her enduring patience and technical expertise in the preparation of this report. We also thank Shannon Powell of Westover Consultants for coordinating the meeting at the University of Maryland Conference Center. Logistical support for the High-Resolution Ocean Topography Science Working Group meeting was provided by the Jet Propulsion Laboratory under contract with the National Aeronautics and Space Administration. The preparation of this report was supported by Contract 1206715 from the Jet Propulsion Laboratory to Dudley B. Chelton at Oregon State University.

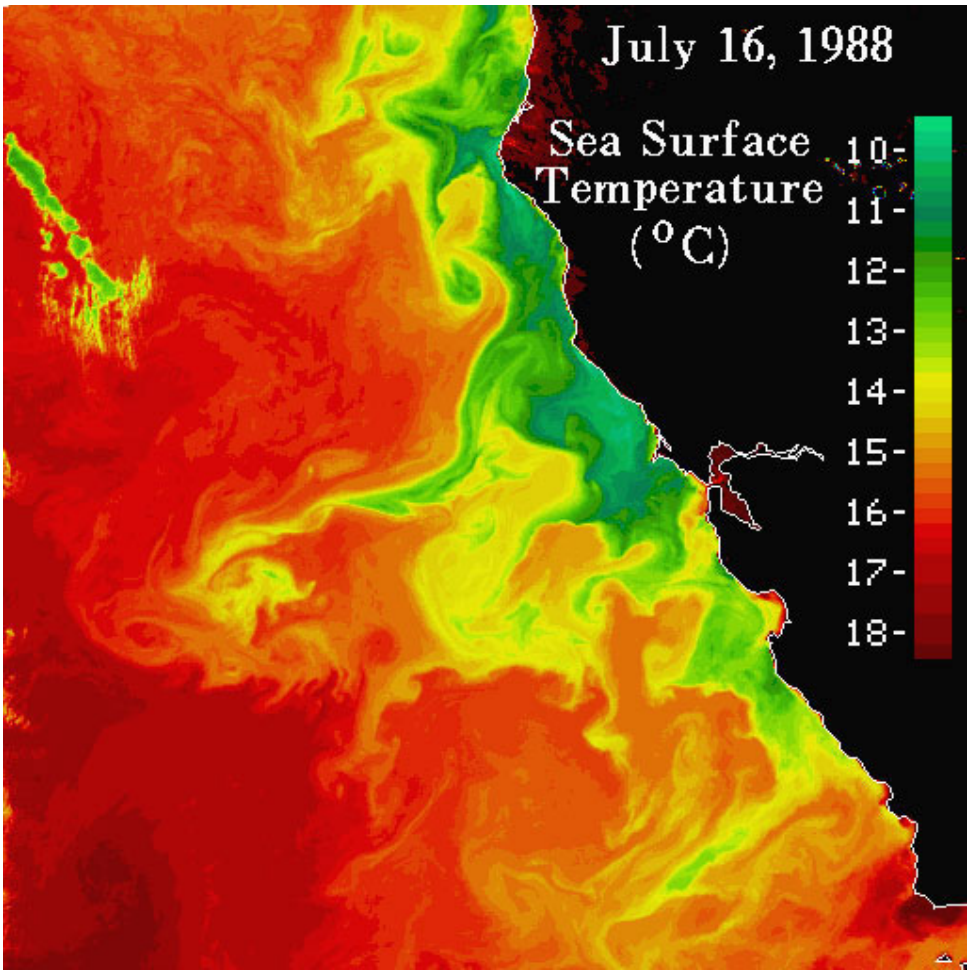

Satellite image of sea surface temperature (SST) off the west coast of North America constructed from National Oceanic and Atmospheric Administration (NOAA) Advanced Very High Resolution Radiometer (AVHRR) infrared observations analyzed by Ted Strub and Corinne James of the College of Oceanic and Atmospheric Sciences at Oregon State University. The small-scale features in this image are of interest to studies of coastal ocean circulation and physical-biological interaction from high-resolution altimetric measurements of ocean topography.

Cover Figure: Satellite image of SST in the Gulf Stream region off the east coast of North America in June 1984 constructed from NOAA AVHRR infrared observations analyzed by Mark Carle, Robert Evans and Otis Brown of the Rosenstiel School of Marine and Atmospheric Science at the University of Miami. The open-ocean mesoscale circulation features in this image are of interest to studies from high-resolution altimetric measurements of ocean topography.

Table of Contents

Executive Summary

The nine-year record of TOPEX/POSEIDON (T/P) altimeter data has demonstrated the utility of highly accurate ocean topography measurements for a wide range of scientific and operational applications. While the 9.9156-day exact-repeat sampling pattern of the T/P orbit minimizes temporal aliasing of mesoscale variability at the measurement locations along the satellite ground track, the corresponding 2.834° longitudinal spacing of ground tracks restricts the spatial scales of sea surface height variability that can be resolved by the T/P sampling pattern. There are many physical processes that occur on spatial scales that are not fully resolved by the T/P dataset. In recognition of the importance of these shorter-scale phenomena, the National Aeronautics and Space Administration (NASA) established a High-Resolution Ocean Topography Science Working Group to review the scientific and operational rationales for high-resolution measurements of ocean topography, and to review the status of existing and developing technologies for measuring ocean topography with higher resolution than has heretofore been possible.

To address these issues, a two-day meeting was convened on 28-29 March 2001 at the University of Maryland Conference Center in College Park, Maryland. The meeting began with presentations summarizing the resolution capability of ocean topography measurements from presently operating and soon-to-be launched altimeters. This was followed by a series of presentations articulating ***the scientific and operational needs for higher resolution measurements of ocean topography:***

- Studies of mesoscale eddies and fronts that are essential to understanding the dynamics of ocean circulation on all space and time scales, including the large-scale meridional transport of heat by eddies and the mass transport by large-scale currents through eddy-mean flow interaction.
- Studies of mesoscale and shorter-scale variability in the coastal regions associated wind-driven upwelling, flow perturbations by abrupt bathymetric features, and eddies and meanders generated by flow instabilities.
- Operational applications for prediction of ocean circulation on a wide range of scales. Military applications include naval operations such as sea-lift ship routing, search and rescue, antisubmarine warfare, and coastal and mine warfare. Civilian applications include tidal information for navigation and hazard mitigation, ship routing, fisheries forecasting, pollutant spill dispersion forecasting, El Niño and other seasonal-to-interannual anomaly forecasting, oil rig design, location and monitoring of hazardous currents, marine resource management, and water level changes in the Great Lakes.
- Data constraints for data assimilation models being developed for research and operational forecasts of open-ocean and coastal ocean circulation.
- Improved resolution of global tide models in coastal regions and near major bathymetric features in the open ocean.
- Studies of deep-ocean mixing associated with internal tides, and an investigation of the importance of this small-scale mixing to the large-scale circulation and climate variability of the world ocean.
- Studies of physical-biological interaction associated with mesoscale and shorter-scale variability in the open ocean and coastal regions, determination of gas transfer velocity across the air-sea interface, and an investigation of the importance of these biogeochemical processes in the global carbon cycle.
- Estimation of short-scale features of ocean bathymetry and their association with lithospheric and mantle processes in the Earth's interior, and an investigation of the importance of the short-scale roughness of the seafloor on the overlying large-scale and mesoscale ocean circulation.

Following the presentations on applications, the High-Resolution Ocean Topography Science Working Group heard presentations summarizing ***new technologies for high-resolution measurements of ocean topography:***

- A constellation of dual-frequency Ku-band (~14 GHz) and C-band (~6 GHz) altimeters named WITTEX. The WITTEX altimeters are based on the delay-Doppler design that provides

measurements with high accuracy and small footprint size from small, low-power and low-cost altimeters.

- A constellation of Ka-band (~35 GHz) altimeters named AltiKa. The AltiKa altimeters are based on altimetric measurements at high frequencies for which ionospheric effects are negligible. The ability to measure ocean topography with a single-frequency altimeter allows for a low-power, low-cost design with a small footprint size.
- A Wide-Swath Ocean Altimeter (WSOA) that is based on interferometric measurements of ocean topography with a 15 km sample spacing across a swath width of 200-km centered on the satellite ground track.
- Altimetric measurements from the reflections of signals from the Global Positioning System (GPS) constellation of satellites, which could potentially provide global ocean topography measurements with a 25 km sample spacing.

Written summaries of all of the meeting presentations are included in this report. The meeting concluded with an open discussion of the strengths and limitations of the various new technologies for obtaining higher resolution measurements of ocean topography than have been possible from traditional altimeter systems.

Through email correspondence subsequent to the March 2001 meeting, near-term and long-term strategies were developed for establishing high-resolution measurements of ocean topography. On the basis of these proceedings, ***the High-Resolution Ocean Topography Science Working Group recommends an evolutionary development of a system for addressing the scientific and operational needs for high-resolution measurements of ocean topography:***

- NASA should continue operation of T/P for as long as the instrument continues to function well. In tandem with the Jason-1 altimeter, this will provide the first opportunity to acquire high-resolution measurements of ocean topography from a coordinated tandem sampling pattern. A tandem T/P and Jason-1 sampling pattern will address many of the needs for high-resolution ocean topography. This will enable fundamentally new scientific studies and applications, as well as provide a framework for future mission formulation. In addition to improved spatial resolution, extended operation of T/P will provide backup in case of instrument malfunction or failure of the Jason-1 satellite.
- After the initial 6-month calibration and validation phase of the Jason-1 mission, Jason-1 should be maintained in the present T/P orbit and T/P should be maneuvered into an orbit that samples along ground tracks half way between the present T/P ground tracks, thus doubling the resolution of ocean topography measurements from the tandem mission. The resolution obtainable from such a tandem T/P-Jason sampling pattern is significantly better than that from tandem Jason-ENVISAT sampling. After the January 2002 launch of ENVISAT, simultaneous operation of T/P, Jason-1 and ENVISAT would further improve the resolution of ocean topography measurement through the triplet altimeter sampling pattern.
- In the same manner, Jason-1 should be operated in tandem with Jason-2 after a 6-month calibration and validation phase following the planned December 2005 launch of Jason-2.
- Planning should begin immediately to build and launch a constellation of at least three low-cost, low-risk altimeters (e.g., WITTEX or AltiKa) as a follow-on of the ENVISAT and Jason-2 altimeters. In a coordinated sampling pattern with the 9.9156-day orbit repeat period of T/P, Jason-1 and Jason-2, such a multi-satellite mission would provide significantly higher-resolution measurements of ocean topography than are possible from the triplet T/P-Jason-ENVISAT sampling pattern.
- At the earliest possible opportunity, which appears to be on the Jason-2 platform with a planned launch in December 2005, flight demonstration of WSOA should be conducted as a proof of concept of very high-resolution measurements of ocean topography by interferometric altimetry.
- More extensive flight demonstrations of GPS altimetry should be conducted in concert with further technology development to improve the understanding of the GPS capability for high-resolution measurements of ocean topography.

List of Participants

High-Resolution Ocean Topography Science Working Group Meeting

University of Maryland Conference Center
College Park, Maryland
March 28-29, 2001

Name	Organization	Telephone	e-mail
Adamec, David	NASA/GSFC	301-614-5698	adamec@gsfc.nasa.gov
*Chao, Yi	JPL	818-354-8168	yi.chao@jpl.nasa.gov
*Chelton, Dudley (chair)	OSU	541-737-4017	chelton@coas.oregonstate.edu
*Cheney, Robert	NOAA	301-713-2857	Robert.Cheney@noaa.gov
*DeMey, Pierre	LEGOS	335-613-94758	pierre.de-mey@cnes.fr
Fu, Lee-Lueng	JPL	818-354-8167	llf@pacific.jpl.nasa.gov
*Glover, David	WHOI	508-289-2656	dglover@whoi.edu
*Hurlburt, Harley	NRL	228-688-4626	hurlburt@nrlssc.navy.mil
*Jacobs, Gregg	NRL	228-688-4720	jacobs@nrlssc.navy.mil
Kaki, Said	JPL	818-354-3048	skaki@jpl.nasa.gov
Leeuwenburgh, Olwijn	SIO	858-822-3787	oleeuwenburgh@ucsd.edu
*LeProvost, Christian	LEGOS	335-613-32923	Christian.Le-Provost@cnes.fr
*Le Traon, Pierre-Yves	CLS	335-613-94758	letraon@cfs.fr
Lindstrom, Eric	NASA HQ	202-358-4540	elindstr@hq.nasa.gov
McGuire, Jim	IPO/NASA	301-427-2121x127	James.McGuire@noaa.gov
Menard, Yves	CNES	335-612-76872	yves.menard@cnes.fr
Pollard, Brian	JPL	818-351-7718	brian.pollard@jpl.nasa.gov
Porter, David	JHU/APL	443-778-4230	David.L.Porter@jhuapl.edu
*Raney, Keith	JHU/APL	240-228-5384	keith.raney@jhuapl.edu
*Ray, Richard	NASA/GSFC	301-614-6102	richard.ray@gsfc.nasa.gov
*Rodriguez, Ernesto	JPL	818-354-5668	Ernesto.rodriguez@jpl.nasa.gov
*Samelson, Roger	OSU	541-737-4752	rsamelson@coas.oregonstate.edu
*Smith, Walter	NOAA	301-713-2860x126	walter@raptor.grdl.noaa.gov
*Stammer, Detlef	SIO	858-822-3376	dstammer@ucsd.edu
*Strub, Ted	OSU	541-737-3015	tstrub@coas.oregonstate.edu
*Thouvenot, Eric	CNES	335-612-82568	Eric.Thouvenot@cnes.fr
Wang, Yan M.	RAYTHEON ITSS	301-794-5459	ywang@magus.stx.com
*Zuffada, Cinzia	JPL	818-354-0033	cinzia.zuffada@jpl.nasa.gov

* Indicates Science Working Group member.

Overview of the High-Resolution Ocean Topography Science Working Group Meeting

Introduction

The present state of the art of satellite altimetry is based upon three decades of heritage. Soon after the earliest earth-observing satellites were launched in the 1960s, it was realized that the surface topography of the ocean could be measured from space by a radar altimeter. Proof-of-concept missions were flown during the 1970s, beginning with an altimeter that operated briefly on Skylab in 1973 and the GEOS-3 altimeter that operated with intermittent temporal and geographical coverage from 1975 to 1978. This proof-of-concept phase culminated with the Seasat altimeter that operated from July to September 1978.

Based largely on the Seasat altimeter design, the U.S. Navy launched the Geosat altimeter in March 1985 for the primary purpose of high-resolution mapping of the global marine geoid for military applications. Upon completion of the geoid-mapping objective, Geosat was maneuvered into the Seasat orbit in September 1986 and continued to operate until October 1989. Although the data quality for oceanographic applications was compromised because of shortcomings in the system design owing to the military objectives of the mission (principally the lack of a water vapor radiometer, the lack of dual-frequency altimeter for ionospheric corrections, and the use of a passive attitude control system), and although some of the data were initially classified for several years, the Geosat data were nonetheless useful for a variety of scientific applications (see the review by Fu et al., 1990). However, the limited overall measurement accuracy of the Geosat altimeter and the lack of consideration of the effects of tidal aliasing in selection of the orbit configuration restricted the scope of scientific questions that could be addressed from Geosat data.

Despite the limitations of the data quality from the Skylab, GEOS-3, Seasat and Geosat altimeters, these early altimeter missions clearly demonstrated the wide range of potential oceanographic and geophysical applications of altimetric measurements of ocean topography. The European Space Agency has subsequently operated single-frequency altimeters since July 1991 onboard the Earth Remote Sensing satellites ERS-1 and ERS-2, which will be succeeded by the ENVISAT satellite scheduled for launch in January 2002. Constrained by the requirements of other instruments onboard the satellites, the orbit configuration of the ERS and ENVISAT satellites consists of a sun-synchronous orbit with a 35-day repeat period. Although the ERS altimeter data are compromised by temporal aliasing of mesoscale variability because of the long repeat period and by temporal aliasing of tidal variations because of the sun-synchronous orbit, the data have proven useful for many scientific investigations (see reviews in Fu and Cazanave, 2001).

The first dedicated satellite altimeter mission optimally designed for scientific study of the ocean is TOPEX/POSEIDON (T/P), launched in August 1992 by the U.S. National Aeronautics and Space Administration (NASA) and the French space agency Centre National d'Etudes Spatiales (CNES). By all measures, T/P is the most successful radar mission ever launched. Compared with its predecessors, the instrumental measurement accuracy of the dual-frequency altimeter onboard T/P improved by more than a factor of two and the orbit accuracy improved by more than an order of magnitude, resulting in an overall measurement accuracy of about 4 cm (Chelton et al., 2001). The dual-frequency altimeter has now operated for more than 9 years, far surpassing the original design of a 3-year mission with contingencies for extension to 5 years. The long data record provides the first opportunity for altimeter-based studies of short-term climate variability of the ocean on time scales from monthly to interannual. The climate record of sea surface height (SSH) variability along the T/P ground tracks will be continued by the Jason-1 altimeter that is scheduled for launch in December 2001.

Measurements of ocean topography by radar altimetry inevitably involve a tradeoff between spatial resolution and temporal resolution (Figure 1). Improvement of one results in degradation of the other. For example, the sampling pattern for the early Geodetic Phase of the ERS-1 mission had a very fine longitudinal ground track spacing of 0.15°, but the data are not very useful for oceanographic studies because of temporal aliasing of mesoscale variability owing to the long 168-day orbit repeat period. At the other extreme, the short 3-day exact repeat during the Ice Phases of the ERS-1 mission and during the last few weeks of the Seasat mission resulted in a coarse longitudinal ground track spacing of 8.37°. The tradeoff between spatial resolution and temporal resolution thus forces a compromise in mission design.

The T/P orbit configuration was chosen specifically for measuring the large-scale SSH field for studies of ocean variability on monthly and longer time scales. This dictates an orbit with approximately a 10-day repeat period in order to minimize temporal aliasing of mesoscale variability at the measurement locations along the exactly repeating ground track. The precise repeat period of 9.9156 solar days for T/P was chosen to minimize the effects of tidal aliasing (Parke et al., 1987). The corresponding 2.834° longitudinal spacing of ground tracks (Figure 1) significantly limits the spatial scales of SSH variability that can be resolved by the T/P sampling pattern. Processes with spatial scales shorter than approximately 500 km are not fully resolved in T/P data (see upper left panel of Figure 2; see also Greenslade et al., 1997, and paper 12 in this report).

SSH varies over a continuum of space and time scales in association with a wide range of physical processes that interact in very complicated ways. A schematic diagram of the spatial and temporal scales of various oceanic phenomena is shown in Figure 3. The dashed lines indicate the approximate lower limits of the spatial and temporal scales that can be fully resolved by a single altimeter in the T/P orbit configuration (see paper 12 in this report). Variability with spatial scales that fall outside of the upper right quadrant defined by these intersecting dashed lines cannot be adequately addressed from T/P data. Different orbit configurations result in slightly different resolutions, but the fundamental limitation is imposed by the tradeoff between spatial and temporal resolution shown in Figure 1. While very useful for studies of large-scale phenomena such as seasonal variability of SSH, interannual variability associated with the El Niño-Southern Oscillation phenomenon, Rossby wave dynamics and basin-scale variability (Fu and Chelton, 2001), it is evident from Figure 3 that there are many processes with spatial and temporal scales that are too short to be resolved by the sampling pattern of a single altimeter.

In recognition of the importance of phenomena with scales shorter than can be resolved in past and present altimeter datasets, NASA established a Science Working Group of users of ocean topography measurements who have interests in scientific investigations and applications that require higher-resolution measurements of SSH. As summarized in Figure 1, one approach to obtaining high-resolution measurements of ocean topography is from a constellation of altimeters in coordinated orbit configurations. For the 10-day exact repeat orbit of T/P, for example, the 2.834° longitudinal spacing of ground tracks for a single altimeter would be reduced to 0.945° with a triplet altimeter mission with evenly spaced ground tracks. The ground track spacing would decrease to 0.567° with a pentad altimeter mission with 10-day exact repeat. Another approach is to explore new technologies that have recently been developed for high-resolution measurements of ocean topography over broad swaths using methods different from traditional nadir-looking radar altimetry.

In assessing the utility of any observational technique for high-resolution measurements of ocean topography, it is essential to take into consideration the signal-to-noise ratio of the measurement system. As shown schematically by the red and blue curves in Figure 4, the power spectral density of SSH variability decreases with increasing wavenumber (i.e., decreasing wavelength) owing to the "redness" of geophysical variability (e.g., Hasselmann, 1976). Likewise, the power spectral density of measurement errors also decreases with increasing wavenumber, but less rapidly than the signal spectrum, as shown schematically by the black curve. The steepness of the measurement error spectral rolloff depends on the spatial correlation structure of the measurement errors. The resolution capability of the measurement system is restricted to wavenumbers smaller than the value k_{max} (i.e., wavelengths longer than $2\pi/k_{max}$)

that corresponds to the intersection of the signal and measurement error spectra. While the measurement error spectrum may be relatively uniform geographically, the signal spectrum varies considerably geographically in terms of energy level and perhaps in terms of shape as well. It is to be expected, then, that the spatial resolution capability of any measurement system will vary geographically, depending on the signal characteristics. For example, a measurement system capable of detecting mesoscale features with wavelengths of 30 km near energetic western boundary currents might only be able to detect features with wavelengths longer than 150 km in the quiescent regions of weak mesoscale variability in the middle of the ocean. This is shown schematically in Figure 4 by the different values of k_{max} for the spectra corresponding to regions of high- and low-energy mesoscale variability represented by the red and blue curves, respectively.

To initiate a coordinated effort to establish a system for high-resolution measurements of ocean topography, a NASA-sponsored meeting was convened on 28-29 March 2001 at the University of Maryland Conference Center in College Park, Maryland. ***The purposes of the meeting were threefold:***

1) To review the scientific and operational rationales for high-resolution measurements of ocean topography.
2) To review the status of existing and developing technologies for measuring ocean topography with higher resolution than has heretofore been possible.
3) To recommend a strategy for the evolutionary development of a system for obtaining high-resolution measurements of ocean topography.

The results of the High-Resolution Ocean Topography Science Working Group meeting are presented in this report. Written summaries of the individual workshop presentations follow, organized into three parts. The needs for high-resolution measurements of ocean topography are articulated in the the ten papers in Part 1. These papers include descriptions of applications for physical oceanographic and biogeochemical scientific studies, for bathymetric estimation, and for operational applications within the U.S. Navy and the National Oceanic and Atmospheric Administration (NOAA). The resolution capabilities of single and multiple conventional altimeters are summarized in the four papers in Part 2 along with assessments of the errors of geostrophic velocity estimates derived from altimeter measurements of SSH. Four new technologies for obtaining high-resolution measurements of ocean topography are summarized in Part 3. This overview concludes with a summary and the recommendations of the workshop.

The format of each written contribution in this report consists of text and references, followed by the figures and figure captions that are referred to in the text of that paper. The papers are referred to in this overview according to the numbering in the table of contents.

Applications of High-Resolution Measurements of Ocean Topography

The strength of an altimeter mission with a single satellite in the T/P orbit configuration is in the measurement of large-scale climatic signals of ocean variability (Fu and Chelton, 2001). However, a large fraction of the kinetic energy of the ocean is concentrated in eddies and currents (Robinson, 1982; Le Traon and Morrow, 2001) with spatial scales shorter than can be resolved by the space-time sampling pattern of T/P or any other single nadir-looking altimeter (see the cover figure and the figure on the Acknowledgments page of this report). For some purposes, current velocity is of more interest than sea surface height. The determination of ocean velocity requires the vector sea surface slope. Conventional radar altimeter measurements, by nature, determine only the along-track slope, from which the cross-track component of geostrophic velocity can be estimated. The two-dimensional geostrophic velocity vector can thus be estimated at the crossover points, but with latitudinally varying uncertainty owing to the geometry of the intersecting ground tracks (Morrow et al., 1994; see also paper 14). In particular, the zonal component becomes highly uncertain at high latitudes where the satellite ground tracks become nearly zonal. Likewise, the meridional component of geostrophic velocity becomes most uncertain at low

latitudes where the ground tracks are most nearly meridional. The low-latitude uncertainties are amplified by the decrease of the Coriolis parameter toward a value of zero at the equator.

Reliable estimates of cross-track slope, from which the along-track component of geostrophic velocity can be computed, require simultaneous measurements along two adjacent tracks with a spacing about 0.5°-0.75° (see paper 13). Closer track spacing amplifies the effects of measurement errors on estimates of the along-track component of geostrophic velocity and wider track spacing increases sampling errors from unresolved mesoscale variability with spatial scales shorter than the track spacing. Depending on the magnitudes of the measurement errors, it may be possible to estimate surface geostrophic velocity more accurately by this parallel track method than by the crossover method (see papers 13 and 14). From Figure 1, uniform global coverage of ocean topography measurements for geostrophic velocity mapping with the T/P 10-day orbit configuration and a ground track spacing of 0.75° would require measurements along at least four parallel, evenly spaced tracks (see also paper 11). [It is noteworthy that measurements along multiple tracks can be obtained from a smaller number of altimeters if the conventional monostatic radar is replaced with a bistatic radar that measures reflections of its own signals, as well as the signals from the other radars in the multi-satellite altimeter constellation (see paper 15). With such a system, measurements from n bistatic radar altimeters would yield altimetric measurements along 2n-1 parallel tracks. Measurements along five tracks could thus be obtained from only three spacecraft to maximize the efficiency of a multi-satellite altimeter mission.]

A multiple satellite configuration would also be required to resolve the high-frequency, large-scale barotropic variability that aliases into the low-frequency variations of interest (Stammer at al., 2000; Tierney et al., 2000; Shriver and Hurlburt, 2001). To the extent that this barotropic variability can be accurately simulated by state-of-the-art ocean general circulation models, it may be possible to remove these signals in the SSH field in much the same manner that the effects of atmospheric pressure loading and tidal variations are routinely removed from altimeter data (Chelton et al., 2001). Though highly desirable because the accuracies of models of barotropic ocean circulation are not yet fully understood, multiple satellites therefore may not be essential for de-aliasing of barotropic variability.

The most problematic features of ocean circulation from the perspective of altimeter sampling are the mesoscale eddies and fronts that are of interest in the SSH and ocean velocity fields. These features are essential to understanding the dynamics of ocean circulation on all space and time scales. Theoretical studies of the cascade of energy over scales from 100-1000 km have always suffered from the lack of high-resolution observations (paper 1). Numerical model simulations indicate that, in many regions of the world ocean, this mesoscale variability plays a key role in the large-scale ocean circulation and climate variability in the form of eddy transport of momentum in eddy-mean flow interaction and in the form of meridional eddy transport of heat (paper 2). Global synoptic observations of the eddy field have never been available to test the accuracy of the model simulations.

In coastal regions, the spatial scales of the ocean circulation are even smaller, approaching a few kilometers (papers 3 and 4; see also the figure on the Acknowledgements page of this report). Indeed, some of these coastal processes are too short in space and time to be amenable to ocean topography measurements, but an increased resolution approaching 10 km scale would go a long way toward providing the information on nearshore mesoscale variability that is crucial for understanding coastal ocean circulation and its effects on the nearshore environment. Another consideration is that many coastal applications require knowledge of the ocean topography closer to land than can be measured by conventional altimetry. Altimetric measurement techniques that could resolve SSH within a few kilometers of land (e.g., the WITTEX and AltiKa technologies summarized in papers 15 and 16) could open new coastal ocean research opportunities.

In view of the extreme challenges in resolving the shortest space and time scales of mesoscale variability from satellite altimetry in coastal regions, data assimilation will play a key role in developing a complete description of coastal ocean circulation. Numerical models are especially challenged in the

coastal ocean because of the much finer scales of mesoscale variability and the multiplicity of physical processes that includes the large-scale geostrophic circulation, tidal variability, wind-driven upwelling, flow perturbations by abrupt bathymetric features, and eddies and meanders associated with flow instabilities. Assimilation of high-resolution ocean topography measurements into numerical models would thus lead to significant improvements in the understanding of coastal ocean circulation (see paper 4).

Data assimilative numerical models of mesoscale variability in the open ocean are also in need of high-resolution measurements of ocean topography. True eddy-resolving global ocean modeling is only now becoming feasible computationally. The accuracies of these models are significantly improved with assimilation of ocean topography measurements from even a single altimeter (see paper 5). Dramatic improvements can be achieved with assimilation of SSH data from a tandem altimeter mission. The optimal tandem orbit configuration for open-ocean data assimilation applications appears to be a T/P and Jason-1 mission with evenly spaced ground tracks and a 10-day exact repeat (paper 5). Further improvements could be achieved from a triplet altimeter mission with coordinated orbit configurations. Present data assimilative numerical models improve only slightly for constellations of more than three altimeters (paper 5). This is more a reflection of limitations of the data assimilation techniques than a statement of limited information content in multiple altimeter missions. Most problematic is the handling of the non-steric, wind-driven contribution to SSH that is temporally unresolved by satellite altimetry. To the extent that these signals are largely deterministic in nature, it may be possible to remove them based upon a high-resolution wind-driven barotropic ocean model (Shriver and Hurlburt, 2001).

High-resolution measurements of ocean topography would have a significant impact on other scientific investigations besides the mesoscale and coastal studies summarized above. For example, satellite altimetry has already revitalized the science of ocean tides (Le Provost, 2001). This is an area of research that progressed only slowly during the decades prior to the availability of highly precise altimeter data from T/P owing to the sparse sampling of the global network of tide gauges. The most energetic tidal variations have periodicities near semidiurnal and diurnal, which are temporally aliased in observations by any single altimeter (Le Provost, 2001). The T/P orbit was specifically chosen to avoid aliasing of the major tidal constituents to undesirable periodicities. Indeed, this was one of the primary constraints on selection of the 66° inclination and 9.9156-day exact repeat orbit configuration of T/P (Parke et al., 1987). By aliasing the most energetic tidal constituents into frequencies that can be distinguished from other SSH signals, the tidal signals are easily identified in the T/P data. As a result, it has been possible to estimate the tides globally from T/P data to an accuracy of 2-3 cm over the open ocean. Higher-resolution measurements of ocean topography would also benefit the estimation of the few tidal constituents that alias into undesirable periodicities (paper 7). An example is the K1 constituent that aliases into a period very near semiannual.

Spatial sampling of tidal variability becomes more of an issue in coastal regions and near major bathymetric features where tides have spatial scales much shorter than in the open ocean. Tidal variability in these regions cannot be resolved by measurements from a single nadir-looking altimeter. Studies of ocean tides in coastal regions and near bathymetric features would therefore benefit greatly from high-resolution measurements of ocean topography (paper 6).

One of the important discoveries from the T/P mission has been the observation of internal tides in ocean topography data (Ray and Mitchum, 1997). The expected wavelengths of internal tides are on the order of 100 km at midlatitudes, which cannot be adequately observed without higher resolution measurements of ocean topography than are presently available (paper 7). Internal tides play a very important role in the large-scale ocean circulation. The generation of internal tides is a mechanism for tidal dissipation and its resultant vertical mixing in the deep ocean (Munk and Wunsch, 1997). High-resolution ocean topography is required to map the global internal tide field in order to develop an accurate parameterization of vertical mixing for ocean general circulation models.

There are also important biogeochemical applications that could be investigated from altimeter data. Most physical-chemical-biological interaction occurs at scales shorter than the resolution of a single altimeter (paper 8). The ocean color data from SeaWiFS indicate the dominance of mesoscale variance with time scales of days to weeks and spatial scales of 40-400 km. Variability on these time and space scales accounts for 30-50% of the total variance, even in regions with strong seasonal variability. High-resolution ocean topography would provide information on the ocean circulation field for understanding this biogeochemical variability. Parameterization of these processes in models of the carbon cycle is key to understanding long-term climate variations. It is also noteworthy that a combination of simultaneous measurements from a traditional Ku-band altimeter (~14 GHz) and a Ka-band altimeter (~35 GHz, see paper 16) would yield improved estimates of the gas-transfer velocity across the air-sea interface based on surface roughness near the corresponding ocean wavelengths of 2.4 cm and 6.3 cm that are relevant to ocean-atmosphere gas exchange (see paper 8).

Non-oceanographic applications of altimeter data are also in need of higher resolution measurements of ocean topography than are available from past and present altimeter datasets. An example is the estimation of gravity anomalies associated with a variety of geophysical processes that occur within the earth's interior. Short-scale features in the gravity field can be inferred from the slope of the mean sea surface. The cumulative database from all past altimeter missions has already revolutionized the knowledge of marine gravity anomalies and their relation to lithospheric and mantle processes (Cazenave and Royer, 2001). Gravity anomalies with length scales of order 10 km and shorter and the associated short-scale features of ocean bathymetry could be estimated from high-resolution measurements of ocean topography (see paper 9; see also Sandwell and Smith, 2001). High-resolution measurements of the sea surface slope would result in advances in a host of marine geophysics applications, including a detailed mapping of seafloor roughness and its effects on the ocean circulation, determination of the structure of the continental margin, and exploration of offshore sedimentary basins. The ideal sampling pattern for such applications is a multiyear mission of highly precise measurements (instrumental errors of 1 cm or less) in a nonrepeating orbit that would sample the global ocean with a ground track spacing of about 5 km (paper 9). None of the high-resolution ocean topography technologies described in Part 3 of this report would achieve this goal. Measurements from these high-resolution ocean topography missions would nonetheless provide useful data for some geodetic applications.

Although a great deal has been learned from past altimeter studies, it is apparent from the above summary that there are many potential scientific applications of ocean topography measurements that have been limited by the coarse spatial resolution of SSH fields that can be constructed from a single altimeter dataset. There is clearly a strong scientific rationale for the need for higher-resolution measurements of ocean topography.

There are also important operational needs for higher resolution measurements of ocean topography (see paper 10). Operational applications for prediction of large-scale phenomena such as El Niño in the tropical Pacific are adequately addressed from SSH measurements by a single altimeter, assuming that the data are available in near real time. Outside of the tropics, however, prediction of seasonal-to-interannual variability of the ocean circulation and its effects on the overlying atmospheric circulation requires high-resolution ocean models constrained by high-resolution measurements of ocean topography (see paper 5). Moreover, operational needs of the U.S. Navy and NOAA for observations of shorter-scale phenomena associated with open-ocean mesoscale variability and coastal processes (see papers 2-5) suffer from the same sampling problems that limit scientific studies of these phenomena. These applications would benefit greatly from the higher resolution afforded by constellations of two or more satellites in coordinated orbit configurations. The much higher spatial resolution from a wide swath altimeter would be especially beneficial to operational needs for high-resolution measurements of ocean topography in the coastal environment. Navy applications include military and naval operations such as sea-lift ship routing, search and rescue, antisubmarine warfare, and coastal and mine warfare. NOAA applications include tidal information for navigation and hazard mitigation, ship routing, fisheries

forecasting, pollutant spill dispersion forecasting, forecasting of El Niño and other seasonal-to-interannual variability, oil rig design, location and monitoring of hazardous currents, marine resource management, and water level changes in the Great Lakes. Navy and NOAA coastal applications need measurements of ocean topography closer to land than is possible with conventional altimeters.

Measurement Opportunity from a Tandem T/P-Jason Mission

The overlap of the T/P mission with the ERS-1 and ERS-2 succession of altimeters has provided an opportunity to attempt high-resolution mapping of the SSH field from tandem altimeter datasets. The errors in mapping the SSH and geostrophic velocity fields are much reduced when compared with the results from a single altimeter mission (see papers 11 and 12). By the criteria described in the caption of Figure 2, a single altimeter in the T/P orbit can resolve variability with wavelengths and periods as short as about 5.5° and 20 days (see the upper left panel of Figure 2). In comparison, a tandem T/P-ERS (or, equivalently, a tandem Jason-ENVISAT) sampling pattern could resolve variability with wavelengths and periods as short as about 3.2° and 20 days (see the upper right panel of Figure 2). Because of the mismatch between the 10-day repeat and 66° inclination of the T/P and Jason orbits and the 35-day repeat and 98° inclination of the ERS and ENVISAT orbits, the resolution of the tandem Jason-ENVISAT sampling pattern falls short of the resolution that could be obtained from a tandem sampling pattern with coordinated orbit configurations (see below).

The launch of the Jason-1 altimeter scheduled for December 2001 offers the first opportunity for a coordinated tandem satellite mission for high-quality altimetric measurements of SSH. The Jason-1 altimeter is expected to have an accuracy as good as or better than that of T/P. Jason-1 will be launched into the same orbit as T/P, thus continuing the 9-year record of SSH along the T/P ground tracks. The value of continuing the T/P mission for as long as the dual-frequency altimeter and other system components continue to function well is self-evident. After an initial 6-month calibration and validation period following the launch of Jason-1, T/P could be maneuvered into a wide range of complementary orbits to enhance the sampling capability of a tandem mission. The specifics of a coordinated tandem mission therefore merit careful consideration.

One option for a tandem T/P-Jason mission is to maneuver T/P into an orbit that samples a ground track that is shifted longitudinally by 0.5°-0.75° for the purposes of estimating the surface geostrophic velocity along the satellite ground track. The extent to which this would be useful depends on the nature of the measurement and orbit errors, as well as the precise longitudinal and temporal separations of the parallel sampling by the two altimeters (see papers 13 and 14). In view of the 2-3 cm long-wavelength measurement and orbit errors in the T/P data and similar errors that can be anticipated for Jason-1, even after empirical orbit error reduction, the merits of a tandem T/P-Jason mission with closely spaced parallel ground tracks may not outweigh the disadvantage that many applications of high-resolution ocean topography would not benefit from this sampling pattern (see the papers in Part 1 of this report).

For mapping the SSH field, the optimal tandem orbit configuration consists of an interleaved sampling pattern in which the ground tracks of T/P fall half way between the Jason-1 ground tracks. Such a tandem T/P-Jason mission could achieve a wavelength and period resolution of about 2.8° by 20 days (see the lower left panel of Figure 2), which is about a factor of two better than the approximate 5.5° wavelength resolution of SSH fields constructed from a single altimeter in the T/P orbit configuration. This would enable scientific investigations that have not heretofore been possible from past and present altimeter datasets. Among the numerous science benefits, the enhanced resolution of the SSH field the tandem T/P-Jason sampling pattern would allow the study of the puzzling nondispersive characteristics of short-scale Rossby waves (paper 12). The interleaved, evenly spaced sampling pattern would further provide the data constraints needed for data-assimilative eddy-resolving numerical models for research and operational applications (paper 5). The interleaved tandem T/P-Jason sampling pattern would also benefit tidal studies (papers 6 and 7) and numerous operational applications (papers 5 and 10).

An evenly spaced, interleaved T/P-Jason sampling pattern would also result in a four-fold increase in the number of crossover points at which the geostrophic velocity can be estimated by the crossover method (papers 13 and 14). This would enable investigation of the effects of eddy Reynolds stresses on currents such as Gulf Stream (paper 14).

After the launch of ENVISAT scheduled for January 2002, the wavelength resolution of SSH fields constructed from a triplet T/P-Jason-ENVISAT mission would further improve to about 2.5° (see the lower right panel of Figure 2). It should be noted, however, that, because of the mismatch between the 35-day repeat and 98° inclination of the ENVISAT orbit and the 10-day repeat and 66° inclination of the T/P and Jason orbits, the resolution capability of the triplet T/P-Jason-ENVISAT sampling pattern falls short of what could be achieved with a triplet sampling pattern with coordinated orbit configurations. For example, the wavelength resolution capability of a triad of altimeters in the T/P 10-day orbit configuration with evenly spaced ground tracks would be expected to be better than 2°.

Although not sufficient for addressing the full range of short-scale phenomena in the open ocean and coastal regions, a tandem T/P-Jason mission with evenly spaced ground tracks would nonetheless benefit these studies as summarized in the papers in Part 1. The enhanced resolution obtainable from a triplet T/P-Jason-ENVISAT mission would further address the needs of many of these applications. It is important to re-emphasize that the resolution capability of such a triplet mission depends critically on the coordinated T/P and Jason orbits with interleaved, evenly spaced ground tracks; the 3.2° wavelength resolution of SSH fields constructed from Jason and ENVISAT alone falls short of the 2.8° wavelength resolution that would be obtained even from just a tandem T/P-Jason mission (see the upper right and lower left panels of Figure 2). A tandem T/P-Jason mission and the added benefit of simultaneous ENVISAT data therefore offer an opportunistic stepping-stone toward an ultimate goal of obtaining high-resolution ocean topography measurements from a constellation of three or more altimeters with coordinated orbit configurations (papers 15 and 16) or a wide swath altimeter system such as WSOA (paper 17) or GPS altimetry (paper 18).

New Measurement Technologies

Low-Cost Altimeter Constellation

A direct approach to obtaining high-resolution measurements of ocean topography is to fly multiple altimeters in formation flight. Aside from multiple satellite altimeter missions of opportunity (e.g., the simultaneous operation of T/P, Jason-1 and ENVISAT discussed in the previous section), cost is a significant consideration in the design of a multi-satellite altimeter mission. The overall cost of the system can be minimized by reducing the physical size and power consumption of the altimeters. An important advantage of a multi-satellite altimeter mission is the robustness of the system design; if one of the altimeters in the constellation fails, the other altimeters would still provide valuable measurements of ocean topography. Indeed, if all but one of the multiple altimeters were to fail, the last remaining altimeter (based on one of the new instrument designs summarized below) would provide data that are more accurate than the data that are presently provided by T/P. As summarized below, two approaches to multi-satellite altimeter constellations have been proposed.

WITTEX Delay-Doppler Altimetry. The Doppler shift of the frequency of the radar return echoes can be utilized to reduce the effective footprint of the radar (see paper 15). It then becomes possible to average more pulses to reduce the measurement noise for a given along-track spatial resolution. Alternatively, the power of the instrument can be reduced to maintain the same level of noise as a conventional altimeter. The intrinsic higher resolution also makes the instrument potentially more useful for coastal applications that would benefit from measurements of ocean topography closer to land than has been possible from past and present altimeters. Based on the delay-Doppler altimeter design (Raney, 1998), it is possible to build low-power, small-size altimeters that are affordable for multi-satellite deployments. A constellation of 3 to 5 such altimeters deployed from a single launch vehicle is described in paper 15. Each satellite in

the system would include a dual-frequency altimeter with a 3-frequency microwave radiometer sharing the same antenna. This instrument package would enable corrections for ionospheric and tropospheric range delays. In a given orbital plane, the individual satellites can be maneuvered into sequential orbits to produce interleaved ground track patterns with a wide range of possible sampling characteristics. In honor of Emil Witte, who first formulated the geostrophic equation in 1878, this concept is named WITTEX.

If each satellite in the WITTEX constellation includes a bistatic radar (i.e., a radar that can receive the reflections from the radars on the other satellites in the constellation, as well as its own reflected signals), then additional SSH measurements can be obtained along tracks between neighboring satellite ground tracks. By this technique, n satellites could provide measurements along 2n-1 parallel tracks. Thus, for example, measurements of SSH along five evenly spaced parallel lines could be obtained from only three altimeters.

AltiKa Ka-band Altimetry. In the Ka band of microwave radio frequencies (~35 GHz), the ionospheric range delay becomes sufficiently small that accurate range measurements can be obtained from a single-frequency altimeter. Other advantages of a Ka-band altimeter over the conventional Ku-band (~14 GHz) altimeter include a shorter decorrelation time scales of radar echoes, which allows a higher pulse repetition frequency that can be exploited to reduce measurement noise. In addition, the smaller antenna beamwidth for Ka-band radar measurements would allow a sharper return echo that would enable measurements closer to land for coastal applications. The higher-frequency altimeter system would also allow an increased frequency bandwidth, which would improve the vertical resolution of the range measurements. A limitation of Ka-band altimetry is that the measurements are more sensitive to liquid cloud droplet and rain attenuation (Monaldo et al., 1986). This would result in a greater loss of Ka-band altimeter data compared with conventional Ku-band altimetry. The data loss would typically be 5-10% globally, with a greater loss in the tropical regions of persistent heavy cloud cover and rain.

A low-cost instrument package for multiple deployments of Ka-band altimeters is described in paper 16. Launching multiple (up to 3) satellites by a single launcher is also feasible. This system is called AltiKa. Each altimeter in the AltiKa constellation would include a dual-frequency radiometer that would share the antenna with the altimeter for tropospheric corrections of the range measurements.

Wide-Swath Ocean Altimeter

A wide-swath ocean altimeter (WSOA) system that measures the range to the sea surface over a swath based on the concept of radar interferometry is described in paper 17. The instrument consists of two side-looking fan-beam antennae separated by a boom with a length of 5-10 m. Interferometry performed on the returned signals from the same targets on the ocean surface within a small off-nadir angle of incidence of about 4° yields SSH measurements across a swath width of about 200 km centered along the satellite ground track. This interferometric system would be used in conjunction with a dual-frequency altimeter with a 3-frequency water vapor radiometer that would provide nadir observations and environmental corrections. The lateral separation between the nadir water vapor and ionospheric corrections and the off-nadir range measurements from WSOA would introduce some error, but this is relatively small over the ±100 km distances between nadir and the outer edges of the WSOA swath. The effects of sea-state bias on interferometric measurements of range need further investigation.

Because the off-nadir returns measured by the interferometer are not from "natural" reflection points of specular return, as are the measurements made by nadir-looking or bistatic off-nadir altimeters (see paper 15), the accuracy of interferometric measurements of range are very sensitive to the attitude of the antenna. Crossover adjustments similar to the techniques used in the past for orbit error corrections (e.g., Fu and Vazquez, 1988) would have to be applied to correct for the effects of pitch and roll of the satellite. Simulations that take into account all of the measurement errors and the sampling errors from unresolved high-frequency mesoscale variability that would corrupt the crossover adjustment conclude

that the off-nadir measurement errors can be reduced to 3 cm at 15 km along-track and cross-track resolution. This measurement accuracy has not yet been demonstrated from in-flight measurements.

It should be noted that the ~3 cm instrumental errors for WSOA compared with the 1-2 cm instrumental errors of conventional altimeters effectively reduces the spatial resolution of the WSOA data somewhat. The extent to which WSOA measurements would be useful depends on the exact magnitude of the measurement errors and their detailed spatial structure, as well as the relationship between the resulting wavenumber spectrum of measurement errors and the signal spectrum of interest (see Figure 4). The analysis presented in paper 11 suggests that, after a crossover adjustment to remove measurement biases, WSOA may yield SSH fields in typical open-ocean conditions with spatial resolution only as good as that which could be obtained from a constellation of four conventional altimeters. In regions of energetic mesoscale variability (e.g., near the western boundary currents and the Antarctic Circumpolar Current), the resolution capability of WSOA would be much better than that of a quartet of conventional altimeters. The utility of the WSOA data in regions of less energetic mesoscale variability may improve significantly with further refinements of the measurement techniques and ground-based processing to reduce the measurement biases.

WSOA could be implemented for a flight demonstration on a conventional altimeter satellite such as Jason-2. Because of the yaw-steering of the Jason-2 satellite, data return from the WSOA would be limited to about 50%. Simulations indicate that an accuracy of 3 cm could be achieved from a 6.4 m baseline mast on Jason-2 (see paper 17). The errors could be further reduced by forming mosaics of the data over the 10-day orbit repeat period. These accuracies depend on the efficiency of the crossover calibration technique. Verification of this technique is a primary objective of including WSOA on the Jason-2 platform. Note that simulations indicate that interferometric measurements from a longer baseline mast length of 10 m on an operational WSOA mission could achieve a measurement accuracy of 2 cm (paper 17). When flown on a satellite that does not require yaw-steering, WSOA would provide near-global coverage of the ice-free ocean surface every 10 days.

Since the WSOA concept requires independent and simultaneous measurements from a highly accurate nadir-looking altimeter to enable the removal of measurement biases by crossover adjustments, it is important to note that the data along the nadir track would in no way be compromised by the WSOA. When included on Jason-2 or on one of the satellites in a constellation of WITTEX or AltiKa altimeters, the nadir-looking altimeter would maintain a long record of highly accurate measurements of ocean topography along the present T/P ground tracks (to be continued by Jason-1 and Jason-2) for large-scale ocean circulation studies.

Altimetry from GPS Reflections

The reflections of signals from the satellite constellation of the Global Positioning System (GPS) can be measured by a receiver on an earth-orbiting satellite to obtain altimetric measurements of ocean topography as described in paper 18. Such a concept has been demonstrated by analysis of signals measured by a receiver on a Space Shuttle. Over a 10-day period, a single receiver at an altitude of 400 km is capable of receiving about 12 reflections from any given 50 km cell on the earth's surface with the current constellation of 24 GPS satellites. Simulations indicate that a group of 8 optimally deployed low-power and low-cost receivers and multibeam high-gain antennas on satellites of opportunity could provide 10-day maps of SSH with an rms accuracy of 6 cm and a resolution of 25 km. Receivers mounted on the ground at some elevation (~200 m) have also been demonstrated to be useful for monitoring sea level variations in the coastal regions.

As with the WSOA system, the utility of GPS measurements of high-resolution ocean topography depends on the spectral characteristics of the measurement errors. It should also be noted that the effects of sea-state bias on GPS altimetry need further investigation. Although the technique of altimetry from

GPS reflections is less mature than the other new technologies summarized above, the potential for obtaining global high-resolution ocean topography from GPS is appealing.

Discussion and Recommendations

The earth system involves a continuum of variability across all space and time scales, as well as non-linear interactions between the different scales. The papers in Part 1 of this report summarize a broad range of scientific and operational applications that demonstrate various aspects of the linkages between small and large scales of oceanography and geophysics. Fundamental advancements in scientific and operational applications are anticipated if the resolution of ocean topography can be significantly improved relative to what has heretofore been available from past and present altimeter missions.

A variety of approaches to high-resolution measurements of ocean topography are addressed in this report. First and foremost, existing mission opportunities should be fully exploited to improve the resolution compared with what can be obtained from a single altimeter in the T/P orbit (see papers 5, 11 and 12). The benefits of combining T/P and ERS altimeter data have been demonstrated (compare the upper two panels of Figure 2). Improved accuracy could be obtained from the tandem mission opportunity that will become available with the launch of Jason-1 (see the lower left panel of Figure 2), which will provide the first opportunity to conduct a coordinated tandem mission for optimizing the benefits of two simultaneously operating altimeters. Among many scientific and operational applications, the ability to produce much improved measurements of ocean current and eddy fields would allow the study of eddy-mean flow interaction, a topic of great importance to ocean climate that has been unaddressable because of a lack of adequate observations (see papers 2 and 14).

As a first step toward obtaining measurements of ocean topography with spatial resolution higher than has been possible from past and present altimeter datasets, ***the High-Resolution Ocean Topography Science Working Group strongly recommends that NASA continue operation of T/P for as long as the instrument continues to function well. Specifically, we endorse the November 2000 recommendation of the Jason Science Working Team for the optimal sampling pattern for mapping the SSH field from simultaneous operation of T/P and Jason-1 after the initial 6-month calibration and validation phase of the Jason-1 mission.*** This would be achieved by maintaining Jason-1 in the present T/P sampling pattern and maneuvering T/P to sample along ground tracks half way between the present T/P ground tracks, resulting in a tandem mission with evenly spaced ground tracks separated by 1.417° of longitude. T/P would have to be maintained in this new orbit for at least six months, and preferably more than a year, to obtain an accurate estimate of the geoid and mean sea surface and scientifically useful measurements of SSH variability.

We note that the time offset between the parallel tracks of the tandem sampling pattern is in need of further review, taking into consideration the relative merits of an optimal 0-day offset for parallel track estimates of geostrophic velocity (paper 13) versus an optimal 5-day offset for mapping the SSH field (paper 12), as well as any engineering constraints that may exist for the orbit maneuvers required to adjust the T/P orbit. ***The High-Resolution Ocean Topography Science Working Group therefore defers recommendation of the time offset between parallel T/P and Jason-1 ground tracks to the judgement of the Jason Science Working Team.***

In addition to improved spatial resolution of ocean topography, extended operation of T/P beyond the 6-month calibration and validation phase of the Jason-1 mission would provide backup in case of instrument malfunction or failure of the Jason-1 satellite. The premature termination of the NASA Scatterometer (NSCAT) data record after 9 months of flawless operation owing to the catastrophic failure of the solar array on ADEOS-I is a sobering reminder that such an event can occur at any time during a satellite mission.

The interleaved T/P and Jason-1 sampling pattern with evenly spaced ground tracks would double the spatial resolution of SSH fields constructed from a single altimeter in the T/P orbit configuration. Moreover, the 2.8° wavelength resolution of such a tandem T/P-Jason mission would significantly improve the 3.2° wavelength resolution that can be obtained from the uncoordinated tandem sampling patterns of Jason-1 and ENVISAT (see Figure 2). After the January 2002 launch of ENVISAT, continued simultaneous operation of T/P and Jason-1 would result in a triplet T/P-Jason-ENVISAT sampling pattern that would further improve the resolution capability of SSH fields to wavelengths as short as about 2.5°. It is important to emphasize that the high resolution obtainable from the triplet mission depends critically on the interleaved, evenly spaced ground tracks of the T/P and Jason components of the triad of altimeters; the lack of coordination of the ENVISAT orbit with the T/P and Jason-1 orbits lessens the resolution that could be obtained from coordinated orbit configurations. For example, a triad of altimeters with 10-day orbit repeat periods and evenly spaced ground tracks would be expected to resolve wavelengths as short as about 2°, which is a significant improvement over the 2.5° wavelength resolution of the triplet T/P-Jason-ENVISAT sampling pattern.

A Jason-2 follow-on altimeter mission has been approved for a new start. Planning is proceeding for a December 2005 launch date. Assuming that Jason-1 continues to function well at that time, ***the High-Resolution Ocean Topography Science Working Group recommends that operation of the Jason-1 altimeter be continued beyond the 6-month calibration and validation phase of the Jason-2 altimeter mission.*** Specifically, Jason-2 should maintain the present T/P sampling pattern (extended by Jason-1) and Jason-1 should be maneuvered into the interleaved, evenly spaced sampling pattern recommended above for T/P.

There is presently no approved follow-on to the ENVISAT altimeter. The high-resolution measurements of ocean topography from combinations of T/P, Jason and ENVISAT data are therefore in jeopardy of being discontinued at the termination of the ENVISAT mission. Moreover, while tandem T/P-Jason, tandem Jason-ENVISAT and triplet T/P-Jason-ENVISAT missions would significantly expand the range of scientific questions that could be investigated, there are still many processes with spatial and temporal scales of variability that cannot be adequately addressed from such sampling patterns.

A cost effective and straightforward approach to continuing multi-satellite altimetry beyond ENVISAT, while at the same time further increasing the resolution of the ocean topography measurements, is to fly a constellation of 3 or more altimeters in coordinated orbit configurations. In the past, such an approach has been infeasible because of cost considerations. New technologies provide promising approaches with greatly reduced costs. The WITTEX concept based on the delay-Doppler technique (paper 15) consists of several low-cost altimeters launched on a single vehicle and maneuvered into different orbits with a wide range of possible ground track separations. The AltiKa concept based on Ka-band altimetry, which obviates the need for dual-frequency altimetry because of the small ionospheric effects in Ka band, leads to a different scenario for launching multiple low-cost nadir-looking altimeters from a single launcher (paper 16). The WITTEX approach also addresses the possibility of bistatic radar altimeter measurements for maximizing the resolution from a given number of altimeters; a constellation of n altimeters with bistatic radars would yield SSH measurements along 2n-1 parallel ground tracks.

An advantage of the WITTEX and AltiKa approaches to obtaining higher-resolution measurements of ocean topography is that they are based on a heritage of nadir-looking altimetry and the robustness of the so-called natural point measurements of specular radar returns (paper 15). In multi-satellite configurations, they therefore represent low-risk systems for obtaining higher-resolution measurements of ocean topography than has been available from past and present altimeter datasets. The multiple altimeters also provide backup for a reduced mission in case of failures of individual instruments or spacecraft. A concern is the effects of the large-scale orbit errors, which are independent from track to track. Orbit errors become progressively more problematic as the ground track spacing decreases, especially for ocean velocity estimates (papers 13 and 14). The technique developed by Le Traon et al.

(1998) and the synchronous crossovers of the parallel ground tracks at their maximal latitudes could be utilized to reduce the orbit errors of the multiple satellites. With the AltiKa concept, an additional concern is the limiting effects of cloud and rain on the Ka-band data return, which would result in increased data loss compared with the traditional Ku-band altimeter systems, especially in the tropics.

The new technologies for swath measurements of high-resolution ocean topography (see below) are not yet sufficiently mature to be considered replacements for nadir-looking altimeter systems. To assure a continuation of the high-resolution measurements established by the tandem and triplet sampling from T/P, Jason-1, ENVISAT and Jason-2, ***the High-Resolution Ocean Topography Science Working Group recommends that planning begin immediately to build and launch a constellation of low-cost, low-risk altimeters (e.g., WITTEX or AltiKa) as a follow-on of ENVISAT and Jason-2.*** In view of the lead-time required to establish such an altimeter system, the importance of the immediacy of this action cannot be overstated.

It should be emphasized that the specific orbit configuration is a very important consideration in the design of any single or multi-satellite nadir-looking altimeter system. In particular, sun-synchronous orbits are to be avoided because of the detrimental effects of tidal aliasing on the SSH estimates (Parke et al., 1987; Le Provost, 2001; Chelton et al., 2001). Likewise, the 17-day repeat of the Geosat orbit is to be avoided because it aliases the dominant tidal constituent into a period that is difficult to distinguish from the annual period (Schlax and Chelton, 1994).

The viability of a multi-satellite altimeter mission for high-resolution measurements of ocean topography becomes more of an issue as the desired sampling resolution increases. For example, measurements of ocean topography along parallel ground tracks separated longitudinally by 0.15° would require a constellation of 15 altimeters. This is clearly beyond the feasibility of even the low-cost WITTEX or AltiKa altimeter systems. For such high spatial resolution, the only feasible system is one that measures ocean topography over a swath. Wide-swath altimeters have been considered in the past (Bush et al., 1984), but the large pointing errors have prevented a realistic design of the approach. As a result of new antenna technologies, wide-swath altimetry by interferometry has become technologically and economically feasible (paper 17). Although the errors in the knowledge of the spacecraft attitude are still a significant source of measurement error, it has been demonstrated from simulations that it should be possible from ground processing to reduce such errors to a level where the data become useful for scientific studies. The unique advantage of a wide-swath altimeter, such as WSOA described in paper 17, is its ability to sample more than 90% of the surface of the global oceans from a single spacecraft with a 15-km resolution. Such an approach has not yet been demonstrated in orbit and the effectiveness of the ground processing in removing the attitude errors is a concern. However, given the superior coverage and potential cost-effectiveness of WSOA, ***the High-Resolution Ocean Topography Science Working Group recommends that a flight demonstration of this new technique be conducted at the earliest possible opportunity. In particular, WSOA should be included on the Jason-2 platform that is presently planned for a launch in December 2005.***

Another promising approach for obtaining "swath" measurements of ocean topography is a synthesis of the wealth of information contained in the reflections of the signals from the constellation of GPS satellites (paper 18). The GPS signals are available at no cost. The altimetric application of these signals requires only low-cost, low-power receivers and multibeam high-gain antennas on satellites of opportunity. The coverage of the GPS reflections is spatially dense and frequent, making it potentially powerful for mapping ocean topography globally with high resolution. Furthermore, the maintenance and operation of the GPS constellation is driven by other applications and therefore does not incur any costs on oceanography programs. Presently, the GPS technology lags behind the other new technologies for high-resolution measurements of ocean topography. The details of the ocean reflection of L-band signals are not fully understood. Because the GPS system is not designed for precision ranging of the ocean surface, the measurement errors are a major concern. For example, the effects of the sea-state bias on range measurements at L-band frequencies is not yet known. However, because of the exciting potential

of global coverage from GPS altimetry, ***the High-Resolution Ocean Topography Science Working Group recommends that more extensive flight demonstrations of GPS altimetry be conducted in concert with further technology development to improve the understanding of the GPS capability for high-resolution measurements of ocean topography***.

Summary

The recommendations in the previous section form a framework for the evolutionary development of a system for addressing the scientific and operational needs for high-resolution measurements of ocean topography. The first and easiest step is to continue the T/P mission in tandem with the Jason-1 altimeter mission. After an initial 6-month calibration and validation phase following the December 2001 launch of Jason-1, T/P should be maneuvered into an interleaved orbit to sample ground tracks half way between the present T/P ground tracks. This would yield SSH fields with double the spatial resolution that can be obtained from a single altimeter in the T/P orbit configuration; spatial variability with wavelengths as short as about 2.8° would be resolved by the tandem mission, compared with a wavelength cutoff of about 5.5° from the single-altimeter T/P sampling pattern. Moreover, after the January 2002 launch of ENVISAT, the simultaneous operations of T/P, Jason-1 and ENVISAT would further improve the resolution capability to wavelengths as short as about 2.5°.

In addition to improved spatial resolution of ocean topography, extended operation of T/P would provide backup in the event of premature failure of the Jason-1 or ENVISAT altimeters.

For the same reasons, after an initial 6-month calibration and validation phase following the launch of Jason-2 (currently planned for December 2005), Jason-1 should be maneuvered into the interleaved orbit to continue the higher-resolution measurements of ocean topography established by a tandem T/P-Jason-1 mission.

There are presently no plans for follow-ons of the ENVISAT or Jason-2 altimeters. A second step toward sustaining a long record of altimetric data and obtaining high-resolution measurements of ocean topography is to begin planning immediately for a multi-satellite altimeter mission as a follow-on to the ENVISAT and Jason-2 altimeters. This system could be based upon the low-cost, low-risk WITTEX or AltiKa altimeter designs and should include at least three altimeters in carefully coordinated orbit configurations. To maximize the efficiency of the multi-satellite constellation of altimeters, the use of bistatic radars should be given careful consideration. A constellation of three satellites would thus provide measurements along five parallel tracks. More generally, a constellation of n altimeters would provide measurements along 2n-1 parallel tracks.

In parallel with the planning of a multi-satellite constellation of altimeters, there should be continued investigation of the new technologies of WSOA and GPS for obtaining very high-resolution measurements of ocean topography. This should include flight demonstrations and further technology development. Specifically, WSOA should be included on the Jason-2 platform for in-flight proof of concept of the interferometric measurement technology. As the WSOA and GPS measurement technologies become mature, a transition from a multi-satellite constellation of altimeters to WSOA and/or GPS altimetry can be envisioned to satisfy the scientific and operational needs for high-resolution measurements of ocean topography summarized in the papers in Part 1 of this report. At such time as this becomes feasible, it will still be necessary to operate at least one nadir-looking altimeter for calibration of the WSOA and GPS altimetric data and to maintain a long record of highly accurate measurements of ocean topography along the present T/P ground tracks (to be continued by Jason-1 and Jason-2) for large-scale ocean circulation studies.

References

Bush, G. B., E. B. Dobson, R. Matyskiela, C. C. Kilgus, and E. J. Walsh, 1984: An analysis of a satellite multibeam altimeter. *Mar. Geod*., **8**, 345-384.

Cazenave, A and J.-Y. Royer, 2001: Applications to marine geophysics. In *Satellite Altimetry and Earth Sciences,* L.-L. Fu and A. Cazenave, Eds., Academic Press, San Diego, pp. 407-440.

Chelton, D.B., J.C. Ries, B.J. Haines, L.-L. Fu and P.S. Callahan, 2001: Satellite altimetry. In *Satellite Altimetry and the Earth Sciences: A Handbook for Techniques and Applications*, L.-L. Fu and A. Cazenave, Eds., Academic Press, pp. 1-131.

Fu, L.-L., and A. Cazenave, editors, 2001: *Satellite Altimetry and Earth Sciences: A Handbook of Techniques and Applications*, Academic Press, San Diego, 463 pp.

Fu, L.-L., and D. B. Chelton, 2001: Large-scale ocean circulation. In *Satellite Altimetry and Earth Sciences,* L.-L. Fu and A. Cazenave, Eds., Academic Press, San Diego, pp. 133-169.

Fu, L.-L., W. T. Liu and M. R. Abbott, 1990: Satellite remote sensing of the ocean. In *The Sea.* Vol. 9, pp. 1193-1236, John Wiley and Sons, New York.

Fu, L.-L., and J. Vazquez, 1988: On correcting radial orbit errors for altimetric satellites using crossover analysis. *J. Atmos. Oceanic Technol*., **5**, 466-471.

Greenslade, D. J. M., D. B. Chelton and M. G. Schlax, 1997: The midlatitude resolution capability of sea level fields constructed from single and multiple satellite altimeter datasets. *J. Atmos. Ocean. Technol*., **14**, 849-870.

Hasselmann, K., 1976, Stochastic climate models. Part I. Theory, *Tellus*, **28**, 473-485.

Le Provost, C., 2001: Ocean tides. In *Satellite Altimetry and Earth Sciences,* L.-L. Fu and A. Cazenave, Eds., Academic Press, San Diego, pp. 267-303.

Le Traon, P.-Y., F. Nadal and N. Ducet, 1998: An improved mapping method of multisatellite data. *J. Atmos. Oceanic Technol*., **15**, 522-534.

Le Traon, P.-Y., and R. Morrow, 2001: Ocean currents and eddies. In *Satellite Altimetry and Earth Sciences,* L.-L. Fu and A. Cazenave, Eds., Academic Press, San Diego, pp. 171-215.

Monaldo, F. M., J. Goldhirsh and E. J. Walsh, 1986: Altimeter height measurement error introduced by the presence of variable cloud and rain attenuation. *J. Geophys. Res.*, **91**, 2345-2350.

Morrow, R., R. Coleman, J. Church and D. Chelton, 1994: Surface eddy momentum flux and velocity variances in the Southern Ocean from Geosat altimetry. *J. Phys. Ocean*., **24**, 2050-2071.

Munk, W. H., and C. Wunsch, 1997: The moon, of course. *Oceanography*, **10**, 132-134.

Parke, M.E., R.L. Stewart, D.L. Farless and D.E. Cartwright, 1987: On the choice of orbits for an altimetric satellite to study ocean circulation and tides. *J. Geophys. Res*., **92**, 11,693-11,707.

Raney, R. K., 1998: The delay-Doppler radar altimeter. *IEEE Trans. Geosci. Rem. Sens*., **36**, 1578-1588.

Ray, R. D., and G. T. Mitchum, 1997: Surface manifestation of internal tides in the deep ocean. *Prog. Oceanogr.*, **40**, 135-162.

Robinson, A. R., ed., 1982: *Eddies in Marine Science*. Springer-Verlag, Berlin, 609 pp.

Sandwell, D. T., and W. H. F. Smith, 2001: Bathymetric estimation. In *Satellite Altimetry and Earth Sciences,* L.-L. Fu and A. Cazenave, Eds., Academic Press, San Diego, pp. 441-457.

Schlax, M. G., and D. B. Chelton, 1994: Detecting aliased tidal errors in altimeter height measurements. *J. Geophys. Res.*, **99**, 12,603-12,612.

Shriver, J. F., and H. E. Hurlburt, 2001: Non-steric, wind-forced variability, can it be reliably nowcasted? *Geophys. Res. Lett*., submitted.

Stammer, D., C. Wunsch, and R. M. Ponte, 2000: De-Aliasing of Global High Frequency Barotropic Motions in Altimeter Observations, *Geophys. Res. Lett*., **27**, 1175-1178.

Tierney, C., J. Wahr, F. Bryan, and V. Zlotnicki, 2000: Short-period oceanic circulation: implications for satellite altimetry. *Geophys. Res. Lett*., **27**, 1255-1258.

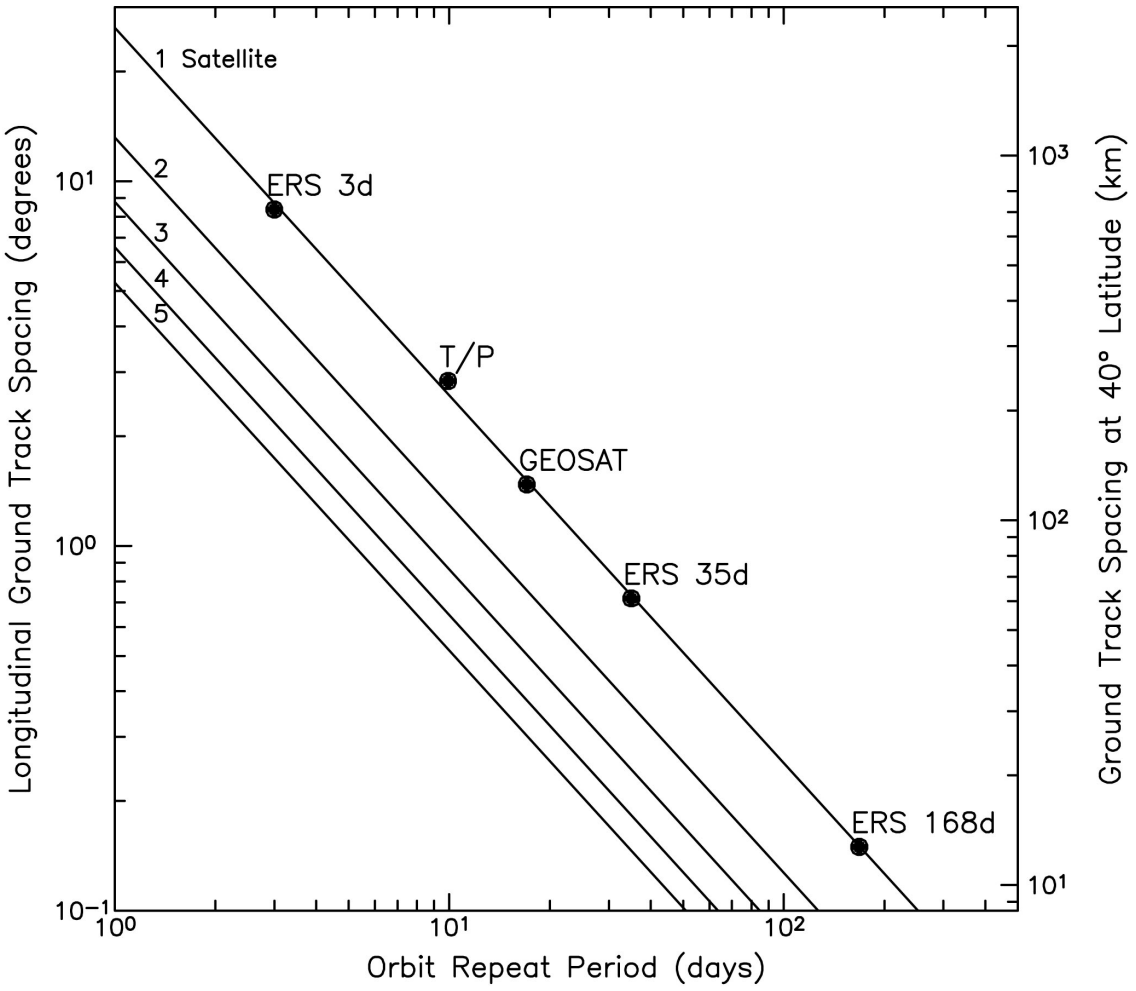

Figure 1. The relationship between orbit repeat period and the longitudinal separation of neighboring ground tracks for altimeters in exact repeat orbit configurations. The ground track spacing is displayed in degrees along the left axis and in kilometers at 40° latitude along the right axis. In log-log space, the choices of exact repeat period and ground track spacing for a single satellite fall approximately along the top straight line in the figure. The repeat periods and ground track separations of past and present altimeter missions are shown by the solid circles. The three sampling patterns shown for the ERS altimeter correspond to the Ice Phase (3-day repeat), the Multi-Disciplinary Phase (35-day repeat) and the Geodetic Phase (168-day repeat) of the ERS-1 satellite. The improvements in the resolution that would be obtained from multiple satellites in coordinated orbit configurations with evenly spaced ground tracks are shown for constellations of 2, 3, 4 and 5 satellites.

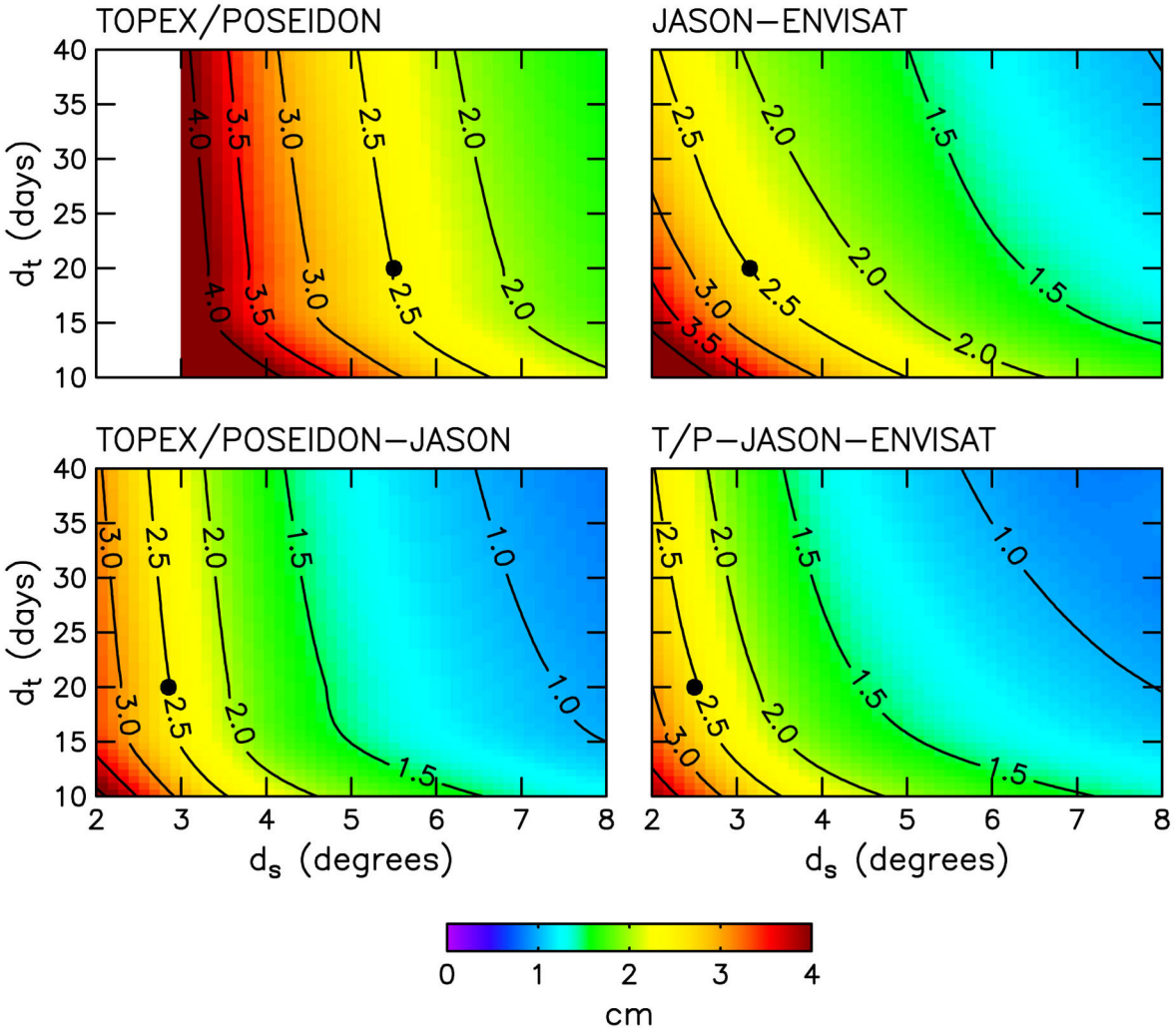

Figure 2. The root mean squared errors of SSH fields constructed at subtropical latitudes from four different altimeter sampling patterns with smoothing parameters that correspond to spatial filter cutoff wavelengths d_s ranging from 2° to 8° and temporal filter cutoff periods d_t ranging from 10 to 40 days (see paper 12 for details). Mapping errors are slightly larger at lower latitudes and smaller at higher latitudes (see paper 12 in this report). Error estimates are based on an SSH signal with assumed spatial and temporal autocorrelation scales of 50 km and 30 days and a standard deviation of 10 cm. Mapping errors scale roughly linearly with the signal standard deviation. The sampling patterns shown are a single altimeter in the T/P orbit (upper left panel), a tandem Jason-ENVISAT (upper right panel), a tandem T/P-ERS or, equivalently, a tandem T/P-Jason (lower left panel), and a triplet T/P-Jason-ENVISAT (lower right panel). The mapping errors in the upper left panel are not shown for d_s less than 3° because the coarse 2.834° ground track spacing is unable to resolve such short scales. The dots in each panel indicate the spatial and temporal resolution capability based on the choice of a temporal filter cutoff period of 20 days and a threshold tolerance of 2.5 cm for the average mapping error. By these criteria, the T/P, Jason-ENVISAT, T/P-Jason and T/P-Jason-ENVISAT sampling patterns can resolve variability with spatial filter cutoff wavelengths of about 5.5°, 3.2°, 2.8° and 2.5°, respectively. If a different threshold tolerance for the average mapping error is adopted, the conclusions about the precise values of the wavelength resolution sapability would differ somewhat. However, the relative accuracies of the various sampling patterns would not differ much from the values stated above.

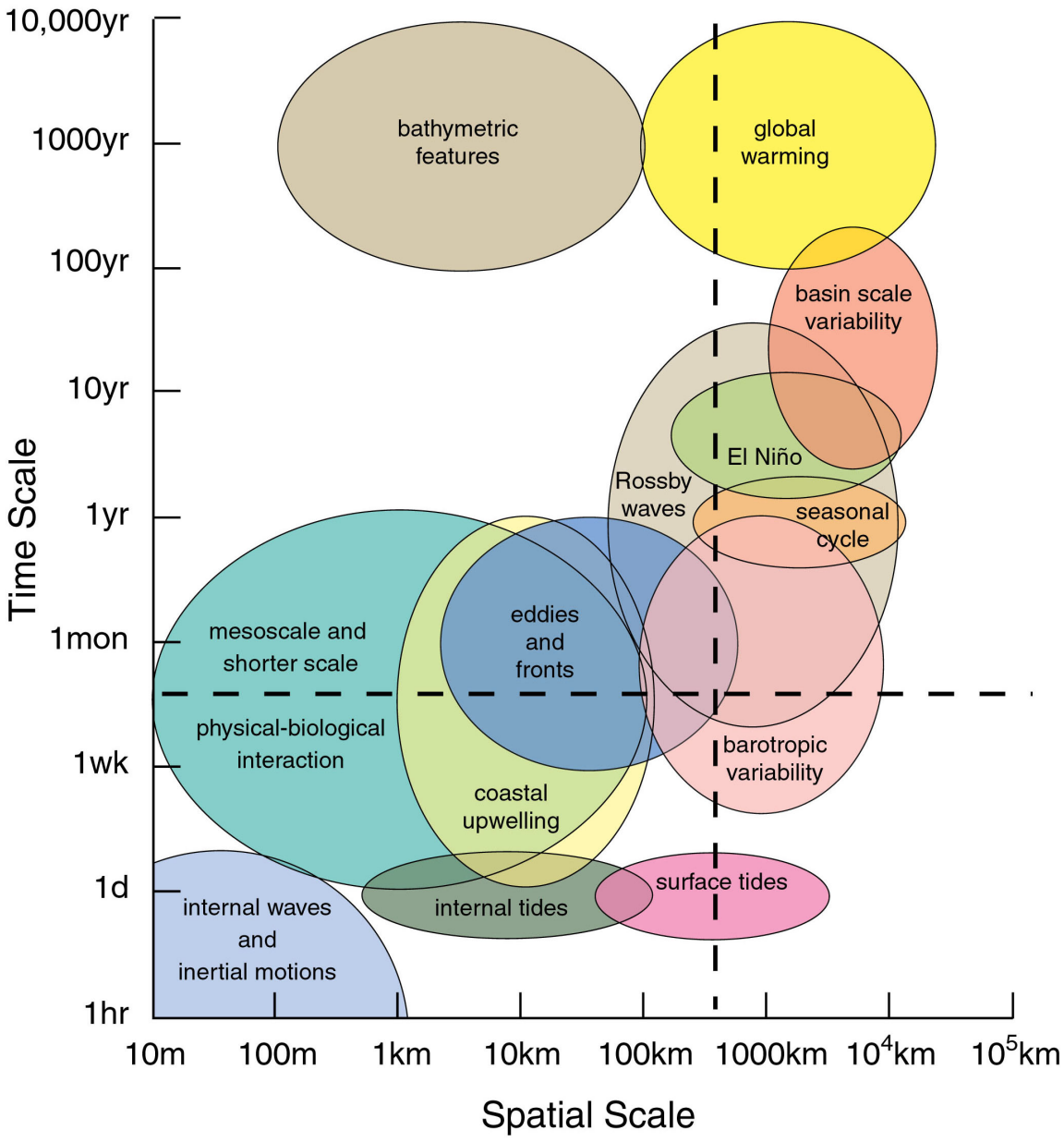

Figure 3. The approximate space and time scales of phenomena of interest that could be investigated from altimetric measurements of ocean topography with adequate spatial and temporal resolution. The dashed lines indicate the approximate lower bounds of the space and time scales that can be resolved in SSH fields constructed from measurements by a single altimeter in the T/P 10-day repeat orbit configuration. Processes with spatial scales to the left of the vertical dashed line and time scales below the horizontal dashed line require higher resolution measurements of ocean topography from a constellation of nadir-looking altimeters or a wide-swath altimeter.

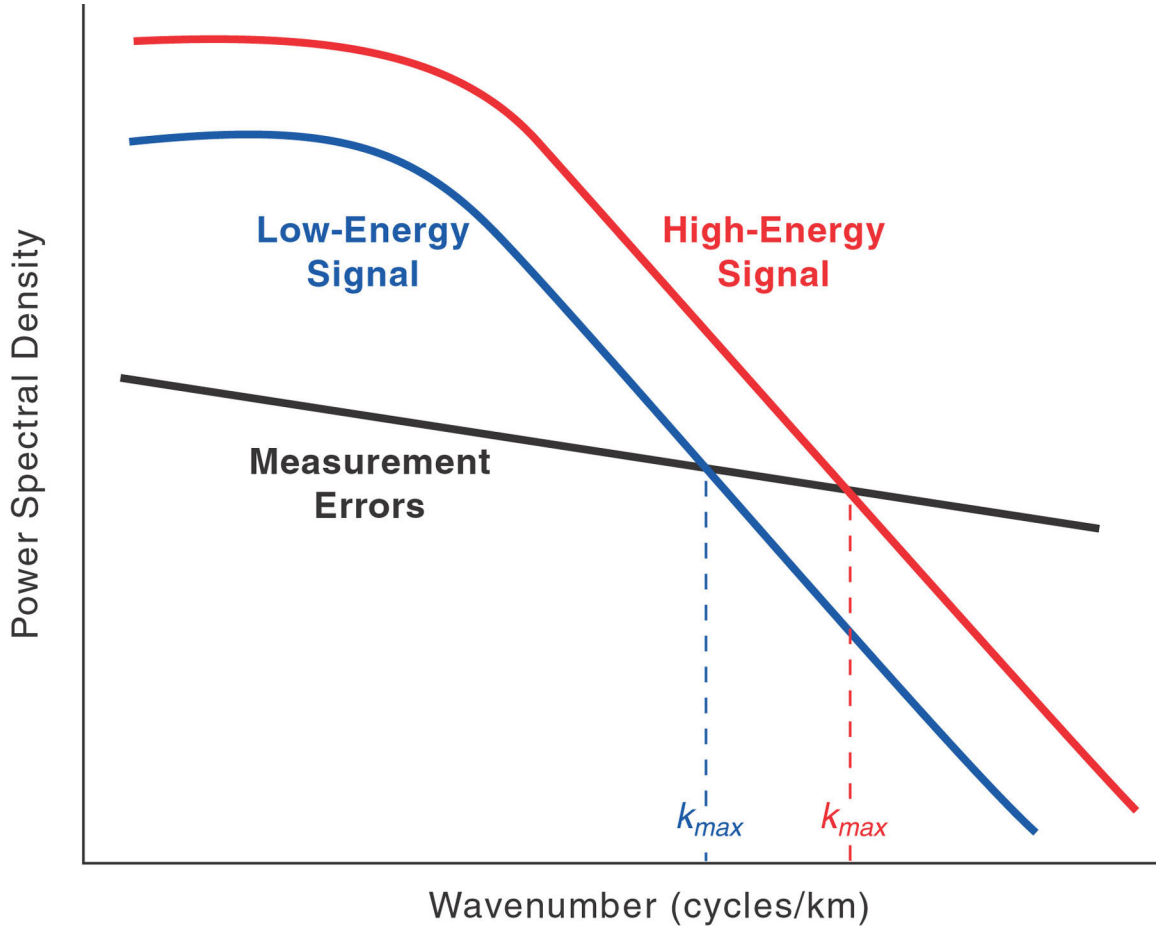

Figure 4. A schematic description of the relationship between the wavenumber spectra of the signal of interest in regions of energetic (red curve) and weak (blue curve) mesoscale variability and the system measurement noise (black curve). The spatial resolution limitation of the measurement system is imposed by the intersection of the signal and error spectra. Signals with wavenumbers higher than k_{max} (i.e., wavelengths shorter than $2\pi/k_{max}$) cannot be observed above the more energetic measurement noise. Because the signal spectrum varies considerably geographically while the measurement error spectrum is relatively constant geographically, the value of k_{max} will vary geographically for any measurement system as shown by the red and blue curves.

Part 1

Applications of High-Resolution Ocean Topography Measurements

High-Resolution Ocean Topography and Geostrophic Turbulence

Roger M. Samelson
College of Oceanic and Atmospheric Sciences
Oregon State University
Corvallis, OR 97331-5503

Zonally averaged along-track wavenumber spectra of TOPEX/POSEIDON altimeter observations of sea-surface height have been found to have a shape that is approximately independent of latitude, when expressed in terms of a nondimensional wavenumber that is scaled by a mean local internal deformation radius (Stammer, 1997). This combination of approximate universality and geostrophic scaling in the 100-1000 km wavenumber band raises the possibility that a universal, geostrophic, turbulent process, presumably driven by baroclinic instability of the large-scale flow, may determine the spectrum of mesoscale motion in much of the mid-latitude ocean. The purpose of this brief review is to summarize the development of the theory of geostrophic turbulence and outline some aspects of the theory that may be particularly relevant to the altimeter observations.

The term "geostrophic turbulence" has more than one meaning. It originated with Charney (1971), who proposed, on the basis of an analogy that will be explored below, a specific form of the energy spectrum for a rotating, stratified fluid in turbulent, quasi-geostrophic motion:

$$E(k) = C\,\eta^{2/3}\,k^{-3},$$

where $E(k)$ is the spectral energy density at wavenumber k, C is a dimensionless constant of order one, and η is the enstrophy dissipation rate. However, a much more general notion is frequently intended, following the usage of Rhines (1979): "Geostrophic turbulence is the chaotic, nonlinear motion of fluids that are near to a state of geostrophic and hydrostatic balance..." To make sense of this confusion of names, it's useful to look briefly at the history.

The starting point is Kolmogorov's (1941) universality theory for stationary, homogeneous, isotropic, three-dimensional turbulence. Based on dimensional considerations, Kolmogorov proposed that, in the limit of large Reynolds number, the second-order velocity correlation function $S_2(l) = \langle[v(\mathbf{x}+l)-v(\mathbf{x})]^2\rangle$ (where v is a horizontal velocity component, $\mathbf{x}$ is a position vector, l is a relative displacement, and the angle brackets indicate a suitable average; e.g., Frisch, 1995) should have the form

$$S_2(l) = C\,\varepsilon^{2/3}\,l^{2/3}.$$

Here ε is the energy dissipation rate and C is again a dimensionless constant of order one. This implies that the spectral energy density has the form

$$E(k) = C\,\varepsilon^{2/3}\,k^{-5/3},$$

for a third constant C. The energy dissipation rate is the rate at which energy is dissipated at small scales, and is equal to the rate at which energy cascades from large scales to small scales. These forms of the velocity correlation and spectral energy density for homogenous, isotropic three-dimensional turbulence have been verified by numerous experiments under a wide variety of conditions, for displacements and wavenumbers in the "inertial" or "energy cascade" range between the small scales at which viscosity is important and the large scales at which the flow is forced (e.g, Frisch, 1995).

On the 100-1000 km horizontal scales that are of interest here, however, oceanic motions are highly anisotropic, and the Kolmogorov theory does not apply. Fjortoft (1953) considered spectral energy

transfers in the two-dimensional, barotropic vorticity equation, as a simple model of large-scale atmospheric motion, and, remarkably, found that enstrophy conservation was generally consistent only with energy transfer toward larger, rather than smaller, scales. Kraichnan (1967) developed analogs of the Kolmogorov theory for the essentially equivalent problem of two-dimensional Navier-Stokes turbulence. Two distinct inertial ranges emerge from the Kraichnan theory: an "inverse" energy cascade range, in which the energy transfer is toward larger scales and the enstrophy transfer vanishes, and an enstrophy cascade, in which the enstrophy transfer is toward smaller scales and the energy transfer vanishes. The corresponding forms for the spectral energy density are

$$E(k) = C\,\varepsilon^{2/3}\,k^{-5/3},\ \eta = 0,$$

in the energy cascade range, and

$$E(k) = C\,\eta^{2/3}\,k^{-3},\ \varepsilon = 0,$$

in the enstrophy cascade range. In Kraichnan's (1967) interpretation, the two-dimensional, turbulent fluid is forced at an intermediate wavenumber, and both cascades occur simultaneously, with energy cascading to larger scales and enstrophy to smaller scales.

It is relatively easy to generate or observe three-dimensional turbulence in geophysical fluids, either in a laboratory apparatus or in nature. The geophysical relevance of two-dimensional turbulence is less obvious since geophysical fluids are not two-dimensional. Because of the reduction in spatial dimensions, however, it is relatively easy to simulate two-dimensional turbulence numerically, and this has made it an important object of study in itself.

The main difficulty in applying the theory of two-dimensional turbulence to the ocean or atmosphere is that both the ocean and the atmosphere are stratified. Charney (1971) showed that this difficulty could be partially overcome, through a formal mathematical analogy between energetic, high-wavenumber, stratified, quasi-geostrophic motion, and the enstrophy cascade regime of two-dimensional turbulence. Charney coined the term "geostrophic turbulence" to describe this geostrophic motion. As indicated above, the corresponding energy spectrum is the enstrophy cascade form of two-dimensional turbulence, where k is now an isotropic wavenumber, with Prandtl (f/N) scaling of vertical distance. Charney listed six conditions required for the analogy to hold: horizontal scales must be small relative to the internal deformation radius, excitation energies must be high (internal potential vorticity gradients large relative to the planetary gradient), stratification must vary slowly relative to the turbulence, the turbulence must be homogeneous and isotropic, nonlinear interactions must be local in wavenumber, and viscous and boundary layer frictional effects must be small.

The restriction to scales small relative to the deformation radius means that the Charney (1971) geostrophic turbulence theory cannot apply to the 100-1000 km wavenumber band identified in the altimeter observations. That this restriction had to be overcome for the oceanographic problem was apparent already during the time of the MODE program (MODE Group, 1978) in the 1970's. Rhines (1975) and Salmon, Holloway, and Hendershott (1976) turned to numerical simulations to develop a more general phenomenology of nonlinear geostrophic motion that would allow several of Charney's assumptions to be dropped. These simulations focused on scales comparable to or greater than the deformation radius, on the interplay between turbulent and planetary wave-dynamical motions, and on the transfer of energy between the barotropic and the gravest baroclinic modes, far from three-dimensional isotropy even in the Prandtl-scaled coordinates. As summarized, for example, by Rhines (1979) or Salmon (1998), the resulting picture was of large-scale forcing of the gravest baroclinic mode inducing baroclinic instability near the deformation radius scale, which transferred energy to the barotropic mode, where it cascaded back to large scales and was eventually dissipated; enstrophy cascaded from the deformation radius scale toward smaller scales in both the barotropic and baroclinic modes. At large scales (that is, near the "Rhines scale," which depends on the energy of the flow), planetary wave effects

became important, and a tendency for formation of elongated zonal structures was observed. A general tendency for the energy spectra to follow the k^{-3} scaling was found in these and later simulations (e.g., McWilliams and Chow, 1981), but it lacked the clear theoretical underpinning of the Charney or Kraichnan results. The term "geostrophic turbulence" was co-opted to describe this more general set of ideas.

One of the directions in which this more general geostrophic turbulence theory has recently been extended involves the important problem of the relation of eddy fluxes to the mean flow and, specifically, the parameterization of eddy fluxes in terms of mean-flow quantities. Larichev and Held (1995) and Held and Larichev (1996) have considered this problem for fully developed, doubly-periodic, 2-layer, quasi-geostrophic turbulence. They found that both energy production and potential vorticity fluxes were dominated by motions at the largest scales to which the barotropic inverse energy cascade and the mean-flow baroclinicity extended, and not by motions near the deformation scale, as some of the previous results might have suggested. They proposed that the eddy potential vorticity flux could be represented as a diffusion down the mean gradient, with diffusivity equal to the product of characteristic velocity and length scales of the large-scale, energy-containing barotropic eddies.

Unfortunately, even this more general geostrophic turbulence theory seems to have at best a relatively tenuous connection to the dynamics of the ocean mesoscale. In contrast to the several decades of wavelength over which the Kolmogorov inertial range of three-dimensional turbulence occurs and can be measured in many different settings, barely a single decade separates deformation-radius wavelengths (200-300 km) from the basin scale in the ocean. This range would probably be too narrow to establish the existence of a power-law spectral regime even if the observations closely resembled the theory. Although there have been some isolated in-situ measurements of upper ocean properties that resolve some or all of this range of wavelengths (Samelson and Paulson, 1988; Rudnick and Ferrari, 2000), it is the satellite altimeter observations that have made it possible for us to begin to measure the relevant spectra in a systematic way. The altimeter observations instead indicate a clear departure from the theory: they contain little indication of a barotropic inverse energy cascade. The kinetic energy spectra computed from altimeter-derived sea-surface slope spectra peak at scales within a factor of two of the deformation radius wavelength, and do not show the increase toward larger scales that would be consistent with the inverse cascade (Fig. 1; see Stammer (1997) for more detail). The reasons for this discrepancy are not clear, but presumably include surface forcing, bottom roughness, and the strong inhomogeneity of the large-scale fields. Related to the latter is the disappointing fact that the elegant and often revealing quasi-geostrophic approximation is not entirely appropriate on these larger scales, and may be providing poor theoretical guidance.

The inhomogeneity of the ocean on scales between the basin scale and the mesoscale—the presence of features like western boundary currents and their extensions, the subtropical frontal zones, the equatorial and eastern boundary currents—is well known, and perhaps it should not come as a surprise that theories based on homogeneity of the large-scale fields do not match up well with observations. This does not diminish the importance of the fundamental question, what is the relation between mesoscale ocean motions and the large-scale circulation? But it clearly indicates that answering that question will require detailed study of the interaction of mesoscale motions with the local mean field.

High-resolution satellite altimetry offers a unique opportunity to address this fundamental question. To do so successfully, it will be necessary to obtain vector velocity fields on sufficiently small space and time scales to compute reliable estimates of second-order statistics—fluxes, covariances, structure functions—and combine them with mean-field estimates on similar spatial scales. The 200-300 km mid-latitude cross-track resolution of the current TOPEX/POSEIDON mission is too coarse to achieve this. A joint TOPEX/POSEIDON-JASON 2 mission would bring the cross-track spacing down by a factor of two, and resolve enough of the mesoscale to make important progress.

The truly exciting prospect is a high-resolution altimetric mission using technologies summarized in this report. Such a mission, capable of producing vector velocity and Reynolds stress fields, and potentially also vorticity and vorticity flux, on a 50-km grid every 10-20 days, with smaller scales less temporally aliased, would be sufficient to directly resolve for the first time a major part of the mesoscale eddy field and its interaction with the large-scale circulation. This would be a major contribution to understanding how the ocean works as a physical system, and a major step towards overcoming one of the basic obstacles to global climate prediction.

References

Charney, J., 1971: Geostrophic turbulence. *J. Atmos. Sci*., **28**, 1087-1095.

Ferrari, R., and D. Rudnick, 2000: Thermohaline variability in the upper ocean. *J. Geophys. Res*., **105**, 16857-16883.

Fjortoft, R., 1953: On the changes in the spectral distribution of kinetic energy for two-dimensional, nondivergent flow. *Tellus*, **5**, 225-230.

Frisch, U., 1995: Turbulence: The legacy of A. N. Kolmogorov. Cambridge University Press, New York, 296 pp.

Held, I., and V. Larichev, 1996: A scaling theory for horizontally homogeneous, baroclinically unstable flow on a β-plane. *J. Atmos. Sci*., **53**, 946-952.

Kolmogorov, A., 1941: The local structure of turbulence in incompressible viscous fluids for very large Reynolds numbers, *and* Dissipation of energy in locally istropic turbulence. English translations: Proc. Roy. Soc. Lon., A434, Turbulence and stochastic processes: Kolmogorov's ideas 50 years on, pp. 9-17.

Kraichnan, R., 1967: Inertial ranges in two-dimensional turbulence. *Phys. Fluids*, **10**, 1417-1423.

Larichev, V., and I. Held, 1995: Eddy amplitudes and fluxes in a homogeneous model of fully developed baroclinic instability. *J. Phys. Oceanogr*., **25**, 2285-2297.

McWilliams, J., and J. Chow, 1981: Equilibrium geostrophic turbulence. I: A reference solution in a β-plane channel. *J. Phys. Oceanogr.*, **11**, 921-949.

MODE Group, 1978: The Mid Ocean Dynamics Experiment. *Deep-Sea Res*., **25**, 859-910.

Rhines, P., 1975: Waves and turbulence on a β-plane. *J. Fluid Mech*., **69**, 417-443.

Rhines, P., 1979: Geostrophic turbulence. *Ann. Rev. Fluid Mech*., **11**, 401-441.

Salmon, R., 1998: Lectures on geophysical fluid dynamics. Oxford University Press, New York, 378 pp.

Salmon, R., G. Holloway, and M. Hendershott, 1976: The equilibrium statistical mechanics of simple, quasi-geostrophic models. *J. Fluid Mech*., **75**, 691-703.

Samelson, R., and C. Paulson, 1988: Towed thermistor chain observations of fronts in the subtropical North Pacific. *J. Geophys. Res*., **93**, 2237-2246.

Stammer, D., 1997: Global characteristics of ocean variability estimated from TOPEX/POSEIDON altimeter measurements. *J. Phys. Oceanogr*., **27**, 1743-1769.

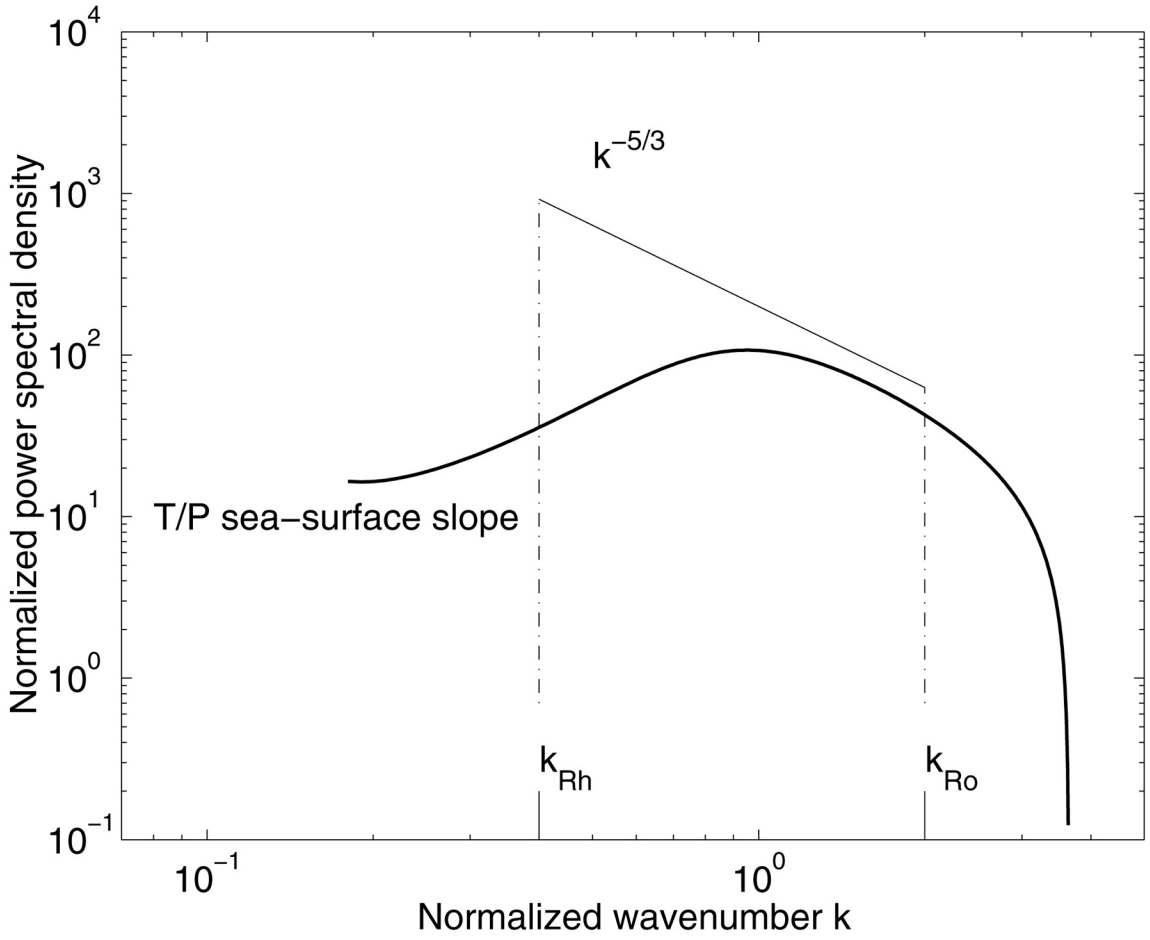

Figure 1. Analytic approximation to normalized altimeter-derived sea-surface slope spectra (thick solid line; from eq. (18) of Stammer, 1997) and theoretical slope of kinetic energy spectrum in the inverse cascade regime (thin solid line). The approximate locations of the deformation radius and Rhines cut-off wavenumbers (k_{Ro} and k_{Rh}, respectively) from Stammer (1997) are indicated. At low wavenumbers, the observed spectral slope departs markedly from the theory. Note that the wavenumber range between k_{Rh} and k_{Ro} is less than one decade and narrows toward low latitudes.

The Role of Ocean Eddies in Large-Scale Circulation and Climate Variability

Yi Chao
Jet Propulsion Laboratory, California Institute of Technology
Pasadena, CA 91109

1. Introduction

This note was presented to the High-resolution Ocean Topography Science Working Group (HOTSWG). Several examples (mostly the author involved in) are reviewed with an aim to demonstrate that ocean eddies play an important role in determining the large-scale circulation and climate variability. Implications on the future high-resolution ocean topography mission are also discussed.

2. Synoptic description of ocean eddies

Satellite altimetry has made a unique contribution to the description of ocean eddies. The TOPEX/Poseidon satellite, with a spatial resolution of 7-km along the satellite track and 10-day repeat orbit, has allowed us to describe the synoptic evolution of ocean eddies. Using TOPEX/Poseidon altimetric observations, Carton and Chao (1999) concluded that the strong sea level variability in the Caribbean Sea is associated with anticyclonic eddies propagating westward with a periodicity of approximately 100 days and a propagation speed of 15 cm s^{-1}. Furthermore, these anticyclonic eddies in the Caribbean Sea are related to those anticyclonic eddies found outside the Caribbean Sea in the North Brazil Current retroflection region (Pauluhn and Chao, 1999). These observed features associated with anticyclonic eddies outside and inside the Caribbean Sea have been used to evaluate a number of eddy-resolving Atlantic Ocean general circulation models (e.g., Chao et al., 1996; Barnier et al., 2001).

However, because of the large cross-track distance (314 km at the equator) for the TOPEX/Poseidon satellite, it is very difficult to track these eddies between the adjacent satellite tracks. The typical spatial scale associated with ocean eddies is on the order of 100 km (see Figure 1). Another limiting factor in monitoring eddies is the temporal resolution. With TOPEX/Poseidon, the 10-day repeat is sometimes too long to describe the life cycle of eddies, which usually has a time scale on the order of several weeks. To monitor the synoptic evolution of ocean eddies therefore requires higher resolutions in both space and time.

3. The role of ocean eddies in large-scale circulation

It has been hypothesized for a long time that ocean eddies may play an important role in determining the large-scale circulation (e.g., the meridional heat transport). The recent modeling studies (e.g., Bryan et al., 1998; Smith et al., 2000) have demonstrated a strong sensitivity of the simulated mean ocean circulation to the extent of mesoscale eddies being resolved. Three experiments have been carried out with the Parallel Ocean Program (POP, Dukowicz and Smith, 1994) primitive equation ocean model that differ only in their horizontal resolutions and the associated dissipation parameters. A Mercator grid is used with equatorial resolution of 0.1°, 0.2° or 0.4°. The domain includes the Atlantic Ocean from 20°S to 73°N. In addition to the striking differences in the Gulf Stream region and subtropical-subpolar gyre boundary, the meridional heat transport increases in magnitude by 50% from the lowest to highest resolution case (see Figure 2, taken from Bryan et al., 1998). The majority of the increase in the total heat transport is accounted for by changes in the time mean flow (Smith et al. 2000).

At the intermediate depths, 1000-2500 m, a large region of nearly homogenized mean Potential Vorticity (PV) is found to the west of the Mid-Atlantic Ridge (Lozier, 1997). It is located underneath a region of strong near-surface eddy activity. A $1/6^{o}$ Atlantic POP (Chao et al., 1996) has been shown to be able to reproduce this deep and large pool of nearly homogenized PV as observed by Lozier (1997). The

modeling results further suggest that the PV homogenization is accomplished by strong eddy mixing (Nakamura and Chao, 2001). A calculation of the vertical component of transient wave activity fluxes using the output of the eddy-resolving Atlantic POP shows predominantly downward fluxes below the top 1000 m (Nakamura and Chao, 2000a). This is consistent with the theory (Rhines and Holland, 1979; Rhines and Young, 1982) that the strong eddy mixing in the upper ocean drives the intermediate depth large-scale ocean circulation.

Given the fact that eddies are an essential component of the ocean and climate system, one has to address the question that to what extent the effect of eddies on the large-scale circulation can be parameterized (e.g., Gent and McWilliams, 1990). Output from an eddy-resolving Atlantic OGCM (Chao et al., 1996) is used to diagnose the eddy diffusivity defined by Gent and McWilliams (1990) in their quasi-adiabatic parameterization for transports by mesoscale eddies. The results (Nakamura and Chao, 2000b) suggest that eddy diffusivity as formulated by Gent and McWilliams(1990) has fairly complex spatial and temporal variations, with negative values about half of the time. We interpret this 50/50 ratio between positive and negative eddy diffusivity as an indication of a nonlinear balance between the mean and eddy fields: eddies force the mean state until it reaches a certain point at which the mean state starts releasing the available potential energy to eddies. Our results indicate the complexity and therefore the difficulty of an eddy parameterization (e.g., Gent and McWilliams, 1990) in none-eddy-resolving ocean and climate models. Observations at eddy-resolving resolutions are therefore required in order to further improve the eddy parameterization of Gent and McWilliams (1990).

4. The role of ocean eddies in long-term climate variability

Given the important role played by ocean eddies in determining the large-scale mean circulation, it is natural to hypothesize that ocean eddies could also impact the long-term climate variability. There is increasing evidence supporting the hypothesis that nonlinear interactions between ocean eddies and the large-scale mean flow (e.g., the western boundary current of the Gulf Stream) could give rise to long-term climate variability.

Figure 3 (Chao, 2001, unpublished manuscript) shows the monthly time series of the Gulf Stream position at three longitudinal locations (70^{o}W, 65^{o}W, and 60^{o}W) overlaid by the winter time North Atlantic Oscillation (NAO) index. The Gulf Stream position is defined by the position of the 15^{o}C isotherm from the Global Ice SST data set (Parker et al., 1995), while the NAO index is measured by the pressure difference between Iceland and Azores. A dominant signal in both Gulf Stream position and NAO index is the upward trend from 1970 to present. Interestingly, there is also an apparent downward trend from 1950 to 1970, suggesting that the recent upward trend is part of the natural climate variability. While the Gulf Stream was in its southern-most position during the 1960s, it attained the northern-most position during the 1950s and also during the 1980s. In addition to this multi-decadal fluctuations, the Gulf Stream also exhibits pronounced interannual fluctuations. It is intriguing that the fluctuations of the Gulf Stream are correlated with the NAO index, although there seems to be a phase shift between the signals during later half of this century.

Apparently further studies are required to confirm and eventually understand this statistical correlation, our preliminary results suggest that the Gulf Stream (or ocean eddies through their nonlinear interactions with the Gulf Stream) plays an important role in the long-term climate variability in the Atlantic Ocean. In general, ocean eddies could play a more important role in the long-term climate variability than previously anticipated.

5. Concluding remarks

The following conclusions have been made addressing the role of ocean eddies in the large-scale circulation and long-term climate variability.

- A better understanding of the large-scale ocean circulaton and long-term climate variability requires the knowledge of ocean eddies.
- To monitor ocean eddies from space requires a fine spatial resolution (e.g., 20 km or less) as well as a short temporal resolution (e.g., 5 days or less).
- Development of eddy-resolving ocean and coupled ocean-atmosphere models requires global measurements at eddy-resolving resolution.
- Ocean eddies (through their nonlinear interactions with the large-scale circulation) could play a more important role in the long-term climate variabilily than previously anticipated.

Satellite altimetry has made major advances in studying the large-scale ocean circulation. Future altimetric missions with higher spatial and temporal resolutions should lead to improved description of ocean eddies and ultimately determine the impact of ocean eddies on the large-scale circulation and long-term climate variability.

6. References

Barnier. B., T. Reynaud, A. Beckmann, C. Bonïng, J.M. Molines, S. Barnard, and Y. Jia, 2001: Seasonal variability and eddies in the North Brazil Current and the North Equatorial Counter Current system. *Progress in Oceanography*, in press.

Bryan, F.O., R.D. Smith, M.E. Maltrud, M.W. Hecht, 1998: Modeling the North Atlantic: From Eddy Permitting to Eddy Resolving. Poster presented at International WOCE Conference on Ocean Circulation and Climate, Halifax.

Carton, J., and Y. Chao, 1999: Caribbean Sea eddies inferred from TOPEX/POSEIDON altimetry and an eddy-resolving Atlantic Ocean model. *J. Geophys. Res.,* **104**, 7743-7752.

Chao, Yi, A. Gangopadhyay, F.O. Bryan, W.R. Holland, 1996: Modeling the Gulf Stream system: how far from reality? *Geophys. Res. Letts.,* **23**, 3155-3158.

Gent, P.R., and J.C. McWilliams, 1990: Isopycnal mixing in ocean circulation models. *J. Phys. Oceanogr.*, **20**, 150-155.

Lozier, M.S., 1997: Evidence for large-scale eddy-driven gyres in the North Atlantic. *Science*, **277**, 361-354.

Nakamura, M., and Y. Chao, 2000a: Characteristics of three-dimensional quasi-geostrophic transient eddy propagation in the vicinity of a simulated Gulf Stream. *J. Geophys. Res.,* **105**, 11,385-11,406.

Nakamura, M., and Y. Chao, 2000b: A note on the eddy thickness diffusivity of the Gent-McWilliams subgrid mixing parameterization in the vicinity of the Gulf Stream. *J. Climate*, **13**, 502-510.

Nakamura, M., and Y. Chao, 2001: Diagnoses of an eddy-resolving Atlantic Ocean model simulation in the vicinity of the Gulf Stream. Part I: Potential Vorticity. *J. Phys. Oceanogr.,* **31**, 353-378.

Parker, C.K., C.K. Folland, M. Jackson, 1995: Marine surface temperature: observed variations and data requirements. *Climate Change*, **31**, 559-570.

Pauluhn, A., and Y. Chao, 1999: Tracking eddies in the subtropical north-western Atlantic Ocean. *Phys. Chem. Earth(A),* **24**, 415-421.

Rhines, P.B., and W.R. Holland, 1979: A theoretical discussion of eddy-driven mean flows. *Dyn. Atmos. Oceans*, **3**, 289-325.

Rhines, P.B., and W.R. Young, 1982: Homogenization of potential vorticity in planetary gyre. *J. Fluid Mech.,* **122**, 347-368.

Smith, R.D., M.E. Maltrud, F.O. Bryan, and M.W. Hecht, 1999: Numerical simulation of the North Atlantic Ocean at $1/10^{o}$. *J. Phys. Oceanogr.,* **30**, 1532-1561.

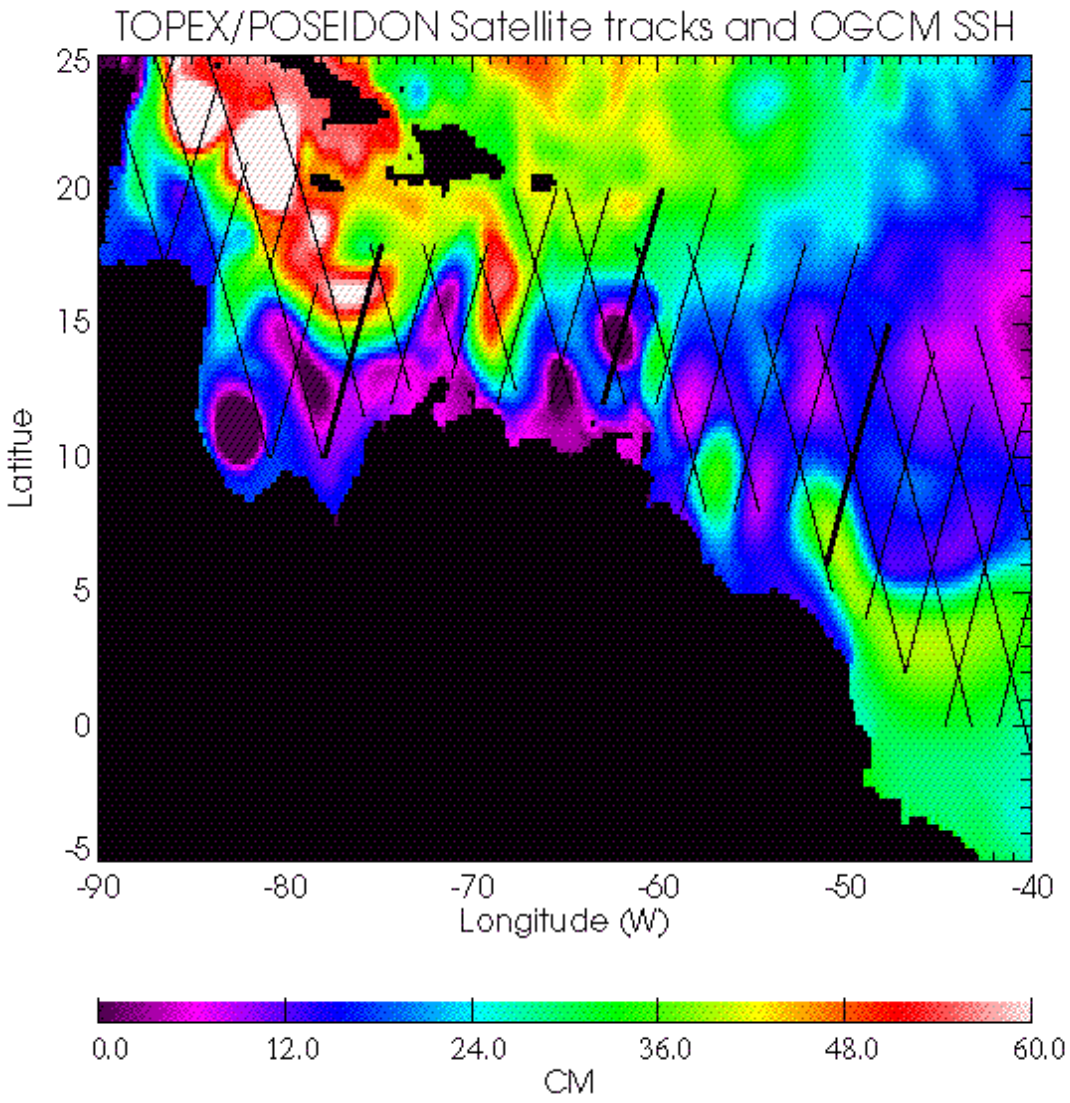

Figure 1. Snapshot of sea surface height simulated by a 1/6° Atlantic OGCM (Carton and Chao, 1999) overlaid by the TOPEX/Poseidon ground tracks in the Caribbean Sea region.

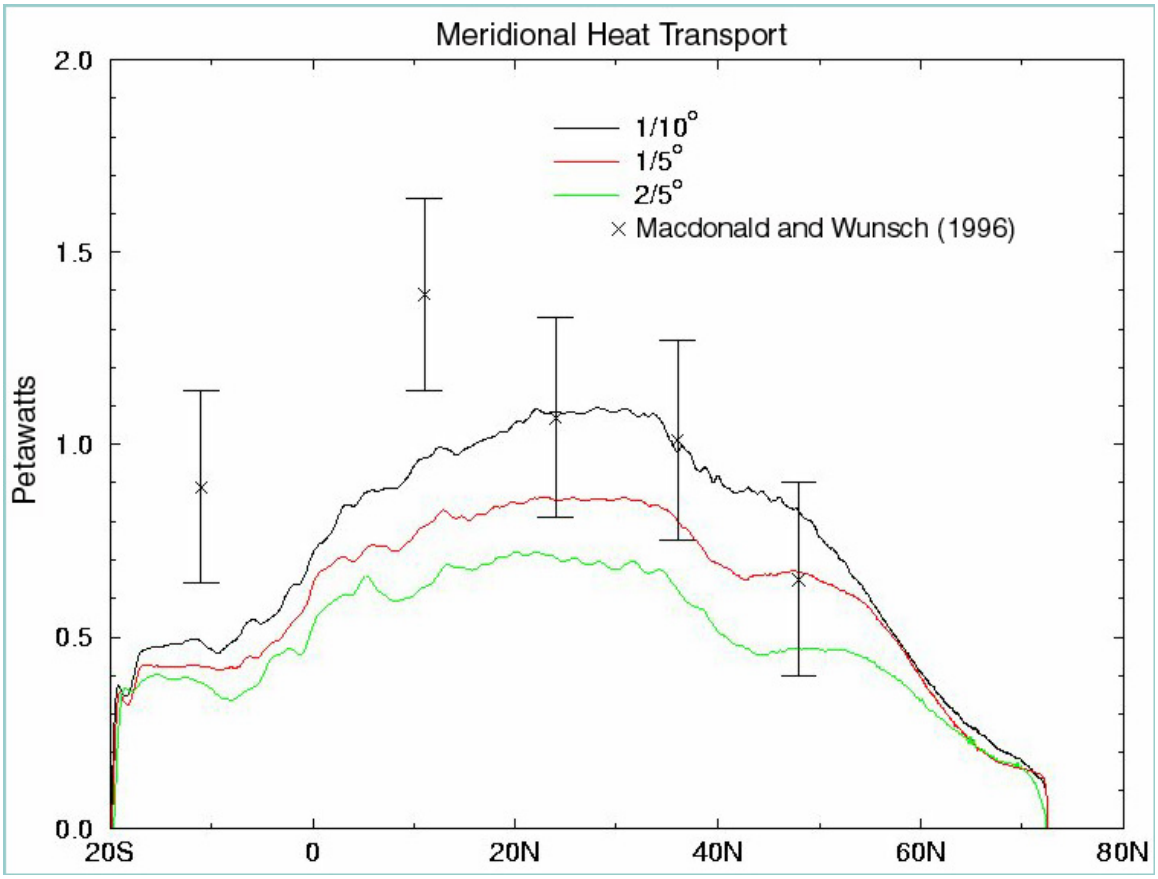

Figure 2. Meridional heat transport simulated by the Atlantic POP (taken from Bryan et al., 1998; Smith et al., 2000) with a horizontal resolution of 0.1°, 0.2° and 0.4°, respectively. Also shown is the inverse model estimate of Macdonald (1998).

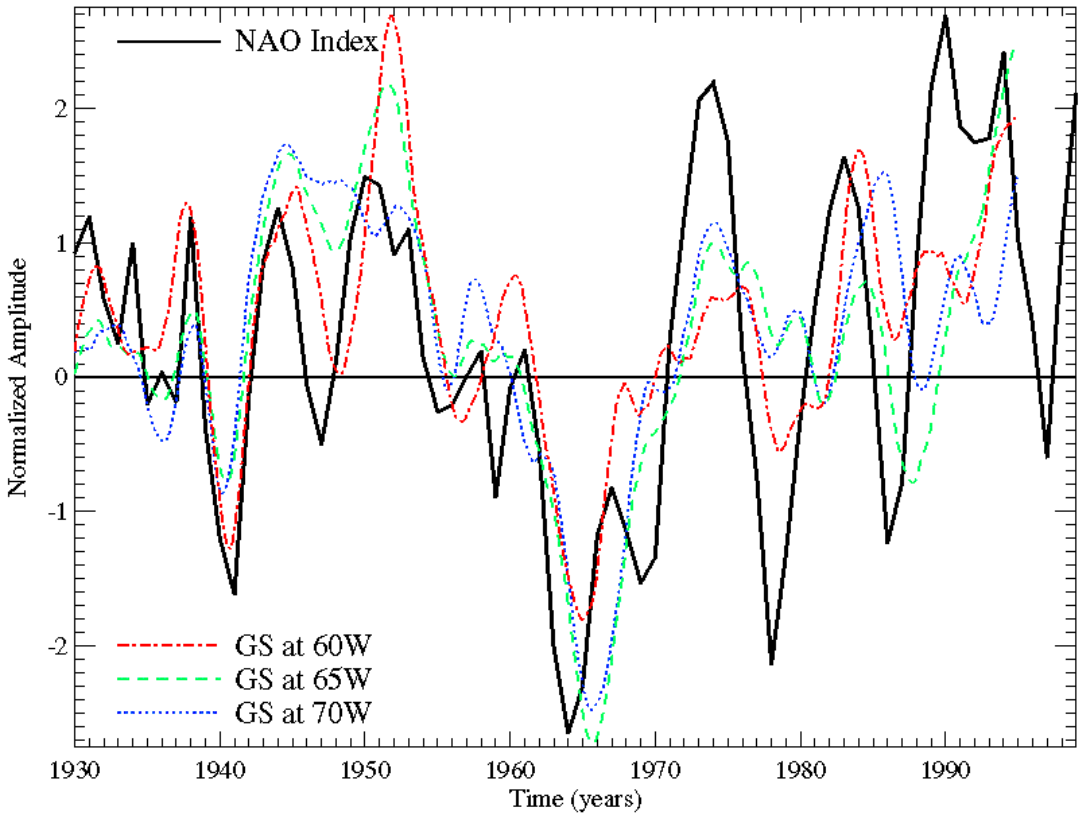

Figure 3. Time series of the Gulf Stream position (as defined by the 15°C isotherm in sea surface temperature) at 70°W, 65°W, and 60°W overlaid with the winter time NAO index (Chao, 2001; unpublished manuscript). Sea surface temperature data was taken from the Global Ice SST data set as described in Parker et al. (1995).

High-Resolution Ocean Topography
Science Requirements for Coastal Studies

Ted Strub
College of Oceanic and Atmospheric Sciences
Oregon State University
Corvallis, OR 97331-5503

Transport processes in the coastal ocean are of interest for both scientific and operational purposes. Scientific issues include: the processes that create three-dimensional structure of the coastal circulation, enhancing or inhibiting cross-margin transport; the degree of topographic control over the shelf (widths of 20-300 km); the effect of the coastal circulation on the successful survival of marine organisms; changes to coastal ocean ecosystems caused by climate variability (interannual to interdecadal to long-term climate change), etc. The need for operational nowcasts and forecasts of the coastal ocean circulation arises from the large number of human uses of the coastal ocean – fishing, transportation, recreation, waste disposal, habitation next to the water's edge, and the search and rescue services needed by those engaged in the above activities. Increased altimeter resolution will allow more accurate nowcasts and forecasts; the first opportunity to test the effects of doubled resoltion could occur during an interleaved tandem T/P and Jason-1 mission, during which a number of planned field surveys in the coastal ocean off the U.S. west coast (GLOBEC, CoOP, CalCOFI, and CCOAST) can be used to quantify the improvement in the circulation fields.

What are the sampling characteristics needed by a "high-resolution ocean topography" (HOT) sensor, in order to monitor coastal ocean circulation or contribute new insights into processes that govern that circulation? Considerations of the coastal ocean circulation address the same question as faced for mesoscale circulation fields in the deep ocean – *What are the spatial and temporal scales of the dominant transport processes?* An additional consideration occurs in the region next to the land, however – the size of the gap in altimeter coverage next to the coast. Even a sensor with very high resolution will not be of use in the coastal ocean if its data are flagged as unreliable over the shelf. In regions where there are offshore islands, each small island then produces a larger gap in the data. Working over the shelf and next to land poses other challenges, in terms of tidal corrections and use of passive microwave sensors to correct for atmospheric water vapor. These and other specific problems in retrieving usable data over the coastal ocean are not addressed here. Rather, the approach is to describe several examples of coastal systems in terms of their distance from the coast and the space and time scales over which the systems vary. The examples chosen are those familiar to the author. Others might choose different systems; but the final assessment would probably not differ by more than a factor of 2.

Some general characteristics of coastal circulation fields are:

- Truly coastal studies concern the circulation over the shelf, from the coast to the shelf-break (typically 20-50 km off the U.S. west coast, several 100 km off the U.S. east coast).
- In most cases, the onshore-offshore spatial scales are smaller than the alongshore spatial scales.
- In addition, space and time scales decrease as one approaches the coast.
- Some processes are constrained to lie within the first baroclinic Rossby radius of the coast – again around 20-50 km in many locations.

Thus, in many coastal regions, most of the information of interest lies within 20-50 km of the coast. This is not only true of narrow shelves. Over wider shelves, gradients of sea surface height (SSH) are often concentrated along topographic features (the shelf break, edges of banks, etc.) due to tidal mixing and topographic steering. This poses a challenge to altimeters, both due to the typical size of data gaps next to the coast and due to the expected limits of resolution for proposed HOT sensors (5-15 km). However, any improvement in resolution will benefit those interested in coastal circulation, since it will

allow better definition of the offshore mesoscale circulation features that impact the coastal region, while other technologies (coastal radars and autonomous vehicles) define the circulation over the shelf.

It has long been realized that the variability of SSH at tide gauges on the coast is different from the steric height of the deep ocean not far offshore (Pattullo et al., 1955). Using tide gauges at Newport, Oregon and Neah Bay, Washington, Reid and Mantyla (1976) perfected a method of extending the calculation of steric height (relative to a deep reference level) over the much shallower slope and shelf to within 5 km of the coast. Use of this method reveals that changes in sea level at the coastal tide gauges are controlled by the cross-shelf geostrophic slopes in SSH associated with narrow jets found over the shelf – equatorward in summer and poleward in winter (Huyer, 1990). By extending the deep ocean steric height signals over the shelf, Reid and Mantyla made possible a more realistic resolution of these shelf circulation features by hydrographic measurements.

The questions for a HOT sensor are similar to those for hydrography: *"Can reliable SSH data be retrieved close enough to the coast to mimic the tide gauge variability and with sufficient resolution to define the circulation structure over the shelf?"* If the altimeter SSH measurements can be extended to within ~5 km of the coast with ~5 km horizontal resolution, they can define these coastal currents as well as traditional hydrography. As a start, we might ask, *"How well can present altimeters reproduce tide gauge data?"* Two tracks of the TOPEX/POSEIDON (T/P) altimeter off northern California cross the coast near tide gauges at Crescent City and North Spit (Figure 1, from Strub and James, 1997). Alongtrack SSH data are flagged as unreliable within the first 10 km from the coast over 50% of the time. The squares in Figure 1a next to the coast are the closest points where unflagged data are usually found (approximately 10 km from the coast). Detided data from the two tide gauges and from the altimeter are shown individually and as averages of the two tide gauges and and of ground tracks at points identified by squares. The averaged tide gauge data are further filtered (20-day half power) to remove the influence of coastal trapped waves (Figure 1b, top) and a 5-point running mean is applied to the altimeter data, treating the two tracks as a single data set (Figure 1b, lower panels). The smoothed altimeter data from approximately 10 km are capable of following the low-passed tide gauge data moderately well at this location.

The coastal ocean off northern California is particularly energetic. Satellite SST and color fields, along with more fine-scaled field surveys, have established the presence of a complex 3-D meandering jet and eddy system that stays closer to the coast in the north than in the south and migrates from the shelf to several hundreds of kilometers offshore between spring and fall (Brink and Cowles, 1991; Strub and James, 1995; Kelly et al., 1998; Strub and James, 2000). Barth et al. (2000) show that the separation of the jet from the shelf off the U.S. west coast occurs at least as far north as Cape Blanco (42.8ºN). Strub and James (1997) found that fields constructed from the combination of T/P and ERS data do not see the equatorward upwelling jet off northern California when it first appears next to the coast, even though the jet causes tide gauge SSH values to drop markedly. Only when the jet moves farther offshore (three weeks later) does the altimeter data find it. Strub and James were able to reproduce the earlier jet by combining tide guage and altimeter SSH, but this produces a simple straight jet, missing cyclonic features with scales of 50 km that are visible in the satellite SST fields. Once the jet separates from the coast and develops meanders and eddies with scales of 100 km or more, the combined T/P and ERS SSH fields are qualitatively able to detect the strong mesoscale features (height differences of 20 cm or more) as found by ship surveys (Figures 1, 3, 4 and 5 in Strub and James, 1997). Resolution of these features would be greatly improved by almost any of the proposed HOT sensors. The first opportunity to test the degree of improvement would come during an interleaved tandem mission of TOPEX and Jason-1.

In the less energetic region off northern Oregon, the conceptual picture developed by field work in the 1970's consists of a more well-behaved alongshore jet that follows an upwelling front, as the jet and front move offshore and onshore in response to the local winds. However, more recent fine-scale SeaSoar surveys, satellite fields, measurements from a coastal radar system (CODAR, Kosro et al., 1997) and numerical models (Oke et al., 2001) reveal more complex 3-D circulation fields over the shelf off central

Oregon 43.0ºN-44.6ºN), just downstream of the more well behaved jet that was sampled in the 1970's (44.6º-46.0ºN). Figure 2 (Oke et al., 2001) shows an example of the July 1999 surface velocity fields from a wind-driven numerical model of the circulation in this region, clearly depicting the separation of the jet from the coast near 44.6ºN, following the topographic banks (colors indicate density – denser and colder upwelled water is red). Figure 3 (Kosro, 2000) presents an example of the surface velocity field in June 2000, estimated from coastal radars, showing the jet veering offshore at the northern edge of the bank near 44.7ºN (colors denote jet speeds of 0.5-0.6 m/s – other radar fields and a radar animation are available at http://www-currents.coas.oregonstate.edu/seasonde). The satellite SST field in Figure 4 (August 2000) covers a slightly larger region from 41º-46.5ºN. It shows colder upwelled water next to the coast north of 44.6ºN (the well-behaved region), separation from the coast at around 44.6ºN, a return to the coast at 43.6ºN and a final separation again just north of Cape Blanco (42.8ºN). Larger mesoscale meanders and eddies form offshore of Cape Blanco and this more complex field extends to southern California. Colder temperatures follow the mesoscale flow field fairly well in this region (Strub et al., 1991; Strub and James, 1995), demonstrating the wide range of scales (30-250 km) of the "coastal" circulation (visit http://globec.coas.oregonstate.edu/groups/nep for examples of fields measured by ship surveys during summer 2000).

Finally, the contoured SSH field formed from the combination of 35 days of T/P and ERS-2 data, centered on August 1 2000, is presented in Figure 5 for comparison to the SST field in Figure 4. Contours and colors in Figure 5 both indicate SSH, mapped to a grid with 0.1 degree spacing. In this region, high SST values should correspond to high SSH. Although the altimeter SSH field cannot hope to resolve features in the 30 km next to the coast over the shelf and bank regions (there is almost no data there due to flags in the AVISO data), it does begin to pick out the larger features offshore of 30 km: the higher SSH in the middle of an anticyclonic feature at 43.5ºN, 124.8ºW; a low/cold region next-to and SW-of Cape Blanco (42.8ºN); a warm/high anticyclonic feature in the SW corner of the region; and a narrow low/cool feature extending north from 42.5ºN past 44ºN between 125.5º-126ºW. In the SST image (Figure 4), the cool feature between 125.5º-126ºW ends around 44ºN and a surface drifter followed a counterclockwise elliptical path around this narrow feature in late June/early August, confirming the presence of the cyclonic surface low. Thus, as off California, the offshore mesoscale features are indicated but are imprecisely defined by combinations of present altimeter data, with nominal "resolution" of approximately 100 km. During summer 2002, fields of mesoscale circulation will be measured during the U.S. GLOBEC intensive sampling. These fields will provide the opportunity to test improvements in resolution allowed by the interleaved tandem TOPEX and Jason-1 sampling. If funded, a proposed study by the California Current Observing and Analysis Team (CCOAST) would conduct a similar field program off central and southern California during 2002-2005.

With respect to time scales of these features, moorings over the shelf off Newport, Oregon (44.6ºN) (Kosro et al., 1997) and at other locations along the west coast (Huyer, 1990) indicate an energetic "weather" band, with periods of 2-5 days. In winter this is related to the passage of synoptic storms. In summer this periodicity corresponds to strengthening and weakening of the high pressure system that causes southward alongshore winds. In the deeper ocean offshore of the shelf, the mesoscale features (100-300 km in scale) evolve more slowly. A SST image from Aug 16 contains many of the same features as found in Figure 4, indicating that the largest features evolve only slowly over the 2-week period. Thus, resolution of the temporal variability over the shelf would require the shortest repeat periods of 1-2 days; the mesoscale features offshore of shelf can be resolved with 10-day or even longer repeats.

Several examples from other regions with wider shelves provide support for the above qualitative examination of scales of motion over the shelf and in the regions offshore of the shelf. Repeated offshore CTD sections have recently been made in the Gulf of Alaska, SW of Prince William Sound (http://murphydome.ims.uaf.edu/globec/results). These consist primarily of approximately north-south sections south of Seward (59-60ºN, 149ºW). The shelf here is several hundred kilometers wide, but these sections document the presence of a narrow jet within 30-40 km of the coast, with current speeds often above 0.5 m/s. This is the westward Alaska Coastal Current (Johnson et al., 1988). Farther offshore along

the shelf break, we expect the westward Alaska Current/Alaska Stream, although measurements of this current are sparse. Recent papers by Thomson and Gower (1998) and Crawford et al. (2000) demonstrate the existence of a large-scale and vigorous eddy field that develops around the Gulf of Alaska margin. Preliminary examination of combined T/P and ERS SSH fields indicate that these can be at least qualitatively tracked in the offshore area (Crawford et al., 2000; Strub, unpublished data).

Another example comes from the Gulf of Maine (Andrew Thomas, pers. comm.), where coastal currents sometimes carry toxic algal blooms. Surveys with 5 km grid spacing in the offshore direction and 10 km spacing in the alongshore direction define a coastal jet next to the coast, approximately 30 km wide, extending at least 300 km in the alongshore direction. Dynamic heights across the jet (relative to 80 m) have large differences (0.5 m), providing a robust signal for altimeters with sufficient spatial resolution. Satellite SST images show that this jet carries colder water (thus presumably nutrients, algal blooms and other biological populations, etc.) to the SW. Other features in the same region include the circulation around Georges Bank and other banks, critical for the survival of larval cod, haddock and other commercially important species (Limeburner and Beardsley, 1996). Spatial scales for these topographically controlled currents are also 10's of kilometers across jets and 100's of kilometers in the along-current direction.

Two final examples come from another eastern boundary current, the Peru-Chile Current System. The region off northern Chile (19º-24ºS) is the site for productive sardine and anchovy fisheries. Dynamic height fields from the region, however, show normal SSH differences across this slow current of only 3-5 cm. During the 1997-98 El Niño, the signals increased to 10-20 cm (Blanco et al., 2001). Attempts to reproduce these signals using combinations of T/P and ERS data have had only marginal success (none for the normally weak seasonal signals; some success for the El Niño signal). This brings out the point that the SSH signal of interest in many regions requires greater precision (1-2 cm) than do the strong signals discussed above.

Also along the coasts of Peru and Chile, a recently recognized dominant signal consists of coastal trapped waves with periods of ~50 days and maximum currents of 0.75 m/s (Shaffer et al., 1997). The currents associated with these waves are believed to affect the transport of biological populations (phytoplankton and zooplankton, larval fish) as strongly or more strongly than the currents associated with upwelling. These long period waves along the coast of South America are somewhat unique in that they are believed to originate along the equator and propagate eastward to Ecuador, then poleward along the fairly direct path off South America. They presumably propagate north along Central America as well, but tide gauge data are not as available or reliable along that path. Attempts to use T/P data to track these waves have been hindered by the gap between the coast and the reliable altimeter data and by the artificial aliasing of tidal errors into 50-60 day periods by T/P sampling. Coastal trapped waves with shorter period (5-20 days) are also well documented off South and North America and along most coastal regions. These signals are limited to the first baroclinic deformation radius of the coast (20-40 km). Thus, sampling requirements needed to resolve these waves include coverage to within 5-20 km of the coast and temporal sampling that can resolve periods of 6-50 days with an emphasis on the longer periods, since currents associated with these long periods can advect water properties and organisms substantial distances.

Summary of Coastal Requirements

Most of the SSH signals associated with energetic coastal currents have height differences of 10 cm or more, although some are only 2-5 cm. The 1-2 cm precision desired of future altimeters for other purposes will provide good resolution of these signals. Degrading that resolution to 5 cm would make resolution of many coastal features more difficult.

Narrow (order 20-30 km) energetic jets are found in the coastal systems described above, whether the shelf is narrow or wide. Thus, the spatial and temporal resolutions needed to accurately resolve most truly coastal circulation features over the continental shelves are fairly stringent – a gap between the coast

and reliable data of 5 km or less and independent SSH samples every 5 km or less. The temporal repeat period needs to be 1-2 days for these rapidly changing currents. Gaps of 10 km and independent SSH samples separated by 10 km will marginally detect these features. However, even the coarsest resolution considered for the next generation of altimeters (a 10-20 km coastal gap, 10-15 km spatial separation between SSH points and repeats of 10 days or longer) would result in significant improvement in the resolution of the offshore mesoscale circulation fields next to the shelf break, which often connect to and interact with the currents over the shelf. Combined with other technologies that provide more detailed fields over the shelves (coastal radars, autonomous vehicles, etc.), high-resolution altimeter data will allow a more complete specification of coastal circulation, especially when the various data are assimilated into coastal circulation models (Oke et al., 2001).

References

Blanco, J.L., M.E. Carr, A.C. Thomas, and P.T. Strub, 2001: Oceanographic conditions off northern Chile during the 1996-1998 cold and warm events: Part 1: Hydrographic conditions. *J. Geophys. Res.* (accepted).

Brink, K.H., and T.J. Cowles, 1991: The coastal transition zone program. *J. Geophys. Res*., **96**, 14,637-14,647.

Barth, J.A., S.D. Pierce, and R.L. Smith, 2000: A separating coastal upwelling jet at Cape Blanco, Oregon and its connection to the California Current System. *Deep-Sea Res. II*, **47**, 783-810.

Crawford, W.R., J.Y. Cherniawsky, and M.G.G. Foreman, 2000: Multi-year meanders and eddies in the Alaskan Stream as observed by TOPEX/POSEIDON altimeter. *Geophys. Res. Lett*., **27**, 1025-1028.

Johnson, W.R., T.C. Royer, and J.L. Luick, 1988: On the seasonal variability of the Alaska Coastal Current. *J. Geophys. Res*., **93**, 12,423-12,437.

Huyer, A., 1990: Shelf circulation. In: Le Mehaute, B., Hanes, D.M. (Eds.) The Sea, vol. 9: Ocean Engineering Science. Wiley, New York, 423-466.

Kelly, K.A., R.C. Beardsley, R. Limeburner, K.H. Brink, J.D. Paduan, T.K. Chereskin, 1998: Variability of the near-surface eddy kinetic energy in the California Current based on altimeter, drifter, and moored current data. *J. Geophys. Res*., **103**, 13,067-13,083.

Kosro, P.M., J.A. Barth, and P.T. Strub, 1997: The coastal jet: Observations of the surface currents over the shelf from HF Radar. *Oceanogr*., **10**, 53-56.

Kosro, P.M., 2000: Time-series mapping of currents in the coastal ocean. Eastern Pacific Ocean Conference, Vancouver, British Columbia, Canada.

Limeburner, R. and R.C. Beardsley, 1996: Near-surface receirculation over Georges Bank. *Deep-Sea Res. II*, **43**, 1547-1574.

Oke, P.R., J.S. Allen, R.N. Miller, and G.D. Egbert, 2001: A modeling study of the three-dimensional continental shelf circulation off Oregon. *J. Phys. Oceangr*. (submitted).

Pattullo, J., W. Munk, R. Revelle, and E. Strong, 1955: The seasonal oscillation in sea level. *J. Mar. Res.*, **14**, 88-155.

Reid, J.L., and A.W. Mantyla, 1976: The effect of the geostrophic flow upon coastal sea level variations in the northern Pacific Ocean. *J. Geophys. Res*., **81**, 3100-3110.

Shaffer, G., O. Pizarro, L. Djurfeldt, S. Salinas, and J. Rutllant, 1997: Circulation and low-frequency variability near the Chilean Coast: Remotely forced fluctuations during the 1991-1992 El Niño. *J. Phys. Oceanogr*., **27**, 217-235.

Strub, P.T., P.M. Kosro, A. Huyer, and CTZ Collaborators, 1991: The nature of the cold filaments in the California Current System. *J. Geophys. Res*., **96**, 14,743-14,768.

Strub, P.T. and C. James, 1995: The large-scale summer circulation of the California Current. *Geophys. Res. Lettr.*, **22**, 207-210.

Strub, P.T. and C. James, 1997: Satellite comparisons of eastern boundary currents: Resolution of circulation features in "coastal" oceans, Monitoring the Oceans in the 2000s: An Integrated Approach. Preprint Volume, NASA-CNES, Biarritz, France.

Strub, P.T., and C. James, 2000: Altimeter-derived variability of surface velocities in the California Current System: 2. Seasonal circulation and eddy statistics. *Deep-Sea Res. II*, **47**, 831-870.

Thomson, R.E., and J.F.R. Gower, 1998: A basin-scale oceanic instability event in the Gulf of Alaska. *J. Geophys. Res.*, **103**, 3033-3045.

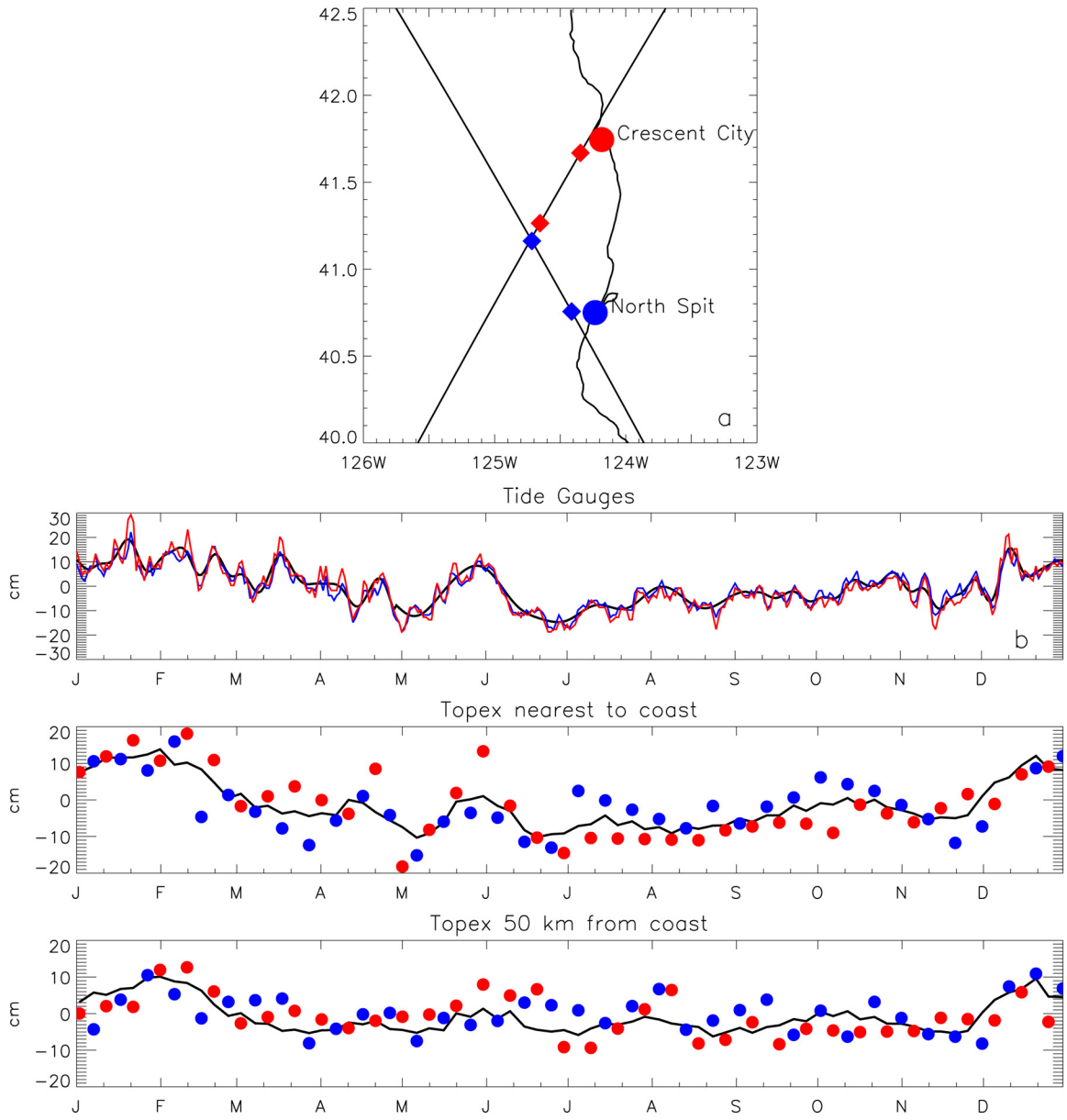

Figure 1. (a) T/P tracks and tide gauge locations; (b-top) tide gauge data from individual gauges and 20-day smoothed average SSH; (b-middle) T/P data from indivual tracks approximately 10 km from the coast [nearshore squares in (a)] and smoothed with a 5-point running mean (line); (b-bottom) T/P data from individual tracks approximately 50 km from the coast [offshore squares in (a)], as in (c).

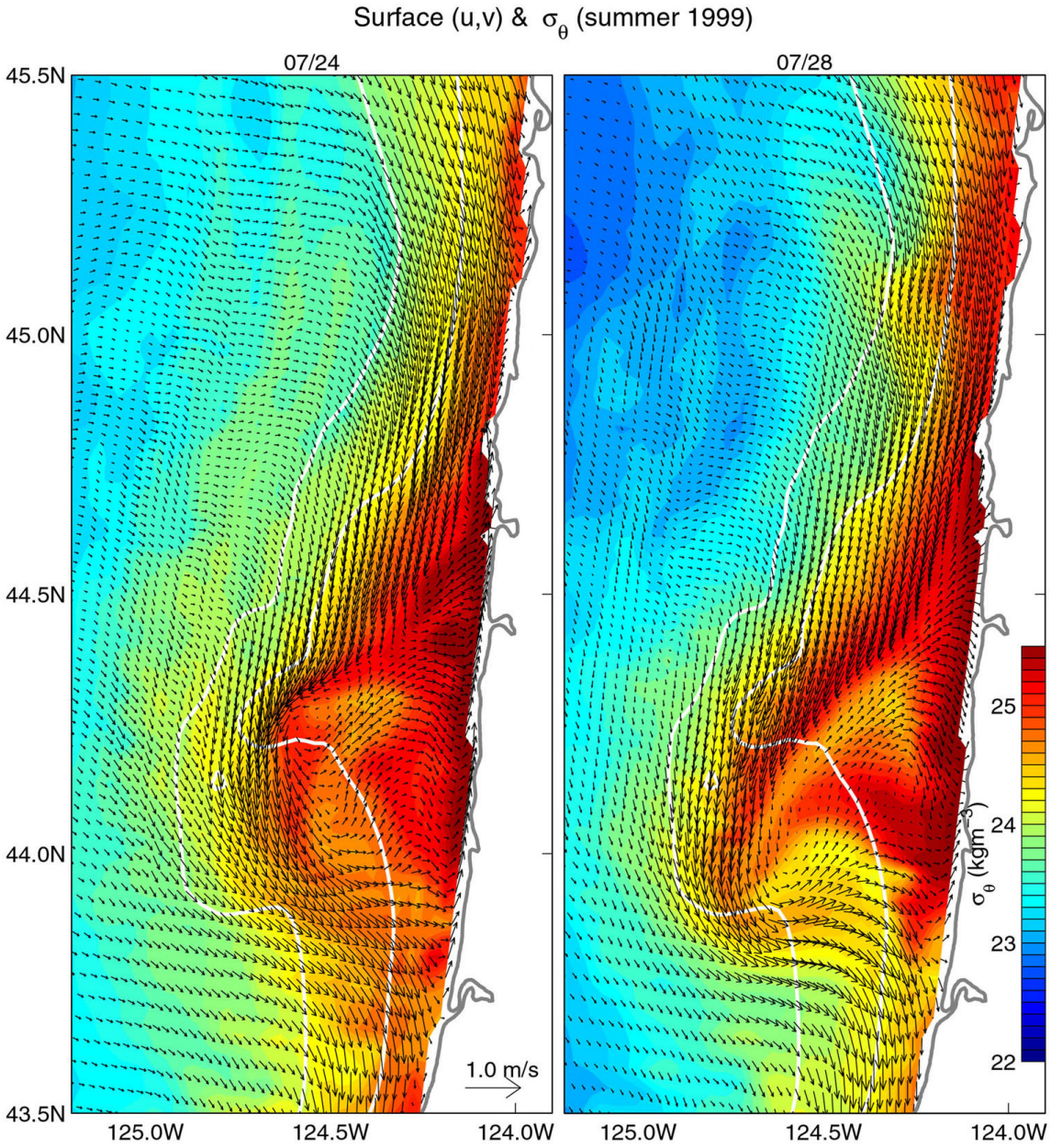

Figure 2. Surface velocities (vectors) and densities from a numerical model forced by wind fields from July 1999 (Oke et al., 2001).

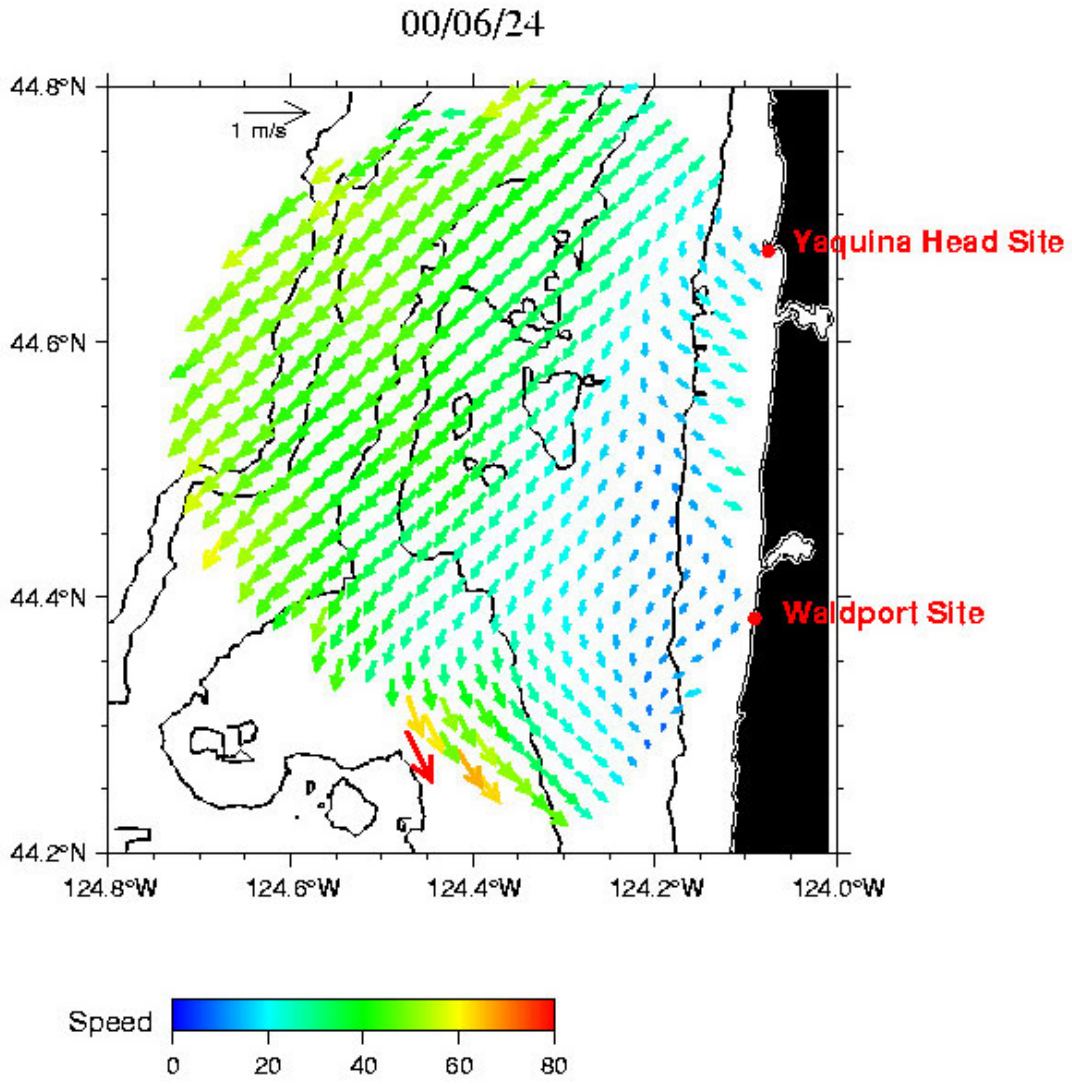

Figure 3. Surface velocities estimated from coastal radars (locations shown) off Oregon. Colors (and vector length) denote speed (Kosro, 2000).

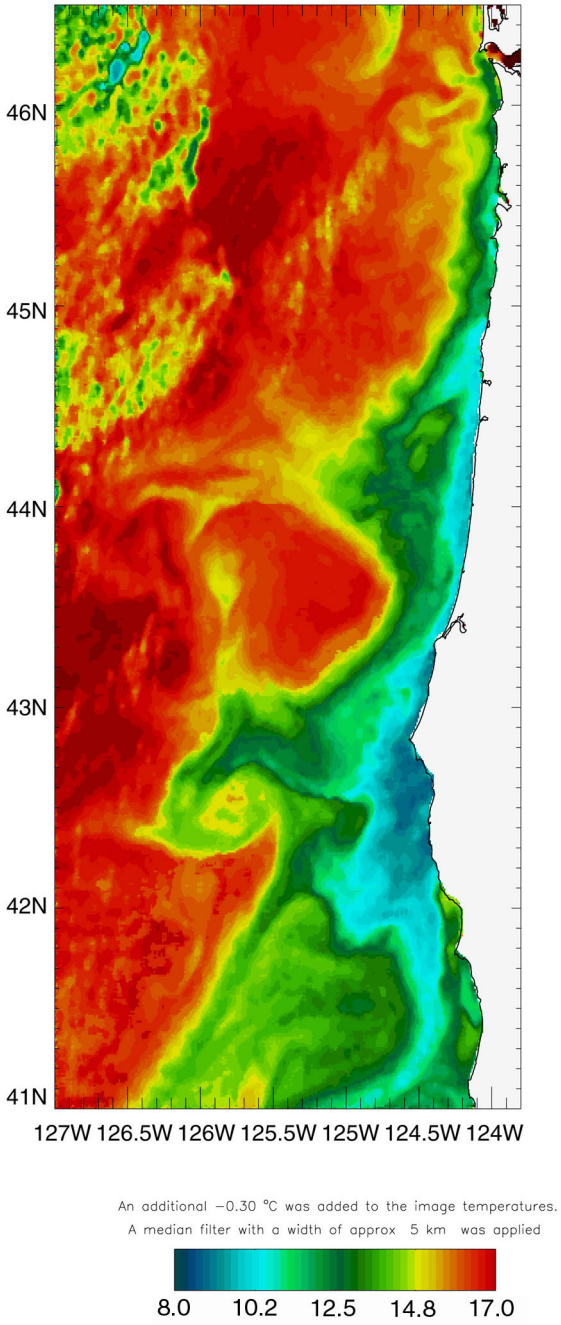

Figure 4. Satellite (AVHRR) SST from August 1, 2000.

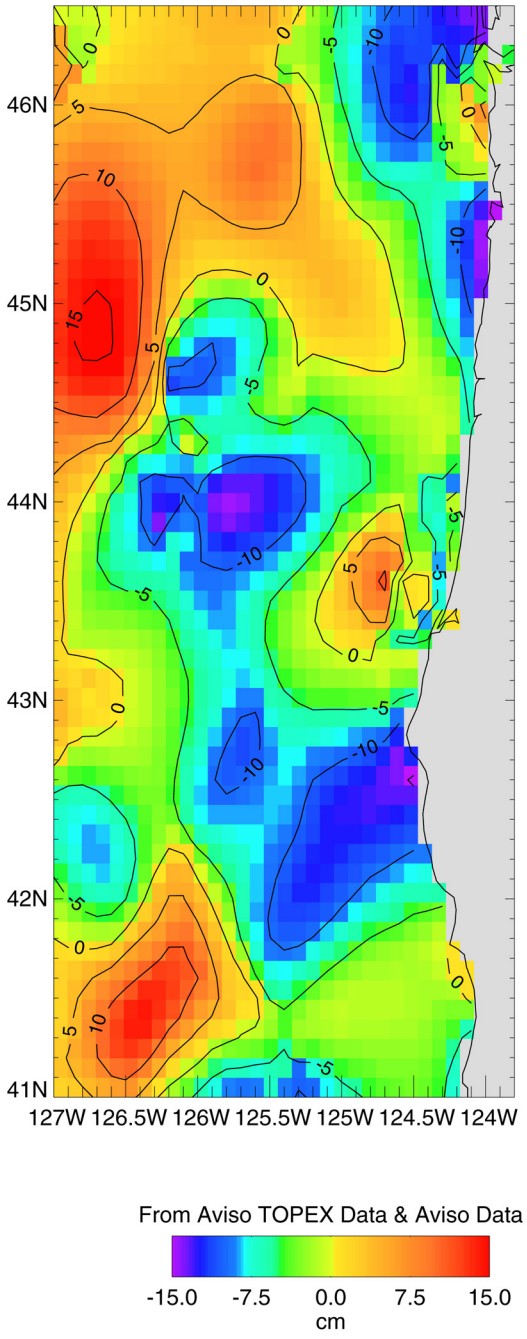

Figure 5. Combined T/P and ERS-2 altimeter SSH, 35 days centered on August 1, 2000.

The Impact of High-Resolution Altimetry on Mesoscale and Coastal Data Assimilation

Pierre De Mey
GRGS/LEGOS
18 Ave. Edouard Belin
31401 Toulouse Cedex 4, France

Introduction

The critical impact of conventional, nadir-observing altimetry onto large-scale and mesoscale ocean data assimilation requires no further demonstration. It has been consistently shown over the last 10-15 years that sea-level anomaly measured along repeat tracks and assimilated with appropriate methods had the potential to improve both numerical simulations and predictions of the ocean. It has also been shown that two or three nadir altimeters were better than one when it comes to constraining the ocean mesoscale. The present document addresses the question of the impact of new technology (High-Resolution Ocean Topography -- HROT) onto the measurement, understanding, assimilation and prediction of some of the most highly-variable ocean processes, namely the ocean mesoscale and subinertial processes in the coastal and shelf seas.

Generally speaking, state estimation and prediction require three elements linked to a common state vector: (1) deterministic prognostic equations ("the numerical model"), (2) a stochastic model of errors (probability density functions, covariances), and (3) observations. A control vector is defined and the three elements are integrated in a minimum variance/maximum likelihood principle.

In practice, data assimilation schemes use dynamical, statistical and cross-variable *interpolation* to mix observations with model estimates. This interpolation is performed in the error subspace. In general, the error subspace is modelled in a particular way (e.g. De Mey, 1997). When considering a new observation system, the question of *what particular physics* this observation system can help correct in the model is central, and will translate in questions on the way the error subspace is going to be modelled.

There are a variety of algorithms to solve the ocean assimilation problem (e.g. Ghil and Malanotte-Rizzoli, 1991; Bennett, 1992). The methods may be perceived as "degraded" (e.g. *nudging*: Verron *et al.*, 1992; Blayo *et al.*, 1994; *optimal interpolation*: De Mey and Robinson, 1987; Rienecker and Miller, 1991; De Mey and Benkiran, 2001), or "advanced" (*adjoint variational methods*: Courtier and Talagrand, 1990; Schröter, 1994; Greiner and Périgaud, 1994, 1996; Morrow and De Mey, 1995; Bennett *et al.,* 1996, 1997; Courtier, 1997; *ensemble methods*: Evensen and van Leeuwen, 1996; Lermusiaux and Robinson, 1998; Echevin *et al.,* 2000; Auclair and De Mey, 2001). However the choice of the method is chiefly the consequence of the type of problem to which the state estimation approach is to be applied.

In the following, we will not consider a particular algorithm. We will consider HROT as a *constraint* on models and see what HROT could change for ocean data assimilation. In that perspective, specific references to error-subspace exploration methods such as the adjoint approach and ensemble forecasting will be used in the purpose of illustration of that constraint.

The document is written as a series of comments and recommendations and is structured in three main parts: the open ocean, the coastal and shelf seas, and ocean forecasting systems. Some of the points follow discussions started at the College Park meeting.

Interest of HROT for data assimilation in the open ocean

General

1. A "10-km/10-day" resolution HROT instrument would constrain the ocean mesoscale like no other altimeter before. However, even better spatial resolution would be needed for submesoscale features or at high latitudes.
- HROT would sample processes which are *hard to model*: we would get better spatial resolution of small-scale features such as fronts, better temporal resolution of fast processes such as developing instabilities, etc.

Nature of data constraint

- With respect to conventional along-track nadir altimeters, assimilating HROT data does come close to assimilating sea-level maps. Adding one dimension in information subspace is a very big difference in essence on the constraint to ocean models. For instance, Morrow and De Mey (1995) show that vector information such as drifter velocities had a much larger impact on simulations than scalars such as sea level.
- Some people still objectively map their altimeter data before assimilation. We believe that this is not the thing to do because mapping makes the observation error covariances non-diagonal. However in high-resolution models maps can be a stabilizing constraint: drifts, instabilities, and open-boundary problems are observed and can therefore be corrected.
- HROT would get us closer to continuous data assimilation and farther from sequential. We can therefore expect the inadequacy of our numerical models to become more apparent. These inadequacies will probably have to be taken into account, and may even be formalized ("weak-constraint methods" such as 4D-PSAS, representer methods), especially if it can be shown that HROT can constrain this additional degree of freedom, and if such a weak-constraint formulation can enhance predictability.

Adequacy of conventional altimeters for large-scale state estimation

With conventional observing altimeters, we have a more or less regular grid of observations to assimilate. However having data constraints on a regular grid does not mean that the impact of the observations onto the model is going to be regular. Therefore the regular grid of conventional altimetry (e.g. TOPEX/POSEIDON) does not even guarantee that we will get the general circulation right. There is less extrapolation with HROT so we should get better large scales. The limits of conventional altimetry are illustrated in the following points:

- Euler-Lagrange equations for a constrained minimization problem yield forced adjoint dynamics (e.g. Courtier and Talagrand, 1990, using Ide *et al.*, 1997 notations):

$$-\partial_t \lambda + E^*(\lambda) = -\frac{\partial J}{\partial \mathbf{x}} \equiv \mathbf{H}^T \mathbf{R}^{-1}(\mathbf{y} - \mathbf{H}\mathbf{x}) \qquad (1)$$

  The adjoint variables λ for a unit observation yield the space-time structure of the influence functions or representers for that observation at any instant before observation time. Approximate cross-sections of representers can also be obtained by ensemble methods (Echevin *et al.*, 2000).
- Time cross-sections of sea-surface height representers (figure 1, and another figure presented at meeting) show that the influence of sea-level anomaly measurements is extremely irregular, and in any case far from the elliptical influence functions used in OI. This can be due to mean currents, the thermocline, barrier layers, whatever modifies or restricts the influence of one observation. Therefore, in some areas, even the most dynamically-consistent methods such as the adjoint methods

will not be able to extrapolate from conventional altimetry, while the OI-based methods will give the wrong answer.

- With a conventional altimeter, one needs a long assimilation period such that there will be no remaining gaps in the adjoint variables (Tropics: Schröter *et al.*, pers.comm., 1993), or several altimeters. Several studies on how ERS captures the space-time variability found heavy aliasing problems

Essentially the same limitations are found for the steady-state problem: Schröter *et al.* show that ERS along-track data does not project well on a spherical harmonic expansion as is done in the natural description of the geoid. Only on long scales will the geoid be of sufficient accuracy. The SSH must be projected onto the same space to make use of the low error budget at these wavenumbers. There exist however no good filters/projectors as yet which could be of real help

Adequacy of temporal resolution for DA

In the low-frequency part of the spectrum (large scales), the temporal redundancy will helps reduce the *a posteriori* error level

Observation subspace considerations

- Some assimilation experiments (e.g. Ezer and Mellor, 1997) indicate that the assimilation of SST and SSH together yields smaller errors at all depths than the assimilation of each data type alone. This is likely to be even more efficient if the resolutions of both data types are similar.
- There are cases when conventional altimetry degrades the solution when combined with much higher-resolution or higher-content observations in an imperfect data assimilation system. For instance, conventional altimetry and XBTs do not project onto the same error subspace, in particular on the vertical. HROT should project on the model error subspace better. It should be better able to constrain subsurface dynamics because some of that subsurface dynamics has a complex space-time surface signature -- such as eddies. Subsurface processes with no surface signature such as meddies still will not be visible and will have to be sampled by conventional profiling methods or ARGO floats.
- The HROT innovation sequence will contain more information than for conventional altimetry. *Adaptive estimates* of forecast error variances are relatively easy to get in observation subspace. If the information subspace is bigger, then we get more estimates:
-

$$diag(\mathbf{HBH}^T) \approx diag\left(\left\langle \mathbf{dd}^T \right\rangle \right) - diag(\mathbf{R}) \qquad (2)$$

(again using Ide *et al.*, 1997 notations). Beyond this point, estimates of $diag(\mathbf{B})$ can be obtained by several methods such as the so-called *adaptive filter* (Hoang *et al.* 1997).

Interest of HROT for data assimilation in coastal and shelf seas

Differences with respect to the open ocean for data assimilation

Let us first look at a few important differences between shelf/coastal seas (SCS) and open-ocean (OO) areas.

In the SCS, the physical processes are coupled, much more so that in the OO. These couplings involve: the large-scale wind-driven circulation, local instabilities, inertial and topographically-trapped features, fronts, tidal currents, storm surges, tidal mixing, bottom roughness and bottom boundary layer, surface layer effects, sea state, upwellings, etc. This has consequences onto numerical model physics in

the SCS: treatment of the free surface, treatment of bathymetry/pressure gradients (sigma coordinates, advection schemes), of boundary layers, etc. It also has consequences on the numerical model configuration (e.g. mesh and time step) and therefore on the relative cost of SCS models.

In the SCS, the needs are for finer scales, and for a much greater variety of variables (currents, turbidity, biology, etc.), while the forcings (lateral boundary conditions, surface fluxes) are usually only available at the larger scales and involve large-scale bathymetry and orography. This "downscaling" concept is transverse to data, model, and assimilation approach, and concerns both the atmospheric and oceanic components. In the atmosphere, dedicated analyses and predictions in the surface boundary layer are a solution. In the ocean, one must consider the joint, consistent use of a large-scale estimate (from a general circulation model) and an SCS assimilation system able to accept the available multidisciplinary local data as inputs.

Let us now turn to the specific difficulties linked to state estimation and prediction in the SCS (again, mostly in contrast to the OO and atmospheric practice).

A major difficulty relates to the presence of open boundaries, and the need to seek a coherence between the exterior and interior solutions. A short list of relevant questions include: What is in the control vector of the assimilation problem? Should it contain both interior and boundary variables? How and for how long in time must the boundaries be controlled?

Errors of coastal models are generally unknown. This applies to both forecast and representativity errors, and is not unique to SCS models. However SCS model errors are inhomogeneous at least in the cross-shore direction, and strong couplings exist between components of the forecast errors. As a consequence, the atmospheric and open-ocean "recipes" for error modelling, error propagation and order reduction (e.g. Dee, 1991) cannot be directly applied to SCS forecasting systems. The inconvenience of the error space being "hard to simplify" adds up to the relative cost of SCS models. One tendency will therefore be for very "specialised" coastal models, such as storm-surge prediction models where the error space only contains the shallow-water dynamical variables.

A last category of difficulties is related to the available observations in the SCS. Their availability and density are insufficient everywhere in the ocean, but even more so in shallow areas where the scales are finer and the processes are coupled. In addition the various signals are superimposed in the data; for instance the tidal effects, large-scale wind-induced and geostrophic circulation, and the sea-state jointly influence the sea level at sometimes neighbouring frequencies and are almost impossible to deconvolute without the help of dedicated numerical models and sophisticated assimilation systems. Also, since a priori estimates are deficient, it is difficult to optimise observing networks in a useful way. HROT could indeed significantly contribute to solving the space-time sampling problem in the coastal areas in the next decade.

Vorticity

Estimating *vorticity balances* requires mapping the properties. The vorticity balance is important in predicting the penetration of coastal currents onto the shelf (with applications such as oil spill drift into coastal waterways). The large-scale solution *will not* provide the right vorticity constraint at the boundary of the regional model.

While the *shear vorticity* of surface coastal currents can be obtained from cross-shore tracks of conventional altimetry, the *curvature vorticity* cannot:

$$\zeta = \partial_x v - \partial_y u = \partial_r u_\theta - \tfrac{1}{r}\partial_\theta u_r \qquad (3)$$

The mapping capabilities of HROT could provide the complete constraint. That is, provided that the error budget and space scales makes it possible to calculate derivatives.

Observation subspace considerations

- Altimetry is not very sensitive to cloud cover and rain. It is an advantage over SST and SSS in coastal oceans and would make HROT a very critical constraint. (This may not apply to some of the HROT instruments, such as those operating in the Ka band.)
- As announced above, sea-level signals due to various phenomena add up in shelf/coastal areas and are tricky to deconvolute. A better resolution in space and time can help deconvolute them and provide a more physically meaningful constraint. Applying that improved space-time resolution to the *model error subspace*, HROT should be able to phase-lock model error features much better than conventional altimetry.
- The forecast error covariance matrix exhibits *fine-scale but coherent three-dimensional error patterns* in coastal models (Auclair and De Mey, 2001; figure 2). Conventional altimeters cannot take advantage of this because their tracks are too far apart and because they do not come sufficiently close to the coast.
- Altimetry representers in coastal areas show that the potential influence of sea-level observations is *very inhomogeneous spatially*, and that high resolution is needed to fill in the gaps (Echevin *et al.*, 2000; figure 1). Figure 1 also illustrates the fact that sea level constrains all variables in the interior of the coastal ocean (which is not yet obvious to everyone!).

Large-scale and coastal forecasting systems

Along with climate prediction, coastal and shelf seas are major customers of large-scale ocean prediction products. The large-scale forecasting systems are themselves primary customers of the existing earth observation data. Ongoing projects of operational Large-scale Ocean Forecasting Systems (LOFS) such as FOAM in the UK and MERCATOR in France are expected to play a pivot role in ocean research and applications in the next decades. The Global Ocean Dynamics Experiment, GODAE, will provide a framework to intercompare those LOFS on a worldwide basis and learn about what works and what does not. The highest-resolution LOFS such as MERCATOR and NLOM could *directly* benefit from HROT observations by assimilating them at full resolution.

The coastal and shelf applications must be prepared to *use better boundary forcing products*, and to *focus on their specific observing and estimation needs*. Examples of Coastal/shelf Ocean Forecasting Systems (COFS) include HOPS (the Harvard Ocean Prediction System), and MFS (the Mediterranean Forecasting System), to name only two of them.

Downscaling: COFS typically run high-resolution free-surface models which represent most of the coastal/shelf physics and are initialized and forced at their boundaries by variables from large-scale solutions (LOFS). HROT would accompany downscaling, which is a concept including, but not limited to, model nesting (Table 1).

Table 1

	LOFS	***COFS***
Models	GCMs	Free-surface, σ-coord., nested
In situ data	ARGO, XBT, etc.	Tide gauges, moored stations, AXBTs, etc.
Atm. forcings	Operational analyses	Dedicated products
Space data	ALT, SST	HROT, SST, color

- HROT would accompany downscaling in terms of models, and also in terms of the use of local data (tide gauges, moored stations such as C-MAN, M3A, etc., drifting buoys, AXBTs), better use of satellite data (SST, SSMI-type winds, ocean color), and better coupling with the atmosphere.
- Routinely-available LOFS solutions suitable for COFS boundary forcing do/will exist (GODAE data assimilation systems).
- Methods to initialize coastal free-surface models from large-scale rigid-lid solutions do/will exist (Auclair *et al.*, pers.comm., 2000, use a variational method that kills the spurious gravity transients and adjusts the solution to the new bathymetry).

An important recommendation is that COFS should not rely solely on large-scale solutions as their initial and boundary conditions, because of the deficiencies of the large-scale solutions (too wide coastal currents, etc.) and because of the specific model physics. Predictability is enhanced in regional/coastal models if they assimilate data too.

Concluding remarks

Recommendations
- A general recommendation is that the HROT retrievals must first be shown to be acceptable for use in ocean models. The amplitudes and spectra of observational errors must be known.
- A special point about WSOA, which is a statement more than a recommendation: the numerical models and assimilation schemes of 2010 will provide dynamical interpolation at fine scales that will beat sample averaging over 14-km resolution cells. My feeling is that we will need to extract as much spatial information as possible at those scales and that the ground communications should be built to support the full data resolution.

General comments
- HROT will provide an *improved*, more homogeneous data constraint on the open ocean, including variability at the larger scales.
- HROT will provide a *critical* data constraint on data assimilation at the mesoscale, in the shelf seas and in the coastal ocean.
- Direct assimilation of HROT in coastal models along with local data (stations, gauges, etc.) and large-scale model constraints will make it possible to extract information from the local in situ measurements and enhance predictability.
- There are still many uncertainties concerning the bathymetry in the global ocean. There may exist a possibility to solve for bathymetry using data assimilation/inverse approaches with the added redundancy of HROT, in particular in coastal/shelf seas.

Control of model trajectory
- HROT will help reduce the *gaussian part of the forecast error variances*, through the dual principle: (1) "Less extrapolation, more interpolation" (2) Better job with space-time correlated errors.
- HROT will help reduce the occurrence of *catastrophic error growth* (bigger observation subspace).
- HROT will promote *new assimilation technologies* (adaptive methods, weak-constraint methods, inverse methods with gravity wave penalty).

References

Auclair, F., and P. De Mey, 2001: Space-time structure and dynamics of the forecast error in a coastal circulation model of the Gulf of Lyons. *In preparation.*

Bennett, A.F., 1992: Inverse methods in physical oceanography. Cambridge University Press, New York, 346 pp.

Bennett, A.F., B.S. Chua, and L.M. Leslie, 1996: Generalized Inversion of a Global Numerical Weather Prediction Model. *Meteor. Atmos. Phys.*, **60**, 165-178.

Bennett, A.F., B.S. Chua, and L.M. Leslie, 1997: Generalized Inversion of a Global Numerical Weather Prediction Model, II: analysis and implementation. *Meteor. Atmos. Phys.*, in press.

Blayo, E., J. Verron, and J.-M. Molines, 1994: Assimilation of TOPEX/POSEIDON altimeter data into a circulation model of the North Atlantic. *J. Geophys. Res.,* **99(C12),** 24691-24705.

Courtier, P. and O. Talagrand, 1990: Variational assimilation of meteorological observations with the direct and adjoint shallow-water equations. *Tellus*, **42A**, p531-549.

Courtier, P., 1997 : Dual Formulation of four dimensional variational assimilation. *Q. J. R. Meteor. Soc.*, **123**, 2449-2461.

De Mey, P. and A. Robinson, 1987: Assimilation of Altimeter Eddy Fields in a Limited-Area Quasi-Geostrophic Model. *J. Phys. Oceanogr.*, **17**, 2280-2293.

De Mey, P., 1997: Data assimilation at the oceanic mesoscale: A review. *J. Meteorol. Soc. Japan,* **75,** 415-427. In: Data assimilation in meteorology and oceanography: Theory and Practice, Ghil *et al.*, Eds, Universal Academy Press, Tokyo, 496pp.

De Mey, P., and M. Benkiran, 2001: A multivariate reduced-order optimal interpolation method and its application to the Mediterranean basin-scale circulation. In: Ocean Forecasting, Conceptual basis and applications, N. Pinardi and J.D. Woods, Eds., Springer-Verlag, in press.

Dee, D.P., 1991: Simplification of the Kalman filter for meteorological data assimilation. *Q.J.R. Meteorol. Soc.,* **117**, 365-384.

Echevin, V., P. De Mey, and G. Evensen, 2000: Horizontal and vertical structure of the representer functions for sea surface measurements in a coastal circulation model. *J. Phys. Oceanogr.,* **30,** 2627–2635.

Evensen, G. and P.J. van Leeuwen, 1996: Assimilation of GEOSAT altimeter data for the Agulhas current using the ensemble Kalman filter with a quasi-geostrophic model. *Mon. Wea. Rev.,* **124,** 85-96.

Ezer, T., and G.L. Mellor, 1997: Data assimilation experiments in the Gulf Stream region: how useful are satellite-derived surface data for nowcasting the subsurface fields*? J. Atm. Ocean. Tech.,* in press.

Ghil, M., and P. Malanotte-Rizzoli, 1991: Data assimilation in meteorology and oceanography. *Adv. Geophys.,* **33,** 141-226.

Greiner, E., and C. Périgaud, 1994: Assimilation of Geosat altimetric data in a nonlinear reduced-gravity model of the Indian Ocean by adjoint approach, Part 1: method and statistical results. *J. Phys. Oceanogr.,* **24,** 1783-1804.

Greiner, E., and C. Périgaud, 1996: Assimilation of Geosat altimetric data in a nonlinear reduced-gravity model of the Indian Ocean by adjoint approach, Part 2: physical results. *J. Phys. Oceanogr.,* **26,** 1735-1746.

Hoang, S., R. Baraille, O. Talagrand, X. Carton, and P. De Mey, 1997: Adaptive filtering: application to satellite data assimililation in oceanography. *Dyn. Atmos. Oceans*, **27,** 257-281.

Ide, K., P. Courtier, M. Ghil, and A.C. Lorenc, 1997: Unified notation for data assimilation: operational, sequential and variational. *J. Met. Soc. Japan,* **75,** 181-189. In: Data assimilation in meteorology and oceanography: Theory and Practice, Ghil *et al.*, Eds, Universal Academy Press, Tokyo, 496pp.

Lermusiaux, P.F.J., and A.R. Robinson, 1998: Data assimilation via Error Subspace Statistical Estimation, Part I: theory and schemes. *Month. Wea. Rev.,* in press.

Morrow, R.A., and P. De Mey, 1995: Four-dimensional assimilation of altimetric and cruise data in the Azores current in 1992-93. *J. Geophys. Res.,* **100(C12),** 25007-25025.

Rienecker, M.M., and R.N. Miller, 1991: Ocean data assimilation using optimal interpolation with a quasi-geostrophic model. *J. Geophys. Res.,* **96,** 15093-15103.

Schröter, J., 1994: A sensitivity analysis of variational data assimilation. In: *Data Assimilation: Tools for modelling the ocean in a global change perspective*, P. Brasseur and C. J. Nihoul, Eds, NATO ASI Series 1, Vol. 19, Springer-Verlag, Berlin, 253 pp.

Verron, J., J.M. Molines, and E. Blayo, 1992: Assimilation of GEOSAT data into a QG model of the North Atlantic between 20N and 50N: preliminary results. *Oc. Acta,* **15,** 575-583.

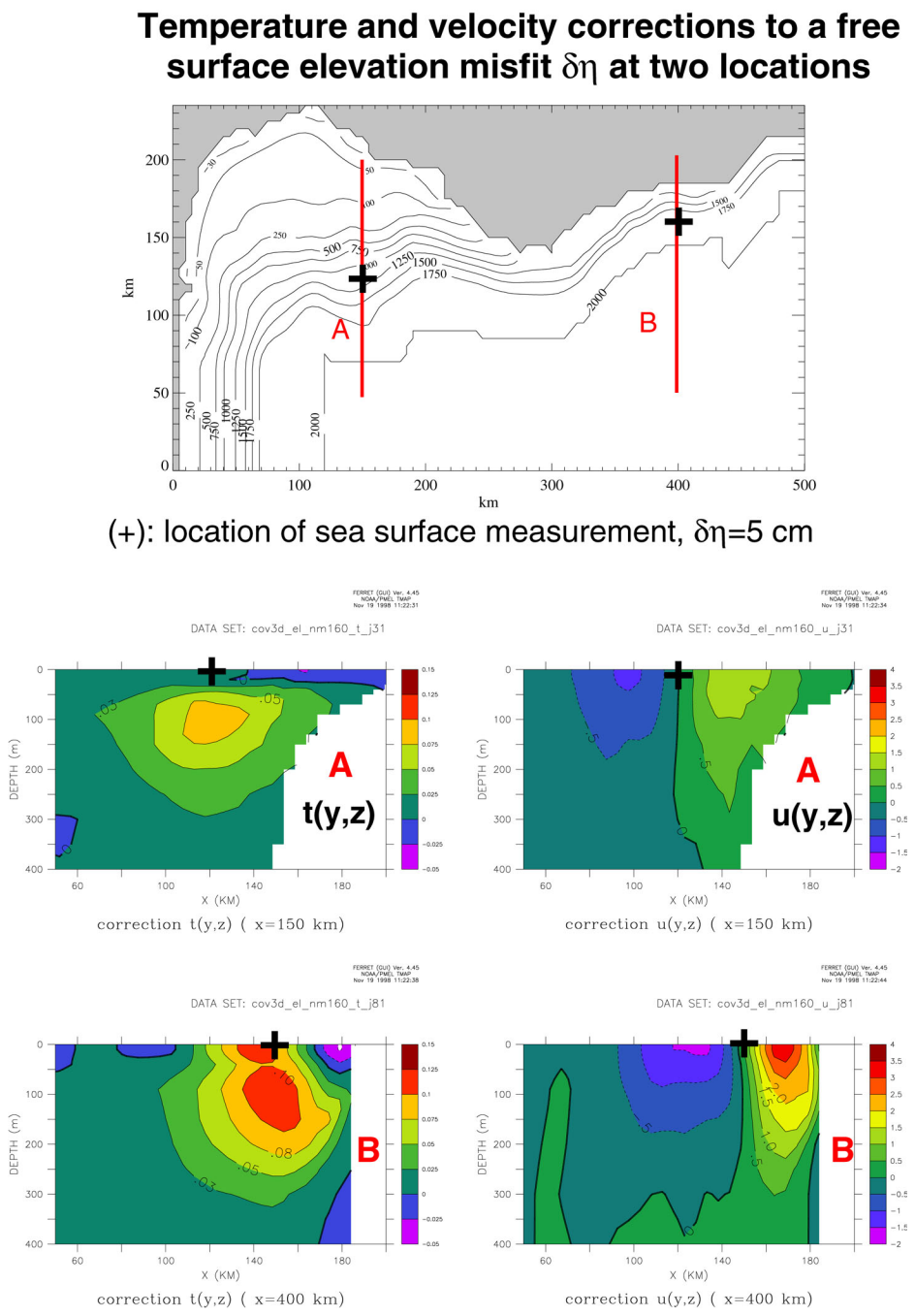

Figure 1. (from Echevin *et al.*, 2000) Temperature and velocity corrections corresponding to a free-surface elevation observation at two locations denoted A and B in a coastal model of the Gulf of Lyons and Liguro-Provençal-Catalan coastal current. The forecast error covariances and approximate representers for altimetry are calculated with an ensemble forecasting method. The bottom panel shows vertical sections of the representers for temperature (left) and zonal currents (right) (the sections are indicated in red in the upper panel). The potential influence of sea-level observations is very different at both sites, both in the surface and subsurface layers. See also text.

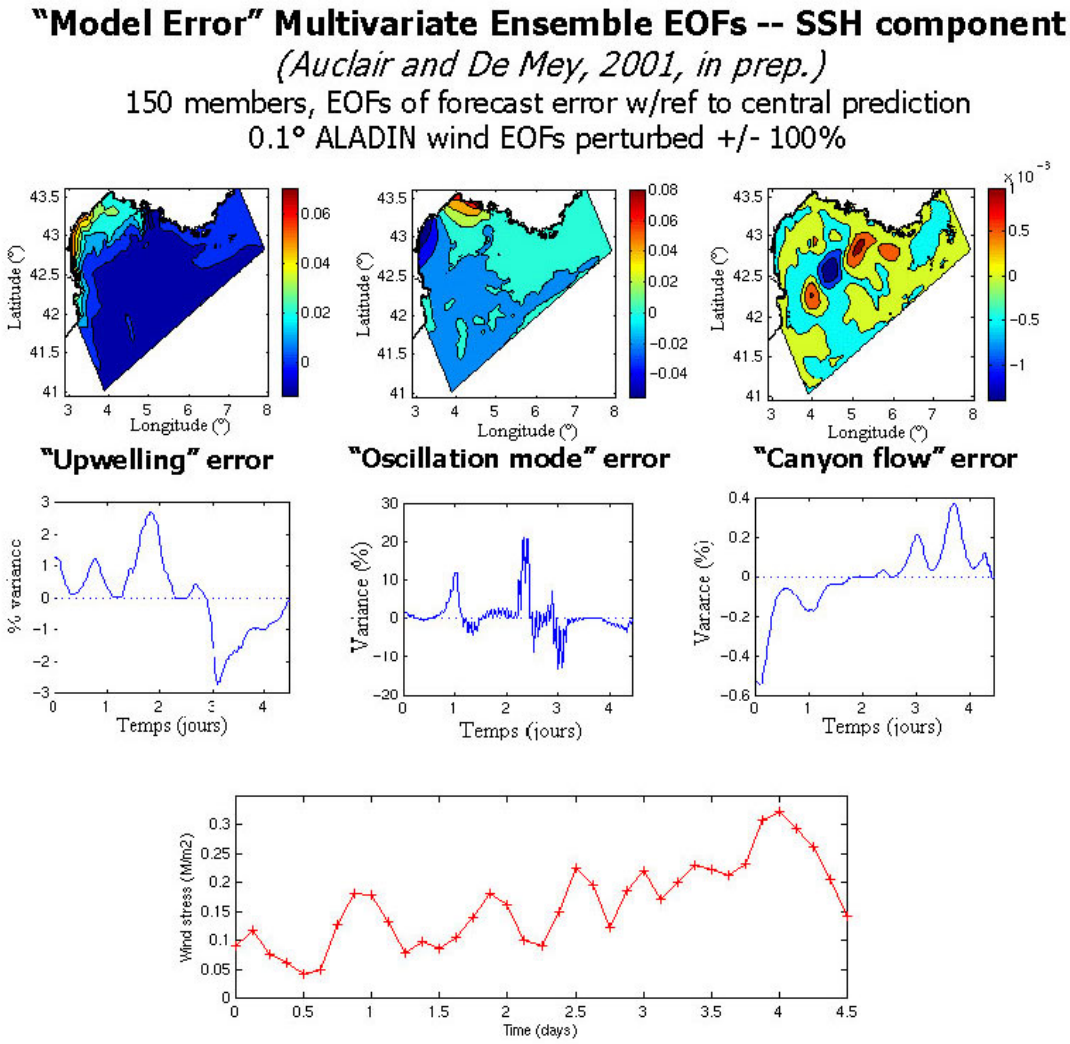

Figure 2. (from Auclair and De Mey, 2001) Forecast error EOFs in a smaller domain in the Gulf of Lyons. The EOFs are eigenmodes of the forecast error covariance matrix, obtained by perturbing the wind field and running an ensemble forecast. Three particular error EOFs are shown, corresponding to three physical processes for which the model can be in error: an upwelling, a free oscillation mode, and a mode in which the coastal current is "sucked" though the canyons at the shelf edge. The EOFs are bivariate (sea-level anomaly, three-dimensional temperature). Top panel: sea-level anomaly. Middle panel: amplitude as a function of time in the reference simulation. Bottom: wind stress as a function of time, in phase with some of the processes associated with the EOFs shown. The figure illustrates that model errors in coastal models have fine-scale but coherent patterns. See also text.

A Real-Time, Eddy-Resolving 1/16° Global Ocean Prediction System

Harley E. Hurlburt[1], Robert C. Rhodes[1], Ole Martin Smedstad[2], Alan J. Wallcraft[1], E. Joseph Metzger[1], Jay F. Shriver[1], A. Birol Kara[3]

[1]Naval Research Laboratory, Stennis Space Center, MS; [2]Planning Systems, Inc., Stennis Space Center, MS; [3]Florida State University, Tallahassee, FL

The Global Ocean Data Assimilation Experiment (GODAE) is a multinational effort designed to help justify a permanent global ocean observing system by demonstrating useful real-time ocean products with a customer base. The GODAE Strategic Plan (2000) identifies sea surface height (SSH) from satellite altimetry, sea surface temperature (SST), atmospheric forcing/satellite scatterometry and hydrographic data/ARGO PALACE floats as the most critical GODAE data requirements. Satellite altimetry is the essential available data source for eddy-resolving global ocean circulation monitoring and prediction, except for the mixed layer and SST, shallow water and some ageostrophic currents such as Ekman surface currents. For the exceptions atmospheric forcing and/or SST data are more important. While subsurface data such as the ARGO PALACE floats are needed, there is no prospect on the horizon for sufficient subsurface data to constrain the evolution of mesoscale variability in a data-assimilative eddy-resolving global ocean model. For example, 3000 PALACE floats spaced 50 km apart along TOPEX/POSEIDON (T/P) altimeter tracks (70% over water) each providing one profile every 10 days is the equivalent of 5.4 T/P revolutions per 10-day repeat cycle. Since T/P makes 127 revolutions per repeat cycle (Fu et al., 1994), 3000 PALACE floats would provide only 4% of the coverage of one T/P altimeter. However, statistics from the historical hydrographic database are used in generating synthetic temperature and salinity profiles from real-time SSH and SST (Carnes et al., 1990, 1994, 1996; Fox et al., 2001). The ARGO PALACE float data could greatly enhance this capability.

Only recently has truly eddy-resolving global ocean prediction reached computational feasibility. A 1/16° eddy-resolving, nearly global ocean prediction system has been developed by the Naval Research Laboratory (NRL), Stennis Space Center, MS. It has been run in real time by the Naval Oceanographic Office (NAVO), Stennis Space Center, MS since 18 Oct 2000 with daily updates for the nowcast and 30-day forecasts performed every Wednesday. Real-time and archived results from the system can be seen at web site: http://www7320.nrlssc.navy.mil/global_nlom/index.html. This includes many zoom regions, nowcasts and forecasts of SSH, upper ocean currents and SST, forecast verification statistics, subsurface temperature cross-sections and profiles, the amount of altimeter data used for each nowcast from each satellite and nowcast comparisons with unassimilated data. Fig. 1 illustrates the ability of the model with assimilation of real-time SSH from three altimeters to accurately map mesoscale oceanic features such as Gulf Stream meanders. Greater than 30-day forecast skill is routinely obtained globally. Fig. 2 shows the average model forecast skill in terms of anomaly correlation for the global domain and three subregions representing different dynamical regimes and subregion sizes as illustrated in Figs. 1, 3 and 4. It is noteworthy that a weak-current, ocean interior regime like that near New Caledonia (Fig. 4) is dominated by mesoscale eddies which can be tracked and forecast by the model with assimilation of SSH data from the three altimeters.

This system and its development are discussed by Hurlburt and Wallcraft (2000a,b), Hurlburt et al. (2000), Metzger et al. (2001) and Rhodes et al. (2001). Hurlburt (1984) discussed the potential for an eddy-resolving ocean prediction system and the role of altimeter data, including the need for High Resolution Ocean Topography (HROT) from satellite altimetry, such as the multi-beam altimeter proposed by Bush et al. (1984) in the same issue of *Marine Geodesy*. Both NRL and NAVO are participants in GODAE and are represented on the International and U.S. GODAE Steering Teams.

The NRL Layered Ocean Model (NLOM) is used as the ocean model component (Hurlburt and Thompson, 1980; Wallcraft, 1991; Wallcraft and Moore, 1997; Moore and Wallcraft, 1998). The model

domain is the global ocean within the latitude range 72°S to 65°N, excluding most regions shallower than 200 m depth. The grid resolution is 1/16° in latitude by 45/512° in longitude (≅ 7 km at mid latitudes) for each model variable. The model has seven layers in the vertical, including a bulk mixed layer. The primary data inputs are real-time SSH from the ERS-2, GFO, and TOPEX altimeters, SST from satellite IR and atmospheric forcing from Fleet Numerical Meteorology and Oceanography Center (FNMOC), Monterey, CA (Hogan and Rosmond, 1991). The atmospheric forcing for forecasts reverts toward climatology after four days. The statistical inference technique of Hurlburt et al. (1990) is used for downward projection of the SSH updates in the ocean model data assimilation.

Hurlburt et al. (2000) present a feasibility demonstration of ocean model eddy-resolving nowcast/forecast skill using satellite altimeter data. This study uses a 1/16° Pacific Ocean model north of 20°S and a 1/4° global ocean model to assimilate satellite altimeter data and then to perform month-long forecasts initialized from the data assimilative states. Some parts of the study used real altimeter data from T/P and ERS-2 while others used simulated altimeter data from the eddy-resolving 1/16° Pacific Ocean model. The results demonstrate (1) that satellite altimetry is an effective observing system for mesoscale oceanic features, (2) that an ocean model with high enough resolution can be a skillful dynamical interpolator for satellite altimeter data in depicting mesoscale oceanic variability, and (3) that the high resolution ocean model can provide skillful forecasts of mesoscale variability for at least a month, when model assimilation of the altimeter data is used to define the initial state. Even one altimeter gave large error reduction for the mesoscale when an eddy-resolving 1/16° model with dynamical interpolation skill was used to assimilate the data. That was true even though one nadir beam altimeter cannot resolve the observed space scales of mesoscale variability (Jacobs et al., 1999, 2001; Jacobs and Cheney, 2001, this volume). However, using simulated data, Hurlburt et al. (2000) found that the error in depicting the mesoscale was greatly reduced when data from three nadir beam altimeters in ERS, GFO and T/P orbits were used. Figure 5 contains results for additional satellite configurations, including T/P + Jason 1 (offset by 5 days and 1/2 the equatorial track spacing) and 3-altimeter configurations with simultaneous equatorial crossings 1/3 the equatorial track spacing apart. Of the 2-altimeter configurations tested, the T/P + Jason 1 gave the lowest error, and of the 3-altimeter configurations tested, the three T/P gave the lowest error in the Kuroshio region, a region of very high mesoscale variability.

Eddy-resolving global ocean monitoring and prediction is one application that would greatly benefit by using HROT from satellite altimetry. So far, seasonal to interannual climate forecasts, aimed mostly at El Niño, have been performed using much coarser ocean model grids (Stockdale et al., 1998; Ji et al., 2000; Segschneider et al., 2000a,b; Vossepoel and Behringer, 2000). As climate modeling and prediction become increasingly region specific, high resolution ocean models will be required for success in many regions and HROT is required to constrain these models. Example #1, high-resolution models are required for realistic prediction of the Kuroshio/Oyashio current system. That includes a strongly inertial Kuroshio with sufficient eastward penetration and advection of heat as well as cold southward currents along the east coast of Japan rather than warm northward flow as found in coarse resolution models (Hurlburt et al., 1996; Hurlburt and Metzger, 1998). Example #2, they are needed to obtain sharp ocean fronts that span major ocean basins, such as the North Pacific (Hurlburt et al., 1996). Example #3, they are required to accurately simulate the Gulf Stream pathway between Cape Hatteras and the Grand Banks and to obtain the large nonlinear recirculation gyre associated with the Gulf Stream (Hurlburt and Hogan, 2000). The latter changes the large-scale shape of the subtropical gyre into a C-shape. These are examples in regions of high interest where the errors due to coarse resolution in ocean models would lead to errors in climate anomaly predictions. Global and basin-scale ocean models with sufficient resolution are just beginning to emerge. HROT is needed to constrain these models for ocean nowcasting and forecast initialization. Of the data types on the horizon, HROT has the greatest potential to constrain the mass and velocity fields in these ocean models. The latter half of this decade would be excellent timing for HROT and high-resolution global ocean modeling to come together for this purpose.

Acknowledgments. The 1/16° global ocean prediction system was developed and transitioned to NAVO as part of the NRL 6.4 Large-scale Models, 6.4 Ocean Data Assimilation, and 6.4 Altimeter Data Fusion Center Support projects, managed by the Space and Naval Warfare Systems Command under program element 0603207N, and the

6.2 Basin-Scale Ocean Prediction System project which was sponsored by the Office of Naval Research under program element 0602435N. The development effort also used large grants of computer time at NAVO and the Engineer Research and Development Center, Vicksburg, MS, which were provided by the DoD High Performance Computing Modernization Office.

References

Bush, G.B., E.B. Dobson, R. Matyskiela, C.C. Kilgus and E.J. Walsh, 1984: An analysis of a multibeam altimeter. *Mar. Geod*., **8**, 345-384.

Carnes, M.R., J.L. Mitchell, and P.W. DeWitt, 1990: Synthetic temperature profiles derived from Geosat altimetry: Comparison with air-dropped Expendable Bathythermograph profiles. *J. Geophys. Res*., **95**, 17979-17992.

Carnes, M.R., W.J. Teague, and J.L. Mitchell, 1994: Inference of subsurface thermohaline structure from fields measurable by satellite. *J. Atmos. Oceanic Technol*., **11**, 551-566.

Carnes, M.R., D.N. Fox, R.C. Rhodes, and O.M. Smedstad, 1996: Data assimilation in a North Pacific Ocean monitoring and prediction system. *Modern Approaches to Data Assimilation in Ocean Modeling*, P. Malanotte-Rizzoli (ed.), Elsevier, Vol. 61, pp. 319-345.

Fox, D.N., W.J. Teague, C.N. Barron, M.R. Carnes and C.M. Lee, 2001: The Modular Ocean Data Assimilation System (MODAS). *J. Atmos. Oceanic Technol.* 45 pp. (in press)

Fu, L.L., E.J. Christensen, C.A. Yamarone Jr., M. Lefebvre, Y. Menard, M. Dorrer, and P. Escudier, 1994: TOPEX/Poseidon mission overview. *J. Geophys. Res*., **99**, 24369-24381.

Hogan, T. and T.E. Rosmond, 1991: The description of the Navy Operational Global Atmospheric Prediction System's spectral forecast model. *Mon. Wea. Rev*., **119**, 1786-1815.

Hurlburt, H.E., 1984: The potential for ocean prediction and the role of altimeter data. *Mar. Geod*., **8**, 17-66.

Hurlburt, H.E. and P.J. Hogan, 2000: Impact of 1/8° to 1/64° resolution on Gulf Stream model-data comparisons in basin-scale subtropical Atlantic Ocean models. *Dyn. Atmos. Ocean*., **32**, 283-329.

Hurlburt, H.E. and E.J. Metzger, 1998: Bifurcation of the Kuroshio Extension at the Shatsky Rise. *J. Geophys. Res*., **103**, 7549-7566.

Hurlburt, H.E. and J. D. Thompson, 1980: A numerical study of Loop Current intrusions and eddy shedding. *J. Phys. Oceanogr.,* **10**, 1611-1651.

Hurlburt, H.E. and A.J. Wallcraft, 2000a: Eddy-resolving global ocean modeling and prediction. *2000 Innovation Collection* Case Study for the Smithsonian Institution's Permanent Research Collection at http://www.cwheroes.org/cgi-bin/db_main/db1.pl?fid=981489338.36018&Search& cgifunction=form.

Hurlburt, H.E. and A.J. Wallcraft, 2000b: A real-time 1/16° global ocean nowcast/forecast system. *NAVO MSRC Navigator*, Spring 2000, NAVO MSRC, Stennis Space Center, MS, pp 4-6.

Hurlburt, H.E., D.N. Fox, and E.J. Metzger, 1990: Statistical inference of weakly correlated subthermocline fields from satellite altimeter data. *J. Geophys. Res.*, **95**, 11375-11409.

Hurlburt, H.E., R.C. Rhodes, C.N. Barron, E.J. Metzger, O.M. Smedstad, and J.-F. Cayula, 2000: A feasibility demonstration of ocean model eddy-resolving nowcast/forecast skill using satellite altimeter data. NRL/MR/7320--00-8235, Naval Research Laboratory, Stennis Space Center, MS, 23 pp.

Hurlburt, H.E., A.J. Wallcraft, W.J. Schmitz Jr., P.J. Hogan, and E.J. Metzger, 1996: Dynamics of the Kuroshio/Oyashio current system using eddy-resolving models of the North Pacific Ocean. *J. Geophys. Res*., **101**, 941-976.

International GODAE Steering Team, 2000: Global Ocean Data Assimilation Experiment Strategic Plan. GODAE Report #6. Published by the GODAE International Project Office, c/- Bureau of Meteorology, Melbourne, Australia, 26 pp.

Jacobs, G.A. and R. Cheney, 2001: Navy and NOAA Operational Requirements for High-Resolution Ocean Topography (this volume).

Jacobs, G.A., C.N. Barron, M.R. Carnes, D.N. Fox, H.E. Hurlburt, P. Pistek, R.C. Rhodes, W.J. Teague, J.P. Blaha, R. Crout, and K.R. Whitmer, 1999: Navy altimeter requirements. NRL/FR/7320--99-9696, Naval Research Laboratory, Stennis Space Center, MS, 20 pp.

Jacobs, G.A., C.N. Barron, and R.C. Rhodes, 2001: Mesoscale characteristics, *J. Geophys. Res*. (in press)

Ji, M., R.W. Reynolds and D.W. Behringer, 2000: Use of TOPEX/Poseidon sea level data for ocean analyses and ENSO prediction: Some early results. *J. Climate,* **13**, 216-231.

Metzger, E.J., O.M. Smedstad, H.E. Hurlburt, A.J. Wallcraft, and R.C. Rhodes, 2001: Nowcasting and forecasting the global ocean. *Backscatter*, AMRS Association, Winter 2001, pp. 25-30.

Moore, D. R. and A. J. Wallcraft, 1998: Formulation of the NRL Layered Ocean Model in spherical coordinates. Naval Research Laboratory Rep. NRL/CR/7323-96-0005, Naval Research Laboratory, Stennis Space Center, MS, 24 pp. [Available from Naval Research Laboratory, Stennis Space Center, MS 39529.]

Murphy, A.H., and E. S. Epstein, 1989: Skill scores and correlation coefficients in model verification. *Mon. Wea. Rev.*, **117**, 572-581.

Rhodes, R.C., H.E. Hurlburt, A.J. Wallcraft, E.J. Metzger, J.F. Shriver, O.M. Smedstad, and A.B. Kara, 2001: A real-time 1/16° global ocean nowcast/forecast system. *2001 NRL Review*, Naval Research Laboratory, Washington, D.C., pp. 156-160.

Segschneider, J., D.L.T. Anderson and T.N. Stockdale, 2000a: Toward the use of altimetry for operational seasonal forecasting. *J. Climate*, **13**, 3115-3138.

Segschneider, M. Balmaseda and D.L.T. Anderson, 2000b: Anomalous temperature and salinity variations in the tropical Atlantic: Possible causes and implications for the use of altimeter data. *Geophys. Res. Lett.*, **27**, 2281-2284.

Stockdale, T.N., D.L.T. Anderson, J.O.S. Alves and M.A. Balmaseda, 1998: Global seasonal rainfall forecasts using a coupled ocean-atmosphere model. *Nature*, **392**, 370-373.

Vossepoel, F.C. and D.W. Behringer, 2000: Impact of sea level assimilation on salinity variability in the western equatorial Pacific. *J. Phys. Oceanogr.*, **30**, 1706-1721.

Wallcraft, A. J., 1991: The Navy Layered Ocean Model users guide. NOARL Rep. 35, Naval Research Laboratory, Stennis Space Center, MS, 21 pp. [Available from Naval Research Laboratory, Stennis Space Center, MS 39529.]

Wallcraft, A. J. and D. R. Moore, 1997: A scalable implementation of the NRL Layered Ocean Model, *Parallel Comput.,* **23**, 2227-2242.

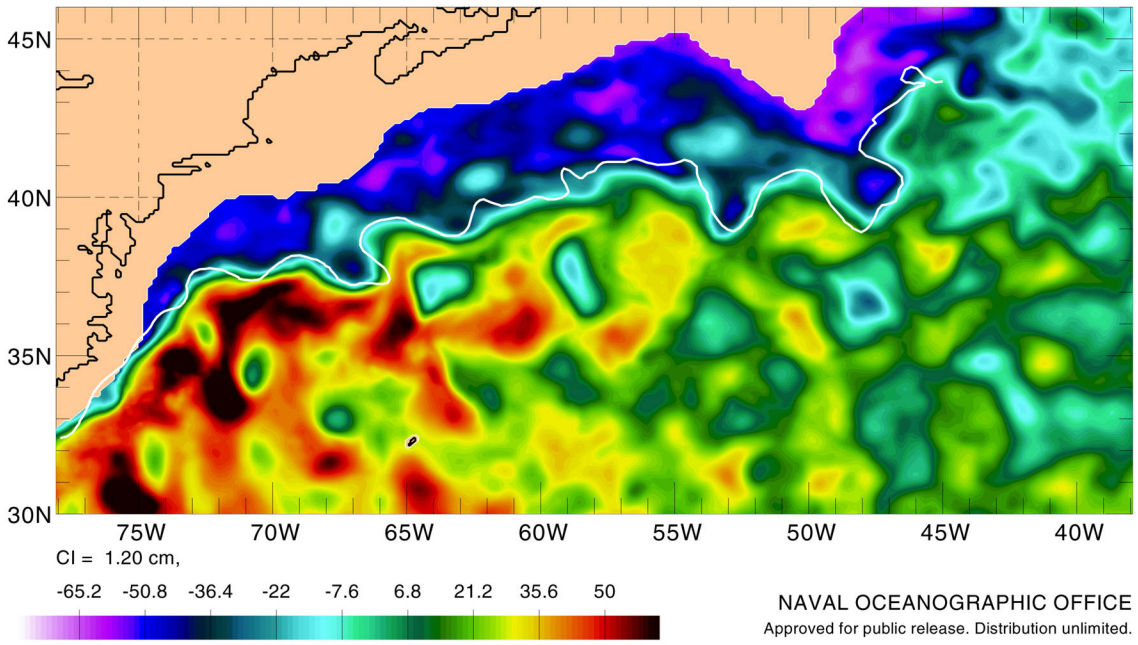

Figure 1. Real-time SSH snapshot in the Gulf Stream region for 11 June 2001 from the 1/16° eddy-resolving global ocean prediction model operational at NAVO. Real-time SSH from three satellite altimeters (ERS-2, GFO and TOPEX) was assimilated along with SST from satellite IR. The line overlaid provides a Gulf Stream pathway comparison, model SSH vs an independent analysis from satellite IR imagery by NAVO (no model products used). This comparison required recent, clear, cloud-free IR imagery, which is not often available over the full length of the pathway.

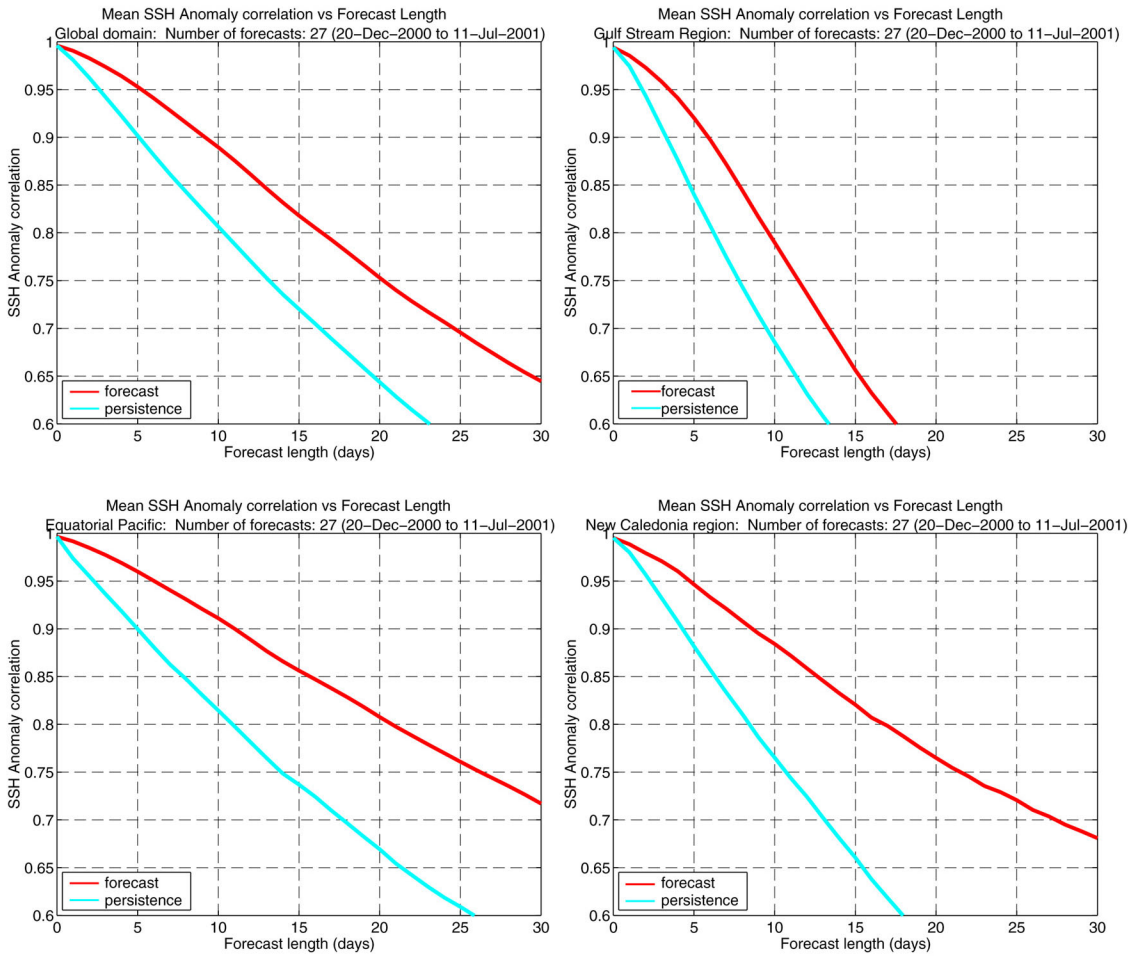

Figure 2. 30-day forecast verifications using SSH anomaly correlation vs time over the global domain and three diverse subregions, the Gulf Stream, the equatorial Pacific and the New Caledonia region. Persistence is a forecast of no change. The forecasts are verified against subsequent final analyses for each day. These are performed 3 days in arrears when more satellite altimeter data surrounding that date is available, some with reduced orbit error. The forecasts are made from the first of 4 daily analyses made for each date, so the anomaly correlation at day "0" $\neq 1$. The minimum anomaly correlation plotted, .6, is the minimum for useful forecast skill (Murphy and Epstein, 1989).

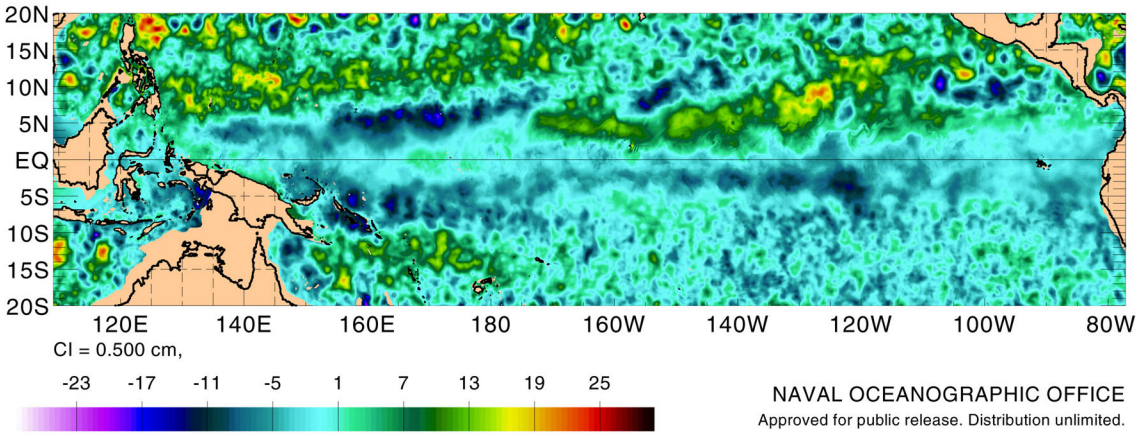

Figure 3. Real-time snapshot of SSH anomaly for 17 Aug 2001 in the equatorial Pacific region from the 1/16° global ocean prediction system operational at NAVO.

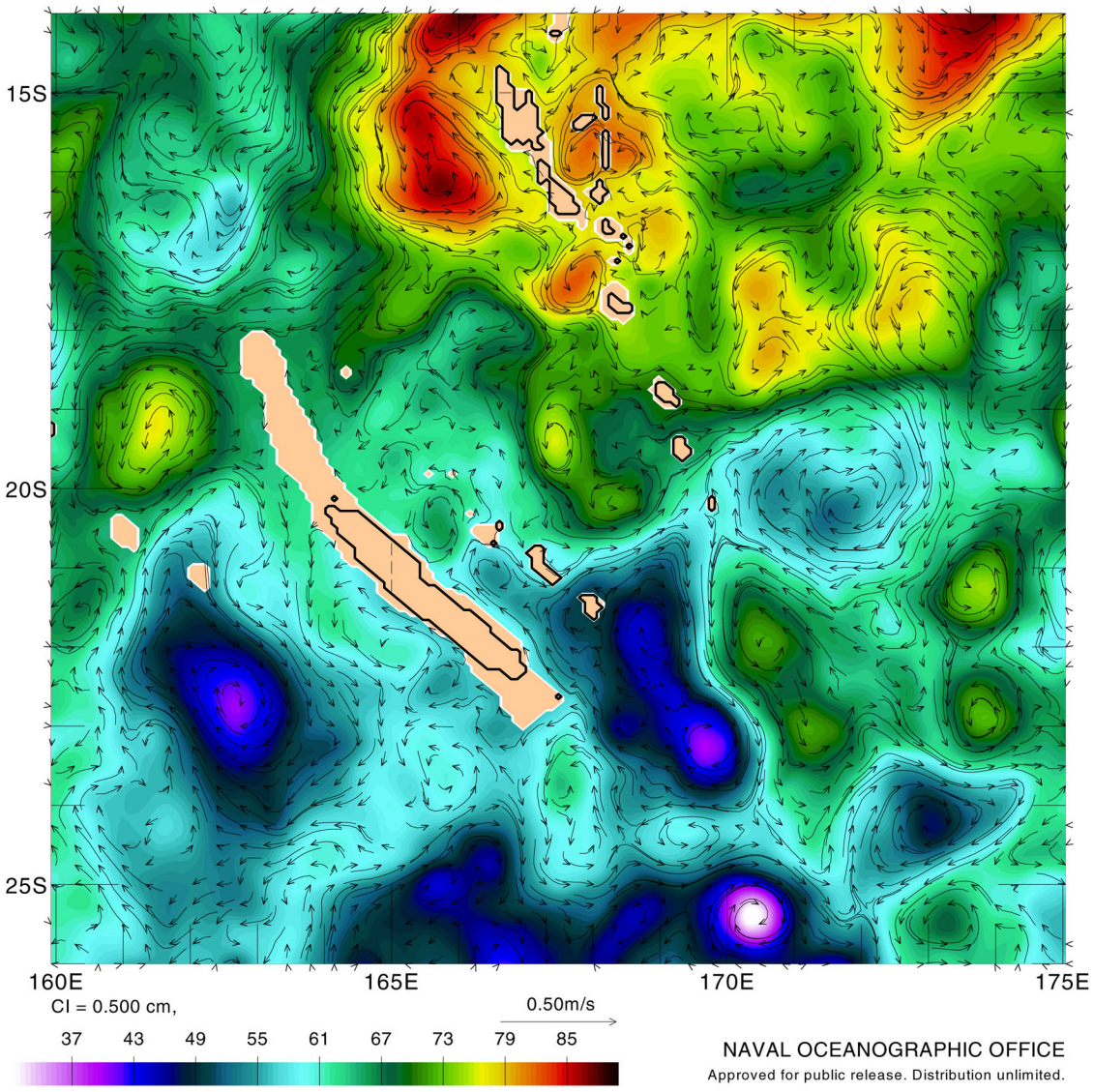

Figure 4. Real-time snapshot of SSH with surface layer currents overlaid on 15 May 2001 in the New Caledonia region from the 1/16° global ocean prediction system operational at NAVO.

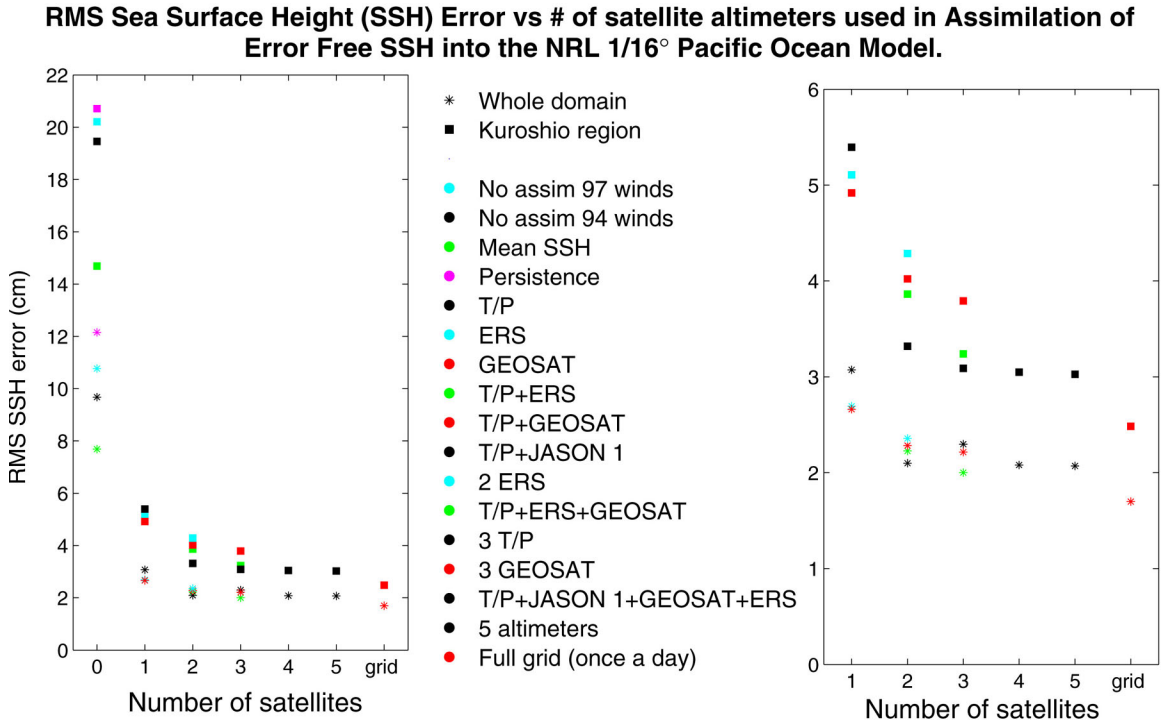

Figure 5. Test of altimeter data capability to constrain a realistic highly eddy-resolving ocean model. Control run (CR) was forced 1990-1998 using 12-hourly FNMOC winds. Starting from a 1997 CR initial state, 1994 wind forcing and simulated CR altimeter data from 1994 were assimilated for 80 days to make the model in 1997 look like the model CR in 1994. Many features take >80 days to respond to wind forcing or are a nondeterministic response to forcing. SSH RMS error is the value over the last 30 days of assimilation. The right panel is the same as the left except that "0" satellites is omitted and the ordinate is expanded to better show the impact of increasing the number of satellites. The two ERS are for altimeters covering the same ground tracks 1/2 a repeat cycle apart, while the T/P + Jason 1 are for altimeters offset by 5 days and 1/2 the equatorial T/P track spacing. These plus Geosat are the 5-altimeter configuration. The three T/P and three Geosat are for simultaneous equatorial crossings 1/3 the equatorial track spacing apart. Adapted from Hurlburt et al. (2000) with some more recent results.

Tides Over Ridges, Shelves and Near the Coasts

Christian Le Provost
GRGS/LEGOS
18 Ave. Edouard Belin
31401 Toulouse Cedex 4, France

T/P and ERS satellite altimetry, together with improved hydrodynamic models, has allowed to map the characteristics of the ocean tides over the global ocean. Over the deep ocean, it is commonly agreed that the barotropic tides are now known and predictable with an accuracy of the order of 3 cm. The more recent solutions (for example GOT99 and FES99) are very close to each other. As a typical example, for the major M_2 tide, the maximum differences are of the order 2.5 cm in a very limited number of locations. The major uncertainties remain over the shelves and in coastal areas. Some improvements are also expectable over mid ocean ridges and seamounts.

High resolution altimetry and tides over mid ocean ridges

Most of the state of art global ocean tide models derived from altimetry have been generated by applying long wavelength corrections to a priori hydrodynamic model results. The short wavelengths in these solutions are thus the ones of the hydrodynamic models.

However, with the accuracy of the last altimeter missions (mainly T/P, but also ERS), and the amount of data available, it is possible to get accurate tidal estimates from along track altimetry. By analyzing only 3 years of T/P data along track, Ray and Mitchum (1996) showed that M_2 baroclinic signal could be found in the altimetric measurements, phase locked with the barotropic tides. Also, Tierney et al (1998) have carefully investigated the potential and limiting factors of along track tidal analysis with 4.5 years of T/P data. They have, among other points, clearly shown that along track analysis allows to catch short wavelength tidal signals, *which are not baroclinic tides*. These short wavelength signatures are due to mid ocean ridges: they are also recovered in the purely hydrodynamic barotropic solutions FES 94 (Le Provost et al, 1994) and the more recent ones FES95 (Le Provost et al, 1998) and FES 98 (Lefevre et al, 2000-b). On figure 1, the map of the amplitude of the M2 tidal velocities can be used as a proxy to illustrate the expected location of these short wavelength signatures.

To fully observe the 2D structure of these short wavelength tidal characteristics due to mid ocean ridges, high-resolution altimetry is needed. Measurements must be at the level of accuracy of the on going altimeter missions T/P and ERS, with a space resolution to be defined more specifically, but typically of the order of 10 km in 2D on the horizontal. The time resolution for tidal applications is not so crucial, as far as the tidal aliasing problem is considered with care, except for well known limitations for a few constituents such as K_1 with the T/P sampling, and the solar tides with the ERS sampling.

Barotropic tides over continental shelves and near the coasts

Over shelves and when approaching the coasts, tidal amplitudes can increase up to several meters. Also, the horizontal gradients can reach up to several centimeters per km, and the horizontal patterns in amplitude and phase of the main tidal components are strongly reduced. The typical wavelength of the shallow water gravity wave are indeed controlled by the local bathymetry as $(gh)^{1/2}$. Table 1 gives typical wavelengths versus depths for the different tidal groups. By 50-m depth, the semi-diurnal wavelength is typically 1000 km. By 20 m, it reduces to 600 km. Illustrations of the complexity of the co-tidal patterns can be found over areas where regional high resolution numerical hydrodynamic models have been developed: the European continental shelf (Flather, 1981), the Patagonian shelf (Glorioso and Flather,

1997) and the Yellow Sea (Lefevre et al, 2000-a). Figure 2.1 shows how limited is the information coming from the T/P observations over the European Continental Shelf, where the tidal characteristics are complex as illustrated by figure 2.2.

This is the reason why even now, high precision altimetry has not allowed to correctly map the characteristics of the major tidal components over the shelves and in coastal areas. Recent attempts to merge T/P and ERS data are on going (Andersen, personal communication, Ray, personal communication) but they are facing big trouble when approaching the coasts, because of lack of altimetric data, and because of too coarse inter-track resolution. Besides, the hydrodynamic models, which can help to fill the gaps and extrapolate up to the coast, are very dependent on the bathymetry, which accuracy is still poor in many areas.

The analysis of long enough records of along track T/P and ERS data has demonstrated the feasibility to extract the characteristics of the major tidal waves, at the 2 cm level accuracy (Andersen, 1999) even in coastal areas.

High resolution altimetry can thus help to improve the mapping of the tidal characteristics of the major constituents in coastal areas, by allowing to resolve their 2D spatial structures and observe the strong horizontal gradients in amplitude and phase observed along the coastlines. As above, the level of accuracy must be the one of the on going altimeter missions T/P and ER. The space resolution must be typically of the order of 5 km in 2D on the horizontal. The time resolution for tidal applications is not crucial, as far as, again, the tidal aliasing problem is considered with care.

Non linear tides over continental shelves and near the coasts

In coastal areas, tides are also more complex because of non-linear dynamical processes, which distort the tidal waves. The dynamical mechanisms at work are well known (Le Provost, 1991). They are due to wave propagation sensitivity to difference in depth between high and low tides, spatial acceleration of the flows around capes, and non linear bottom friction.

In term of harmonic description of the tides, these non linear distortions lead to the generation of harmonic and compound tides, in all the frequency species: diurnal, semi-diurnal, but also quarter diurnal, six diurnal,… These nonlinear constituents can reach several tens of centimeters. And their patterns are the more complex as their frequency is higher. Illustrations of the complexity of the co-tidal maps of these constituents can be found over areas where the astronomical tides are amplified: the European continental shelf, the Patagonian shelf, the Yellow Sea ,…

Attempts to extract the characteristics of such tidal waves (M4, MS4, and M6) have been presented by Andersen (1999) for the European shelf. Although the long altimetric records allow now to extract the amplitude and the phases of these constituents with an acceptable level of accuracy (2.5 cm), the short wavelength of these higher harmonic tidal waves render difficult the inter track interpolations.

High resolution altimetry is need to fully map these non linear high frequency tidal waves. The required accuracy and precision are the same as above (centimetric, 5 km resolution, no major constraint on the time sampling, except the well known limitations due to aliasing). Large swath altimeter satellite missions, like WSOA on T/P-Jason track, with 13 km resolution and 150 km swath will allow to get a full coverage of areas such as the North Sea. Although the space resolution will be at the higher bound, such measurements will help a lot to map these non linear waves. The usefulness of these data is however dependant on the level of accuracy and on the insurance that the elementary pixels over the ocean will not be contaminated by the presence of the coasts in the swath. The limitations over the year in the operation of the instrument could be another important limitation in the de-saliasing of the tidal signal.

Conclusions

Satellite altimetry has renewed the scientific interest on ocean tides. Beside the need to correct the altimetric signals from the tidal contribution, the improved description of the global ocean tides has made possible to revisit basic questions such as "how and where tides are dissipated" (Ray, 1994; Kantha et al, 1995; Le Provost and Lyard, 1997; Egbert, 1997,…) and the possible role of the tides in deep ocean mixing and thermohaline circulation (Munk, 1997, Munk and Wunsch, 1997, Egbert and Ray, 2000). Improvements of our knowledge of the tides over ridges, shelves and coastal areas, through high resolution satellite altimetry will help to do further progress on this renewed topic.

The observation of the tides through high-resolution satellite altimetry in coastal areas will also extend the interest of this technique in new domains of applications such as coastal management, ship routing, marine safety.

References

Andersen, O.B., 1999: Shallow water tides in the Northwest European Shelf region from TOPEX/POSEIDON altimetry. *J. Geophys. Res*., **104**, C4, 7729-7741.

Flather, R.A., 1981: Results from a model of the Northeast Atlantic relating to the Norvegian Coastal Current, in *The Norvegian Coastal Current*, **2**, edited by Saetre and M. Mork, 427-458, Univ. Bergen, Norway.

Egbert, G.D., 1997: Tidal data inversion: interpolation and inference. *Prog. Oceanogr.,* **40**, 53-80.

Egbert, G.D. and R.D. Ray, (2000): Significant dissipation of tidal energy in the deep ocean inferred from satellite altimetry. *Nature*, **405**, 775-778.

Glorioso, P.D. and R.A. Flather, 1997: The Patagonian Shelf tides. *Prog. Oceanogr.,* **40**, 263-283.

Kantha L.H., C. Tierney, J.W. Lopez, S.D. Desai, M.E. Parke and L. Dexler, 1995: Barotropic tides in the global oceans from nonlinear tidal model assimilating altimetric tides. 2. Altimetric and geophysical implications. *J. Geophys. Res.,* **100**, C12, 25,309-25,317.

Kantha, L.H., and C.C. Tierney, 1997: Global baroclinic tides. *Prog. Oceanogr*., **40**, 163-178.

Lefevre, F., C. Le Provost, and F. Lyard, 2000a: How can we improve a global ocean tide model at a regional scale? A test on the Yellow Sea and the East China Sea. *J. Geophys. Res.,* **105***,* C5, 8707-8727.

Lefèvre, F., C. Le Provost, and F. Lyard, 2000b: FES98: a new global ocean tide finite element solution independent of altimetry. *Geophys. Res. Letters,* **27**, 17, 2717-2720.

Le Provost, C., 1991: Generation of overtidess and compound tides (review). In *Tidal Hydrodynamics*, B. Parker, ed., John Wiley and Sons, New York, 269-296.

Le Provost, C., M.L. Genco, F. Lyard, P. Vincent, and P. Canceil, 1994: Tidal spectroscopy of the World Ocean tides from a finite element hydrodynamic model. *J. Geophys. Res.*, **99**, C12, 24777-24798.

Le Provost, C. and F. Lyard, 1997: Energetics of the M2 barotropic ocean tides: an estimate of bottom friction dissipation from a hydrodynamic model. *Prog. Oceanogr.,* **40**, 37-52.

Le Provost, C., F. Lyard, J.M. Molines, M.L. Genco, and F. Rabilloud, 1998: A Hydrodynamic Ocean Tide Model Improved by Assimilating a Satellite Altimeter-derived Data Set. *J. Geophys. Res*., **103**, C3, 5513-5529.

Munk, W., 1997: Once again: once again tidal friction. *Prog. Oceanogr*., **40**, 7-35.

Munk, W. and C. Wunsch, 1997: The Moon, of Course. *Oceanography*, **10**, 3, 132-134.

Ray, R.D., 1994: Tidal energy dissipation: observations from astronomy, geodesy, and oceanography. In *The Oceans: Physical-Chemical Dynamics and Human Impact*, SK Majumdar.

Ray, R.D., and G.T. Mitchum, 1996: Surface manifestation of internal tides generated near Hawaii. *Geophys. Res. Letters*, **23**, 21101-21104.

Ray, R.D., and Mitchum, G.T., 1997: Surface manifestation of internal tides in the deep ocean. *Prog. Oceanogr*., **40**, 135-162.

Tierney, C.C., M.E. Parke, and G.H. Born, 1998: Ocean tides from along track altimetry. *J. Geophys. Res.*, **103**, 10273-10287.

Table 1. Wavelength versus depth for the different tidal groups.

Depth, m	Wavelength, km			
	Diurnal	1/2 Diurnal	1/4 Diurnal	1/6 Diurnal
4000	17700	8860	4430	2950
1000	8860	4430	2215	1476
500	6260	3130	1565	1043
50	1980	990	495	330
20	1250	625	312	270

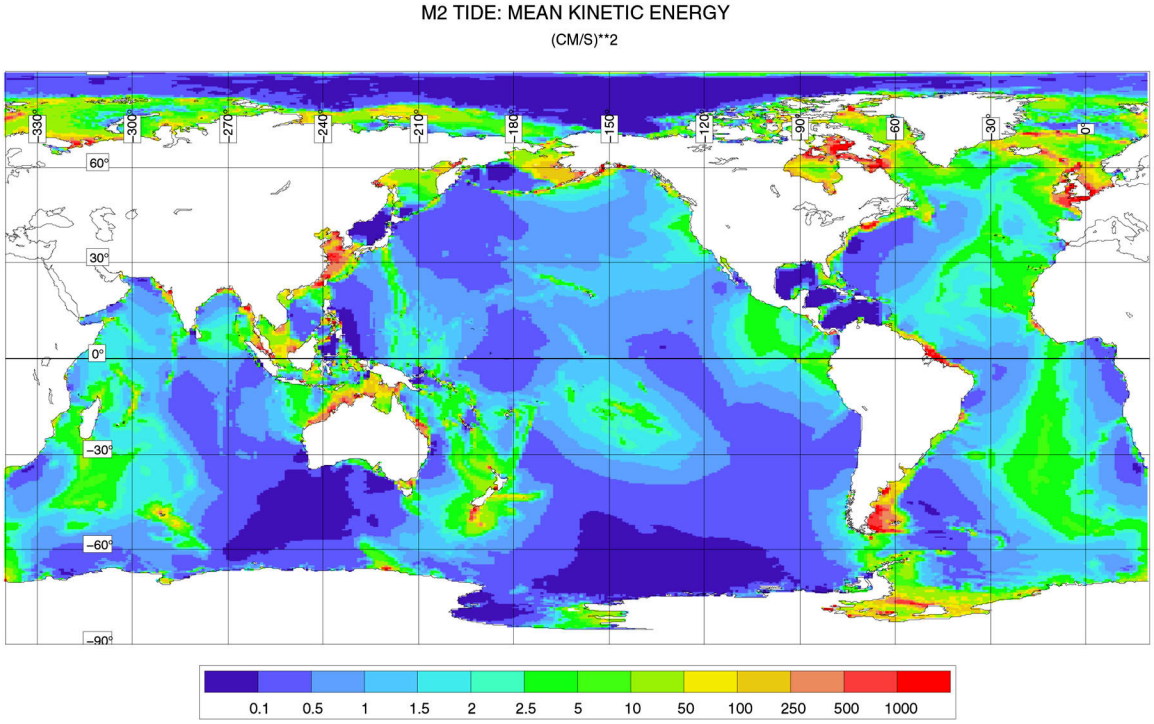

Figure 1. Mean kinetic energy of the M2 tide – short wavelength signatures in the cotidal maps are to be expected over areas where the kinetic energy is in the range 5 to 50 (cm/s)**2 (green to yellow).

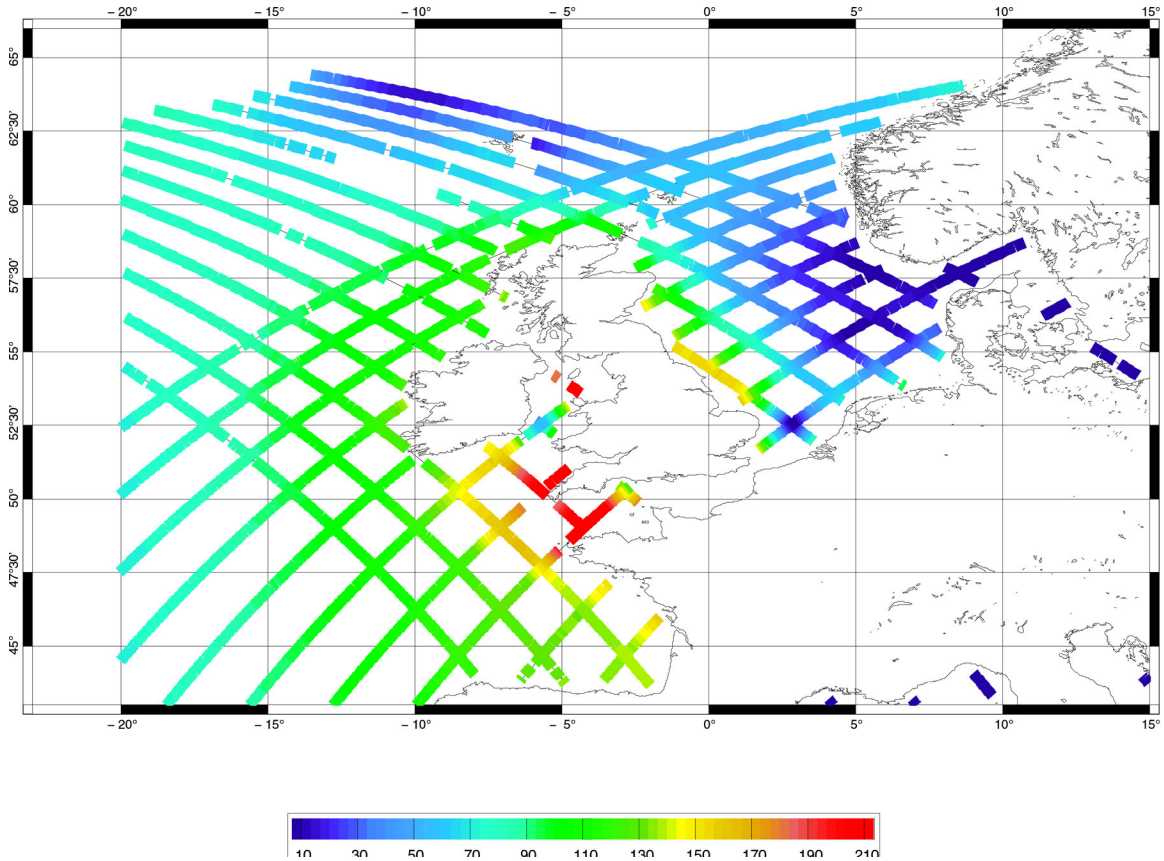

Figure 2.1. Amplitude of the M2 tide obtained from the along track analysis of the T/P altimeter data. The colour scale ranges from 10 cm (dark blue) to 210 cm (red).

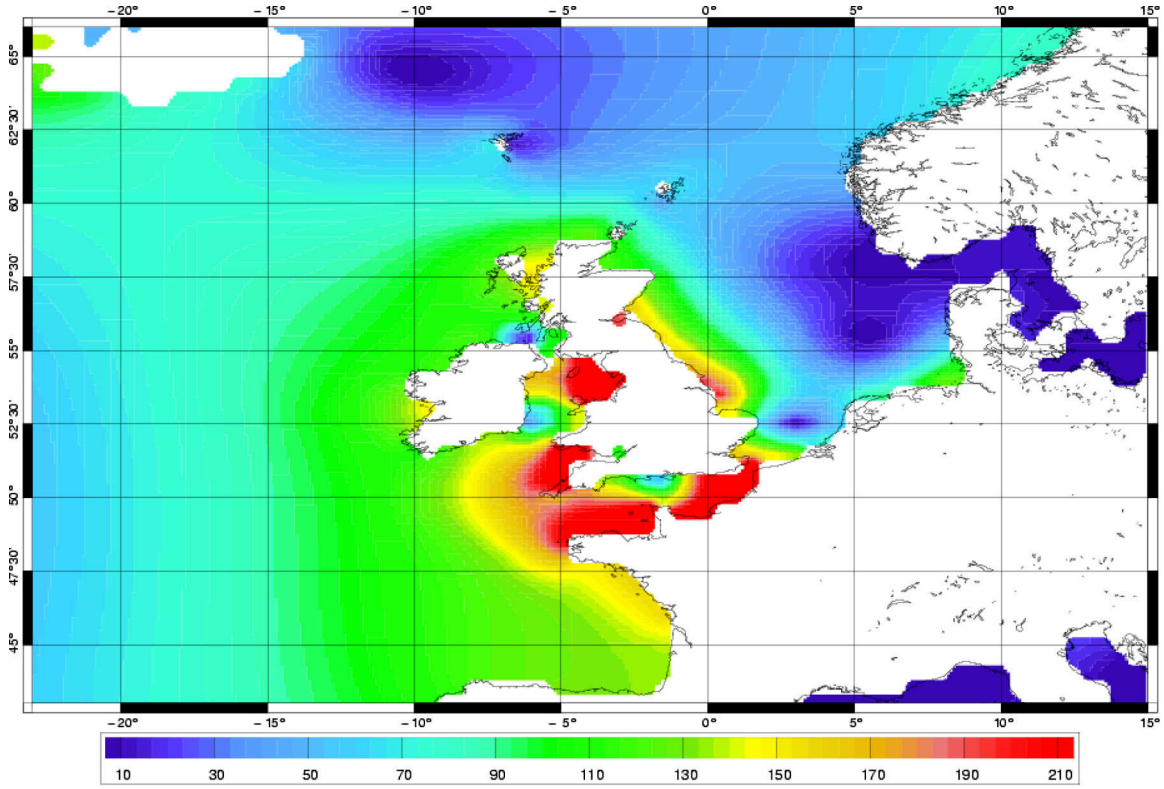

Figure 2.2. Amplitude of the M2 tide over the European Continental shelf, as given by the hydrodynamic model FES94 (Le Provost et al., 1994). The colour scale is the same as for figure 2.1.

Applications of High-Resolution Ocean Topography to Ocean Tides

Richard D. Ray
Space Geodesy Branch, Code 926
NASA Goddard Space Flight Center
Greenbelt, MD 20771

For tides the most obvious applications of high-resolution altimetry are the improved mapping of tides on continental shelves and near coasts and the study of global internal tides. High resolution altimetry, however, would also benefit deep-ocean tidal mapping, which still has room for improvements, even after nine years of Topex/Poseidon observations. This chapter addresses primarily deep-ocean surface and internal tides. Coastal tides are discussed in detail in paper 6 of this report.

Deep-Ocean Barotropic Tides

By "deep-ocean" tides we mean here any tidal phenomena whose spatial scales exceed 1000 km or so. Thus, by definition, such phenomena do not explicitly require "high-resolution" altimetry. But many of the proposed high-resolution schemes would nonetheless aid in the study of deep-ocean tides, primarily by their wealth of additional observational data. To understand these benefits it is worth considering some of the deep-ocean problems still remaining after 9 years of T/P. We list three such problems, in rough order of *increasing* importance; others could be considered as well.

(1) Residual K1/Ssa coupling in high latitudes

As is well known, the 9.9-day orbital repeat sampling of T/P causes short-period tidal signals at any given location to be aliased to longer, sometimes very long, periods. One of the most problematic is K1, which is aliased to a period of 173 days, close to the semi-annual tide Ssa (which is not a sharp spectral line at 183 days but is broadly peaked because it is driven primarily by meteorology). For mapping K1 in deep ocean, the problem is mitigated considerably at lower latitudes by the K1 phase differences between ascending and descending arcs (Schrama and Ray, 1994). At high latitudes, however, the phase differences are minimal and the K1/Ssa coupling most severe. There is some evidence that this cross-talk has not been eliminated, even in more recent tide models. (It is important to realize that any along-track altimetric tide estimates cannot benefit from ascending/descending phase differences, and these estimates are clearly and seriously affected by cross-talk.)

(2) Noisy small tidal constituents

Constituents too small to be well determined by altimetry are, ipso facto, not of great importance when developing tidal model corrections to altimetry. For other reasons, however, such constituents are important in their own right. They define the ocean response at their own distinct frequencies, often revealing subtle and interesting effects (e.g., Cartwright, 1975). Moreover, some are still important for corrections to other geodetic measurements despite their weakness. A prime example is the $\psi 1$ tide, whose frequency is close to that of the earth's nearly diurnal free wobble, which is of utmost importance to solid earth studies of gravimetry and nutations (e.g., Baker, 1984).

There are two aspects:

(i) Short-period constituents. Very small constituents are more severely impacted by measurement noise than large consituents like M2. The problem is most acute for small tides at the edges of the tidal bands -- for example, Q1, J1, and 2N2. Other small tides within the bands can be recovered by a response analysis, but tides at the edges of bands require extrapolation of admittances and are unlikely to be well determined. Tides where the admittance is not smooth are also difficult; again the prime example is $\psi 1$. Mapping these tides will benefit considerably from the additional data in proposed high-resolution missions, including the increased sampling rates and possibly improved aliasing characteristics.

(ii) Long-period consituents. The tides Mf, Mm, Mt are embedded in a background of ocean noise that is strongly red. Increased altimeter sampling rates will hardly improve mapping these tides, but the longer time series from additional missions should help considerably.

It should be acknowledged that many of these small, noisy constituents could be fairly reliably determined by assimilation techniques, where the additional hydrodynamic information can overcome limitations in direct measurements. The extent that this is so depends, of course, on the realism of the hydrodynamic model, including its bathymetry. Some tides like $\psi 1$ are complicated by inaccurately known (radiational) forcing and even inaccurately known Love numbers.

(3) Tides in high latitudes

Tides above the T/P latitude limit of 66° are not well determined. This is of increasing concern to several upcoming NASA missions, especially GRACE and ICESAT. The problem is exceedingly difficult, because there is a general lack of any type of high quality data. Any altimeters flying at the required higher inclinations are impeded by ice. Moreover, any satellite flying at such high inclinations experiences such slow orbit precession that the solar tides are unavoidably aliased into long periods. It appears that only a series of satellites flying in multiple orbit planes could adequately sample S2 and K1 and decouple them from annual, semi-annual, or secular signals. We therefore urge that missions like AltiKa, planned for sun-synchronous orbits, be placed into a series of different orbit planes, especially ones "tidally orthogonal" to the present ERS-1/2 plane.

Internal Tides

The discovery that internal tides could be mapped by altimetry has opened up a new avenue of investigation in a subject that has traditionally relied on *in situ* measurements. In particular, altimetry affords a global view unavailable to traditional methods. By no other method can the large-scale picture of sources, sinks, and fluxes of internal tide energy be so clearly studied (e.g., Ray and Cartwright, 2001). The importance of this subject to vertical mixing in the deep ocean is well recognized (Munk and Wunsch, 1997), which has helped justify such programs as the Hawaii Ocean Mixing Experiment (HOME).

The view so far provided by Topex/Poseidon, however, is limited in several ways. One is caused simply by the difficulty of extracting such small surface signals from a noisy ocean. While an internal tide can have vertical displacements of tens of meters or more at depth, the surface displacements are only a few cm at most. Even now, after nine years of T/P data, it is extremely difficult to extract unambiguously the internal tide in regions of high mesoscale variability. Longer time series and/or more rapid sampling would be clearly beneficial.

The second limitation actually stems from the method's strength. The method presently used exploits the fact -- itself somewhat surprising -- that in some parts of the world a significant component of the internal tide maintains temporal coherence with the astronomical tide. It is only by averaging such data over long time spans that 1-cm or smaller waves are successfully mapped. Yet *in situ* investigations show that internal tides in many regions are often highly incoherent, if not outright intermittent, and these signals remain hidden in the T/P noise. We expect that eventually altimetry can extend its ability to map some incoherent signals; for example, as the altimetry time series grows longer it may be possible to delimit the analysis to certain periods when the stratification of a region is favorable to internal tide generation. A long, and more rapidly sampled, time series would be required.

The third limitation, and the one most readily addressed by high-resolution altimetry, is the limited spatial resolution of T/P (and even ERS). The expected theoretical wavelengths of first-mode M2 internal tides can be calculated from climatological hydrography. These expected wavelengths are shown in Figure 1. The longest waves are 120 to 150 km. At higher latitudes where stratification weakens, the

wavelengths are considerably shorter. In addition, there is evidence in the T/P data (Ray and Mitchum, 1997, Figure 13) that higher baroclinic modes can be seen. The expected second-mode wavelengths would be roughly half those shown in Figure 1. ERS altimetry can certainly help map such short-wavelength phenomena, but it too is spatially too coarse to map in the required detail. The study of internal tides is clearly an ideal application for high-resolution altimetry.

Since the internal tide signals at the ocean's surface are no more than a few cm (often smaller), it is therefore obvious that Topex-class accuracies are required. Also required are long time series of measurements at any location, either by maintaining a long mission (as with T/P) or by obtaining more rapid sampling. As a rough rule of thumb, at least one hundred repeat measurements at any location is a minimum for a reasonably reliable tidal analysis, but the more the better.

Moreover, since the data are analyzed at each point along a satellite ground-track, tidal aliasing problems are of utmost concern. Sun-synchronous satellites are useless for studying solar tides in along-track fashion. The Geosat orbit is also not particularly favorable, because the primary tide M2 is aliased to 317 days, uncomfortably close to the annual cycle. The Topex/Poseidon orbit has been a reasonable compromise; its main drawback is the near aliasing of K1 to the semiannual cycle.

References

Baker, T.F., 1984: Tidal deformations of the Earth. *Sci. Prog.*, **69**, 249-267.

Cartwright, D.E., 1975: A subharmonic lunar tide in the seas off Western Europe. *Nature*, **257**, 277-280.

Munk, W.H. and C. Wunsch, 1997: The moon, of course. *Oceanography*, **10**, 132-134.

Ray, R.D. and D.E. Cartwright, 2001: Estimates of internal tide energy fluxes from Topex/Poseidon altimetry: Central North Pacific. *Geophys. Res. Lett.*, **28**, 1259-1262.

Ray, R.D. and G.T. Mitchum, 1997: Surface manifestation of internal tides in the deep ocean: observations from altimetry and island gauges. *Prog. Oceanogr.*, **40**, 135-162.

Schrama, E.J.O. and R.D. Ray, 1994: A preliminary tidal analysis of Topex/Poseidon altimetry. *J. Geophys. Res.*, **99**, 24799-24808.

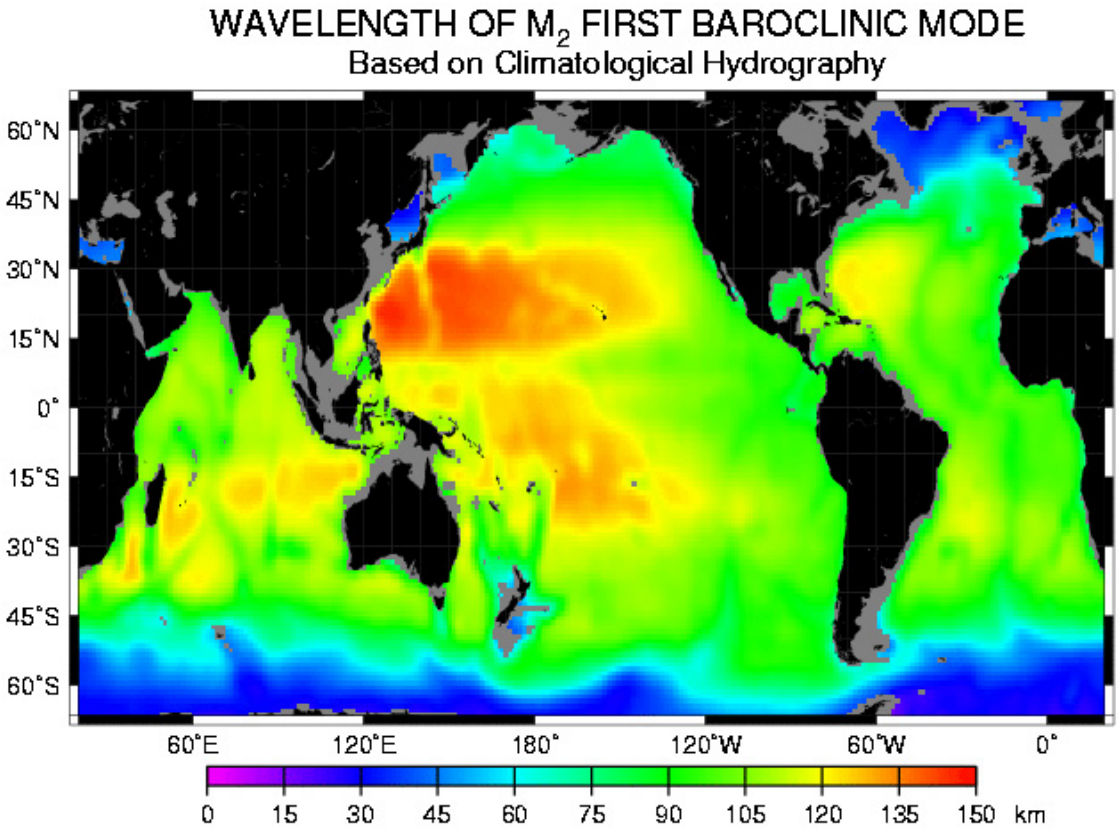

Figure 1. The expected theoretical wavelengths of first-mode M2 internal tides calculated from climatological hydrography.

Biogeochemical Aspects of Mesoscale Variability

David M. Glover
Woods Hole Oceanographic Institution
Dept. of Marine Chemistry and Geochemistry, Mail Stop 25
Woods Hole, MA 02543-1541

Abstract This paper was presented to the High-resolution Ocean Topography Science Working Group to present the biogeochemical aspects of mesoscale variability and how it relates to the observed baroclinic field sensed by on-orbit microwave altimeters. As such, this paper summarizes the results of three projects the author is involved in: space/time patterns of biological variability as evidenced by remotely sensed chlorophyll from SeaWiFS, eddy-biogeochemical interaction near Bermuda shown by correlation analysis of SSH and SST anomalies, and gas transfer velocity of CO_2 from the altimeter backscatter of TOPEX/Poseidon.

Using the semivariogram approach from geostatistics, we characterize for the first time the global patterns of mesoscale (approx. 40-400 km and days to a few weeks) ocean biological variability. The magnitude of the variability and length scale fields are reported for a full year of SeaWiFS ocean color data. The analysis shows a number of coherent geographical patterns across a wide range of biological and physical environments. Mesoscale variance dominates ocean color variability in oligotrophic regimes and is a third to a half of the total variance even in regions with strong seasonality. Our results demonstrate the global generality of previous local and regional findings that physical mesoscale turbulence governs biological spatial scales both directly (e.g. stirring) and indirectly (e.g. nutrient injection).

Objectively analyzed fields for satellite sea surface temperature (SST, AVHRR Pathfinder) and sea surface height anomaly (SSHA, combined TOPEX/Poseidon–ERS-1/2) are used to characterize statistically the mesoscale variability about the U. S. JGOFS BATS site. Using a low-pass spatial filter (nominal 500 km cut-off), we decompose the anomalies from the seasonal cycle into two components: the large-scale regional climate variability and a mesoscale signal. A distinct surface mesoscale expression is observed in SST that has many features in common with the mesoscale SSHA variability: spatial autocorrelations of 100-200 km and westward propagation rates of 3.7-5.5 cm s^{-1}. The mesoscale SST and SSHA fields are positively cross-correlated at a statistically significant level, consistent with near surface isotherm displacements for cyclonic (low SSHA, elevated isotherms, and cold SST) and anticyclonic (high SSHA, depressed isotherms, and warm SST) eddies.

The feasibility of calculating gas transfer velocity directly from a remotely sensed measure of the sea surface roughness presents an unique opportunity. We present here a six year time series (1993-1998) of TOPEX data processed into gas transfer velocity and examine the variability of these results in space and time. The seasonal and interannual variability of the regional patterns yield insight into the sensitivity of the altimeter-based gas transfer velocity to phenomena such as ENSO. Our approach to deriving transfer velocity is subject to parameters calibrated against field and laboratory measurements. *In situ* measurements are one of the best constraints on the remote observations: wind stress vs. surface roughness.

1. Introduction

At space and time scales that we classify as “mesoscale” (40-400 km and a few days to weeks) some aspects of mesoscale biogeochemical (the geochemical signature of biological interactions with the physical environment) variability will be examined. In particular, remote sensing aspects of biological variability (as evidenced by space/time patterns of chlorophyll sensed by SeaWiFS), of eddy-biogeochemical interaction near Bermuda, and gas transfer velocity of CO_2 from altimeter backscatter are given as examples of this variability.

It has been known for quite some time that westward propagating Rossby waves can be observed in sea surface height (SSH) anomalies sensed by altimeters [Chelton and Schlax, 1996]. By plotting filtered SSH data versus longitude the westward propagating waves can be clearly seen. A connection between the physical process the Rossby waves represent and a concomitant biogeochemical response is sought by Uz *et al*. [2001]. Using ocean color data from SeaWiFS and SSH data from a combination of TOPEX/Poseidon and ERS-2 Uz *et al*. [2001] demonstrate a positive coherence between the two at time and space scales of months and thousands of kilometers.

These results immediately raise the question: what is the nature and magnitude of the interaction these correlations seem to imply? and can these interactions also be observed at the mesoscale? In what follows we will examine three aspects of the potential interaction between physical and biogeochemical variability. First a detailed look at the variability of the *biological* signal at mesoscales on a global basis for 1998 will be conducted with the help of some geostatistical machinery. Then the mechanisms will be examined by focusing on the evidence from the Bermuda area of the southwestern North Atlantic. Finally, the derivation of gas transfer velocity from altimeter backscatter is added to provide a link between the physical measurement of radar backscatter and biogeochemical cycles through CO_2 flux.

2. Geostatistical Analysis of Ocean Color

Routine measurements of ocean color from space provide for the first time a globally coherent, synoptic picture of the patterns and variability of upper ocean biology [McClain *et al*., 1998]. The large-scale ocean color field, a proxy for surface layer phytoplankton chlorophyll concentrations, is governed by the seasonal distributions of light, nutrients, upwelling and upper ocean mixing [Yoder *et al*., 1993]. On the mesoscale, ocean color variability is thought to be modulated by physical processes either directly by turbulent advection and stirring [Mackas *et al*., 1985] or indirectly via impacts on phytoplankton growth rates and trophic interactions [Garçon *et al*., 2001]. From a global perspective, satellites provide the only feasible approach for mapping ocean surface chlorophyll at the required time and space scales to characterize mesoscale variability.

Here we use Level 3 daily standard mapped images (version OC3), which are projections of the GAC data onto a global, equal-angle grid ($2\pi/2048$) with a nominal 9 km × 9 km resolution. The natural log transformation, ln(Chl), is applied to the data following the arguments of Campbell (1995) that oceanic bio-optical variability is distributed approximately log-normally. To avoid spurious effects in the semivariogram [Cressie, 1993], large-scale spatial trends are removed by subtracting monthly mean fields smoothed with a moving two-dimensional 24× 24 pixel spatial filter (equivalent to about 200× 200 km scale at the equator or roughly 2°× 2°). The resulting detrended data are referred to as the daily anomalies.

2.1. Geostatistics

Using the semivariogram approach from geostatistics [Journel and Huijbregts, 1978], we calculate the mesoscale variance and spatial decorrelation length scales globally for a full year of SeaWiFS ocean color data [McClain *et al*., 1998]. The resulting spatial structure function provides a useful measure for quantifying biological-physical interactions [Yoder *et al*., 2001] and discriminating among theoretical models. It is also a necessary component of future work to objectively analyze ocean color images using methods such as kriging [Chelton and Schlax, 1991]. A detailed description of the statistical techniques and preliminary results for a single month for the North Atlantic can be found in Fuentes *et al*. [2000]. Here the more extensive full annual and global analysis [Doney *et al*., 2001] is summarized, focusing on relating the observed patterns to underlying physical and biological processes.

The semivariogram $\gamma(\mathbf{v})$ measures the local spatial variation of geophysical data $Z(\mathrm{x})$, describing how samples are related with vector distance $\mathbf{v}$ (Journel and Huijbregts, 1978):

$$\gamma(\mathbf{v}) = \frac{1}{2}\mathrm{var}\{Z(\mathbf{x}+\mathbf{v}) - Z(\mathbf{x})\} \tag{1}$$

The semivariogram is closely related to the covariance function. In general, two neighboring points are more likely to have similar values than sample pairs farther apart. Thus the semivariogram (covariance) function will have low (high) values at small spatial lags, increasing (decreasing) with distance. Beyond some distance, the data points can often be assumed to be uncorrelated or independent, in which case the semivariogram approaches a uniform variance while the covariance function goes to zero.

2.2. Ocean color semivariogram results for 1998

Semivariograms are computed numerically for each month of 1998 for 5° × 5° areas over the globe, the size chosen after some experimentation to minimize the spatial heterogeneity of the ocean color data while retaining sufficient spatial extent to resolve the full span of the mesoscale (40 km-400 km). Separate semivariograms versus distance (in km) are then calculated in the N-S and E-W directions to highlight anisotropy. The daily semivariance estimates at each distance lag are then aggregated over the month weighted by the number of valid data pairs.

Empirical semivariograms are rarely used in their original form but rather are fit with simple statistical models to extract the desired information [Journel and Huijbregts, 1978], and we have chosen to use the spherical model:

$$\hat{\gamma}(\mathbf{v}) = \begin{cases} 0 & \mathrm{v} = 0, \\ c_0 + (\sigma^2 - c_0)\left\{\frac{3}{2}\frac{\mathrm{v}}{r} - \frac{1}{2}\left(\frac{\mathrm{v}}{r}\right)^3\right\} & 0 < \mathrm{v} \le r, \\ \sigma^2 & \mathrm{v} > r, \end{cases} \tag{2}$$

because of its common use and simple interpretation [Clark, 1979]. An example is shown in Figure 1 (variables defined in the caption). A derived parameter, the relative sill σ^2_{rel}, can be defined as that part of the total variance resolved by the observations

$$\sigma^2_{rel} = \sigma^2 - c_0 \tag{3}$$

and is attributable to geophysical processes. For each 5° × 5° area, the spherical model is fit to the monthly semivariograms using a modified version of the Levenberg-Marquardt nonlinear least-squares regression [Press *et al*., 1992], and the model parameters (nugget, range, total and relative sill), estimated errors, and correlation coefficients are stored as final output.

The results of the semivariogram analysis for the 1998 SeaWiFS data are presented in Figure 2. The semivariogram partitions the mesoscale variability in the daily anomalies into resolved (relative sill) and unresolved/noise (nugget) components. The relative sill values (Figure 2b) in the subtropics and tropics are approximately uniform and relatively low (about 0.1-0.2). Moderately larger values are observed in a band across the Equatorial Pacific and in the subpolar gyres while high values are observed along the coasts (particularly in coastal upwelling regimes) and at high latitudes. Strikingly, one sees only a weak signature in the ocean color results (Figure 2b) of the strong east-west asymmetries associated with the high eddy kinetic energy regions of the mid-latitude western boundary current systems such as the Gulf Stream or Kuroshio [e.g. Stammer, 1998]. Although the polar relative sill values are generally high, likely due to summer season bias and more coastal values, they show generally the same relationship to mean chlorophyll data and our current conclusion is that the large relative sills at high latitude are likely real. The spatial pattern of the annual mean nugget or unresolved variance (Figure 2c) is opposite in sense to that of the relative sill, high in the subtropics and low at mid- to high latitude, but with a much smaller overall magnitude. The nugget is inversely correlated with ln(Chl) at low

chlorophyll levels, and in fact, for mean chlorophyll values less than 0.1 mg m^{-3} the nugget generally exceeds the relative sill.

The zonal spatial range field (Figure 2a) exhibits a strong, banded latitudinal pattern with maximal values of 250-300 km along the Equator decreasing poleward to less than 50 km near the poles. The latitudinal decrease in biological spatial scales is similar to results for physical mesoscale variability, suggesting that a common mechanism (eddy-generation by baroclinic instability) may be responsible. Similar spatial autocorrelation lengths have been calculated from satellite observations using TOPEX/Poseidon altimeter sea-surface height data globally [Stammer, 1998] and from Advanced Very High Resolution Radiometer (AVHRR) sea-surface temperature imagery for the eastern North Atlantic from 35°N to 60°N [Krauss *et al*., 1990]. The physical eddy spatial scales outside the tropics vary roughly proportional (though not identical) to the Rossby deformation radius [Stammer, 1998], the horizontal scale where rotation becomes important relative to buoyancy and a key parameter governing turbulent ocean flow [Chelton *et al*., 1998]. A similar correspondence for ocean color spatial scales is demonstrated in Figure 3, a plot of the zonal averages of the east-west and north-south range as well as Rossby radius (from Chelton *et al*., [1998]) and the spatial eddy scale (from Stammer [1998]).

3. Biogeochemical-Physical Interactions

An interaction between physical and biological processes at the mesoscale is expected based on a simple argument. It is known that mesoscale baroclinic instabilities (i.e. eddies) can warp the underlying isopycnal surfaces and their covarying temperature and nutrient fields [McGillicuddy *et al*., 1998]. Anticyclonic eddies depress the isopycnal surfaces pushing the biota and underlying nutrients away from the euphotic zone; this has no net effect on the biogeochemical system. Cyclonic eddies, however, have a tendency to lift relatively nutrient rich water up into the euphotic zone where the biota can utilize them; the net effect is an increase in primary production. "Mode water" eddies tend to depress the permanent thermocline but raise the isopycnals within the seasonal thermocline, which has an effect similar to the cyclonic eddies.

3.1. Evidence from Bermuda

Near Bermuda in the southwestern North Atlantic several time series efforts have been underway, some going back 20 or more years. The Bermuda Atlantic Time-series Site (BATS), with a 10+ year record of approximately monthly cruises, is of particular interest to biogeochemists due to its extensive suite of biogeochemical measurements [Michaels and Knap, 1996]. It has always been suspected that some of these time series measurements have been impacted by mesoscale disturbances (eddies). Modeling efforts in this region [e.g. Doney, 1996; Doney *et al*., 1996] have identified the quantification of this mesoscale influence as an important step towards better understanding the over all biogeochemical response to variability from mesoscale to climatic scales.

Nearby Dickey *et al*. [1993] deployed a multi-sensor mooring designed to capture the time scales of variability in biogeochemical signals that, approximately monthly, cruises to the area could not. The Bermuda Testbed Mooring (BTM) has a string of thermistors, fluorimeters, spectral radiometers, current meters, and NO_3 sensors deployed over the upper 200 m of the ocean water column. Starting on or about 8 July 1995 McNeil *et al*. [1999] believe they captured the passage of a mesoscale eddy over the BTM in the depth range of 70-80 m. The signal they present is consistent with the passage of a "mode water" eddy and a clear biogeochemical response is seen at this depth. However, in this study the mesoscale response is seen at depth, beyond the usual reach of sensors in orbit. What is needed then is a determination of whether or not this signal can also be detected at the surface using the array of remote sensors available to us.

3.2. SST-SSH anomaly cross-correlation

In a related study Glover *et al*. [2001a] cross correlated SSH anomalies with sea surface temperature (SST) anomalies to quantify the magnitude of mesoscale influence on model-data mismatch seen at BATS. The study area is the 10° ×10° area centered on 32°N 64°W, approximately the location of the BATS station. The satellite analysis time window is set by the fourteen years (15 Jan. 1985 through 30 Dec. 1998) of NOAA/NASA AVHRR Ocean Pathfinder SST data [Smith *et al*., 1996] and the nearly six and a half years (Oct 1992-Jul 1998) of TPE altimeter data [AVISO/Altimetry, 1998].

In order to diagnose the role of mesoscale variability about the BATS time-series site, we first separate out the mesoscale signal from other sources of variability in the satellite observations. In particular, we want to remove the climatological seasonal cycle and the large spatial scale regional intraseasonal to interannual climate variability. Equation 4 states the traditional way of expressing a generic variable Z distributed in space and time as an anomaly Z_{Anom} relative to some climatological field Z_{Clim}:

$$Z_{Anom}(\mathrm{x},t) = Z_{Sat}(\mathrm{x},t) - Z_{Clim}(\mathrm{x},t) \tag{4}$$

The anomaly field can be further partitioned by assuming that the space-scales of the mesoscale variability are small relative to the domain size. A residual field Z_{Resid}, which we associate with the mesoscale field, is defined by removing a spatial low-pass (half-power at 500 km) filtered field Z_{Filt} from the anomaly field:

$$Z_{Resid}(\mathrm{x},t) = Z_{Anom}(\mathrm{x},t) - Z_{Filt}(\mathrm{x},t) \tag{5}$$

Figure 4 shows an example from the AVHRR SST data of the spatial nature of the sparse sampling problem and also underlines why space-time interpolation should be used. The objectively analyzed SST data for day 195 in 1993 are displayed in Fig. 4a. The remaining subplots show the decomposition into the SST_{Clim}, SST_{Anom}, SST_{Filt}, and SST_{Resid} fields, with the last sub-panel showing how sparse coverage is at this location in the 18 km AVHRR Pathfinder data for day 195. SST anomalies (SST_{Anom}) as large as ±1.5-2.0°C from the long-term climatology are observed with spatial scales of approximately 500-800 km and are captured reasonably well by the 500 km low-pass filter SST_{Filt}. The amplitude of the residual field SST_{Resid} ±1.0°C is approximately half that of the original anomalies and the spatial scales are considerably smaller as well, on the order of 40-200 km. A similar decomposition of the TPE SSHA data for the same time period was done. Typical SSHA values range from ±25 cm, and in contrast with the SST data, considerably less of the SSHA variability is accounted for by the climatology or the 500 km low-pass filter. The spatial scales of the SSHA residual features are comparable to those of SST and are also consistent with the regional SSHA decorrelation length-scales reported by Stammer [1998]. A comparison of the SST and SSHA residual images suggests a weak positive correlation, i.e. generally warm SSTs overlying positive (anticyclonic) SSHA features and the reverse.

The space and time lagged autocorrelations of the mesoscale SST and SSHA fields as well as their cross-correlation are shown in Figure 5. The spatial correlations are decomposed directionally into separate east-west and north-south lags, and the 95% significance levels for the correlations are indicated by the thick black ellipse (surrounding both positive and negative correlation coefficients). The tilt of the time-space phase relationship in the east-west direction is consistent with westward propagation of the eddies at a mean rate of approximately 5.5 cm/s. Similar, though weaker, signatures for coherent eddies and westward propagation are also found for the AVHRR SST, with perhaps a somewhat slower mean speed. Importantly, a statistically significant cross-correlation is observed between SST and SSHA, again with the characteristic westward propagation signature. The sense of the cross-correlation is positive, that

is cold SSTs are associated with negative (cyclonic) SSHA and the reverse. The cross-correlation patterns are a strong indication that the sub-surface eddy isotherm displacements, at least for the cyclonic case, reach all the way to the surface, perhaps enhanced by submesoscale upwelling along the eddy edges. The SST-SSHA correlation for positive SSHA anomalies reflect the depression of the isotherms and the concomitant increase in SST. This is, to the best of our knowledge, the first demonstration of an on-orbit detection of an interaction between the mesoscale baroclinic and temperature fields of the ocean.

4. Gas Transfer Velocity of CO_2

For certain global biogeochemical applications our understanding of the space and time distribution of the gas transfer velocity (k) is inadequate. Wallace [1995] points out that an uncertainty of a factor of two in our estimation of k, when combined with systematic errors in the measurement of the partial pressure difference of CO_2 across the air-sea interface, can lead to unacceptable error in our ability to calculate the marine flux of this gas. When applied to calculating the global flux of "excess" (anthropogenic) CO_2 the problem becomes amplified. Gruber *et al*. [1998], when examining the flux of $\delta^{13}C$ across the air-sea interface at the BATS, also found that their calculations were particularly sensitive to uncertainties in the gas transfer velocities. Both of these studies approached the calculation of k in the community standard fashion by estimating the transfer velocity from a knowledge of the wind speed and sea surface temperature (SST). However, there is accumulating evidence that the transfer velocity is sensitive to environmental conditions other than wind speed and SST, in particular, the presence of surfactants [Frew *et al*., 1999], boundary layer instability [Erickson, 1993], and wave fetch [Wanninkhof, 1992]. What is needed, then, is a direct measurement of the surface roughness expressed by the small gravity-capillary wave portion (the gas-exchange-active portion) of the surface wave spectrum.

4.1. Algorithm

The details of the development, calibration, and verification of the algorithm that computes gas transfer velocity from normalized radar backscatter is given in Frew *et al*. [2001]. For purposes of discussion we will give a brief description of the algorithm here as summarized in Glover *et al*. [2001b].

From the work of Cox and Munk [1954] there is an expression for backscatter from the geometrical optics (GO) model assuming the surface wave field is best approximated by an isotropic, Gaussian surface. For instruments probing only in the nadir direction, the mean square slope, $\langle m_n^2 \rangle$, is given by Jackson *et al*. [1992] as:

$$\langle m_n^2 \rangle = \frac{\rho_n'}{\sigma^\circ(0^\circ)} \tag{6}$$

where the subscript n is used to indicate nadir and the meaning of the ρ_n' reflects the approximation of the original azimuthally integrated cross-section by the returned power measured at nadir.

We exploit the dual frequency nature of the TOPEX altimeter by making use of the differential scattering (Ku vs. C bands) isolating a portion of the small gravity-capillary wave spectra related to gas exchange. Bock *et al*. [1999] have shown that gas exchange is linearly related to the mean square slope of waves. We effectively remove the contribution of longer waves to the mean square slope by differencing the two bands.

Since the effective wavelength of the surface roughness that determines the altimeter radar backscatter is approximately three times the incident wavelength, the combination of simultaneous measurements from a Ku-band altimeter (2.1 cm radar wavelength) and a C-band altimter (5.5 cm radar wavelength) resolves to examining the gravity-capillary wave spectra near the 6.3 cm and 16.5 cm regions. A combination of measurements from a Ka-band altimeter (0.8 cm radar wavelength) from the

AltiKa altimeter concept described in paper 16 of this report, with simultaneous measurements from a conventional Ku-band altimeter would yield information from the shorter wavelengths near 2.4 cm and 6.3 cm, which better resolves the portion of the capillary wave field that is most active in gas exchange across the air-sea interface (Bock et al., 1999; Hara et al., 2001).

The linear relationship between mean square slope and gas transfer velocity allows us to calculate *k* directly by including a slope and intercept, empirically determined from laboratory wind-wave tank experiments. In this fashion we arrive at the following equation describing our algorithm:

$$k = 7000\left(\frac{0.38}{\sigma^{\circ}_{Ku}} - \frac{0.48}{\left(\sigma^{\circ}_{C} + 0.5\right)}\right)\left(\frac{Sc}{660}\right)^{-0.5} \tag{7}$$

where we have optimized ρ'_n to field slope data from a range of values given in Jackson *et al*. [1992] and 0.5 is a small correction factor applied to the C-band backscatter to account for the lack of an absolute calibration as reported in Chapron *et al*. [1995] (fit to laboratory data). Note: in this version (3.0) of our algorithm the best fit to the calibrating laboratory data was had when the intercept was constrained to be zero. We report transfer velocities calibrated to a Schmidt number (Sc) of 660 at 20°C for CO_2.

4.2. CO_2 gas transfer velocity time-series

In what follows we present the results of applying the above algorithm to the six year record of TOPEX data starting with cycle 11 (Jan. 1993) and concluding at the end of cycle 232 (Dec. 1998), shown as zonal averages in Figure 6. The overall pattern of seasonal variation is clearly seen in Figure 6, with the maximum transfer velocities in each hemisphere's corresponding wintertime. Additionally, there is an anti-correlated period of low to very low transfer velocities along the equator. At mid-latitudes (20°-40°N) there is a period of low transfer velocities developing each year in the summertime. A similarly low austral summertime low, zonally averaged, transfer velocity does not appear in any year in the 20°-40°S zone. This could be explained by the greater fetch at these latitudes when compared to the northern hemisphere. The one exception is 1998, which does not develop the very low summertime zonally averaged transfer velocities at northern mid-latitudes. Additionally, early 1997 has the highest zonally averaged transfer velocities in the northern subpolar region. The extremely low zonal averages along the equator are interrupted during two periods: late winter-early spring in 1997 (El Niño) and in late autumn-early winter in 1998. The causal factor for the weakening of the equatorial low seen in 1998 is not readily obvious, although it appears to be preceded by a similar weakening of the mid-latitude lows farther north.

5. Summary

From analysis of satellite data in three different portions of the electromagnetic spectrum, the relationship between biogeochemical processes and mesoscale variability is seen. Analysis of the mesoscale variability of global SeaWiFS ocean color data shows a number of coherent geographical patterns across a wide range of biological and physical environments. The unresolved variance (nugget), which includes submesoscale geophysical variability as well as instrument/algorithm noise, is inversely correlated with mean chlorophyll concentration in the oligotrophic subtropics (an indication of instrument/algorithm noise) reducing to a low background value elsewhere. The mesoscale spatial scale (range) is approximately zonal, similar to the physical scales estimated from altimeter sea surface height variability data and the first baroclinic Rossby deformation radius. Objectively analyzed fields for satellite sea surface temperature (AVHRR Pathfinder) and sea surface height (TPE) are used to characterize statistically the mesoscale variability about the U. S. JGOFS BATS site. Using a low-pass

spatial filter (nominal 500 km cut-off), the anomalies from the seasonal cycle are decomposed into two components: the large-scale regional climate variability and a mesoscale signal. A clear statistical, at this scale, connection between sea surface SST and SSHA expressions of the mesoscale eddies near Bermuda is shown. For low to moderate sea-state conditions, an algorithm has been derived to yield space-time patterns of global gas transfer velocities from altimeter normalized radar backscatter. Apparently the backscatter-derived transfer velocities are sensitive to factors other than wind speed alone (fetch, surfactants, etc.), but there remain issues to be resolved. Of the future work needed, the following seems to us to be tantamount: a concerted effort to tie ground observations to satellite observations (both altimetry and scatterometry as well as ocean color and SST) and improvement of space-time coverage.

Summarizing the space-time resolutions and accuracies required from a biogeochemical point of view follows. The spatial resolution of the SSH cell on the ground should approach the spatial resolution of objectively interpolated (OI) fields of SST and chlorophyll (currently ~18 km), or support objective interpolation to this resolution. The temporal resolution should also try to approach that of the OI fields of SST and chlorophyll (currently 2 days). The reasoning for such stringent requirements are many, but the most compelling is comportable space and time scales for cross-correlation between the baroclinic field and those fields that are biogeochemically active. While data assimilation into a primitive equation model could yield this level of resolution for SSH and a comparable product could be generated for SST, the ability to create a similar field for chlorophyll is still beyond our grasp. Cross-correlating model output with actual data requires too large a leap of faith. The resolution of height should approach a rms of 2 cm, which we have demonstrated has ramifications for the allowable size of a low-pass filter when separating the mesoscale from the larger scales [Glover *et al*., 2001a]. The requirements for swath, dual vs. single frequency, and type of orbit should be obvious. Coverage should be increased slightly from the ±66° to ±75° to allow for coverage in the polar seas where biogeochemical response to climatic changes are still largely unknown.

Acknowledgments. I would like to acknowledge my co-workers who have had an active part in the work summarized in this paper. Scott Doney (NCAR) and I have been partially supported by NASA SeaWiFS Grants W-19,223 and NAG-5-6456 to work on the ocean color research, Nelson Frew (WHOI) and I have been supported by NASA grant no. NAGW-2431 and JPL contract no. 961425 to work on the gas transfer from radar backscatter project, Montserrat Fuentes (NCSU) was supported by the NCAR Geophysical Statistics Project and worked with SCD and myself on the geostatistics, Arthur Mariano (RSMAS) receives support from ONR grant N00014-95-1-0257, and Robert Evans (RSMAS) have been co-authors with me on several research papers. Scott McCue (WHOI) works with me as my programmer in Woods Hole. A number of colleagues have contributed to this paper through comments and discussions over the last several years. In particular we would like to thank T. Hoar, I. Lima, D. McGillicuddy, J. K. Moore, D. Nychka, and D. Siegel. This work would not be possible without the dedicated efforts of the NASA SeaWiFS project team. Ocean color data used in this study were produced by the SeaWiFS Project at Goddard Space Flight Center. The data were obtained from the Goddard Distributed Active Archive Center. Use of this data is in accord with the SeaWiFS Research Data Use Terms and Conditions Agreement. This work also would not be possible without the dedicated efforts of the scientists and technicians involved with the BATS program at the Bermuda Biological Station for Research. Furthermore we extend our thanks to the data producers at the AVHRR PathFinder project, the JPL PO. DAAC and AVISO for access to altimetry data used in this study. We extend our thanks to the National Snow and Ice Data Center for making the SSM/I ice data available to us.

References

AVISO/Altimetry, 1998: AVISO User Handbook, Sea Level Anomalies (SLAs), AVI-NT-011-312-CN, Edition 3.1, 35 pp.

Bock, E.J., T. Hara, N.M. Frew, and W.R. McGillis, 1999: Relationship between air-sea gas transfer and short wind waves, *J. Geophys. Res*., **104(C11)**, 25821-25831.

Campbell, J. W., 1995: The lognormal distribution as a model for bio-optical variability in the sea. *J. Geophys. Res*., **100**, 13,237-13,254.

Chapron, B., K. Katsaros, T. Elfouhaily, and D. Vandemark, 1995: A note on relationships between sea surface roughness and altimeter backscatter. In: Air-Water Gas Transfer, Selected Papers from the Third International Symposium on Air-Water Gas Transfer July 24-27, 1995, Heidelberg University, edited by B. Jähne and E. C. Monahan, pp. 869-878, AEON Verlag & Studio, Hanau.

Chelton, D.B. and M.G. Schlax, 1991: Estimation of time averages from irregularly spaced observations: with application to coastal zone color scanner estimates of chlorophyll concentration. *J. Geophys. Res*., **96**, 14,669-14,692.

Chelton, D.B. and M.G. Schlax, 1996: Global observation of oceanic Rossby waves. *Science*, **272**, 234-238.

Chelton, D.B., R.A. deSzoeke, M.G. Schlax, K.E. Naggar, and N. Siwertz, 1998: Geographical variability of the first baroclinic Rossby radius of deformation, *J. Phys. Oceanogr*., **28**, 433-460.

Clark, I., 1979: *Practical Geostatistics*. Elsevier Applied Science, New York.

Cox, C. and W. Munk, 1954: Statistics of the sea surface derived from sun glitter. *J. Mar. Res*., **13(2)**, 198-227.

Cressie, N.A.C., 1993: *Statistics for Spatial Data*, Wiley, New York.

Dickey, T., T. Granata, J. Marra, C. Langdon, J. Wiggert, Z. Chai-Jochner, M. Hamilton, J. Vazquez, M. Stramska, R. Bidigare, and D. Siegel, 1993: Seasonal variability of bio-optical and physical properties in the Sargasso Sea. *J. Geophys. Res*., **98**, 865-898.

Doney, S. C., 1996: An atmospheric surface forcing and physical upper ocean model for the JGOFS Bermuda Atlantic Time-series Study (BATS) site. *J. Geophys. Res*., **101**, 25,615-25,634.

Doney, S.C., D.M. Glover and R.G. Najjar, 1996: A new coupled, one-dimensional biological-physical model for the upper ocean: Applications to the JGOFS Bermuda Atlantic Time Series (BATS) site. *Deep-Sea Res. II*, **43**, 591-624.

Doney, S.C., D.M. Glover, S.J. McCue and M. Fuentes, 2001: Mesoscale Variability of SeaWiFS Satellite Ocean Color: Global Patterns and Spatial Scales. *J. Geophys. Res*., (submitted).

Erickson III, D. J., 1993: A stability dependent theory for air-sea gas exchange. *J. Geophys. Res*., **98(C5)**, 8471-8488.

Frew, N.M., E.J. Bock, R.K. Nelson, W.R. McGillis, J.B. Edson, and T. Hara, 1999: Spatial variations in surface microlayer surfactants and their role in modulating air-sea exchange, in 13th Conference on Boundary Layers and Turbulence, 10-15 January 1999, pp. 421-424, American Meteorological Society, Boston, MA.

Frew, N.M., D.M. Glover, E.J. Bock, S.J. McCue, W.R. McGillis, and R.J. Healy, 2001: Estimation of global CO_2 transfer velocity fields using TOPEX altimeter backscatter, in preparation.

Fuentes, M., S.C. Doney, D.M. Glover, and S.J. McCue, 2000: Spatial structure of the SeaWiFS ocean color data for the North Atlantic Ocean, Studies in the Atmospheric Sciences (Lecture Notes in Statistics Vol. 144), ed. M. Berliner, D. Nychka, and T. Hoar, Springer-Verlag, New York, 153-171.

Garçon, V.C., A. Oschlies, S.C. Doney, D. McGillicuddy, J. Waniek, 2001: The role of mesoscale variability on plankton dynamics. *Deep-Sea Res. II*, in press.

Glover, D.M., S.C. Doney, A.J. Mariano, R.H. Evans, and S.J. McCue, 2001a: Mesoscale variability in time-series data: Satellite based estimates for the U.S. JGOFS Bermuda Atlantic Time-Series Study (BATS) site. *J. Geophys. Res*., in press.

Glover, D.M., N.M. Frew, E.J. Bock, and S.J. McCue, 2001b: A Multi-year Time Series of Global Gas Transfer Velocity from the TOPEX Dual Frequency, Normalized Radar Backscatter Algorithm. In *Gas Transfer at Water Surfaces*, M. Donelan, W. Drennan, E. Monahan and R. Wanninkhof, Eds., Geophysical Monograph Series 127, American Geophysical Union, Washington, D.C., in press.

Gruber, N., C.D. Keeling, and T.F. Stocker, 1998: Carbon-13 constraints on the seasonal inorganic carbon budget at the BATS site in the northwestern Sargasso Sea. *Deep-Sea Res. I*, 673-717.

Hara, T., B. Uz, H. Wei, J. Edson, N. Frew, W. McGillis, S. McKenna, E. Bock, H. Haussecker and U. Schimpf, 2001: Surface wave observations during CoOP experiements and their relation to air-sea gas transfer. In *Gas Transfer at Water Surfaces*, M. Donelan, W. Drennan, E. Monahan and R.

Wanninkhof, Eds., Geophysical Monograph Series 127, American Geophysical Union, Washington, D.C., in press.

Jackson, F.C., W.T. Walton, D.E. Hines, B.A. Walter, and C.Y. Peng, 1992: Sea surface mean square slope from Ku-band backscatter date. *J. Geophys. Res*., **97(C7)**, 11,411-11,427.

Journel, A.G. and Ch.J. Huijbregts, 1978: *Mining Geostatistics*. Academic Press, Harcourt Brace Jovanovich Publishers, New York, NY, 600 pg.

Krauss, W., R. Doscher, A. Lehmann, and T. Viehoff, 1990: On eddy scales in the eastern and northern North Atlantic Ocean as a function of latitude. *J. Geophys. Res*., **95**, 18,049-18,056.

Mackas, D.L., K.L. Denman, and M.R. Abbott, 1985: Plankton patchiness: biology in the physical venacular. *Bull. Mar. Sci*., **37(2)**, 652-674.

McClain, C.R., M.L. Cleave, G.C. Feldman, W.W. Gregg, S.B. Hooker, and N. Kuring, 1998: Science quality SeaWiFS data for global biosphere research. *Sea Technology*, **39**, 10-14.

McGillicuddy, D.J. Jr., A.R. Robinson, D.A. Siegel, H.W. Jannasch, R. Johnson, T.D. Dickey, J. McNeil, A.F. Michaels, and A.H. Knap, 1998: Influence of mesoscale eddies on new production in the Sargasso Sea. *Nature*, **394**, 263-266.

McNeil, J.D., H.W. Jannasch, T. Dickey, D. McGillicuddy, M. Brzezinski, C.M. Sakamoto, 1999: New chemical, bio-optical and physical observations of upper ocean response to the passage of a mesoscale eddy off Bermuda. *J. Geophys. Res*., **104**(C7), 15537-15548.

Michaels, A.F. and A.H. Knap, 1996: Overview of the U. S. JGOFS Bermuda Atlantic Time-series Study and the Hydrostation S program. *Deep-Sea Res. II*, **43**, 157-198.

Press, W.H., S.A. Teukolsky, W.T. Vetterling, and B.P. Flannery, 1992: Numerical Recipes in Fortran. 2nd edition, Cambridge University Press, New York, USA, 963pp.

Smith, E., J. Vazquez, A. Tran, and R. Sumagaysay, 1996: Satellite-derived sea surface temperature data available from the NOAA/NASA Pathfinder Program, http:://www.agu.org/eos_elec/95274e.html

Stammer, D., 1998: On eddy characteristics, eddy transports, and mean flow properties. *J. Phys. Oceanogr*., **28**, 727-739.

Uz, M., J.A. Yoder, and V. Osychny, 2001: Pumping of nutrients to ocean surface waters by the action of propagating planetary waves. *Nature*, **409**, 597-600.

Wallace, D.W.R., 1995 Monitoring global ocean carbon inventories. OOSDP Background Report Number 5, 54 pp, Ocean Observing System Development Panel, Texas A&M University, College Station, TX.

Wanninkhof, R., 1992: Relationship between wind speed and gas exchange over the ocean. *J. Geophys. Res*., **97(C5)**, 7373-7382.

Yoder, J.A., C.R. McClain, G.C. Feldman, and W.E. Esaias, 1993: Annual cycles of phytoplankton chlorophyll concentrations in the global ocean: A satellite view. *Global Biogeochem. Cycles*, **7**, 181-193, 1993.

Yoder, J.A., J.E. O'Reilly, A.H. Barnard, T.S. Moore, and C.M. Ruhsam, 2001: Variability in Coastal Zone Color Scanner (CZCS) chlorophyll imagery in ocean margin waters off the U. S. East Coast. *Prog. Oceanogr*., submitted.

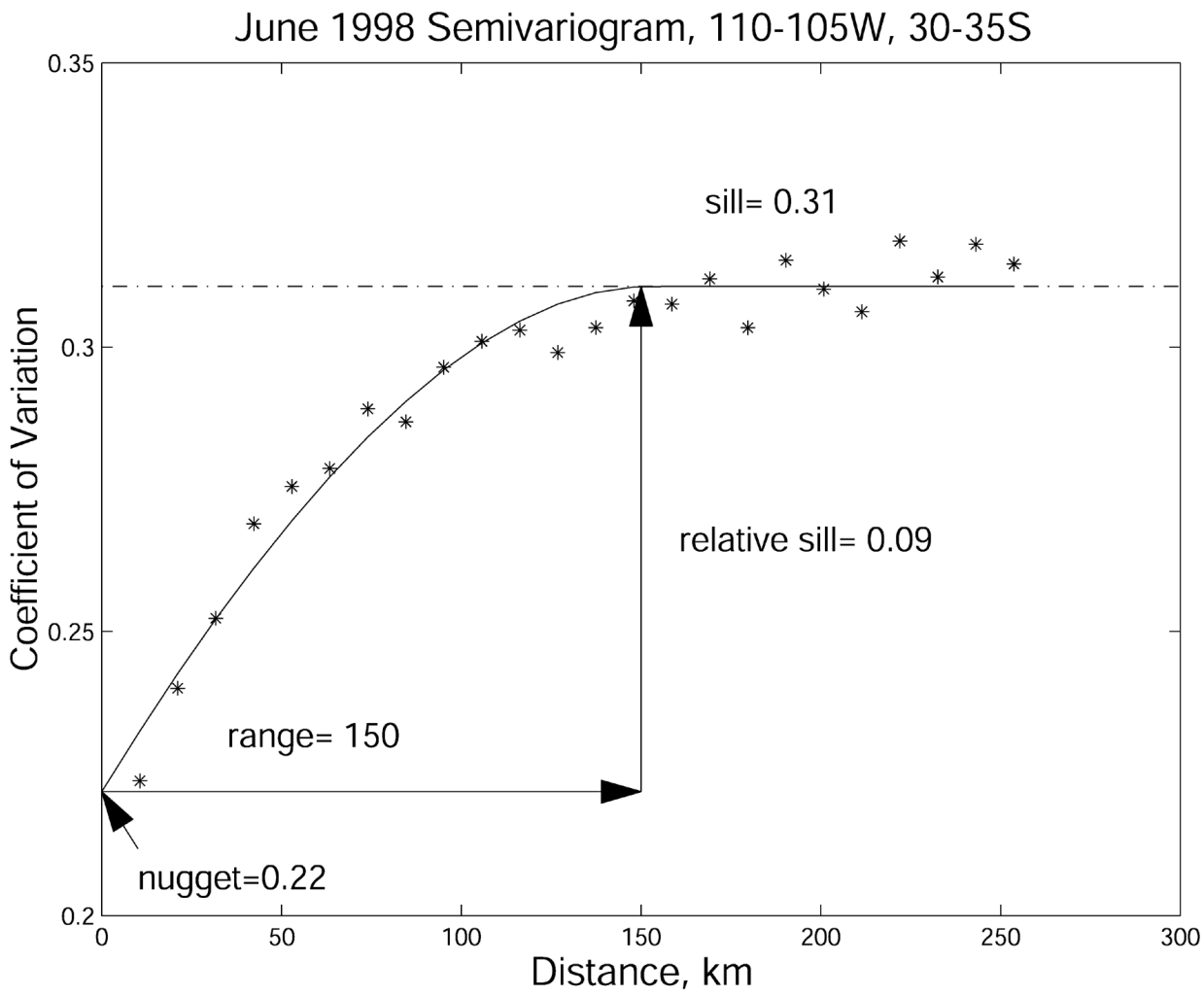

Figure 1. An example empirical semivariogram and spherical model fit for SeaWiFS ocean color data. The data are from the month of June, 1998 for a 5°×5° area bounded by 105-110°W by 30-35°S in the South Pacific. The spherical model parameters (nugget, range, and total and relative sill) are shown. The semivariance has a (typically) small value near the origin set by the nugget c_0, increases with distance out to a range r, and then plateaus at the value of the total sill $\sigma_{rel}^2 + c_0$.

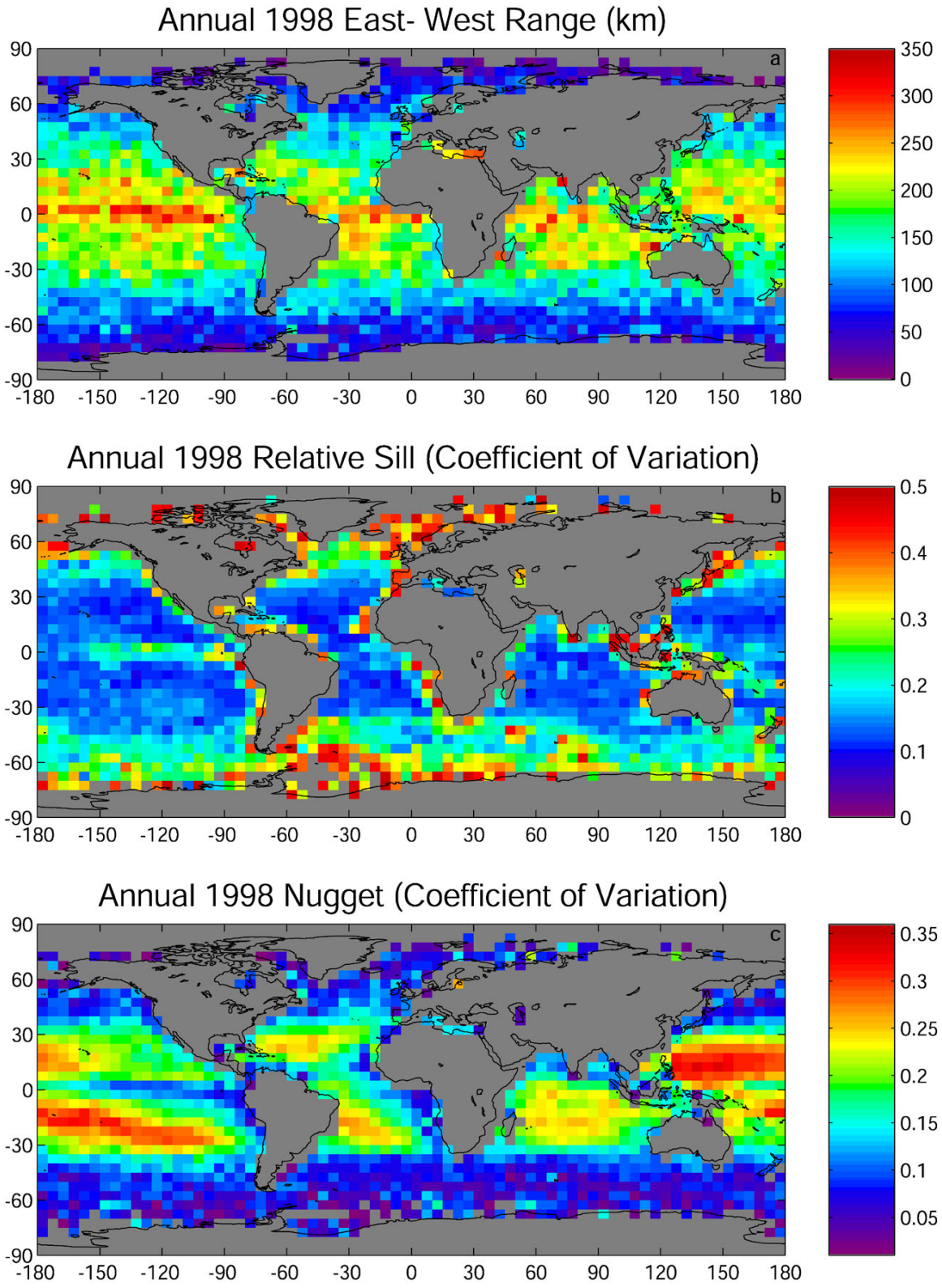

Figure 2. The annual average east-west summary of the three semivariogram parameters: a) range (km), b) relative sill (coefficient of variation), c) nugget (coefficient of variation).

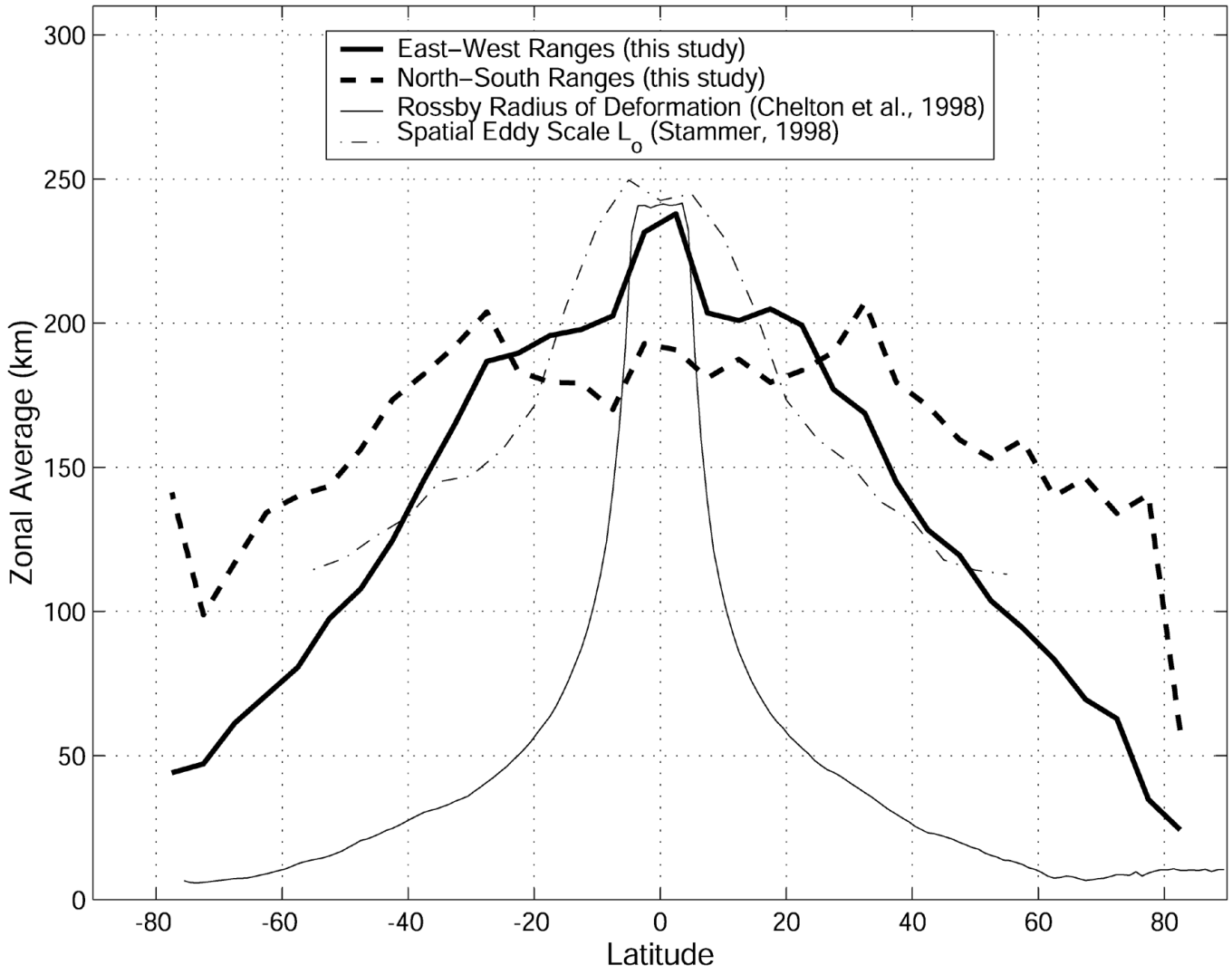

Figure 3. Zonal averages of the east-west ranges (heavy solid line), the north- south ranges (dashed line), the Rossby Radius of Deformation (thin solid line) computed from Chelton *et al.* [1998], and the spatial eddy scale (L_o) from the first zero-crossing of the alongtrack autocorrelation function of TOPEX/Poseidon SSH [Stammer, 1998] as a thin dot-dashed line.

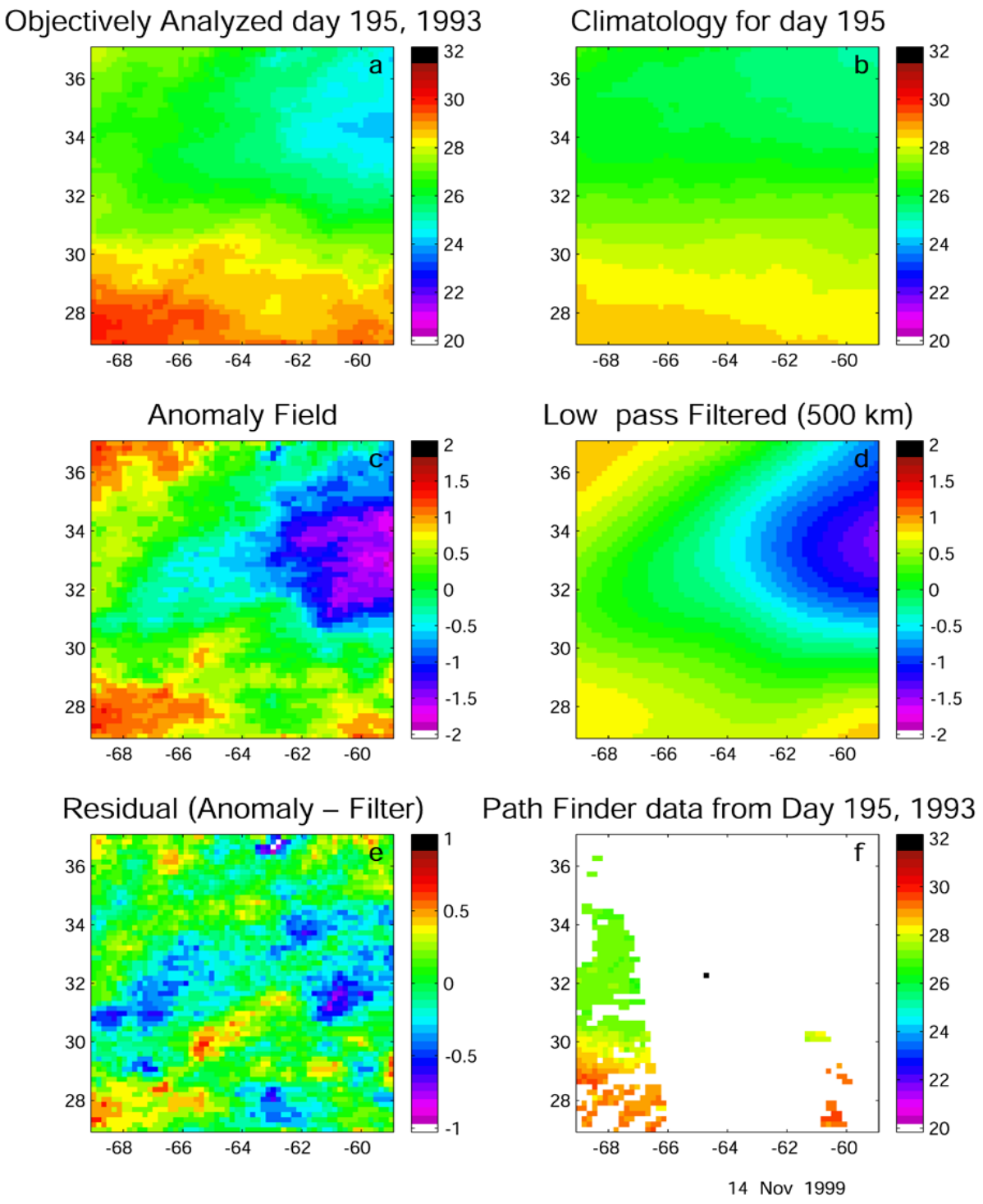

Figure 4. An example of the spatial nature of the problem with respect to SST. a) The objectively analyzed AVHRR PathFinder SSTs for day 195 of 1993; b) the corresponding climatology of SSTs for day 195 derived from the 14 year time series of images; c) the SST anomaly field from the climatology (a minus b); d) the anomaly field after passing through a low-pass filter with an effective wavelength of 500 km; e) the difference between the anomaly field and the filtered surface (c minus d), i.e. the residual; and f) the original AVHRR PathFinder SST from day 195 of 1993 (14 July 1993) showing clearly how clouds reduce coverage.

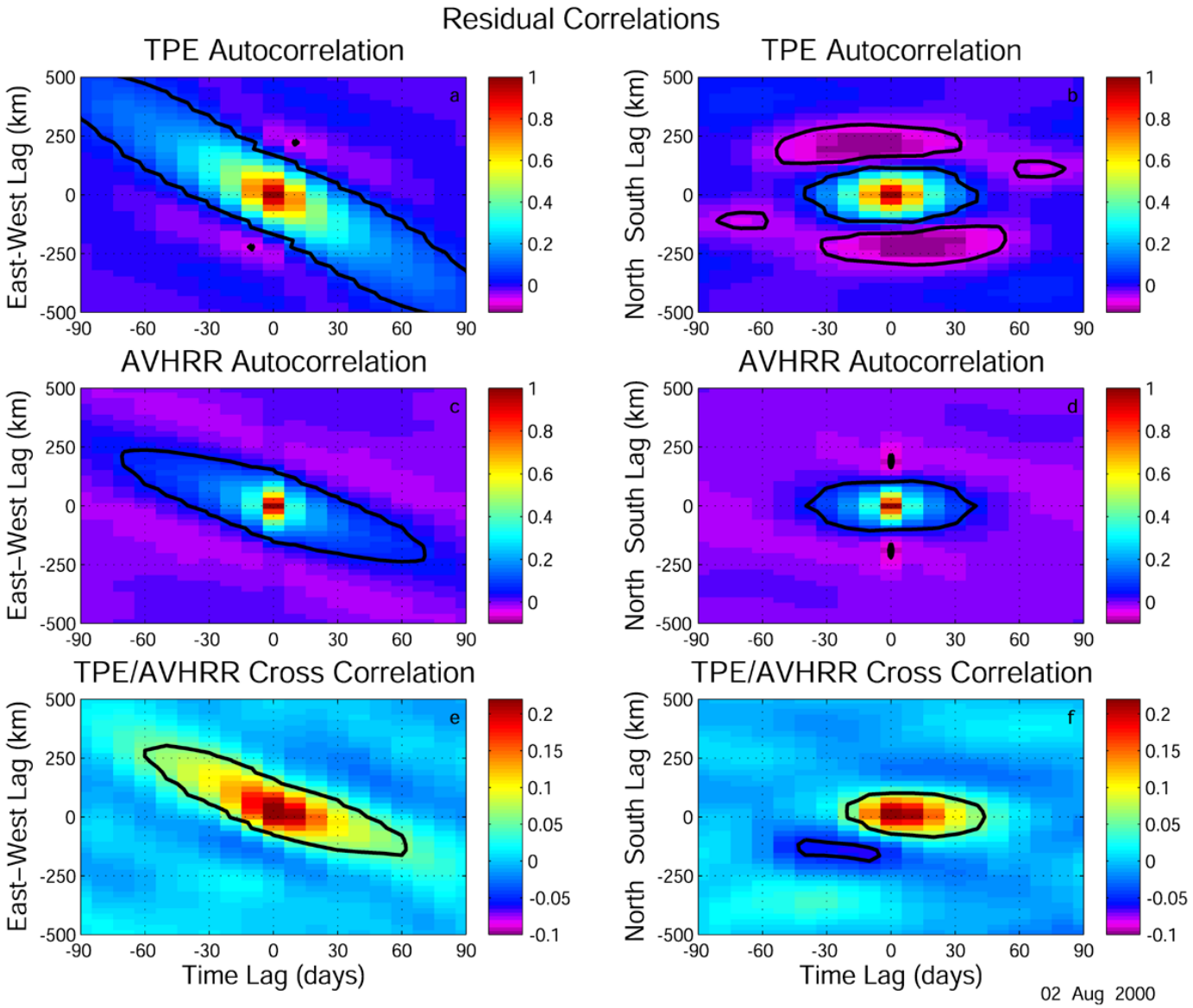

Figure 5. The two-dimensional cross correlations, with time lagging, of the various residual anomaly fields. a) The autocorrelation of the the TPE SSHA residual anomalies as a function of time lag and east-west lag; b) the same as (a) except as a function of time lag and north-south lag; c) The autocorrelation of the the AVHRR SST residual anomalies as a function of time lag and east-west lag; d) the same as (c) except as a function of time lag and north-south lag; e) The cross correlation of the the TPE SSHA and AVHRR SST residual anomalies as a function of time lag and east-west lag; and f) the same as (e) except as a function of time lag and north-south lag. To perform these cross and autocorrelations the AVHRR data was subsampled to match the TPE data space and time scales (0.25° and ten days). The heavy black line surrounds those regions with a correlation coefficient significant at the 95% confidence level.

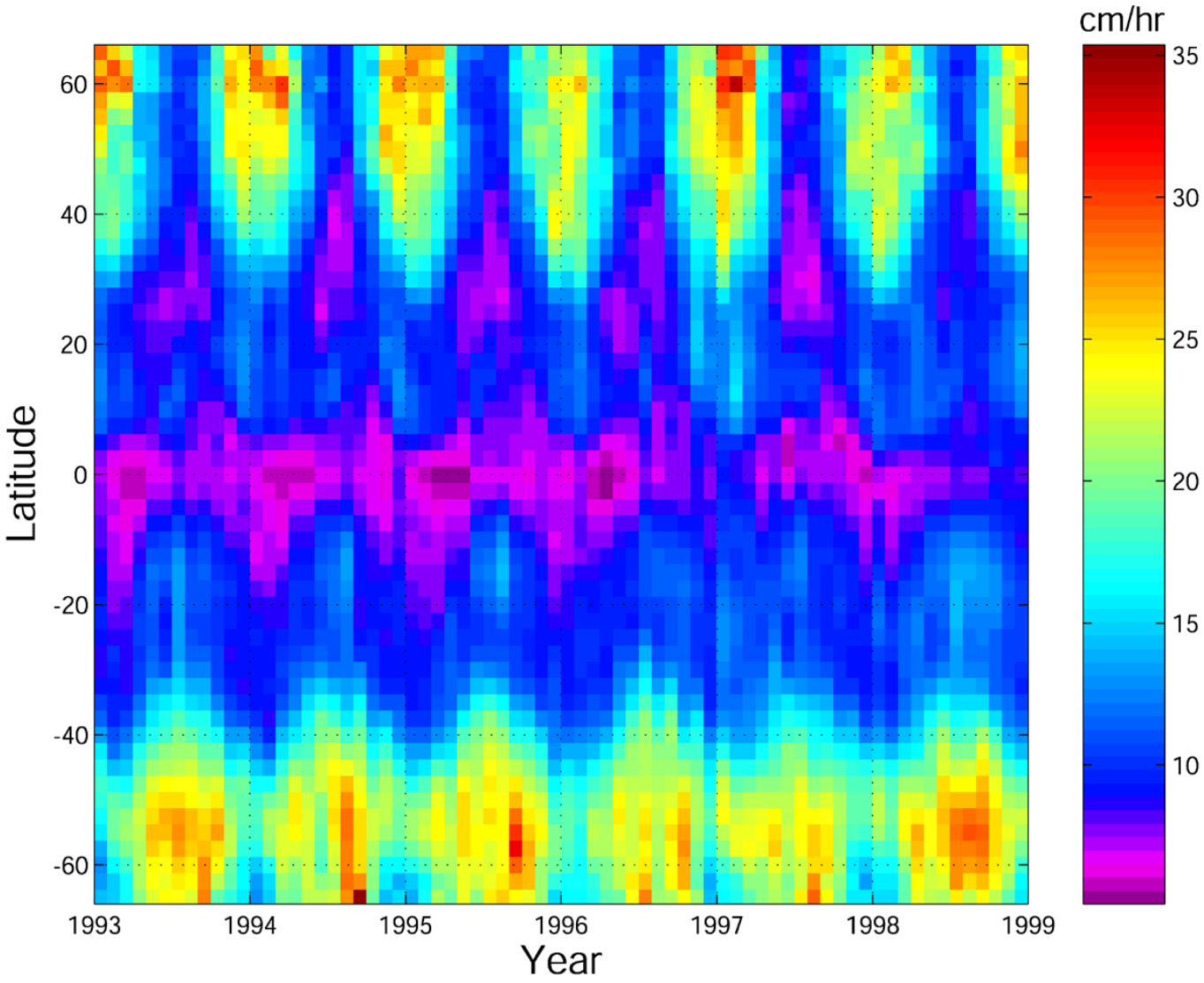

Figure 6. The monthly zonal average time-series (1993-1998) of the TOPEX-derived gas transfer velocity. The minimum value (the darkest purple) is approximately 5 cm/hr.

Bathymetry from Space

David T. Sandwell[1], Walter H. F. Smith[2], Sarah Gille[1], Steven Jayne[3],
Khalid Soofi[4] and Bernard Coakley[5]

[1]Scripps Institution of Oceanography, La Jolla, CA, 92093-0225
[2]Laboratory for Satellite Altimetry, NOAA, Silver Spring Maryland, 20910-3282
[3] Dept. of Physical Oceanography, Woods Hole Oceanographic Inst., Woods Hole, MA 02543
[4]Conoco Inc., 600 North Dairy Ashford, Houston, TX, 77252-2197
[5]Department of Geology, Tulane University, New Orleans, LA 70118

(A more complete version of this paper, with comprehensive appendices, can be copied from
http://topex.ucsd.edu/marine_grav/white_paper.pdf.)

Summary

"High-resolution" in this paper means something quite different than in other papers in this report. Most physical oceanographic applications require both high spatial (>100 km wavelength) and temporal sampling to recover time-dependent variations in ocean topography. Our focus is on the recovery of the permanent ocean topography (geoid) signals with small horizontal spatial scales (12 km to 160 km full wavelength). These are caused by gravity anomalies related to geologic structure on and below the ocean floor, and in the deep ocean these reveal bathymetry. While nearly all areas of ocean science require bathymetric information, we focus on those applications where a new altimeter mission would provide the greatest benefit. These include:

- resolving the fine-scale (~15 km wavelength) tectonic structure of the deep ocean floor (e.g., abyssal hills, microplates, propagating rifts, seamounts, meteorite impacts, . . .);
- measuring the roughness spectra (15-100 km wavelength) of the seafloor on a global basis to better constrain models of tidal dissipation, vertical mixing, and mesoscale circulation of the oceans;
- and resolving the fine-scale (~15 km wavelength) gravity field of the continental margins for basic research and petroleum exploration.

Mission requirements for Bathymetry from Space are much less stringent and less costly than physical oceanography-type missions and it is probably not cost effective or even possible to enhance a repeat-pass oceanographic-type mission to meet our objectives. Long-term sea-surface height accuracy is not needed; the fundamental measurement is the slope of the ocean surface to an accuracy of ~1 μrad. This can be achieved without application of the usual environmental corrections. The main requirements are:

- *Improved range precision* -- A factor of 2 or more improvement in altimeter range precision, with respect to Geosat and Topex, is needed to reduce the noise due to ocean waves. The footprint of the radar should be less than 6 km to recover wavelengths as short as 12 km.
- *Fine cross-track spacing and long mission duration* – A ground track spacing of 6 km or less is required (non-repeat orbit for at least 1.2 years). The Geosat Geodetic Mission (1.5 years) provides a single mapping of the oceans at ~5 km track spacing. Since the measurement noise scales as the square root of the number of independent measurements, a 6-year mission would reduce the error by another factor of 2.
- *Moderate inclination* -- Current non-repeat orbit altimeter data have high inclination (72˚ Geosat, 82˚ ERS) and thus poor accuracy of the E-W slope at the equator. The new mission should have an inclination of ~50˚ or 125˚ degrees to improve E-W slope recovery.

- *Near-shore tracking* -- For applications near coastlines, the ability of the instrument to track the ocean surface close to shore, and acquire the surface soon after leaving land, is desirable.

The Wide Swath Ocean Altimeter concept cannot recover our signal with the required precision because the resolution cell size is 15 km and the off-nadir beams are less accurate than a conventional radar altimeter. A delay-Doppler altimeter (Raney, 1998) in a non-repeat orbit of moderate inclination (50 or 125 degrees) for more than 3 years would meet our science objectives.

Introduction

Detailed bathymetry is essential for understanding physical oceanography, biology, and marine geology. Currents and tides are steered by the overall shapes of the ocean basins as well as by the smaller sharp ocean ridges and seamounts. The interaction of flow with the rugged seafloor mixes the ocean. It has been proposed that variations in tidal amplitude modulate the mixing which may effect climate on decadal to millennial timescales. Sea life is abundant where rapid changes in ocean depth deflect nutrient-rich water toward the surface. Because erosion and sedimentation rates are low in the deep oceans, detailed bathymetry also reveals the mantle convection patterns, the plate boundaries, the cooling/subsidence of the oceanic lithosphere, the oceanic plateaus, and the distribution of volcanoes.

Topographic mapping with orbiting laser and radar altimeters has been the focus of current exploration of Venus, the Moon, and Mars and is providing very high resolution topographic maps of the Earth's land areas. However, since one cannot directly map the topography of the ocean basins from space, most seafloor mapping is a tedious process that has been carried out over a 40-year period by research vessels equipped with single or multibeam echo sounders [*Smith*, 1993]. So far only 0.1% of the oceans have been surveyed at the 100-m resolution. It has been estimated that the 125--200 ship-years of survey time needed to map the deep oceans (100-m resolution) would cost a few billion US$, and mapping the shallow seas would take much more time and funding [*Brown et al.*, 1995; *M. Carron, U.S. Naval Oceanographic Office, pers. commun*. 2001].

While shipboard surveys offer the only means for high-resolution seafloor mapping, moderate resolution (12-17 km wavelength) can be achieved using satellite radar altimetry at a fraction of the time and cost. Radar altimeters aboard the ERS-1 and Geosat spacecraft have surveyed the marine gravity field over nearly all of the world's oceans to a high accuracy and moderate spatial resolution (25-45 km; Figure 1). These data have been combined and processed to form a global marine geoid and gravity grid [*Cazenave et al.*, 1996; *Sandwell and Smith,* 1997; *Tapley and Kim*, 2001]. In the wavelength band 10 to 160 km, variations in gravity anomaly are highly correlated with seafloor topography and thus, in principle, can be used to recover topography. There are ongoing efforts to combine ship and satellite data to form a uniform-resolution grid of seafloor topography [e.g., Figure 1] [*Baudry and Calmant,* 1991; *Jung and Vogt,* 1992; *Calmant*, 1994; *Smith and Sandwell,* 1994; *Sichoix and Bonneville,* 1996; *Ramillien and Cazenave*, 1997; *Smith and Sandwell,* 1997]. The sparse ship soundings constrain the long wavelength (> 160 km) variations in seafloor depth and are also used to calibrate the local variations in topography to gravity ratio associated with varying tectonics and sedimentation. Current satellite-derived gravity anomaly provides much of the information on the intermediate wavelength (25-160 km) topographic variations. The main limitation is the noise in the gravity anomaly measurements (i.e., sea surface slope) since this becomes amplified during the downward continuation process. The bathymetric models can only be improved through more accurate and dense measurements of the ocean surface slope.

Scientific Rationale for a Bathymetric Altimeter Mission

While these satellite-derived maps of marine gravity anomaly and seafloor topography have sufficient accuracy and resolution for certain applications, there are several important science questions that can only be addressed with better accuracy and resolution (Table 1). Here we focus on three science issues but note that seafloor topography is fundamental to all aspects of ocean science.

2. What is the fine-scale tectonic structure of the deep ocean?
3. How does seafloor depth and seafloor roughness affect ocean circulation and deep ocean mixing?
4. *What is the sedimentary and crustal structure of the continental margins?*

Table 1. Applications of High Spatial Resolution Satellite Altimetry

Topography Applications:
fiber optic cable route planning (http://oe.saic.com)
tsunami propagation and hazard models [*Yeh,* 1998]
hydrodynamic tide models and tidal friction [*Egbert and Ray,* 2001]
coastal tide model improvements [*Shum et al.,* 1997; 2000]
ocean circulation models [*Smith et al.,* 2000; R. *Tokmakian, pers. commun*.]
tidal role in ocean mixing [*Jayne and St.Laurent*, 2001]
understanding seafloor spreading ridges [*Small,* 1998]
identification of linear volcanic chains [*Wessel and Lyons*, 1997]
education and outreach (i.e. geography of the ocean basins)
law of the sea [*Monahan et al.*, 1999]
fisheries management [*Koslow,* 1997]
Gravity Applications:
inertial guidance of ships, submarines, aircraft, and missiles
planning shipboard surveys
mapping seafloor spreading ridges and microplates (http://ridge.oce.orst.edu)
continental margin structure (http://www.ldeo.columbia.edu/margins/Home.html)
petroleum exploration (below)
plate tectonics [*Cazenave and Royer,* 2001]
strength of the lithosphere [*Cazenave and Royer,* 2001]
search for meteorite impacts on the ocean floor [*Dressler and Sharpton,* 1999]

Cause and characterization of seafloor roughness

Satellite altimetry has revealed the large-scale manifestations of plate tectonics such as seafloor spreading ridges, transform faults, fracture zones, and linear volcanic chains [*Haxby et al*., 1983; *Gahagan et al.,* 1988] and ridges [*Smith and Sandwell*, 1994], allowing refinement of the history of plate tectonic motions [e.g., *Shaw and Cande,* 1990; *Mayes et al.*, 1990; *Müller and Smith*, 1993]. While altimetry has furnished a spectacular confirmation of the plate tectonic theory, the dense altimeter data available since 1995 have also shown that there are many complex details of plate tectonics that are poorly understood. Here we focus on those processes that produce smaller scale sea floor topography and structure in the oceanic crust.

Until dense altimeter data over ridges became available, many seafloor spreading studies were focused on the East Pacific Rise (EPR) and the Mid-Atlantic Ridge (MAR) and the differences in their bathymetric morphology. The EPR has an axial summit and relatively smooth flanks, while the MAR has a deep median valley and rougher flanks (Figure 2 – left) [*Menard,* 1967]. The lengths of axis segments and their offsets at transform faults also differ from one ridge to the other [*Abbott,* 1986]. The differences are manifest in gravity anomalies as well [*Cochran,* 1979; *Macdonald et al.,* 1986]. Analysis of repeat-track Geosat profiles over ridges revealed an abrupt transition in ridge-axis gravity with spreading rate which occurs at a full-rate of about 80 mm/yr (Figure 2-right) [*Small and Sandwell*, 1989; 1992].

A number of models have been proposed to explain this contrast in terms of spreading-rate-dependent material strength and the transience or permanence of a magma supply [*Sleep,* 1969; *Tapponier & Francheteau*, 1978*; Phipps Morgan et al.,* 1987; *Chen & Morgan,* 1990a, 1990b; *Phipps Morgan & Chen*, 1992, 1993]. Studies of shipboard bathymetric profiles [*Malinverno*, 1991; *Small,* 1998] were limited by the limited geographical distribution and heterogeneity in these data, and altimeter data provided a more uniform and systematic view (Figure 3).

As dense altimeter data became globally available they revealed details in the seafloor spreading process, including propagating rifts [*Phipps Morgan & Sandwell*, 1994], non-transform ridge offsets [*Lonsdale*, 1994], ridge-hotspot interactions [*Small,* 1995], disorganized back-arc spreading [*Livermore et al.*, 1994], small (20 km) ridge jumps [*Marks & Stock,* 1995], and small scale (circa 25 km) spreading-rate-dependent tectonic fabric [*Small & Sandwell,* 1994; *Marks & Stock,* 1994; *Phipps Morgan & Parmentier*, 1995; *Sahabi et al.,* 1996]. *Phipps Morgan & Parmentier* [1995] interpret a new fabric they call "crenulated seafloor" as evidence for stationary and/or migratory localized centers of upwelling magma beneath ridges. Many of these kinds of features are symmetric across ridge flanks.

Seafloor structure at quite small spatial scales (0.2-10 km wavelength) has also been imaged in acoustic swath bathymetry but only in a few small patches totaling less than 0.1% of the deep ocean floor area. To assess the capabilities of current and future bathymetric prediction from a new satellite altimeter mission, we have assembled three 200 km by 200 km areas where multibeam bathymetry data are available. The current and future capabilities will be discussed below. Here we illustrate the major differences in seafloor characteristics in these areas (Figure 4 - upper). The Mid-Atlantic Ridge (MAR) is characterized by an axial valley with relatively rugged surrounding seafloor abyssal hills (493 m rms). The hills are very anisotropic with the long-axis perpendicular to the seafloor spreading direction and visually have a characteristic wavelength of about 10 km. The Pacific Rise (EPR) has similar but lower amplitude abyssal hill; the total roughness is only 209 m reflecting its higher spreading rate. The Gulf of Mexico has quite different seafloor morphology with a more isotropic pattern that formed in response to buoyancy instabilities of salt domes. Spectra for the MAR and EPR are provided in Figure 4 (lower). The amplitudes of the spectra are different but their corner frequency and roll-off slope are similar. Other areas such as the Southwest Indian Ridge studied by *Goff and Jordan* [1988] has more total power (845 m) and a somewhat longer corner wavenumber of about 50 km. *Smith* [1998] found that amplitudes and wavelengths of abyssal hills along the MAR are just large enough to be barely resolved in existing altimeter data over water as deep as 4 km.

Tidal dissipation and deep ocean mixing

Tides are the major process responsible for mixing the deep ocean. Astronomical calculations suggest that tidal mixing should dissipate 3.7 terawatts (TW) of energy throughout the global ocean. *Munk and Wunsch* [1998] estimated that about 1.9 TW of this tidal energy is required to maintain the observed deep ocean stratification. While tidal processes are known to be important in coastal regions and marginal seas [*Shum et al.,* 1997; 2001], tidal dissipation due to shallow ocean boundary layer effects does not account for all tidal dissipation. *Egbert and Ray* [2000] estimated that 25% to 30% of total tidal dissipation takes place in the open ocean, and is generally associated with ridges and other rough topography.

Recent observational efforts have attempted to measure the effect of open ocean tidal dissipation and its corresponding impact on vertical diffusivities in the ocean. In microstructure measurements in the Brazil Basin (Figure 5), *Polzin et al.* [1997] found elevated levels of vertical diffusivity over rough bathymetry. Diffusivity levels appear to be modulated by the fortnightly and monthly tidal cycle [*Ledwell et al*., 2000]. These results are consistent with the idea that tidal motions over rough bathymetry generate vertically propagating internal waves that dissipate tidal energy and vertically mix the ocean.

To test the impact of bathymetric roughness on tides, *Jayne and St. Laurent* [2001] implemented a roughness dependent internal-wave drag term in a barotropic tide model. The inclusion of internal-wave

drag results in substantially more dissipation, particularly in the middle of ocean basins. Jayne and St. Laurent found that the rms difference between observed and modeled tides was 40% smaller when they included a roughness dependent dissipation term. In addition, in agreement with *Egbert and Ray's* [2000] observations, deep-ocean tidal dissipation due to the roughness term was about 30% of total dissipation.

In this model, viscous drag in the deep ocean is primarily due to generation (and subsequent dissipation breaking) of internal waves. A more complete description of this process will require bathymetric roughness spectra over wavelengths of 10 to 30 km [*St Laurent and Garrett,* 2001]. Note that these are the wavelengths that are not currently resolved in existing bathymetry, and this band includes the ubiquitous abyssal hill topography and the corner wavenumbers described above. While these mixing models are still under development and there is some debate about the physics of the internal-wave generation process, numerical simulations are hampered by the lack of high-resolution seafloor bathymetry.

The role of topography in tidal mixing and internal wave generation remains an active area of research in physical oceanography. Underway now is the Hawaii Ocean Mixing Experiment (HOME) [http://chowder.ucsd.edu/home/home.html], a large field program with two dozen investigators. HOME specifically focuses on observing and modeling mixing along the Hawaiian Ridge. HOME is directed towards understanding specific processes, including the impact on tidal conversion of critical bottom slopes over length scales of 1 km or less [*R. Pinkel, personal communication*]. Although such length scales are beyond the reach of altimetry, the lessons learned in HOME appear likely to translate into ways to characterize ocean mixing on the basis of larger scale bathymetry.

A new higher-resolution altimetric bathymetry (10-30 km wavelength) would offer the potential to better refine ocean mixing estimates, extending the results from the Brazil Basin, HOME and other field programs to give them global applicability and making the existing global roughness estimates more reliable. Of particular interest is the western Equatorial Pacific, near the Solomon Islands, a region that is not well mapped but where seamounts and ridges associated with the island chains may substantially influence mixing processes.

Ocean circulation and mesoscale eddies

Ocean circulation is influenced by seafloor topography in a variety of ways, particularly at high latitudes, where stratification is low. Bathymetry can steer the path of currents, determine where upwelling occurs (and supply iron-rich sediment to upwelled water allowing phytoplankton to bloom at the ocean surface), generate topographic lee waves downstream of topography, and dissipate eddy kinetic energy.

Theoretical constraints on vorticity suggest that large-scale barotropic flows in the ocean should be directed along lines of constant f/H, where f is the Coriolis parameter and H is the ocean depth. At high-latitudes where changes in f are small, barotropic oceanic flows should nearly follow bathymetric contours. Although real flows include baroclinic components and are expected to deviate from f/H lines, bathymetry is nonetheless a good predictor for large-scale circulation patterns. *LaCasce* [2000] showed that in both the Atlantic and Pacific Oceans, floats were more likely to travel along f/H contours than across them. *Holloway* [1992] has even suggested that topography should be used as an a priori guess to determine large-scale dissipation in ocean circulation models.

Specific current flow patterns are clearly determined by bathymetry [*Schulman*, 1975]. For example, the path of the wind-driven Antarctic Circumpolar Current (ACC) has long been known to be steered by deep seafloor topography [e.g., *Gordon and Baker,* 1986] (Figure 1). Altimetric investigations suggest that the jets that comprise the ACC are tightly steered around bathymetric obstructions in the Southern Ocean. Figure 1 shows that the paths of the Subantarctic Front and Polar Front (as estimated from altimetry) pass through the Eltanin and Udintsev Fracture Zones, respectively, in the Pacific-Antarctic Ridge [*Gille,* 1994]. Similar effects occur downstream of Drake Passage and south of New Zealand,

where the ACC is steered through troughs between a series of islands. Detailed study of the role that bathymetry plays in controlling ocean circulation has been limited by the lack of accurate bathymetry, particularly in the Southern Ocean where areas as large as $2x10^5$ km^2 are unsurveyed [*Sandwell and Smith,* 2001] and where current altimetric bathymetry cannot resolve all of the details of the bathymetry.

Ridges can generate topographic lee waves [e.g. *McCartney,* 1976]. Altimeter observations have consistently shown elevated levels of eddy kinetic energy downstream of ridges and seamounts, in the Gulf Stream [*Kelly,* 1991] and particularly in the ACC [*Sandwell and Zhang,* 1989, *Chelton et al.,* 1990; *Morrow et al.,* 1992; *Gille and Kelly*, 1996]. In an analysis based on sea surface height variability estimates from altimeter data, *Stammer* [1998] found evidence for high meridional eddy heat fluxes in locations of high eddy kinetic energy, suggesting that high variability regions associated with topography are potentially important in the global heat budget.

Topography also plays a role in vertical motions in the ocean. Horizontal flow that encounters topography can be deflected vertically rather than around topography. At George's Bank, tidal forcing over topography upwells water to the surface. In the equatorial Pacific, topography plays a slightly different role: upwelling is driven by a wind divergence at the equator rather than topography. Near the Galapagos, upwelled water entrains iron rich volcanic sediments resulting in a phytoplankton bloom downwind of the Galapagos [*Feldman et al.,* 1984]. Careful study of high resolution bathymetry in comparison with ocean color data may yield other nutrient blooms associated as much with sediment and bathymetry as with current motions or wind.

Finally, just as tidal dissipation may be linked with bottom roughness, mesoscale motions in the ocean may also be controlled by roughness. A preliminary study by *Gille et al.* [2000] compared bottom roughness (Figure 3) with upper ocean mesoscale variability (Figure 6). Results showed that eddy kinetic energy (EKE) is greatest in the deeper ocean areas and over smooth seafloor. This anti-correlation between roughness and variability is strongest at higher latitudes suggesting a communication of the surface currents with the deep ocean floor in locations with low stratification. Rough bathymetry may transfer energy from the 100-300 km eddy length scales resolved by altimetry to smaller scales or to vertically propagating motions resulting in an apparent loss of EKE. Since numerical ocean models do not yet account for spatial variations in bottom friction and moreover, since they incorporate ad-hoc dissipation mechanisms, improvements in seafloor depth and roughness may ultimately lead to a better understanding of deep ocean mixing. The link between seafloor roughness and spreading rate provides an interesting possibility that vertical mixing of paleo-oceans depended on the average spreading rate of the ocean floor and thus the waxing and waning of the mantle convection patterns.

Structure of continental margins and exploration of offshore sedimentary basins

Continental Margins

All continental margins either were or are active plate boundaries. The transition from oceanic to continental crust is structurally complex and often obscured by thick layers of sediment shed from the continent. The various sedimentary layers and basement are of contrasting composition and density. Changes in the thickness and elevation of these layers can be tracked with gravity anomaly data. The continuous high-resolution data set of altimetric gravity anomalies that would be collected during a high resolution altimeter mission would dramatically improve our understanding of the variety of continental margins. These data would help complete understanding of the processes (plate tectonic and sedimentary) that create and modify these features over geologic time, facilitating more accurate predictions of the location and extent of economically significant oil and gas fields.

Understanding of continental margins has come slowly, through independent surveys pursued by many scientific organizations, governments and corporations over the past fifty years. Each of these surveys has focused on a particular segment of a continental margin with a particular purpose in mind; scientific, legal or commercial. While these data sets have built our understanding, the accumulation of

data has not resulted in a complete or systematic characterization of continental margins worldwide. An altimetric gravity anomaly dataset, continuous along and across the submerged margins of the continents, would provide a means for systematic exploration and inter-comparison of the complex transition from continental to oceanic crust. A high-resolution altimeter mission would provide this dataset.

This comprehensive data set, a uniform survey of the continental margins, has not been obtained during previous altimetric missions, could not be collected from a ship and will not be collected by any of the geopotential satellite missions planned by either NASA or the ESA. Previous and future altimetric missions have and will collect relatively low*er* resolution data. *The increase in resolution with the new mission will greatly increase our ability to* image crustal scale structures of scientific and commercial interest. Shipboard surveys, which can collect high-resolution data, are expensive and particularly difficult to execute in the shallow waters that would be sampled during a high-resolution altimeter survey.

The altimetric gravity anomaly data set will be unique and immensely valuable for science and exploration;

- A complete data set which will facilitate comparisons between continental margins.
- An exploration tool which will direct oil and gas exploration and permit extrapolation of known structures from well-surveyed areas.
- A uniform, high-resolution data set continuous from the deep ocean to the shallow shelf which will make it possible to follow fracture zones out of the ocean basin into antecedent continental structures, to define and compare segmentation of margins along strike and identify the position of the continent-ocean boundary. *Conversely the continuity of geological features on land can be traced on to the Continental Margin*.
- An image of the gravity field useful for the study of mass anomalies (eg sediment type and distribution) and isostatic compensation at continental margins.

Hydrocarbon exploration

More than 60% of the Earth's land and shallow marine areas are covered by >2 km of sediments and sedimentary rocks, with the thickest accumulations on rifted continental margins. Sedimentary basins are the low-temperature chemical reactors that produce most of the hydrocarbon and mineral resources upon which modern civilization depends. The science and technology for the discovery and production of these resources will remain vital to the world's economy for at least the next several decades.

Free-air marine gravity anomalies derived from satellite altimetry are able to outline most of these major basins with remarkable precision. Gravity and bathymetry data derived from altimetry are also used to identify current and paleo submarine canyons, faults and local recent uplifts, active in modern time. These geomorphic features provide clues to where to look for large deposits of sediments. Figure 7 shows the paleo submarine canyons associated with the Indus (left, offshore Pakistan) and Ganges Rivers (right, offshore Bangladesh).

While current altimeter data delineate the large offshore basins and major structures, they do not resolve some of the smaller geomorphic features and they cannot be used to detect some of the smaller basins (Table 2 and Figure 7). Wavelengths shorter than 40 km in the presently available data cannot be interpreted with confidence close to shore, as the raw altimeter data are often missing or unreliable near the coast. The exploration industry would like to have altimeter data with as much resolution as possible and extending as near-shore as possible. The 2-D seismic survey standard in the industry uses a track line spacing of 5 km, yielding structure maps with a 10 km Nyquist wavelength. Altimetry with a similar resolution is desirable.

Table 2. Wavelength and amplitude resolution required for typical geologic targets [*Yale et al.*, 1998].

Target	Wavelength	Amplitude	
Buried cavities, tunnels, tanks	1 – 10 m	5-100 μGal	**not resolvable from space**
Pediment and seismic weathering layer thickness, shallow gas pockets, karst	10 – 200 m	0.05 mGal – 0.2 mGal	
Shallow salt domes and cap rock	200 – 1000 m	0.1 – 0.3 mGal	
Anticlines, faults deep salt, and overhang	500 – 4000 m	0.2 – 2.0 mGal	
Sedimentary basin structure. [Resolution commensurate with grid spacing (5-10 km) of seismic surveys for frontier basins.]	2 – 20 km	5 mGal	**new mission**
Sedimentary basin outlines and boundaries, plate tectonic structures	20 – 100 km	10 mGal	**current resolution of Geosat and ERS is 24-45 km**

Limitations of past, current, and planned gravity missions

There are three approaches to measuring marine gravity anomaly. Shipboard surveys provide the most direct approach. However, like bathymetric surveys, the marine coverage is sparse and inadequate for assessing the global roughness of the ocean floor or exploring the offshore sedimentary basins. The second approach is to measure variations in gravitational acceleration at satellite altitude. Three new satellite gravity missions CHAMP [*Reigber et al.,* 1996], GRACE [*Tapley et al*., 1996], and GOCE will provide extremely accurate measurements of the global gravity field and its time variations [*Tapley and Kim*, 2001]. However, because these spacecraft measure gravity at altitudes higher than 250 km, they are unable to recover wavelengths shorter than about 160 km. Although these new missions offer little short-wavelength information, they provide the ideal reference field for shorter wavelength surveys.

The third approach to measuring marine gravity is satellite altimetry, in which a pulse-limited radar measures the altitude of the satellite above the closest sea surface point. The radar pulse reflects from an area of ocean surface (footprint) that grows with increasing sea state [see *Stewart,* 1985]. There are several sources of error in these measurements but most occur over length scales greater than a few hundred kilometers [*Sandwell,* 1991; *Tapley et al.,* 1994]. For gravity field recovery and bathymetric estimation, the major error source is the roughness of the ocean surface due to ocean waves (Figures 8). Thus the only way to improve the resolution is to make many more measurements.

Other sources of error include tide-model error, ocean variability, dynamic topography, ionospheric delay error, tropospheric delay error, and electomagnetic bias error (Table 3). Corrections for many of these errors are supplied with the geophysical data record. However, for gravity field recovery and especially bathymetric prediction not all corrections are relevant or even useful. For example, corrections based on global models (i.e., wet troposphere, dry troposphere, ionosphere, and inverted barometer) typically do not have wavelength components shorter than 1000 km, and their amplitude variations are less than 1 m so they do not contribute more than 1 μrad of error. *Yale* [1997] has examined the slope of the corrections supplied with the Topex/Poseidon GDR and found only the ocean tide correction [*Bettadpur and Eanes*, 1994] should be applied. The dual frequency altimeter aboard Topex/Poseidon satellite provides an estimate of the ionospheric correction, however, because it is based on the travel time difference between radar pulses at C-band and Ku-band, the noise in the difference measurement adds noise to the slope estimate for wavelengths less than about 100 km [*Imel*, 1994]. The most troublesome errors are associated with mesoscale variability and dynamic topography [*Rapp and Yi,* 1997]. The

variability signal can be as large as 6 μrad [Figure 6] but fortunately it is confined to a few energetic areas of the oceans and given enough redundant slope estimates from nearby tracks [*Sandwell and Zhang*, 1989], some of this noise can be reduced by averaging. Dynamic topography typically has slopes of less than 0.1 μrad. However, along a few areas of steady intense western boundary current, the slopes can be up to 6 μrad; this will corrupt both the gravity field recovery and the bathymetric prediction over length scales of 100-200 km.

Table 3. Signal and Maximum Error in Sea Surface Slope

Signal or Error source	**Length (km)**	**Height (cm)**	**Slope (μrad)**	**Mission-avg. slope (μrad)**
Gravity Signal	12–400	1–300	1–300	1–300
Measurement error sources:				
Orbit errors[1]	8000–20,000	400–1000	< 0.5	< 0.2
Ionosphere[2,3]	> 900	20	< 0.22	< 0.1
Wet Troposphere[4]	> 100	3-6	< 0.6	< 0.3
Sea-state bias[5]	> 20	< 0.6	< 0.3	< 0.1
Inverse barometer[6]	> 250	< 5	< 0.2	< 0.1
Oceanographic error sources:				
Basin-scale circulation (steady)[7]	> 1000	100	< 1	< 1
El Niño[8], inter-annual variability, planetary waves	> 1000	20	< 0.2	< 0.1
Deep ocean tide model errors[4,10]	> 1000	3	< 0.03	< 0.01
Coastal tide model errors[3,10]	50–100	< 13	< 2.6	< 1.1
Eddys & Mesoscale Variability[9]	60–200	30–50	2.5–5	1–2
Meandering jet (Gulf Stream)[7,11]	100–300	30–100	3–10	2–4
Steady Jet (Florida Current)[7,11]	100	50–100	5–10	5–10

[1]Dynamic orbit determination using the ISS SIGI system, considering errors in force, measurement, attitude, center of mass, and effect of EXPRESS nadir pallet moment arm. [2]Imel [1994] [3]Yale [1997] [4]Chelton et al. [2001] [5]Monaldo [1998] [6]Ponte [1994] [7]Fu & Chelton [2001] [8]Picaut & Busalacchi [2001] [9]LeTraon & Morrow [2001] [10]Shum et al. [2001] [11]Smith & Sandwell [1995].

An important remaining issue is the anisotropy in the accuracy of the current marine gravity fields derived from Geosat and ERS [*Sandwell and Smith,* 1997]. Note that the current Topex/Poseidon mission, in its 10-day repeat configuration, provides almost no additional gravity field information because of the wide ground track spacing (315 km). As shown in Figure 9 (left panel), the E-W component of gravity field error at the equator is currently 3.5 times worse than the N-S error. There are two reasons for this. First, it has been shown that estimating sea surface slope by differencing heights on adjacent tracks results in slope estimates that are much less accurate than the along-track slope estimate [*Olgiati et al.,* 1995]. This is because the adjacent tracks, which are acquired at different times, have different environmental path delays and different orbit errors that cannot be entirely corrected with a crossover adjustment. In contrast, height measurements along the satellite tracks have common errors that are largely eliminated by computing the along-track slope. The second reason is simply that, at the equator, the Geosat and ERS tracks run mainly in the N-S direction. The situation is quite different at the turnover latitude of Geosat (72˚latitude), where the tracks are oriented in an E-W direction. The current Geosat/ERS configuration provides adequate control on the E-W slope for latitudes greater than about 60˚ latitude [Figure 9 – left panel].

What is the optimal inclination for gravity field recovery given availability of the passed (Geosat/GM, ERS/GM) and planned (Cryosat) non-repeat radar altimeters? The upper-right panel in Figure 9 shows the area of ocean covered as a function of orbital inclination. Of course about 1/2 of the ocean area lies south of 30^{o}. The lower-right panel shows the area-averaged degree of anisotropy as a

function of orbital inclination for both prograde (solid) and retrograde (dashed). The optimal prograde inclination (Op) is 50˚ while the optimal retrograde (Or) is slightly higher 55˚ (125˚ inclination). Geosat and Topex inclinations provide about the same area-averaged inclination although a more detailed evaluation shows Topex tracks are more orthogonal in the low latitudes (< 20˚) where the current gravity fields suffer from poor E-W control. The International Space Station (ISS), which has a non-repeat orbit, is nearly optimal for this application. The east components shows greater improvement than the north component and the final error level after 6 years is 1 to 1.5 μrad. The desired noise level of about 1 μrad or 1 mGal can be achieved with a new mission, if the mission duration exceeds about 6 years.

The final issue in gravity field recovery from the Geosat and ERS altimeters is related to the coastal data (Figure 10A). The issues for Geosat and ERS are different but both are illustrated in Figure 10B showing the available ground tracks in the Caspian Sea. The ERS-1 geodetic mission data are absent in this inland sea because the altimeter was switched to the ice mode where the ranging resolution is optimized for land or ice topography but inadequate for gravity field recovery. Many of the Geosat tracks over this sea are short or absent because the Geosat altimeter sometimes had trouble re-acquiring the sea surface when transitioning from land to water. Figure 10C shows the track density that would be acquired in 1.5 years in the ISS inclination with perfect ocean tracking. The differences are significant and in this particular area, just 1.5 years of non-repeat coverage would provide a factor of 2 improvement in accuracy.

Mission requirements

How should a new ocean mapping mission be designed? What could it resolve?

We argue that understanding tidal dissipation and ocean mixing may ultimately require sea floor roughness on very short spatial scales, even those too short to be measured by altimetry. However, we have also shown (Figure 4), the roughness at these scales is well-modeled by a self-affine (fractal) surface, so that seafloor topography may be characterized statistically at wavelengths which are shorter than the corner wavenumber [*Goff and Jordan,* 1988]. Thus if one could map the oceans with enough resolution to establish the total power and the corner wavenumber, the statistical properties of the shorter part of the spectrum would follow from the self-affinity.

The corner wavenumber for the two patches we have examined (MAR and EPR) are both 20 km. However, it should be noted that other major complications on the seafloor such as fracture zones and seamounts can change both the total power and corner wavenumber. Moreover, the spectrum of the seafloor is usually anisotropic with fracture zones oriented parallel to the spreading direction and abyssal hills perpendicular to the spreading direction. The important point is that if one could map the full topography of the ocean floor to better than a 20 km wavelength, one could extrapolate the full anisotropic roughness spectrum; the anisotropy is important because deep tidal currents interact with the bottom only along their direction of flow. Current bathymetric prediction can capture wavelengths of only 40 km on smooth seafloor and about 25 km on rough seafloor. A new mission with sufficient accuracy to recover 15-km wavelengths would capture essentially all the interesting geophysics of the seafloor spreading process, and in addition, the statistical properties of the finer-scale roughness.

To achieve significant contributions in several areas of geophysics, physical oceanography, and climate research, an altimeter mission having the following characteristics is needed:

- ***Altimeter Precision*** - The most important requirement of this new mission is improvements in ranging technology to achieve a factor of 2 improvement in range precision (with respect to Geosat and Topex) in a typical sea state of 3 m. In shallow water, where upward continuation is minor, and in calm seas where waves are not significant (e.g. Caspian Sea), it will also be important to have an along-track footprint that is less than 1/4 of the resolvable wavelength of about 12 km. This footprint is smaller than the standard pulse-limited footprint of Geosat or Topex.

- ***Mission Duration*** - The Geosat Geodetic Mission (1.5 years) provides a single mapping of the oceans at ~5 km track spacing. Since the measurement noise scales as the square root of the number of measurements, a 6-year mission will reduce the error by a factor of 2. This combined with the factor of 2 improvement due to instrumentation results in an overall factor of 4 improvement.
- ***Moderate inclination*** - Current non-repeat orbit altimeters have high inclination (72˚ Geosat, 82˚ ERS) and thus poor accuracy of the E-W slope at the equator. The new mission should have an inclination of ~50˚ or 125˚ degrees to improve E-W slope recovery (Figure 9)
- ***Near-shore tracking*** For applications near coastlines, the ability of the instrument to track the ocean surface close to shore, and acquire the surface soon after leaving land, is desirable (Figure 10).

Finally, it should be stressed that the basic measurement is not the height of the ocean surface but the slope of the ocean surface. The height differences over horizontal distances from a few km to a few hundred km must be measured with sufficient accuracy and precision that the horizontal slope of the sea surface along the satellite track can be calculated with a precision of about 1 microradian (6 mm height change over 6 km horizontal distance). The band of wavelengths we need to resolve is from 12 to a few hundred km (full wavelength). This requires careful processing of the radar pulse data at high sampling rates.

The need to resolve height differences, and not heights, means that the mission can be much cheaper than other altimeter missions and can take advantage of spacecraft platforms which are less stable than other missions require. This is because the absolute height, and any component of height which changes only over wavelengths much longer than a few hundred km, is irrelevant, as it contributes negligible slope (Table 3). Therefore one can tolerate large spacecraft motions, and errors modeling them, so long as they vary slowly with distance. Also, one need not measure the radar propagation delays in the ionosphere and troposphere, as the slopes of these corrections are also negligible.

References

Abbott, D., 1986: A statistical correlation between ridge crest offsets and spreading rate. *Geophys. Res. Lett.* **13**, 157-60.

Baudry, N., and S. Calmant, 1991: 3-D Modeling of seamount topography from satellite altimetry. *Geophys. Res. Lett*., **18**, 1143-1146.

Bell, T.H., 1975: Lee waves in stratified flows with simple harmonic time dependence. *J. Fluid Mech*., **67**, 705-722.

Bettadpur, S.V., R.J. Eanes, 1994: Geographical representation of radial orbit perturbations due to ocean tides: Implications for satellite altimetry. *J. Geophys. Res*., **99**, 24,883-24,898.

Brown, R.D., M.R. Abbott, R.N. Baker, W.W. Denner, W.H. Munk, et al., 1995: *Scientific utility of Naval environmental data*. McLean, Virginia: Mitre. 52 pp.

Calmant, S., 1994: Seamount topography of least-squares inversion of altimetric geoid heights and shipborne profiles of bathymetry and/or gravity anomalies. *Geophys. J. Int*., **119**, 428-452.

Cazenave, A., J.-Y., Royer, 2001: Applications to Marine Geophysics. In *Satellite Altimetry and Earth Sciences*. Edited by L.-L. Fu and A. Cazenave, Intl. Geophys. Series., vol. **69**, Academic Press, New York, 407-435.

Cazenave, A., P. Schaeffer, M. Berge, and C. Brossier, 1996: High-resolution mean sea surface computed with altimeter data of ERS-1 (Geodetic Mission) and TOPEX-POSEIDON. *Geophys. J. Int*., **125**, 696-704.

Chelton, D.B., M.G. Schlax, D.L. Witter, and J.G. Richman, 1990: Geosat altimeter observations of the surface circulation of the Southern Ocean. *J. Geophys. Res*., **95**, 17877-17903.

Chelton, D.B., J.C Re`is, B.J Haynes, L-L Fu, and P.S. Callahan, 2001: Satellite altimetry. In *Satellite Altimetry and Earth Sciences*, ed. L-L Fu and A Cazenave, Academic Press, San Diego, 463 pp.

Chen Y-J, W.J. Morgan, 1990a: Rift valley/no rift valley transition at mid-ocean ridges. *J. Geophys. Res.,* **95**, 17571-17583.

Chen Y.-J., W.J. Morgan, 1990b: A nonlinear rheology model for mid-ocean ridge axis topography. *J. Geophys. Res.*, **95**:17583-17604.

Cochran, J.R., 1979: An analysis of isostasy in the world's oceans. 2. Mid-ocean ridge crests. *J. Geophys. Res*., **84**, 4713-4729.

Dressler, B.O., V. Sharpton, 1999: *Large Meteorite Impacts and Planetary Evolution; II*, Special Paper 339. Geological Society of America, Boulder, CO.
Egbert, G.D. and R.D. Ray, 2000: Significant dissipation of tidal energy in the deep ocean inferred from satellite altimeter data. *Nature,* **405**, 775-778.
Feldman, G., D. Clark, and D. Halpern, 1984: Satellite color observations of the phytoplankton distribution in the eastern equatorial Pacific during the 1982-1983 El Niño. *Science*, **226**, 1069-1071.
Fu, L-L. and D. Chelton, 2001: Large-scale ocean circulation. In *Satellite Altimetry and Earth Sciences*, ed. L-L Fu and A. Cazenave, Academic Press, San Diego, 463 pp.
Gahagan L.M., C.R. Scotese, J.Y. Royer, D.T. Sandwell, J.K. Winn, R.L. Tomlins, et al., 1988: Tectonic fabric map of the ocean basins from satellite altimetry data. *Tectonophys*., **155**, 1-26.
Geli, L., D. Aslanian, J.L. Olivet, I. Vlastelic, L. Dosso, H. Guillou, H. Bougault, 1998: Location of Louisville hotspot and origin of Hollister ridge: geophysical constraints. *Earth Planet. Sci. Lett*., **164**(N1-2), 31-40.
Gille, S.T., 1994: Mean sea surface height of the Antarctic circumpolar current from Geosat data: method and application. *J. Geophys. Res*., **99**, 18255-18273.
Gille, S.T. and K.A. Kelly, 1996: Scales of spatial and temporal variability in the Southern Ocean. *J. Geophys. Res*., **101**, 8759-8773.
Gille, S.T., M.M. Yale, and D.T. Sandwell, 2000: Global correlation of mesoscale ocean variability with seafloor roughness from satellite altimetry. *Geophys. Res. Lett*., **27**, 1251-1254.
Goff, J.A., T.H. Jordan, 1988: Stochastic modeling of seafloor morphology: inversion of Sea Beam data for second-order statistics. *J. Geophys. Res*., **93**, 13589-13608.
Goff, J.A., 1991: A global and regional stochastic analysis of near-ridge abyssal hill morphology. *J. Geophys. Res.*, **96**, 21713-21737.
Gordon, A.L., and T.N. Baker, 1986*:* Southern Ocean Atlas. *Published for the International Decade of Ocean Exploration, National Science Foundation.*
Hasumi, H., N. Suginohara, 1999: Sensitivity of a global ocean general circulation model to tracer advection schemes. *J. Phys. Oceanogr*., **29**(N10), 2730-2740.
Haxby, W.F., G.D. Karner, J.L. LaBrecque, and J.K. Weissel, 1983: Digital images of combined oceanic and continental data sets and their use in tectonic studies. *EOS Trans. Amer. Geophys. Union*, **64**, 995-1004.
Hayne, G.S., D.W. Hancock, C.L. Purdy, and P.S. Callahan, 1994: The corrections for significant wave height and altitude effects in the TOPEX radar altimeter. *J. Geophys. Res*., **99**, 24941-24955.
Heiskanen, W.A., and H. Moritz, 1967: *Physical Geodesy*. W.H. Freeman and Co., San Francisco.
Heiskanen, W.A., F.A. Vening Meinesz, 1958: *The Earth and its Gravity Field*. New York: McGraw-Hill. 470 pp.
Holloway, G., 1992: Representing topographic stress for large scale ocean models. *J. Phys. Oceanogr*., **22**, 1033-1046.
Hwang, C., E.-C. Kao, and B. Parsons, 1998: Global derivation of marine gravity anomalies from Seasat, Geosat, ERS-1 and TOPEX/POSEIDON altimeter data. *Geophys. J. Int*., **134**, 449-459.
Hwang, C., and B. Parsons, 1996: An optimal procedure for deriving marine gravity from multi-satellite altimetry. *J. Geophys. Int*., **125**, 705-719.
Imel, D.A., 1994: Evaluation of the TOPEX/POSEIDON dual-frequency ionospheric correction. *J. Geophys. Res*., **99**, 24895-24906.
Jayne, S.R., and L.C. St. Laurent, 2001: Parameterizing tidal dissipation over rough topography. *Geophys. Res. Lett.*, **28**, 811-814.
Jung, W.Y., and P.R. Vogt, 1992: Predicting bathymetry from Geosat-ERM and shipborne profiles in the South Atlantic ocean. *Tectonophysics*, **210**, 235-253.
Kelly, K.A., 1991: The meandering Gulf Stream as seen by the Geosat altimeter: Surface transport, position, and velocity variance from 73 to 46W. *J. Geophys. Res.*, **96**, 16721-16738.
Koslow, J.A. (1997) Seamounts and the ecology of deep-sea fisheries. *Am. Sci. **85***, 168-176.
Laxon, S., and McAdoo, D. (1994). Arctic ocean gravity field derived from ERS-1 satellite altimetry. *Science* **265**, 621-624.
LaCasce, J. H. (2000). Floats and *f/H*. *J. Mar. Res*., **58**, 61-95.
Ledwell, J. L., E. T. Montgomery, K. L. Polzin, L. C. St Laurent, R. W. Schmitt and J. M. Toole, (2000). Evidence for enhanced mixing over rough topohraphy in the abyssal ocean, *Nature, 403, (6766),* 179-182.

Lemoine, F. G., et al. (1998). The development of the joint NASA CSFC and the national Imagery and Mapping Agency (NIMA) geopotential model EGM96. Goddard Space Flight Center, NASA, NASA/TP-1998-206861.

Le-Traon, P.Y. and R. Morrow, 2001: Ocean currents and Eddies. In *Satellite Altimetry and Earth Sciences*, ed. L-L Fu and A Cazenave, Academic Press, San Diego, 463 pp.

Levitus S., J.I. Antonov, T.P. Boyer, 1994: Interannual variability of temperatures at a depth of 125 meters in the North Atlantic Ocean. *Science*, **266**(N5182), 96-99.

Liu, C.-S., D.T. Sandwell and J.R. Curray, 1982: The negative gravity field over the 85° Ridge. *J. Geophys. Res*., **87**, 7673-7686.

Livermore, R., D. McAdoo, K. Marks, 1994: Scotia Sea tectonics from high-resolution satellite gravity. *Earth Planet. Sci. Lett.*, **123**, 255-268.

Llewellyn-Smith, S.G. and W.R. Young, 2001: Conversion of thebarotropic tide. *J. Phys. Oceanogr*., (submitted).

Lonsdale, P., 1994: Structural geomorphology of the Eltanin fault system and adjacent transform faults of the Pacific-Antarctic plate boundary. *Mar. Geophys. Res.,* **16**(N2), 105-143.

Maia, M., et al., 2000: The Pacific-Antarctic Ridge-Foundation hotspot interaction: a case study of a ridge approaching a hotspot. *Marine Geol., **16**7*, 61-84.

Malinverno, A., 1991: Inverse square-root dependence of mid-ocean ridge flank roughness on spreading rate. *Nature*, **352**, 58-60.

Mammerickx, J., 1992: The Foundation Seamounts: tectonic setting of a newly discovered seamount chain in the South Pacific. *Earth Planet. Sci. Lett*., **113**, 293-306.

Marks, K.M., J.M. Stock, 1994: Variations in ridge morphology and depth-age relationships on the Pacific-Antarctic Ridge. *J. Geophys. Res*., **99**, 531-541.

Marks, K.M., J.M. Stock, 1995: Asymmetric seafloor spreading and short ridge jumps in the Australian-Antarctic Discordance. *Marine Geophys. Res*., **17**, 361-373.

Maus, S., C.M. Green, and J.D. Fairhead, 1998: Improved ocean-geoid resolution from retracked ERS-1 satellite altimeter waveforms. *Geophys. J. Int*., **134**, 243-253.

Mayes C.L., L.A. Lawver, and D.T. Sandwell, 1990: Tectonic history and new isochron chart of the South Pacific. *J. Geophys. Res*., **95**, 8543-8567.

McCartney, M.S., 1976: The interaction of zonal currents with topography with applications to the Southern Ocean. *Deep-Sea Res*., **23**, 413-427.

Macdonald, K.C., 1986: The crest of the Mid-Atlantic Ridge: Models for crustal generation processes and tectonics. In *The Geology of North America, vol. M, The Western North Atlantic Region*, ed. P.R. Vogt and B.E. Tucholke, Boulder, CO: Geol. Soc. Amer.

McKenzie, D.P., 1976: Some remarks on heat flow and gravity anomalies. *J. Geophys. Res*., **72**, 6261-6273.

McKenzie, D.P., and C. Bowin, 1976: The relationship between bathymetry and gravity in the Atlantic Ocean. *J. Geophys. Res.,* **81**, 1903-1915.

McNutt, M., 1979: Compensation of oceanic topography: An application of the response function technique to the Surveyor area. *J. Geophys. Res*., **84**, 7589-7598.

McNutt, M., 1984: Lithospheric flexure and thermal anomalies. *J. Geophys. Res*., **89**, 11180-11194.

McNutt, M., H.W. Menard, 1982: Constraints on yield strength in the oceanic lithosphere derived from observations of flexure. *Geophys. J. Roy. Astron. Soc*., **71**, 363-383.

Medea, 1995: Scientific Utility of Naval Environmental Data. MEDEA Office.

Menard, H.W., 1967: Seafloor spreading , topography, and the second layer. *Science,* **157**, 923-924.

Menard, H.W., and S.M. Smith, 1966: Hypsometry of Ocean Basin Provinces. *J. Geophys. Res*., **71**, 4305-4325.

Monahan, D. et al., 1999: A model for using publicly available data and methodologies to begin preparing for a claim to an extended continental shelf under article 76 of the United Nations Convention on Law of the Sea (UNCLOS). In *Proceedings, Technical Aspects of Martime Boundary Delineation and Delimitation,* 171-182, Intl. Hydrographic Org., Intl., Assoc. Geodesy, Intl. Board on Tech. Aspects of Law of the Sea (ABLOS).

Monaldo, F., 1988: Expected differences between buoy and radar altimeter measurements of wind speed and significant wave height and their implications on buoy-altimeter comparisons. *J. Geophys. Res*., **93**, 2285-2302.

Morrow, R., J. Church, R. Coleman, D. Chelton, and N. White, 1992: Eddy momentum flux and its contribution to the Southern Ocean momentum balance. *Nature*, **357**, 482-484.

Müller, R.D., W.H.F. Smith, 1993: Deformation of the oceanic crust between the North American and South American plates. *J. Geophys. Res.*, **98**, 8275-8291.
Munk, W.H., C. Wunsch (1998). Abyssal recipes II: energetics of tidal and wind mixing, *Deep-Sea Res. Part I,* **45**, 1977-2010.
Munk, W.H., C. Wunsch, 1997: The moon of course. *Oceanography*, **10**, 132-134.
Noreus, J.P., 1995: Improved resolution of Geosat altimetry using dense sampling and polynomial adjusted averaging. *Int. J. Remote Sensing*, **16**, 2843-2862.
Olgiati, A., G. Balmino, M. Sarrailh, C.M. Green, 1995: Gravity anomalies from satellite altimetry: comparison between computation via geoid heights and via deflections of the vertical. *Bull. Geod.* **69**, 252-260.
Phipps Morgan, J. et al., (1987).
Phipps Morgan, J., Y.J. Chen, 1992: Dependence of ridge-axis morphology on magma supply and spreading rate. *Nature,* **357**, 706-708.
Phipps Morgan, J., Chen, Y.J., 1993: The genesis of oceanic crust: magma injection, hydrothermal circulation, and crustal flow. *J. Geophys. Res.*, **98**, 6283-6298.
Phipps Morgan, J., E.M. Parmentier, 1995: Crenulated seafloor: evidence for spreading-rate dependent structure of mantle upwelling and melting beneath a mid-ocean spreading center. *Earth Planet. Sci. Lett.,* **129**, 73-84.
Phipps Morgan, J., D.T. Sandwell, 1994: Systematics of ridge propagation south of 30°S. *Earth Planet. Sci. Lett.,* **121**, 245-258.
Picaut, J. and A.J. Busalacchi, 2001: Tropical ocean variability. In *Satellite Altimetry and Earth Sciences*, ed. L-L. Fu and A. Cazenave, Academic Press, San Diego, 463 pp.
Polzin, K.L., J.M. Toole, J.R. Ledwell, and R.W. Schmitt, 1997: Spatial variability of turbulent mixing in the abyssal ocean. *Science*, **276**, 93-96.
Ponte, R.M., 1994: Understanding the relation between wind- and pressure-driven sea level variability. *J. Geophys. Res*., **99**, 8033-8039.
Ramillien, G., and A. Cazenave, 1997: Global bathymetry derived from altimeter data of the ERS-1 Geodetic Mission. *J. Geodynamics*, **23**, 129-149.
Raney, K., 1998: The delay/Doppler radar altimeter. *IEEE Trans on Geosciences and Remote Sensing*, **36**(5), 1578-1588.
Reigber, C., Z. King, R. Konig, and P. Schwintzer, 1996: CHAMP, A minisatellite mission for geopotential and atmospheric research. Spring AGU Meeting, Baltimore, May, 1996.
Rapp, R.H., and Y. Yi, 1997: Role of ocean variability and dynamic topography in the recovery of the mean sea surface and gravity anomalies from satellite altimeter data. *J. Geodesy*, **71**, 617-629.
Sahabi, M., L. Géli, J.-L. Olivet, L. Gilg-Capar, G. Roult, et al., 1996: Morphological reorganization within the Pacific-Antarctic Discordance. *Earth Planet. Sci. Lett.*, **137**,157-173.
Sandwell, D.T., 1991: Geophysical applications of satellite altimetry. *Rev. Geophys. Suppl*., **29**, 132-137.
Sandwell, D.T., and W.H.F. Smith, 1997: Marine gravity anomaly from Geosat and ERS-1 satellite altimetry. *J. Geophys. Res*., **102**, 10039-10054.
Sandwell, D.T. and W.H.F. Smith, 2001: Bathymetric Estimation. In *Satellite Altimetry and Earth Sciences*, edited by L.-L. Fu and A. Cazenave, Intl. Geophys. Series., **69**, Academic Press, New York, 441-457.
Sandwell, D.T., and B. Zhang, 1989: Global mesoscale variability from the Geosat exact repeat mission: Correlation with ocean depth. *J. Geophys. Res*., **94**, 17971-17984.
Schulman, E.E., 1975: A study of topographic effects. In *Numerical models of ocean circulation,* Nat. Acad. Sci. pp. 147-165.
Sichoix, L., and A. Bonneville, 1996: Prediction of bathymetry in French Polynesia constrained by shipboard data. *Geophys. Res. Lett*., **23**, 2469-2472.
Shaw, P.R. and S.C. Cande, 1990: High resolution inversion for South Atlantic plate kinematics using joint altimeter and magnetic anomaly data, *J. Geophys. Res., 95*, 2625-2644.
Shum, C.K. et al., 1997: Accuracy assessment of recent ocean tide models. *J. Geophys. Res.,* **102**(C11), 25173-25194.
Shum, C.K. et al., 2001: Recent advances in ocean tidal science. *J. Geodetic Soc. Japan,* **47**(1), 528-537.
Sleep, N.H., 1969: Sensitivity of heat flow and gravity to the mechanism of seafloor spreading. *J. Geophys. Res*., **74**, 542-549.
Small, C., 1994: A global analysis of mid-ocean ridge axial topography. *Geophys. J. Int*., **116**, 64-84.
Small, C., 1994: Imaging mid-ocean ridge transitions with satellite gravity. *Geology*, **22**, 123-126.

Small C. and D.T. Sandwell, 1989: An abrupt change in ridge axis gravity with spreading rate. *J. Geophys. Res*., **94**, 17383-17392.
Small, C., D.T. Sandwell, 1994: Imaging mid-ocean ridge transitions with satellite gravity. *Geology,* **22**, 123-126.
Small, C., 1995: Observations of ridge-hotspot interactions in the Southern Ocean. *J. Geophys. Res.,* **100**, 17931-17946.
Small, C., 1998: Global systematics of mid-ocean ridge morphology. In *Faulting and Magmatism at Mid-Ocean Ridges* (Vol. **106**, Geophysical Monograph) (Buck, W. R. et al., eds.), pp. 1-25, American Geophysical Union.
Smith, R.D. et al., 2000: Numerical simulation of the North Atlantic Ocean at 1/10 degrees. *J. Phys. Oceanogr*., **30**, 1532-1561.
Smith, W.H.F., 1993: On the accuracy of digital bathymetry data. *J. Geophys. Res*., **98**, 9591-9603.
Smith, W.H.F., 1998: Seafloor tectonic fabric from satellite altimetry. *Ann. Rev. Earth Planet. Sci.,* **26**, 697-738.
Smith, W.H.F., and D.T. Sandwell, 1994: Bathymetric prediction from dense satellite altimetry and sparse shipboard bathymetry. *J. Geophys. Res*., **99**, 21,803-21,824.
Smith, W.H.F., and D.T. Sandwell, 1997: Global seafloor topography from satellite altimetry and ship depth soundings. *Science*, **277**, 1956-1961.
Smith R.D. et al., 2000: Numerical simulation of the North Atlantic Ocean at 1/10 degree. *J. Phys. Oceanogr*., **30**, 1532-1561.
Stammer, D., 1998: On eddy characteristics, eddy transports, and mean flow properties. *J. Phys. Oceanogr*., **28**, 727-739.
St. Laurent, L.C. and C. Garret, 2000: The role of internal tides in mixing the deep ocean. *J. Phys. Oceanogr.* (submitted).
Stewart, R.H., 1985: *Methods of Satellite Oceanography*. University of California Press, Berkeley.
Tapley, B. and M.-C. Kim, (2001). Applications to Geodesy. In *Satellite Altimetry and Earth Sciences*, ed. L.-L. Fu and A. Cazenave, Intl. Geophys. Series., vol. **69**, Academic Press, New York, 371-403.
Tapley, B.D., D.P. Chambers, C.K. Shum, R.J. Eanes, J.C. Ries, and R.H. Stewart, 1994: Accuracy assessment of large-scale dynamic ocean topography from Topex/Poseidon altimetry. *J. Geophys. Res*., **99**, 24605-24617.
Tapley, B., C. Reigber, and W. Melbourne, 1996: Gravity Recovery and Climate Experiment (GRACE) mission. Spring AGU Meeting, Baltimore, May, 1996.
Tapponier, P., J. Francheteau, 1978: Necking of the lithosphere and the mechanics of slowly accreting plate boundaries. *J. Geophys. Res*., **83**, 3955-3970.
Wessel, P., A.B. Watts, 1988: On the accuracy of marine gravity measurements. *J. Geophys. Res.*, **93**, 393-413.
Wessel, P., 1992: Thermal stresses and the bimodal distribution of elastic thickness estimates of the oceanic lithosphere. *J. Geophys. Res.*, **97**, 14177-14193.
Wessel, P., S. Lyons, 1997: Distribution of large Pacific seamounts from Geosat/ERS. 1: Implications for the history of intraplate volcanism. *J. Geophys. Res.*, **102**, 22459-22475
Yale, M.M., 1997: Modeling upper mantle rheology with numerical experiments and mapping marine gravity with satellite altimetry. Ph.D. Thesis, University of Califiifornia, San Diego.
Yale, M.M., D.T. Sandwell, and W.H.F. Smith, 1995: Comparison of along-track resolution of stacked Geosat, ERS-1 and TOPEX satellite altimeters. *J. Geophys. Res*., **100**, 15117-15127.
Yale, M.M., D.T. Sandwell and A.T. Herring, 1998: What are the limitations of satellite altimetry? *The Leading Edge*, January, 1998, p. 73-76.
Yeh, H., 1998: Tsunami researchers outline steps for better data. *EOS Trans. AGU,* **79,** 480, 484.

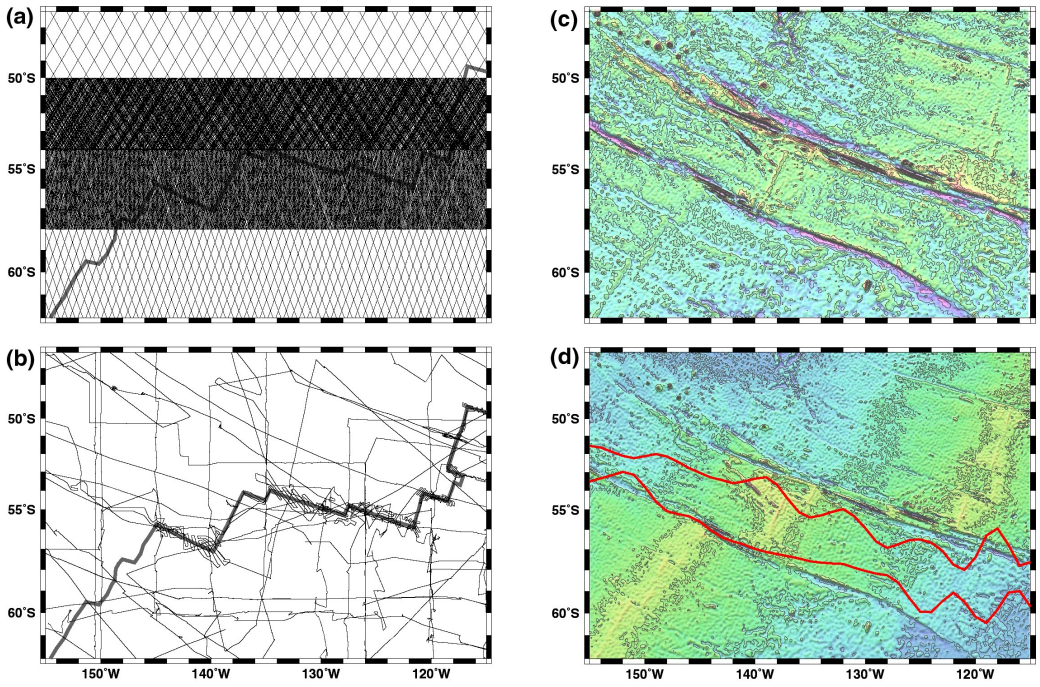

Figure 1. Data needed for predicting bathymetry. (a) Tracks of stacked Geosat/ERM (17-day repeat cycle), Geosat/GM, ERS-1 Geodetic Phase (168-day repeat cycle) and stacked ERS-1 (35-day repeat). (b) Ship tracks in area of the Eltanin and Udintsev transform faults. Track density is sparse except along the Pacific-Antarctic plate boundary. (c) Gravity anomaly (mGal) derived from all 4 altimeter data sets. (d) Bathymetry (m) estimated from ship soundings and gravity inversion. Red curves mark the sub-Antarctic and polar fronts of the Antarctic Circumpolar Current [*Gille,* 1994]. The Sub-Antarctic Front (SAF-red) passes directly over a NW-trending Hollister ridge which has a minimum ocean depth of 135 m [*Geli et al*., 1997]. The Polar Front (PF) is centered on the 6000m deep valley of the Udintsev transform fault.

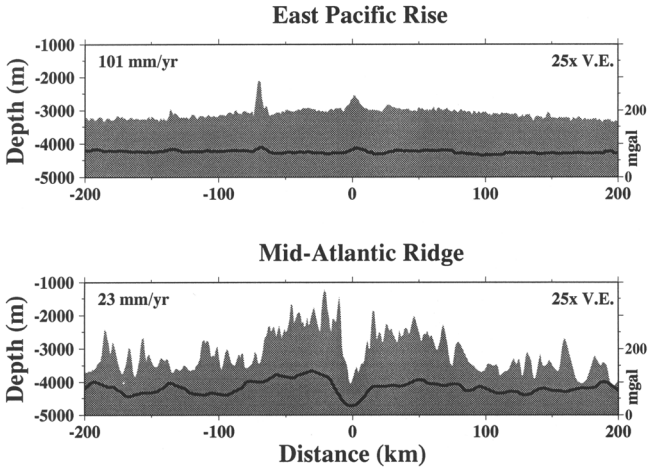

Figure 2. Typical ridge axis relief and gravity amplitude versus spreading rate [*Small*, 1994]. The EPR has a smooth gravity profile with a positive anomaly over the axis of 10 or more mGal, while the MAR has a rougher gravity profile with a negative anomaly over the axis exceeding 30 mGal in magnitude.

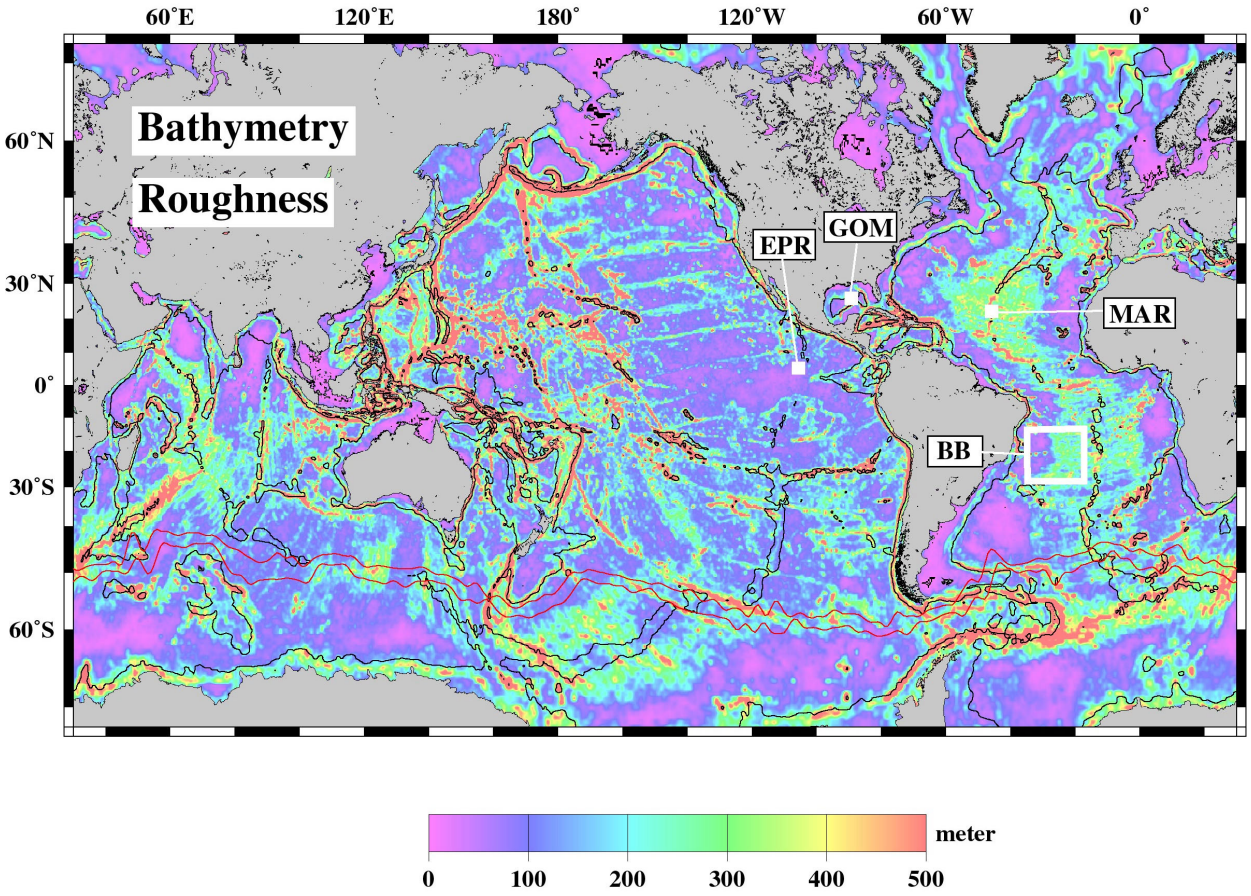

Figure 3. Seafloor roughness from altimeter-derived, high-pass filtered topography (24-160 km wavelength). Because of noise in the gravity field, the smaller-scale seafloor roughness associated with abyssal hills is not captured in this estimate. Analysis of high-resolution bathymetry suggests that the ratio of rough-to-smooth seafloor is at least two times greater than shown in this figure. Detailed bathymetry of the MAR, EPR, and Gulf of Mexico (GOM) are shown in Figure 4. The roughness contrast in the Brazil Basin (BB) is shown in Figure 5.

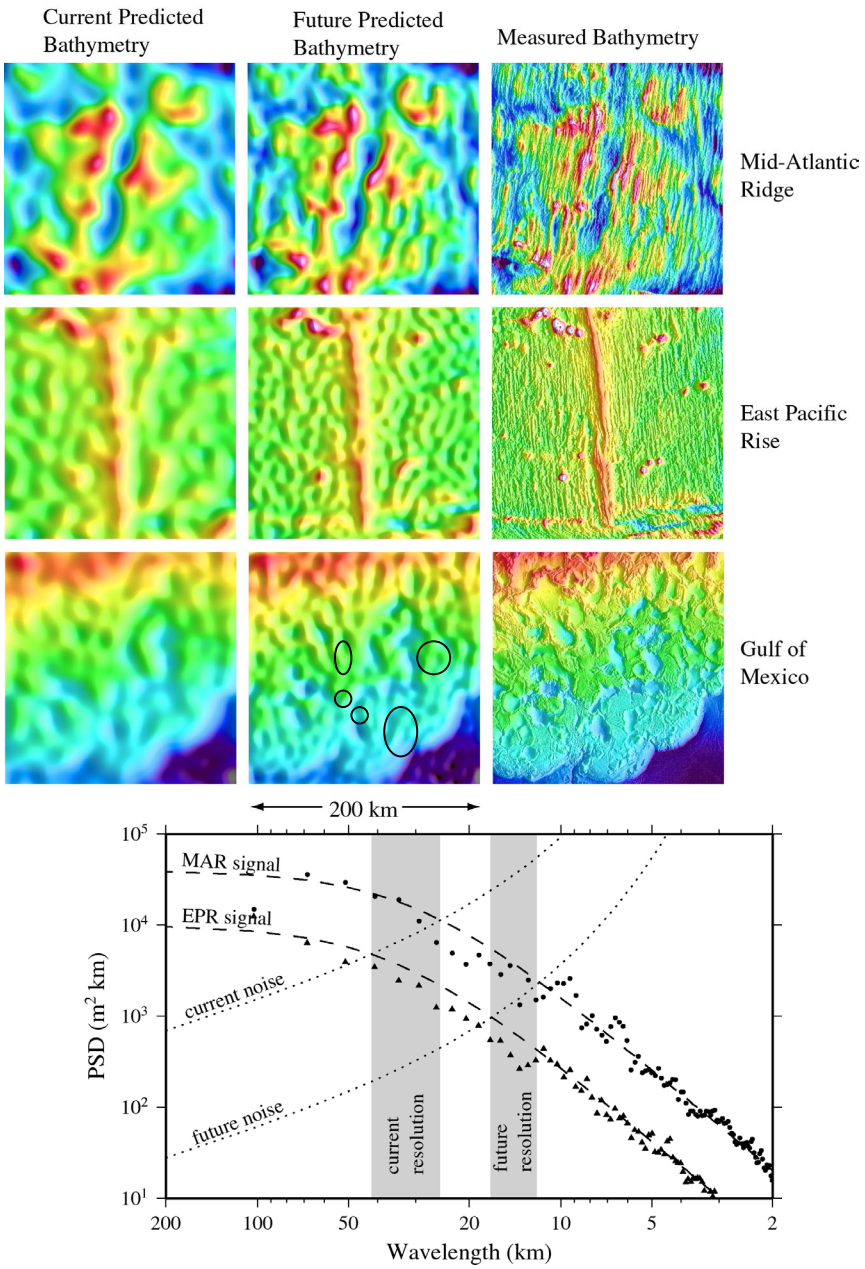

Figure 4. (Upper) Measured bathymetry (right column) and predicted bathymetry (left and center columns) for representative areas on the Mid-Atlantic Ridge, the East Pacific Rise, and the Gulf of Mexico. The Mid-Atlantic Ridge and East Pacific Rise show the characteristic abyssal-hill signature of slow and fast spreading ridges, respectively. While the current prediced bathymetry in the Gulf of Mexico is unable to resolved the salt-related mini-basins (outlined), the future predicted bathymetry reveals some of the more important structures; a global data set would be beneficial in frontier reconnaissance studies. (Lower) East-west spectra of the Mid-Atlantic Ridge and the East Pacific rise area bathymetry. For both areas, the corner wavenumber and roll-off exponent are 20 km and –2.8, respectively. The total power is 493 m for the MAR and 209 m for the EPR. The noise spectra (dotted curves) for current and future bathymetric prediction is discussed in the following section. A signal to noise ratio of 1 defines the resolution limits of current and future bathymetric prediction. The current resolution for rough and smooth seafloor is 25 km and 45 km , respectively. Assuming a factor of 5 noise reduction in a future mission, the resolution improves to 12 and 17 km, respectively. Note this improvement captures the corner wavenumber of 20 km.

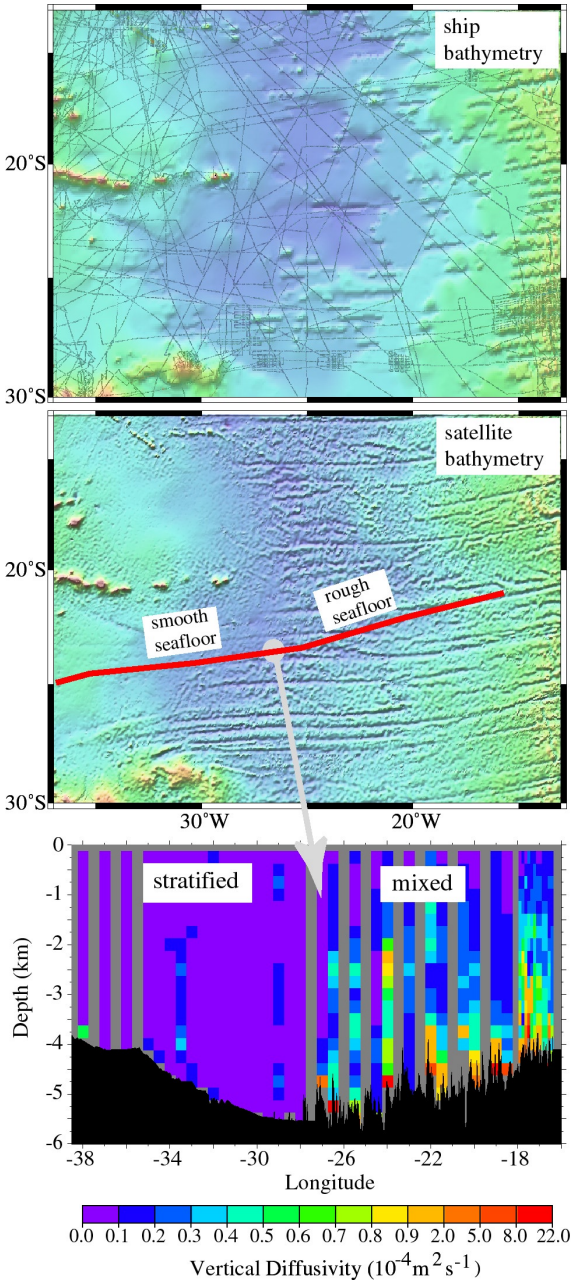

Figure 5. (Upper) Bathymetry of Brazil Basin, South Atlantic derived from ship soundings lacks the resolution needed to distinguish between rough and smooth seafloor. (Center) Bathymetry derived from satellite altimetry and ship soundings resolves the rough seafloor associated with fracture zones but not abyssal hills. (Lower) Vertical diffusivity represents vertical mixing of stratified seawater. Mixing rates are an order of magnitude greater over rough topography (abyssal hills and fracture zones) than they are over smooth topography. Enhanced mixing over rough topography extends from depths of about 1500 m to the bottom of the ocean (>4000 m). Mixing effects the vertical stratification which in turn influences deep currents and their horizontal and vertical stability to perturbations (after *Polzin et al.* [1997]).

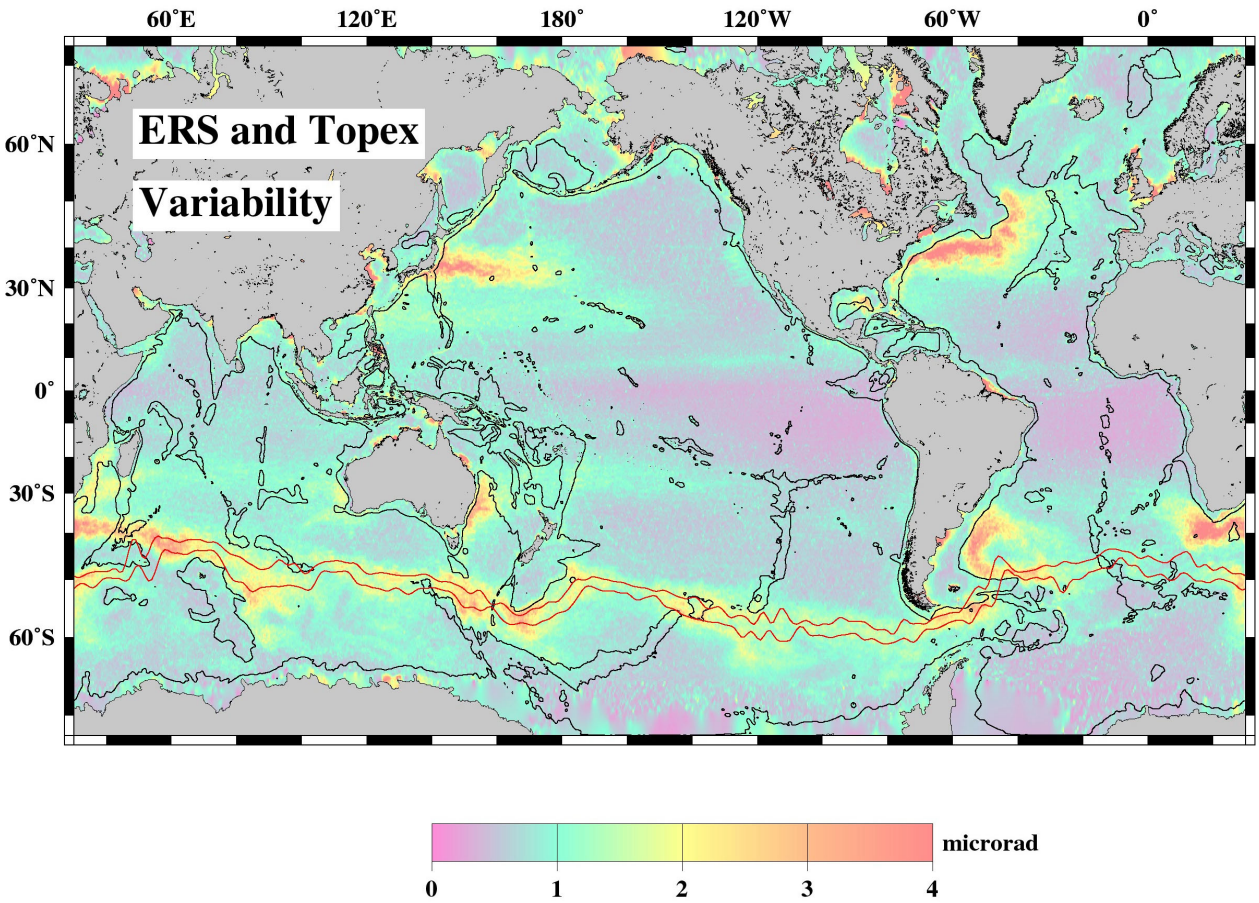

Figure 6. Mesoscale slope variability from Topex and ERS repeat-pass altimetry. Note regions of highest ocean variability are concentrated in ocean areas greater than 3000 m deep (contour lines). A comparison with Figure 3 also that, in the deep ocean, the highest variability occurs over smooth seafloor.

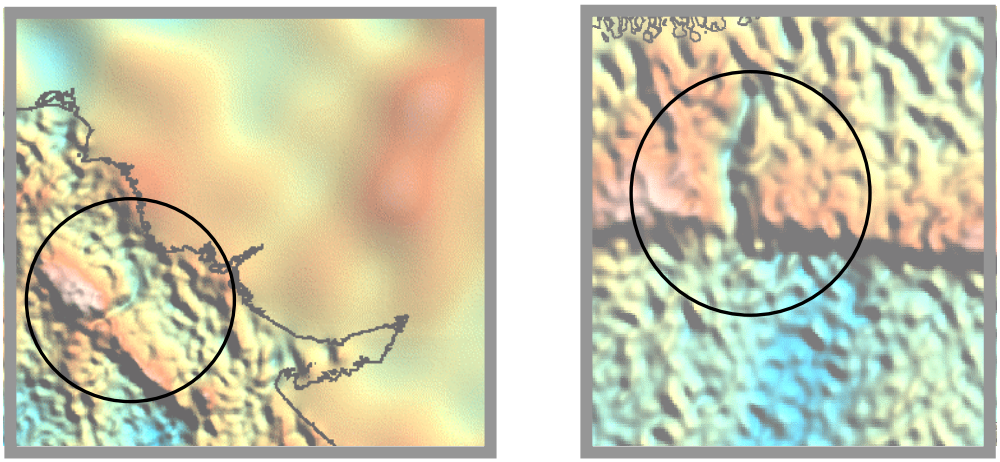

Figure 7. Submarine canyon associated with Indus River, Pakistan (left) Ganges River, Bangladesh (right).

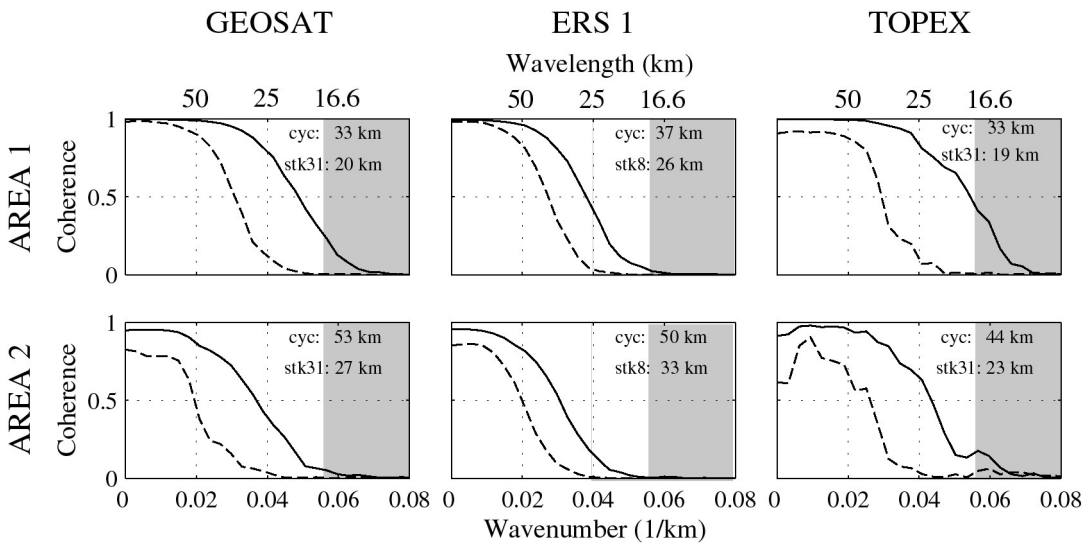

Figure 8. The along-track resolution of three radar altimeters Geosat, ERS1 and Topex, [*Yale et al.,* 1995]. Two areas were selected for analysis. Area 1 over the equatorial Mid-Atlantic Ridge has a high signal due to the rugged seafloor and relatively low wave-height noise. Area 2 over the Pacific-Antarctic Ridge has a lower gravity signal but a much higher noise level because it is an area of large wave height. The two curves in each plot show coherence between individual cycles (dashed) and independent stacks (solid). The resolution of the stacked profiles is better than the individual cycles. Topex and Geosat have generally better resolution than ERS1. The grey vertical box marks the resolution desired from a new altimeter mission. The range of desired resolution reflects the limiting factors of ocean depth and wave height.

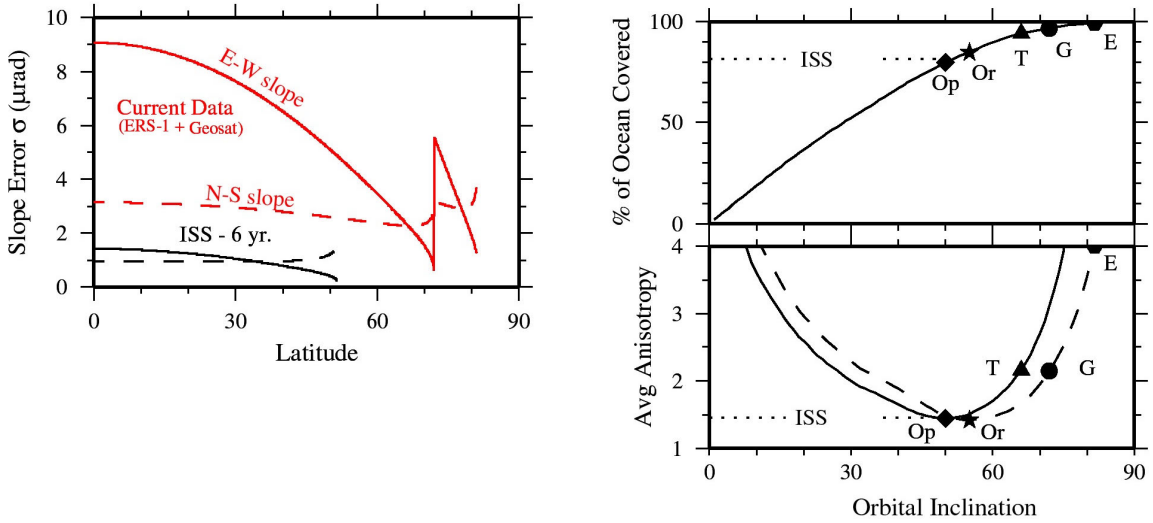

Figure 9. (left - red curves - Current) Propagation of along-track slope error from 1.5 years of dense Geosat coverage and 1 year of dense ERS-1 coverage into east (solid) and north (dashed) components of sea surface slope recovery versus latitude. At the equator, the Geosat and ERS tracks mainly run N-S so the N-S component is well determined (dashed red curve) while the E-W component of sea surface slope is poorly determined (solid red curve). The black curves show the improvement in E-W (solid) and N-S (dashed) slope error resulting from a new delay-doppler altimeter in an ISS (52˚) orbital inclination for 6 years. We assumed the new delay-doppler altimeter has one half the noise level of Geosat (Keith Raney, personal communication, 2001). (right) Trade-off analysis to establish the average N-S to E-W anisotropy as a function of orbital inclination (solid – prograde, dashed – retrograde). The optimal inclinations are 50˚ (Op) and 55˚ (Or), respectively. The ERS (E), Geosat (G) and Topex (T) inclinations are good at higher latitudes but suffer from poor E-W slope recovery at low latitudes where the area of ocean (right-upper) is maximum.

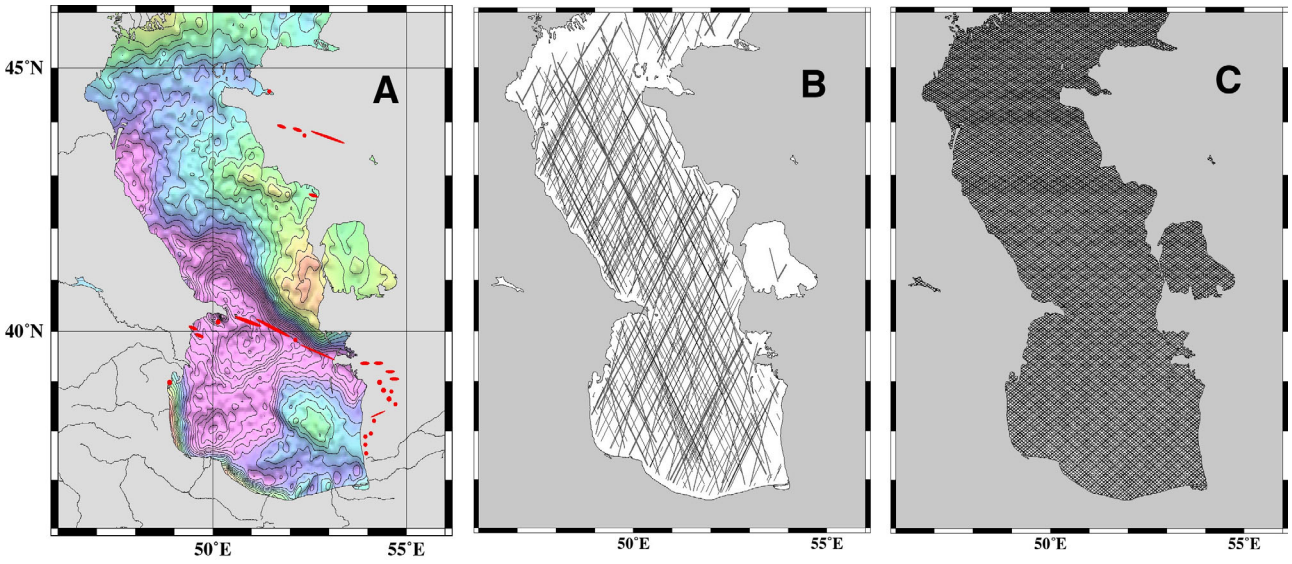

Figure 10. (A) Gravity anomaly of the Caspian Sea (10 mGal contour interval) derived from all available satellite altimeter data (Geosat, ERS and Topex). Major oil fields are sketched in red. Future exploration will focus on the northern Caspian near the outlet of the Volga River. (B) Tracks of available altimeter data show less-than-optimal coverage because ERS data are not available (land mask) and many Geosat profiles are missing due to problems with the onboard tracker re-acquiring the water surface. (C) Tracks from 1.5 years of a new satellite altimeter in an ISS orbital inclination.

Navy and NOAA Operational Requirements for High-Resolution Ocean Topography

Gregg Jacobs
NRL Code 7323
Stennis Space Center, MS 39529

Robert Cheney
NOAA/NESDIS
1315 East-West Highway
Silver Spring, MD 20910

Whereas most of the papers in this volume are concerned with high-resolution ocean topography (HROT) from the viewpoint of scientific research, we present an operational perspective. Operational use implies a requirement for timely reports, analyses, or raw data, but other considerations also differentiate operations and science. Scientific investigation of dynamical processes governing the ocean must approach the problem without prejudice. In order to avoid tainting conclusions or inferences, the scientific researcher must often view data in isolation without prior judgment. In operational applications, the goal is simply to provide an accurate product, and to this end, operational systems aim to make use of every piece of information. This may come in the form of real time HROT observations, equations describing balances of sources and sinks, numerical models that attempt to represent the descriptive equations, or historical observations. An operational system may therefore taint observations by joining them with prior information. Within this report we examine the potential impact of HROT observations in the light of prior dynamical and observational knowledge.

One example of the division between scientific and operational data use is spatial interpolation. The report by *Chelton and Schlax* (2001) in this volume exemplifies this ideal by introducing no prior prejudice into the interpolation or gridding procedures implemented. Isotropic interpolation is used to grid and examine the impact of HROT data. However, based on historical altimeter data, we may estimate eddy spatial length scales, time scales, and propagation speeds (Jacobs et al., 2001), and we may impose this non-isotropic information upon subsequent results. Numerical model assimilation systems provide another method of assessing HROT impact given prior information (*Hurlburt et al*., 2001 this volume). Thus, we may examine HROT data impact in conjunction with prior information through many avenues.

Both the U.S. Navy and the National Oceanographic and Atmospheric Administration (NOAA) require near-real time sea level variation observations for a variety of operational ocean applications. Some of these requirements are needed for observing large-scale phenomena (e.g. El Nino, basin-scale variations in circulation and upper ocean heat) and can be satisfied with a minimal, "low-resolution" satellite altimeter configuration (one conventional radar altimeter in an appropriate orbit). However, mesoscale and coastal phenomena are also of interest to Navy and NOAA operations. Requirements for observing these sea level signatures can only be met with "high-resolution" configurations (multiple altimeter satellites or instruments capable of measuring surface topography over wide swaths). In addition, there is a need to obtain sea level measurements closer to the coast than presently possible. This report summarizes HROT application to three principal operational applications: tides, coastal features, and mesoscale variations.

Tides

Tidal variations constitute a major portion of ocean variability near coastlines. While the tidal sea level variation itself is important for storm surge estimation as well as wetting and drying of tidal plains, it is often the effects associated with the tide that are of greater importance. Tide-related effects include

currents, which in turn relate to turbulence, suspension and transport of sediments, scouring, biological properties, and ocean optical properties. The spatial scales over which tidal amplitude and phase vary are often equivalent to the spatial scales over which the local bathymetric features vary. Near coastal barrier islands, bays, and other regional ocean features, the spatial scales of tides may be on the order of kilometers to tens of meters. Accurate tidal prediction is often difficult due to uncertainty in bathymetry and coastline geometry, both of which may vary in time. Yet the ability to estimate tides on small spatial scales is vital for hazard mitigation. For example, NOAA has undertaken a project to develop a water level data assimilation nowcast/forecast model system for the US east coast. The system is designed to provide mariners and port mangers with real time information on ocean conditions for safe navigation as well as to provide water level boundary conditions for bay circulation models.

An optimal adjoint variational data assimilation technique has been developed to assimilate water levels into simplified barotropic dynamics. The system is presently limited by dynamical accuracy and available data. Dynamical accuracy is dependent upon accurate bathymetry that controls barotropic wave propagation. Data concentration is able to compensate for bathymetry errors to some degree. HROT can provide substantial improvement for operational tide applications in this area. *Ray* (2001) and *Le Provost* (2001) (both in this volume) both provide examinations of the extent to which tide solutions may be improved through HROT.

Coastal Oceanographic Features

Along-shore coastal currents due to wind-driven upwelling and downwelling directly impact the advection of oil spill, red tide, mines, equipment, and personnel. Currents also have implications for changes in coastal temperature. The off-shore extent of the coastal currents varies from hundreds of meters to tens of kilometers, and these spatial scales dictate resolution requirements. In addition, the ocean current transports through critical straits are vital input to numerical ocean models for forecasting ocean conditions. For example, real time monitoring of the transport through the Florida Strait is required for operational ocean forecasting off the eastern U.S. seaboard. Similarly, transports through the Taiwan and Korea Straits are required to monitor the ocean properties throughout the East Asian Seas. While these straits may be hundreds of kilometers across, the currents passing through the straits have scales approaching 30 km. Subtle shifts in these currents within the straits produce dramatic changes in the outflowing circulation. Sea level changes for large inland lakes are required for circulation studies and operational services such as lake nowcasting and forecasting. Lake surface heights and other measurements are required in fine spatial scales (several km) and temporal resolution (<1 day). Operational services such as the Great Lakes forecasting system require lake elevation changes as input to their operational modeling effort.

Mesoscale Oceanographic Features

The mesoscale field is a result of eddies and major current meanderings formed through flow instability processes. Thus, the mesoscale field is typically a first baroclinic mode structure with the sea level reflecting vertical thermocline displacements, and these displacements imply significant changes in currents, heat content, and density variations. The majority of mesoscale energy is concentrated in western boundary current extension regions, though baroclinic eddies are ubiquitous throughout the globe. NOAA's Coastal Ocean Forecast System presently assimilates a variety of ocean data, including sea surface height from satellites. The National Hurricane Center also takes advantage of sea surface height data to improve forecasts of hurricane intensity. For applications such as these, timeliness is critical, with observations required with no more than a 24-hour delay. Absolute accuracy of the sea surface height measurement (i.e. radial orbit determination) is less important because the data can be high-pass filtered to reveal the mesoscale features of interest. Thiebaux et al. (2000), Aikman et al. (1996), and Emanuel (1999) describe these requirements, derived from NOAA's goal of advancing short-term warning and forecasts services.

Thermocline shifts induced by the mesoscale field are closely related to sea level changes

observable from the satellite altimeter. The mesoscale field dramatically alters the ocean environment within which the Navy must operate. Because the mesoscale field is chaotic, not directly related to the wind field, and thus not predictable far in advance, continuous observations of the mesoscale field are required to monitor the environment that may impact Navy acoustic operations for Anti Submarine Warfare (ASW) and prediction of mine drift trajectories. Operational systems are presently in place within the Naval Oceanographic Office to exploit available altimeter data streams. The operational systems provide daily observations to numerical model systems that in turn feed information to the Navy fleet. The spatial scales of open ocean eddies extends upwards from 20 km. The Navy mesoscale requirements are outlined in Jacobs et al. (1999).

Because synoptic mesoscale features control upper ocean heat content, a strong determinant for important information such as atmospheric storm forcing and environmental acoustic prediction, present operational ocean modeling systems are tuned to provide variations due to mesoscale features. Prior studies (Hurlburt, 1984) have indicated that altimeter information is one of the most instrumental data types for operational use in determining mesoscale perturbation effects, and operational systems have evolved to the point at which surface height information provides significant benefit. One example (Figure 1) indicates the inferred sub-surface temperature along the sub-satellite point of the Geosat-Follow On (GFO) ground track across the Gulf of Mexico compared to the observed sub-surface temperature. Aircraft expendable bathythermograph (XBT) instruments provided the observed temperature. Historical XBT data provide the correlation between dynamic height anomaly and the sub-surface temperature anomaly (Carnes et al., 1994), and this information is incorporated into the Modular Ocean Data Assimilation System (MODAS) (Fox et al., 2001). The observed GFO sea level anomaly provides observations upon which the sub-surface temperature inference is based. This example indicates the estimate of the ocean temperature given the GFO observations and the correlation function of sea level anomaly to sub-surface temperature based on historical data. The subsurface temperature inference is not based exclusively upon independent observations but uses all the historical data to form statistics.

By using different conditionals in conjunction with HROT observations (impact given a particular a priori assumption), we provide different perspectives of HROT observation impact. Here we examine three different conditionals:

1. Observation density requirements given no prior information. What are the time and length scales required to observe mesoscale variations without a priori assumptions?
2. Sea level error based on optimal interpolation given prior sea level observation. What spatial and temporal observation density is needed for mesoscale optimal interpolation if we have knowledge of the mesoscale characteristics?
3. Sea level error based on assimilation into numerical dynamics. What spatial and temporal observation density is required for assimilation into numerical dynamics?

We examine question 1 by determining the spatial and temporal scales of the mesoscale field based on the historical altimeter observations. Through a time-space lagged cross covariance of historical altimeter data (*Jacobs et al.*, 2001), the mesoscale characteristic time periods and spatial scales indicate the scales required by a HROT system for operational use (Figure 2). This suggests that more than three nadir-observing altimeters are required to synoptically observe a large portion of the spatial and temporal scales. There are several complexities that must be considered in Figure 2. First, Figure 2 does not take into account Nyquist sampling which would imply that the area resolvable by each satellite would be further to the upper right. Second, the ground track spacing is the distance between parallel tracks. The crossing tracks would increase sampling density near crossover points. This effect would tend to increase the spatial Nyquist resolvable range. Finally, the particular order in which the spatial ground tracks are sampled may further complicate the requirements. With these considerations taken together, it is expected that Figure 2 provides an optimistic viewpoint, and that satellite sampling density would need to be higher than that implied in the figure.

The spatial and temporal sampling requirements for scientific mesoscale mapping applications require that we not consider scales and propagation speeds previously observed. However, for operational purposes, incorporating such information into the analysis provides an improved product. To answer question 2, we consider properties implied by prior data. Observations of the Geosat-Exact Repeat Mission, TOPEX/POSEIDON, ERS-1, and ERS-2 contain the needed prior mesoscale information. The time-space lagged cross-covariance may be used to provide expected covariance function for optimal interpolation, which in turn leads to the expected interpolation error (Figure 3). Expected errors of the different single-satellite orbit configurations indicate the long repeat (decreased ground track separation) scenarios provide improved mesoscale mapping capability under the assumption that we know the mesoscale spatial and temporal scales. As Figure 3 indicates, the combination of 3 nadir-observing satellites and assumptions on the a priori covariance of sea level anomalies provides a reasonable sea level estimate for operational applications. This is different from the result without any mesoscale information (Figure 2) that more than 3 nadir-observing satellites are required to resolve the mesoscale.

Question 3 adds information derived from dynamical equations contained within a numerical model. For this examination, we employ the NRL Layered Ocean Model (NLOM), which represents deep ocean mesoscale processes within an isopycnal vertical coordinate frame. The method for assimilating altimeter observations into NLOM employs an optimal interpolation of sea level difference between the model state and observation along with a data insertion procedure to move the model toward the observed state. The observation system efficacy is measured through the RMS difference between the numerical model nowcast and the observed state prior to the assimilation. Results contained in the report by *Hurlburt et al.* (this volume) indicate a single altimeter provides a large reduction in mapping SSH using simulated data from a numerical model. The decrease in RMS error from 1 to 2 altimeters is substantial and the RMS decreases in the cases from 2 to 3 altimeters.

Conclusions

For operational applications, a single nadir-looking satellite altimeter is adequate for observing basin-scale and global-scale sea level variations, but such phenomena are only a partial contribution in estimating the synoptic ocean state for operational products. The ocean mesoscale field generates deviations from seasonal climatology that are much more significant. Also of great importance are the mesoscale variations in gradient fields which control both geostrophic currents and sound propagation through the ocean. For these reasons, it is important for operational products to estimate the mesoscale field and its impact.

The spatial and temporal sampling of any single nadir-looking altimeter system is inadequate to provide an independent estimate of the synoptic mesoscale field, and such observations must be extended through assimilation techniques. Assimilation systems range from simple optimal interpolation to 4-D variational techniques. Most assimilation systems are capable of providing expected errors associated with estimated fields. The ability of a particular sampling scheme to measure the mesoscale field may be judged through the expected error estimates. Of course, each assimilation scheme is unique and contains a range of assumptions that will strongly affect the error estimates. So expected error fields must be viewed in the light of each system's capabilities. With this point in mind, the conclusion that is reached by all the assimilation systems to date is that expected errors in mesoscale field estimates are dramatically reduced when data from two nadir altimeter satellites are included in the system. Within the optimal interpolation experiments we have examined, extending to three nadir altimeter satellites also provides a significant benefit.

References

Aikman, F. III, G.L. Mellor, T. Ezer, D. Sheinin, P. Chen, L. Breaker, K. Bosley, and D.B. Rao, 1996: Towards an operational nowcast/forecast system for the U.S. East Coast. In: *Modern Approaches to Data Assimilation in Ocean Modeling,* P. Malanotte-Rizzoli (ed), Elsevier Oceanography Series, **61**, 347-376.

Carnes, M.R., W.J. Teague, and J.L. Mitchell, 1994: Inference of subsurface thermohaline structure from fields measured by satellite. *J. Atmos. Ocean Tech*., **11**, 551-566.

Chelton, D.B., and M.G. Schlax: The resolution capability of sea surface height fields constructed from a tandem TOPEX/POSEIDON and JASON-1 mission, HOTSWG report.

Fox, D.N., W.J. Teague, C.N. Barron, M.R. Carnes, and C.M. Lee, 2001: The Modular Ocean data Assimilation System (MODAS). *J. Atmos. Oceanic Technol*, in press.

Hurlburt, H.E., 1984: The potential for ocean prediction and the role of altimeter data. *Mar. Geod.,* **8**, 17-66.

Hurlburt, H.E., R.C. Rhodes, O.M. Smedstad, A.J. Wallcraft, E.J. Metzger, J.F. Shriver, and A.B. Kara: A real-time, eddy-resolving 1/16 global ocean prediction system, HOTSWG report.

Jacobs, G.A., C.N. Barron, M.R. Carnes, D.N. Fox, H.E. Hurlburt, P. Pistek, R.C. Rhodes, W.J. Teague, J.P. Blaha, R. Crout, and K.R. Whitmer, 1999: Navy Altimeter Data Requirements. Naval Research Laboratory, *NRL/FR/7320—99-9696*, 20 pp.

Jacobs, G.A., C.N. Barron, and R.C. Rhodes, 2001: Mesoscale characteristics. *J. Geophys. Res.*, in press.

Le Provost, C.: Tides over ridges, shelves and near coasts, HOTSWG report.

Ray, R.D., 2000: Applications of high-resolution ocean topography to ocean tides, HOTSWG report.

Thiebaux, J., B. Katz, J. Kelley, L. Breaker, and B. Balasubramaniyan, 2000: National Ocean Partnership project advances real-time coastal ocean forecasting". *EOS Trans. AGU,* **81** (14), 145-150.

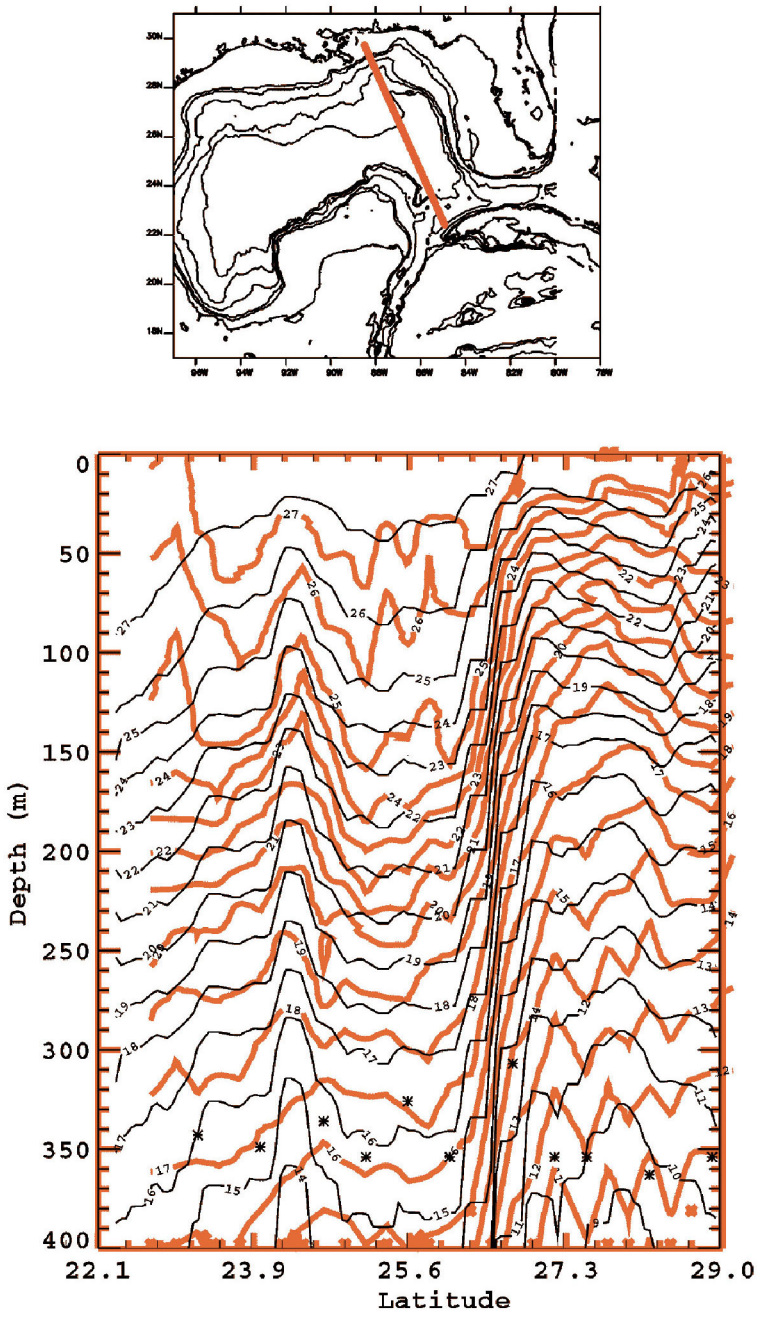

Figure 1. Airborne XBT observations taken along a sub-satellite track of the Geosat Follow On provide direct observation of subsurface temperature (red lines). The observations were taken on May, 19, 2000. The height anomaly (deviation from a long term mean) measured by the altimeter is used to infer subsurface temperature (black lines). The spatial sampling along the altimeter ground track provides reasonable resolution of the mesoscale field.

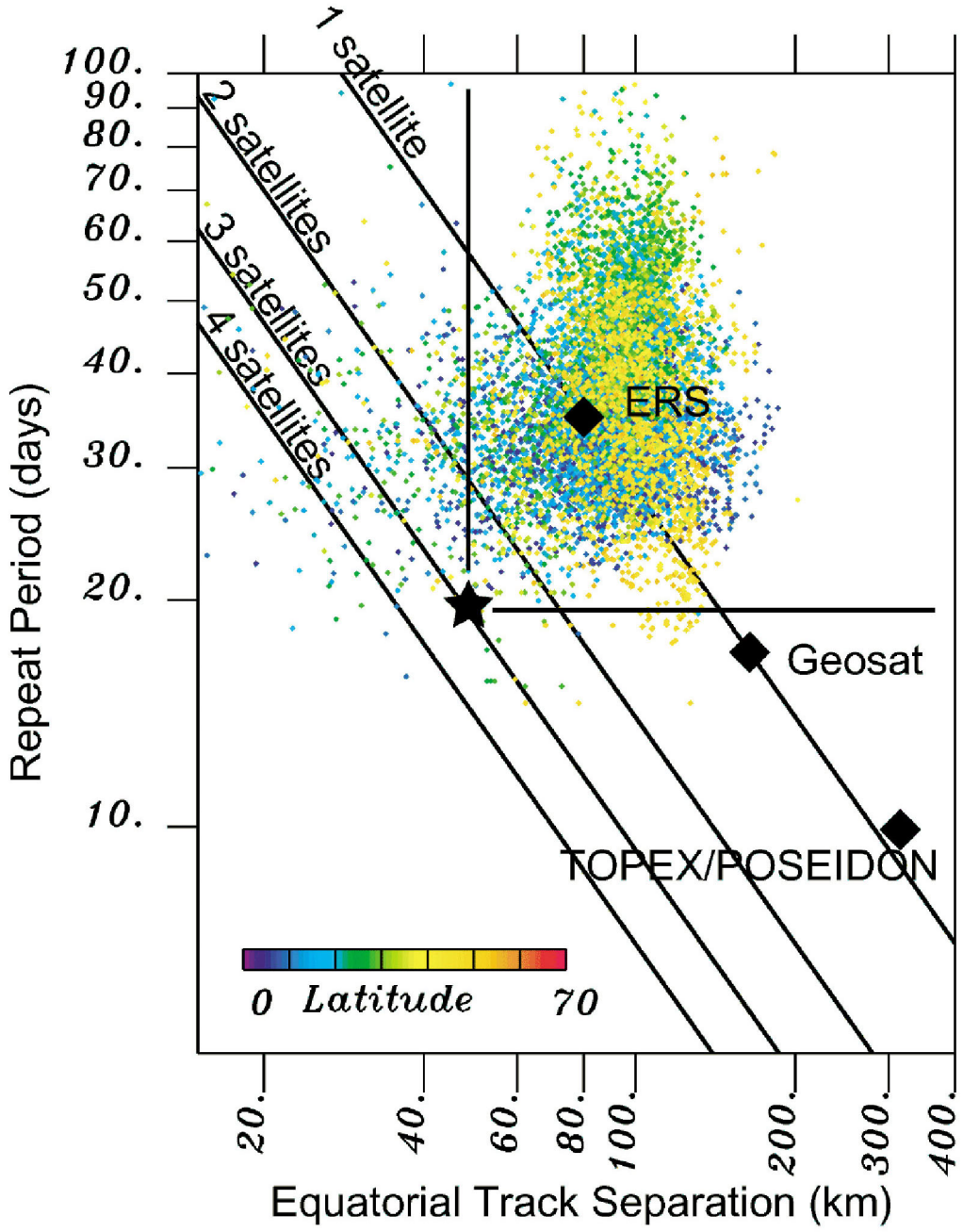

Figure 2. The mesoscale field zonal and temporal distributions provide an indication of the sampling required to synoptically observe mesoscale variability. The sampling capabilities of a single satellite will generally fall on the one-satellite line (with some deviation due to orbit height). The observable spatial scales are greater than the separation of parallel ground tracks at the equator, and the observable time scales are greater than the repeat period. Thus, the observable space of a satellite is to the upper right of the satellite point. The area covered by 3 satellites encompasses much of the mesoscale range. When Nyquist sampling and ground track sampling are considered, the synoptically observing the mesoscale will require much more than 3 satellites. However, these requirements may be relaxed if the data are used in conjunction with prior information contained in either statistical or numerical ocean models.

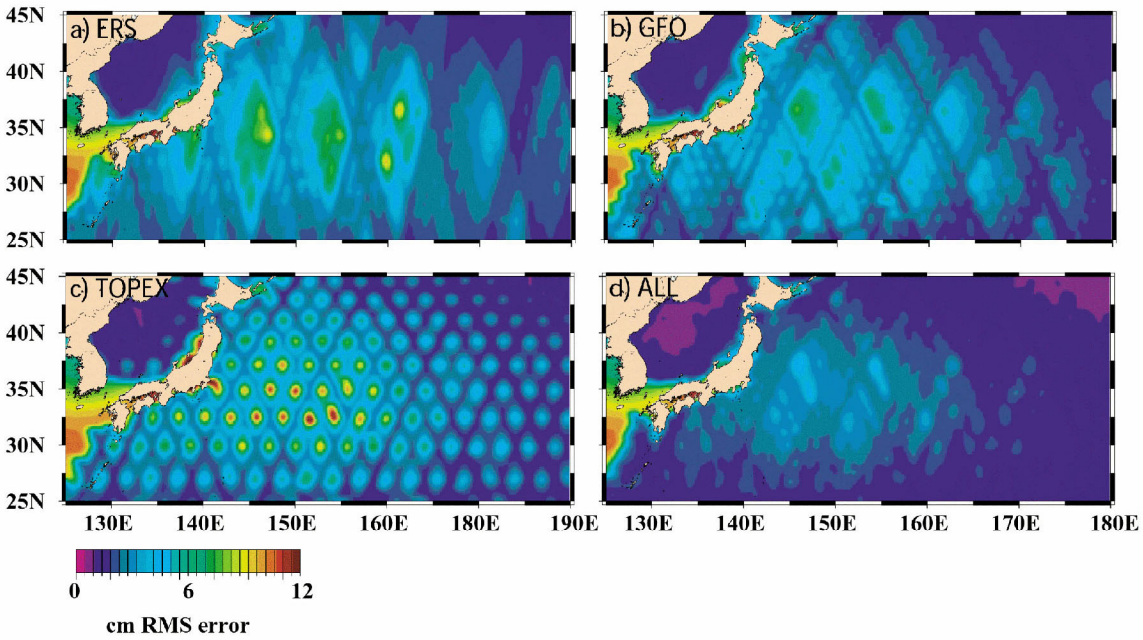

Figure 3. The expected error associated with an optimal interpolation. The covariance function contains non-isotropic length scales as well as propagation in time. The covariance parameters also vary spatially and are designed to represent the mesoscale field. Expected errors are largest in the high variability region of the Kuroshio. Using GFO, ERS, and TOPEX simultaneously (d) significantly reduces errors.

Part 2

High-Resolution Ocean Topography Measurements from Conventional Altimetry

Mesoscale Variability: What Can We Learn from High Resolution Altimetry?

Pierre-Yves Le Traon
CLS Space Oceanography Division

1. Introduction

This note provides an overview of the expected contribution of high resolution altimetry to our understanding of mesoscale variability. Past achievements from GEOSAT, ERS and TOPEX/POSEIDON missions are first briefly recalled. We then summarize the main findings of studies we have carried out on the resolution/mapping capabilities of multiple altimeter missions. This allows us to quantify the signals we are missing with the existing configurations and the improvements expected from high-resolution altimeter systems. We then try to analyze how this improved description could contribute to our understanding of mesoscale variability.

2. What did we learn from altimetry? Contribution of satellite altimetry

Satellite altimetry has made a unique contribution to observing and understanding mesoscale variability (see Le Traon and Morrow, 2000 for a recent review). Altimeter data analyses have provided, for the first time, a global description of the eddy energy and its seasonal/interannual variations. The time and space scales of the mesoscale circulation have been characterized. The eddy/mean flow interactions have also been mapped and provide an important ingredient for understanding the western boundary current and ACC dynamics. Satellite altimetry has also allowed a synoptic mapping of large eddies (e.g. Agulhas eddies) which is useful to better understand the role of eddies in transporting mass, heat, salt and nutrient. All these studies provide a good means of testing and validating models and theories.

Most of these studies have used GEOSAT, T/P or ERS altimeter data separately. The contribution of the merging of T/P and ERS is, however, well illustrated by Ducet et al. (2000) and Ducet and Le Traon (2001). The velocity field was mapped globally; this yielded a characterization of the Eddy Kinetic Energy (EKE), anisotropy and eddy mean flow interactions with a resolution never achieved before (see figure 1).

3. Resolution and mapping capabilities of multiple altimeter missions

3.1. Formal mapping error analysis

Le Traon and Dibarboure (1999) have quantified the mesoscale mapping capability when combining various existing or future altimeter missions in terms of SLA (Figure 2) and zonal (U) and meridional (V) velocity. Their main results are as follows:

- There is a large improvement in sea level mapping when two satellites are included. For example, compared to T/P alone, the combination of T/P and ERS has a mean mapping error reduced by a factor of 4 and a standard deviation reduced by a factor of 5.
- The velocity field mapping is more demanding in terms of sampling. The U and V mean mapping errors are two to four times larger than the SLA mapping error. Only a combination of three satellites can provide a velocity field mapping error below 10% of the signal variance.

3.2. Simulations with the Los Alamos model

Le Traon et al. (2001) (hereafter LDD01) analyzed the sea level mapping capabilities of multiple altimeters using the Los Alamos North Atlantic high resolution model (Smith et al., 2000). Los Alamos Model (hereafter LAM) represents the mesoscale variability quite well and offered a unique opportunity for assessing the mapping capability of multiple altimeter missions.

LDD01 have shown that sea level mapping errors were larger than the ones derived from Le Traon and Dibarboure (1999) formal error analysis (by a factor of 1.5 to 2). This was mainly due to high frequency signals. In areas with large mesoscale variability, these signals represent 5 to 10% of the total sea level variance (see also Minster and Gennero, 1995) and are associated with high wavenumbers. They account for 15 to 20 % of the total velocity variance (figure 3). In shallow and high latitude regions, these high frequency signals account for up to 30-40% of the total sea level and velocity variance; there, part of these signals correspond to large scale barotropic motions.

LDD01 study was recently extended to the analysis of velocity field mapping capabilities. We also included a simulation of the WSOA system using simulated data provided to us by E. Rodriguez (Rodriguez et al., 2000) and analyzed "optimized" three and four satellites configurations (three and four interleaved Jason-1). To better analyze the impact of the high frequency signals on the sea level and velocity mapping, we systematically computed for all analyzed configurations the mapping errors on the instantaneous fields (as in LDD01) and on 10-day averaged fields. For the latter, the estimated fields were compared to the model fields filtered using a Loess filter with a cut-off period of 16 days (which chiefly corresponds to 10-day averages). Results for the T/P+ERS and WSOA configurations are shown on figures 4a and 4b (sea level) and 5a and 5b (zonal velocity). Results for the different configurations in the Gulf Stream area are summarized in table 1.

3.3. Quantifying the improvement of high resolution altimetry

Compared to T/P+ERS, a three or four "optimized" satellite configuration or WSOA (if systematic errors can be sufficiently reduced) will allow a large improvement in the description of mesoscale variability. However, to achieve a mapping accuracy of the total velocity field better than 15-20% of the signal variance, one needs to resolve the high frequency and high wavenumber signals. This will require a much denser space and time sampling (better than 100 km and 10 days). The aliasing of the high frequency signals is also a important issue; thus, even if these signals cannot be resolved, one needs to take into account their impact on lower frequencies/wavenumbers. Note that the large scale high frequency barotropic signals (e.g. Tierney et al., 2000) are likely to be well resolved by an "optimized" three or four satellite configuration.

Note finally that the reduction of altimeter noise and a better understanding of the contribution of inertial/gravity waves are also needed to fully exploit the potential of high resolution missions.

4. Contribution of high resolution altimetry

Despite all the progress made in the last decade, there is still much to learn from altimeter data for mesoscale variability studies. Investigations that could be carried out include:

- More detailed comparisons of altimetry (including comparison of higher order statistics such as frequency/wavenumber spectra and Reynolds stresses) with eddy resolving models.
- Regional characterization of the 3D frequency/wavenumber of sea level (and velocity) and relation with forcings and dynamics. Relation with turbulence theories.
- Better characterization of seasonal/interannual variations in eddy energy and relation with forcings (mean current instabilities, winds).
- Phenomenological (global) characterization of eddies (eddy census): size, rotation, diameter, life time, propagation. Relation with theories and models.
- Detailed dynamical structure of eddies. Estimation of the vorticity field (in and out of the eddy), divergence and deformation fields. Use in synergy with high resolution SST and Ocean Color images. Estimation of vertical circulation and biogeochemical coupling.
- Relation and interaction between eddies and Rossby waves.
- Eddy heat fluxes (in combination with SST remote sensing data). Contribution to the total heat fluxes.
- Eddy mean flow interaction. Role of eddies on the general circulation.

All these studies will benefit from higher space and time resolution. The minimum requirement would be to continue flying a two satellite configuration (after Jason-1 and ENVISAT) but a denser space and time sampling should allow us to much better address these issues. In particular, the phenomenological and dynamical characterization of eddies and the eddy mean flow interaction studies will require a much higher resolution than the one we have today.

Finally, one should note that the best use of high resolution altimetry data will be when they are assimilated with in-situ and other remote sensing data into global eddy resolving models (GODAE) (and nested shelf/coastal models). This will open a large range of scientific (see above) and operational applications. The capability of providing precise velocity estimations will be, in particular, of great importance for operational applications (offshore, fisheries, marine safety).

5. References

Ducet, N., P.Y. Le Traon and G. Reverdin, 2000: Global high resolution mapping of ocean circulation from the combination of T/P and ERS-1/2. *J. Geophys. Res*., **105**, 19,477-19,498.

Ducet, N., and P.Y. Le Traon, 2001: A comparison of surface eddy kinetic energy and Renolds stresses in the Gulf Stream and the Kuroshio current systems from merged T/P and ERS-1/2 altimetric data. *J. Geophys. Res.* (in press).

Le Traon, P.Y. and R. Morrow, 2000: Ocean currents and mesoscale eddies, in Satellite Altimetry and Earth Sciences. Editors L. L. Fu and A. Cazenave. Academic Press.

Le Traon, P.Y. and G. Dibarboure, 1999: Mesoscale mapping capabilities from multiple altimeter missions. *J. Atm. Ocean. Tech*., **16**, 1208-1223.

Le Traon, P.Y., G. Dibarboure, and N. Ducet, 2001: Use of a high resolution model to analyze the mapping capabilities of multiple altimeter missions. *J. Atm. Ocean. Tech.* (in press).

Minster, J.F., and M.C. Gennero, 1995: High-frequency variability of western boundary currents using ERS-1 three-day repeat altimeter data. *J. Geophys. Res*., **100**, 22,603-22,612.

Rodriguez, E., B. Pollard, J.M. Martin, 2000: Wide-Swath Ocean Altimeter Simulated Data, Release 1. May 30.

Smith, R.D., M.E. Maltrud, F.O. Bryan, and M.W. Hecht, 2000: Numerical simulation of the North Atlantic ocean at 1/10°. *J. Phys. Oceanogr*., **30**, 1532-1561.

Tierney, C., J. Wahr, F. Bryan and V. Zlotnicki, 2000: Short-period oceanic circulation; implication for satellite altimetry. *Geophys. Res. Lett*., **27**, 1255-1258.

Table 1. Sea Level (H), zonal (U) and meridional (V) velocity mean mapping error over the Gulf Stream area (34°N-39°N – 70°W-60°W). Errors expressed in percentage of the total sea level and velocity variance are given both for "instantaneous" and 10-day average signal mapping.

	H	U	V
T/P + ERS (Jason-1 + ENVISAT)	8 / 4.9	29 / 10.9	40 / 15.4
T/P+ERS+Jason-1	6.5 / 2.6	23 / 6.9	29 / 9.7
Three interleaved Jason-1	4.8 / 1.9	20.2 / 5.6	21.9 / 6.5
Four interleaved Jason-1	4.3 / 1.7	18.9 / 5.1	20.8 / 5.4
WSOA (assuming uncorrelated errors)	5 / 2.5	18.8 / 6.1	20.5 / 6.7

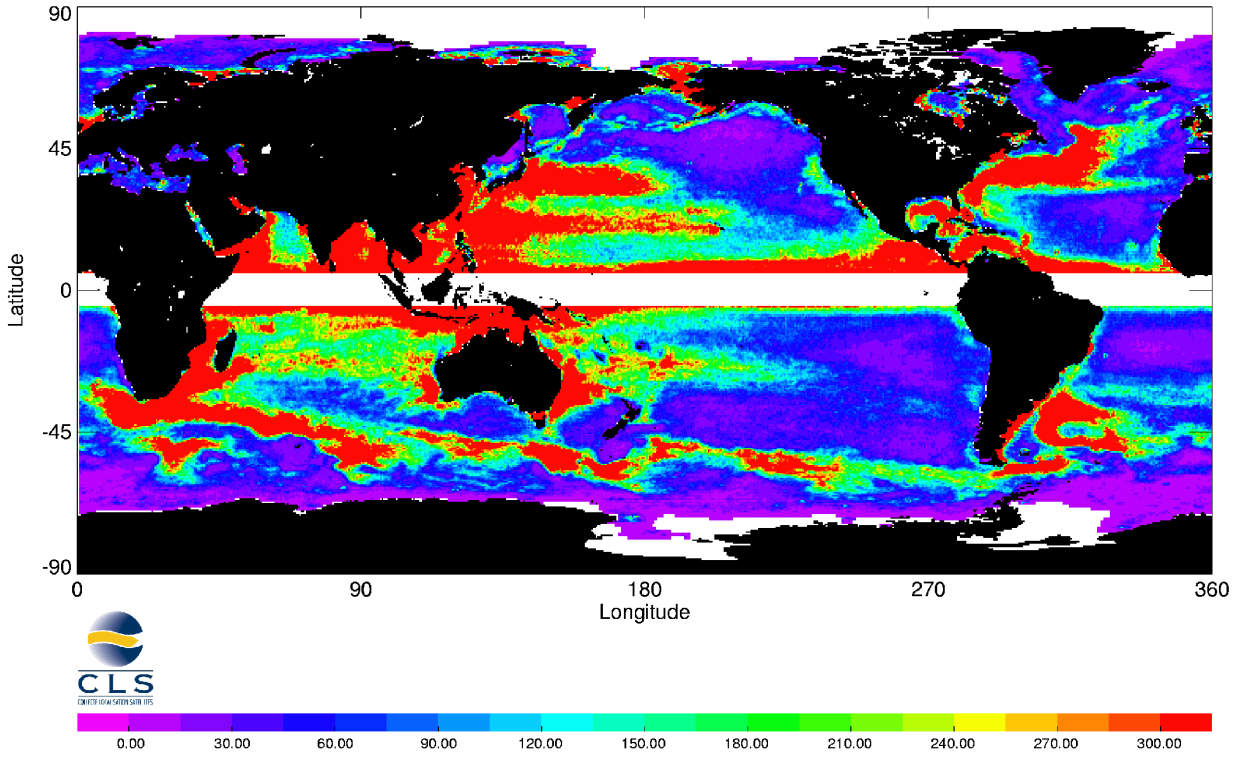

Figure 1. Eddy Kinetic Energy derived from the combination of T/P and ERS-1/2 over a 5 year period (Ducet et al., 2000). The map presents a very detailed description presumably never before achieved at a global scale. Units are cm^2/s^2.

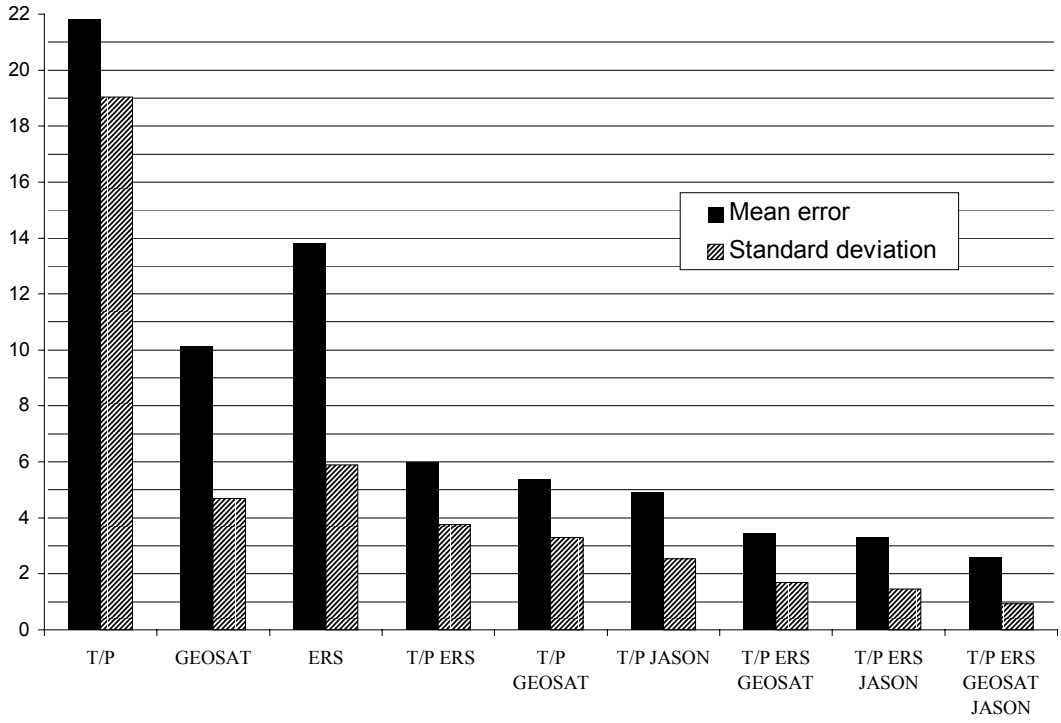

Figure 2. Mean and standard deviation of Sea Level Anomaly (SLA) mapping error for single and multiple altimeter missions. Units are in % of signal variance.

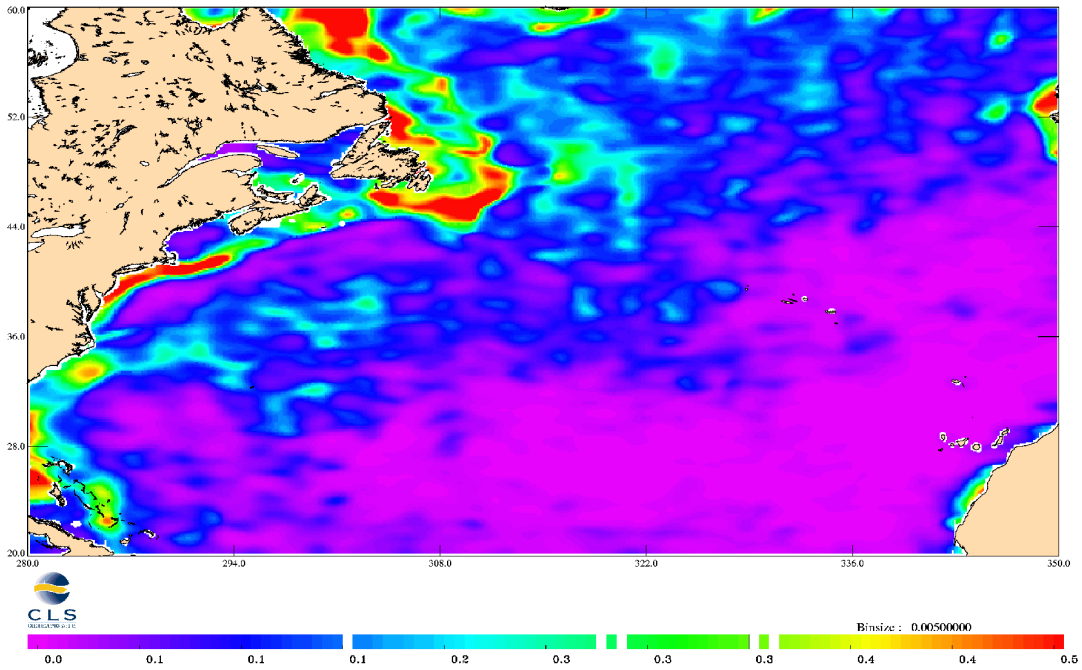

Figure 3. Contribution of high frequency signals (periods <20 days) to the total zonal velocity variance for the Los Alamos simulation.

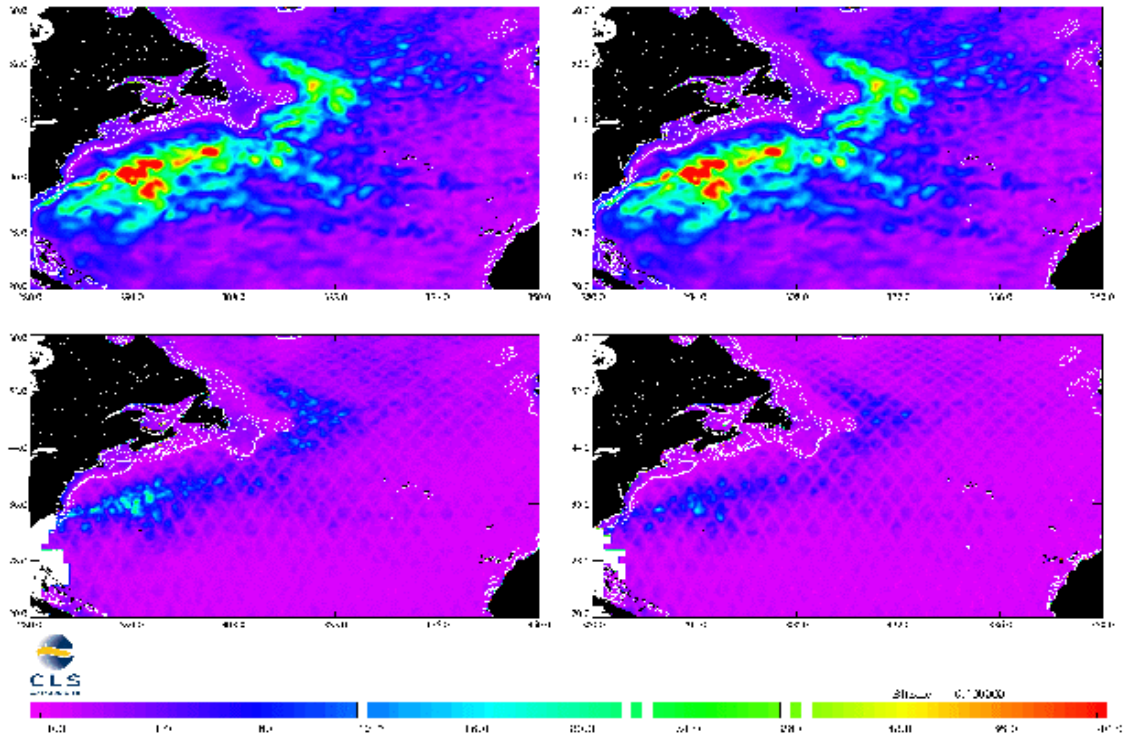

Figure 4a. Rms sea level for the Los Alamos Model simulation (upper figure). Rms sea level mapping error for T/P+ERS (lower figures). Left panel corresponds to instantaneous signal mapping error. Right panel corresponds to 10-day average signal mapping error. Units are cm.

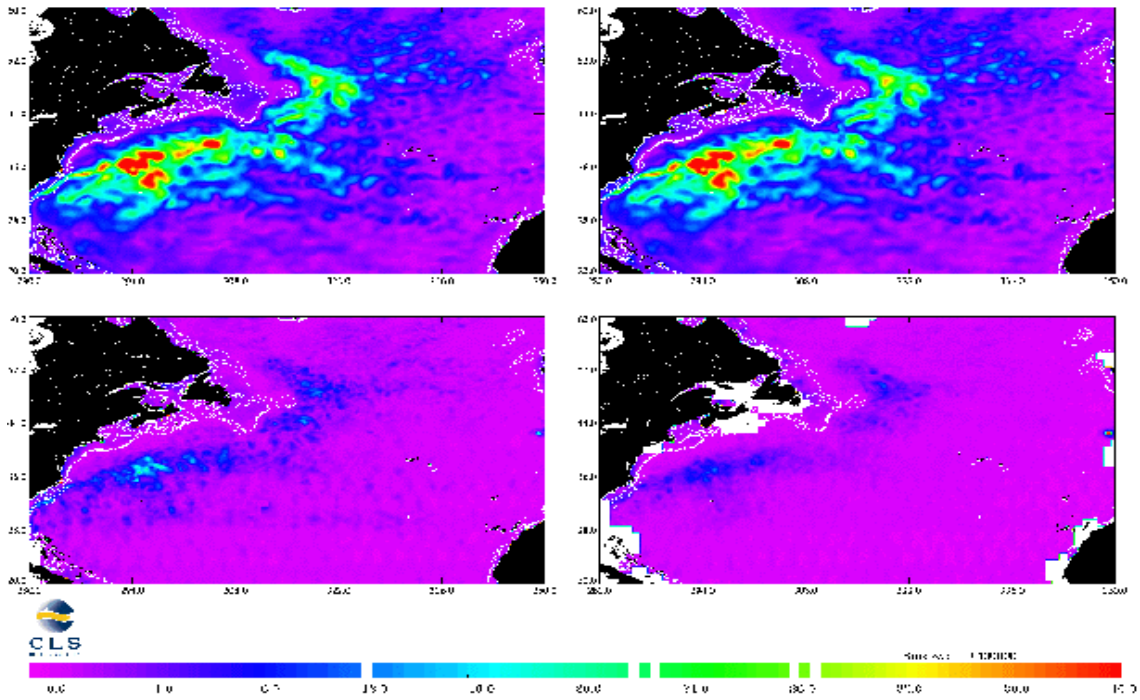

Figure 4b. Same as Figure 4a but for the WSOA simulation.

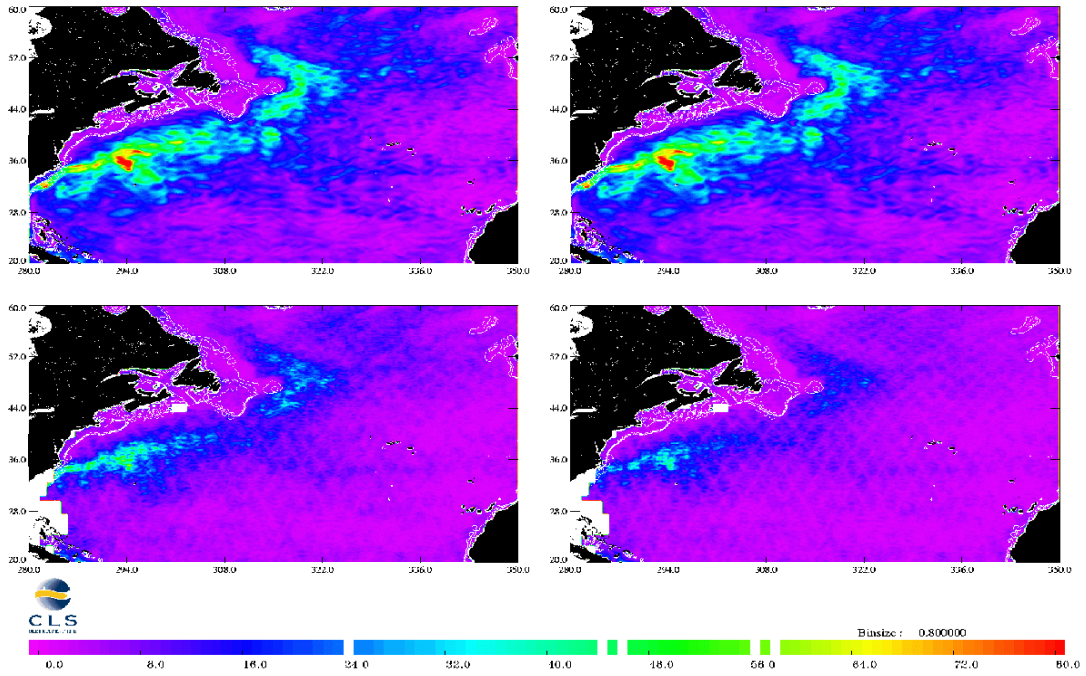

Figure 5a. Rms zonal velocity for the Los Alamos Model simulation (upper figure). Rms zonal velocity mapping error for T/P+ERS (lower figures). Left panel correspond to instantaneous signal mapping error. Right panel correspond to 10-day average signal mapping error. Units are cm/s.

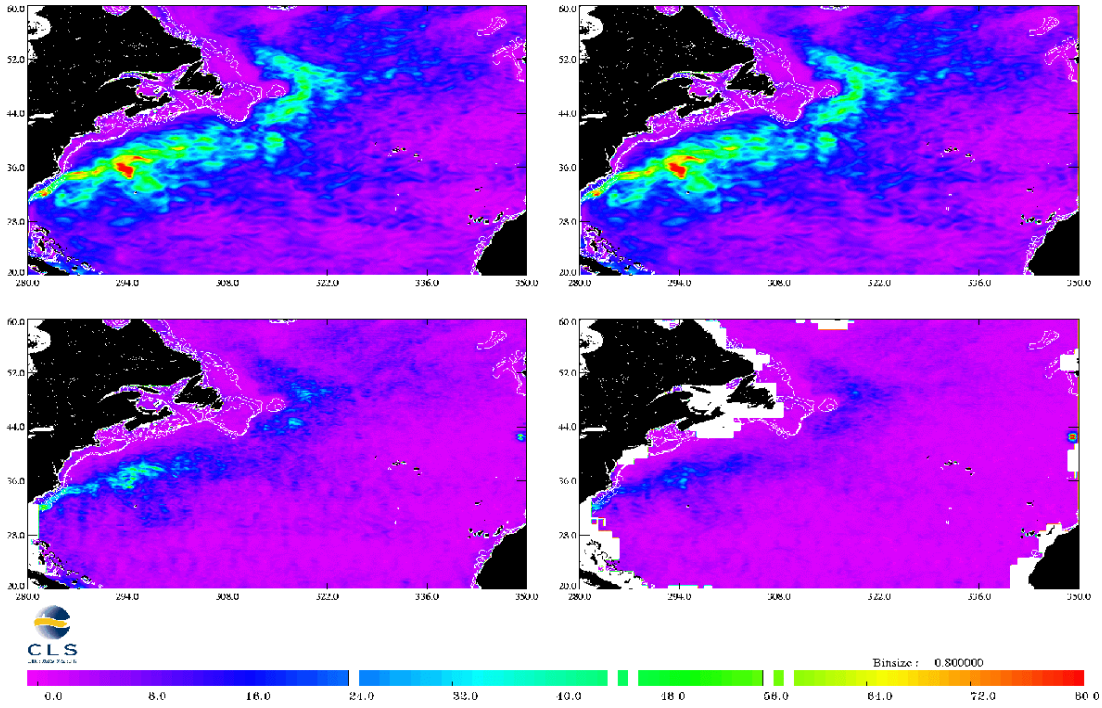

Figure 5b. Same as Figure 5a but for the WSOA simulation.

The Resolution Capability of Sea Surface Height Fields Constructed from a Tandem TOPEX/POSEIDON and JASON-1 Altimeter Mission

Dudley B. Chelton and Michael G. Schlax
College of Oceanic and Atmospheric Sciences
104 Oceanography Administration Building
Oregon State University
Corvallis, OR 97331-5503

1. Introduction

The ability to resolve the large-scale variability of the sea surface height (SSH) field constructed from altimeter measurements along the TOPEX/POSEIDON (T/P) ground tracks has been clearly demonstrated from many analyses of the 9-year T/P data record (see the review by Fu and Chelton, 2001). The coarse ground track spacing of the T/P sampling pattern is not able to resolve signals with spatial scales shorter than approximately 500 km, which renders the T/P data of limited utility for studies of mesoscale variability. The simultaneity of T/P and the altimeters onboard the ERS-1 and ERS-2 satellites offered a tantalizing possibility for obtaining higher resolution SSH fields but the lack of coordination of the T/P and ERS orbits (10-day repeat with 66° inclination for T/P and 35-day repeat with 98° inclination for ERS-1 and ERS-2) complicates the space-time structures of the mapping errors in SSH fields constructed from the combined datasets. The launch of the Jason-1 altimeter scheduled for December 2001 offers the first opportunity for a coordinated tandem satellite mission for high-quality altimeter measurements of SSH. After an initial 6-month calibration and validation phase, and assuming that T/P continues to function well, it will be possible to move T/P into a different 10-day exact-repeat orbit with the same 66° inclination to measure SSH along a ground track pattern that is offset longitudinally by any specified number of degrees and temporally by any number of days relative to the present T/P orbit. Here we consider the impact of two possible tandem orbit configurations on the resolution capability of SSH fields constructed from the tandem dataset.

The most intuitive tandem sampling pattern for mapping the SSH field is an interleaved orbit consisting of evenly spaced ground tracks with a longitudinal separation of 1.417°. Motivated by an interest in estimating geostrophic velocity, Stammer and Dieterich (1999) suggested an alternative orbit configuration for a tandem T/P-Jason mission. They noted that a tandem orbit with ground tracks offset by a relatively small longitudinal spacing would allow estimates of the SSH slope in two orthogonal directions, thus providing estimates of surface geostrophic velocity. From simulations based on the characteristics of T/P measurement errors, the optimal tandem T/P-Jason mission for geostrophic velocity estimation is one for which the ground tracks are offset by 0.5°-0.75° of longitude (Leeuwenburgh and Stammer, 2001; see also paper 13 of this report). Closer track spacing amplifies the effects of measurement errors on estimates of the along-track component of geostrophic velocity and wider track spacing increases sampling errors from unresolved spatial scales of mesoscale variability. The impact of a 0.5° offset tandem mission for mapping the SSH field is considered here along with the case of the evenly spaced interleaved tandem orbit configuration.

The resolution capability can be assessed from the mapping errors of SSH fields constructed from altimeter data with various spatial and temporal smoothing applied. The method for calculating mapping errors is summarized in section 2 along with the results obtained for a single altimeter in the T/P orbit and the two tandem T/P-Jason sampling patterns described above. In view of the fact that the European Space Agency will launch an altimeter in January 2002 onboard the ENVISAT satellite as a successor to the ERS-1 and ERS-2 satellites, we also investigate the mapping errors in SSH fields constructed from the tandem Jason-ENVISAT sampling pattern as a possible alternative for obtaining high-resolution SSH fields. While the sampling patterns of a tandem T/P-Jason mission with 0.5° offset and a tandem Jason-ENVISAT mission offer improvements in the spatial resolution capability compared with what can be obtained from a single altimeter in the T/P orbit configuration, the interleaved tandem T/P-Jason sampling

pattern with evenly spaced ground tracks offers significantly greater improvement, resulting in a doubling of the spatial resolution capability of SSH fields constructed from measurements by T/P or Jason-1 alone. The interleaved tandem T/P-Jason sampling pattern is therefore superior for high resolution mapping of the SSH field.

The benefits of the higher resolution of SSH fields obtainable from the evenly spaced sampling pattern of an interleaved T/P-Jason tandem mission are discussed in section 3 in the context of a specific example: investigation of the wavenumber-frequency dispersion characteristics of oceanic Rossby waves. This application is important to understanding ocean dynamics and, therefore, to understanding the role of the oceans in global climate variability. Rossby wave dispersion cannot be addressed adequately from the sampling pattern of a single altimeter in the T/P orbit configuration.

2. Sampling Errors in SSH Fields

2.1. Summary of the Technique

A technique for assessing the effects of sampling errors on SSH fields constructed from an irregularly sampled dataset was developed by Schlax and Chelton (1992) and has been applied to altimeter data by Chelton and Schlax (1994) and Greenslade et al. (1997). The technique has been modified by Schlax et al. (2001) to be more efficient computationally, thus allowing estimates of the sampling errors at a large number of estimation times and locations with a broad range of smoothing parameters. The method has recently been applied and further extended by Chelton and Schlax (2001) to investigate the effects of measurement errors, as well as sampling errors, on SSH fields constructed from single and tandem altimeter datasets.

A detailed description of the method is given by Chelton and Schlax (2001). Briefly, the quality of SSH fields constructed from the various altimeter datasets is assessed from the overall average root mean squared error (RMSE) and the 90% quantile range in a histogram of RMSE values calculated over a representative collection of estimation times and locations. For presentation purposes, we have assumed that SSH has a signal standard deviation of 10 cm with decorrelation length and time scales of 50 km and 30 days. The random instrumental measurement errors are assumed to have a standard deviation of 2 cm, which is a conservative approximation of the 1.7-cm T/P instrumental measurement errors. For T/P and Jason, we assume that the long-wavelength measurement and orbit errors have a standard deviation of 2 cm. ENVISAT is expected to have instrumental measurement errors comparable to those of T/P and Jason-1. However, because of its lower altitude orbit and the larger physical size of the satellite, the orbit errors for ENVISAT are expected to be larger than the T/P and Jason-1 orbit errors by about a factor of 2. For ENVISAT, we therefore assume a random instrumental measurement error with a standard deviation 2 cm and we consider the case of long-wavelength measurement and orbit errors with a standard deviation of 4 cm.

The overall mean RMSE is an obvious metric for assessing the resolution capability of SSH fields constructed from altimeter data. Because of the complicated space-time characteristics of satellite sampling patterns, the RMSE at a particular location typically varies considerably over the period of an exact-repeat orbit, especially for small spatial and temporal smoothing of the data. Likewise, the RMSE for a particular time typically varies considerably over the mapping area; examples are shown below. When these spatial and temporal inhomogeneities of the mapping errors are large, they can result in artifacts in the SSH fields that might easily be misinterpreted as real oceanographic features (see, for example, Figure 66 of Chelton et al., 2001). Since the RMSE can be calculated for any time and location in the mapping domain, it is possible to restrict analysis of smoothed and gridded SSH fields to the times and locations where the RMSE is deemed to be acceptably small. In practice, however, such selective analysis is seldom implemented. A preferred approach for most applications is to select the smoothing parameters so that the overall RMSE and the spatial and temporal inhomogeneities of the RMSE are reduced to acceptably small levels. For the 10-cm signal standard deviation assumed here, threshold

values of 2.5 cm and 1.0 cm for the average RMSE and 90% quantile range of RMSE are suggested in section 2.2. These values correspond, respectively, to 25% and 10% of the 10-cm signal standard devation. The conclusions about the relative mapping resolution capabilities of the various altimeter sampling patterns are not strongly sensitive to the precise values adopted for these threshold parameters.

2.2. A Single Altimeter in the T/P Orbit

As a benchmark for comparison with the tandem orbit configurations considered below, we first summarize the mapping errors in SSH fields constructed from a single altimeter in the T/P orbit. The mapping errors for a particular estimation time during the T/P 10-day repeat period are shown in Figure 1 for three selected combinations of zonal, meridional and temporal filter cutoffs. The error maps differ somewhat for different estimation times, especially for small smoothing parameters. The errors for the case of 3° by 10-day smoothing (left panel) are far in excess of 4 cm over most of the region. Increasing the temporal smoothing to 20 days (middle panel) reduces the errors to less than 3 cm near the crossover locations, but errors are still far in excess of 4 cm in the unsampled diamond centers. With the coarse 2.834° spacing of the T/P ground tracks, it is necessary to increase the spatial smoothing to at least 5° to reduce the mapping errors to less than 3 cm everywhere, as shown in the right panel of Figure 1.

It is also apparent from Figure 1 that there is a significant latitudinal variation of the mapping errors; for any particular choice of smoothing parameters, the errors decrease with increasing latitude owing to the greater sampling density at higher latitudes from the convergence of ground tracks.

To investigate the effects of smoothing on the accuracy of SSH fields in more detail, the root mean squared errors were computed for a wide range of spatial and temporal smoothing parameters at 40 representative locations and at daily intervals over the 10-day repeat period. Because of the general decrease of mapping errors with increasing latitude, the means and 90% quantile ranges of the T/P mapping errors are summarized in Figure 2 for three different latitude bands: a subpolar band from 35°N to 50°N (top panels), a subtropical band from 15°N to 35°N (middle panels) and a tropical band from the equator to 15°N (bottom panels). It is evident that the mean mapping errors decrease by about 25% from the tropical band to the subpolar band.

It is readily apparent from Figure 2 that the mapping errors for a single altimeter in the T/P orbit are far more sensitive to spatial smoothing than to temporal smoothing. Except for temporal smoothing shorter than about 20 days, the mean and 90% quantile range of mapping errors for a given degree of spatial smoothing depend only weakly on the degree of temporal smoothing. Increasing the temporal smoothing thus has little effect on the accuracy of SSH fields constructed from measurements by a single altimeter in the T/P orbit configuration. For high-resolution mapping of the SSH field, the coarse 2.834° longitudinal spacing of the T/P ground tracks is thus much more limiting than the 10-day orbit repeat period.

Greenslade et al. (1997) concluded that the SSH field can be adequately mapped from a single altimeter in the T/P orbit with a resolution at midlatitudes of approximately 6° in longitude and latitude by about 25 days. The need for such heavy spatial smoothing, which is analogous to filtering by constructing 3° block averages, is illustrated in Figure 66 of Chelton et al. (2001). It can be seen from Figure 1 that the corresponding mapping errors in the subtropical band are about 2.25 cm with a small 90% quantile range of about 0.3 cm.

For assessing the mapping resolution capability, we will adopt slightly more liberal, but still somewhat arbitrary, values of 2.5 cm and 1.0 cm as midlatitude thresholds of acceptable mean and 90% quantile values of RMSE. These thresholds correspond to 25% and 10% of the 10-cm signal standard deviation assumed for the analyses presented here. The general conclusions about the relative resolution capabilities of the various altimeter sampling patterns are not strongly sensitive to the precise values adopted here for these threshold parameters. With a 2.5 cm threshold for the mean RESB, Figure 2 indicates that the resolution capability of the T/P sampling pattern in the subtropical band is about 5.5° by

20 days. The 90% quantile range for this smoothing is about 0.4 cm, which falls well within the 1.0 cm criterion adopted here. The mean and 90% quantile range of mapping errors begin to increase rapidly if the temporal smoothing is reduced to less than 20 days or if the spatial smoothing is reduced to less than 5.5°.

For the threshold mean mapping accuracy of 2.5 cm, the filter cutoff wavelength of the spatial smoothing would have to be increased slightly to about 6° in the tropical band but could be decreased to 4.5° or less within the subpolar band, depending on the exact latitude within this band.

2.3. A Tandem T/P-Jason Sampling Pattern with Interleaved Orbits

The root mean squared errors for SSH fields constructed from two interleaved tandem T/P-Jason sampling patterns with evenly spaced ground tracks separated by 1.417° of longitude are shown in Figure 3 for three choices of smoothing parameters. The upper and lower panels show, respectively, the mapping errors for 0-day and 5-day offsets between neighboring ground tracks of T/P and Jason. The errors of SSH fields constructed from both of these interleaved tandem T/P-Jason orbits decrease by almost a factor of 2 compared with the mapping errors in Figure 1. For the case of the 3° by 10-day smoothing shown in the left panels of Figure 3, there are patches of errors in excess of 4 cm. These patches are larger in geographical extent for the 0-day offset than for the 5-day offset. The precise locations of the patches of large errors migrate around the map for different estimation times during the 10-day repeat cycle. When the temporal smoothing is increased to 20 days (see middle panels of Figure 3), the localized patches of large mapping errors are eliminated and the mapping errors become almost indistinguishable for these two evenly spaced, interleaved tandem sampling patterns.

Since it offers some improvement for small spatial and temporal smoothing, we will consider only the case of the 5-day offset interleaved sampling pattern. The means and 90% quantile ranges of the mapping errors are shown in Figure 4 as functions of spatial and temporal smoothing parameters. It is evident from comparisons of the left panels of Figures 2 and 4 that the mean mapping errors from the interleaved tandem orbit are about a factor of 2 smaller than for the case of SSH maps constructed from a single altimeter. For small spatial filtering, the 90% quantile ranges of the mapping errors (right panels of Figures 2 and 4) decrease by a factor of about 5 for the interleaved tandem sampling pattern.

For the mean error threshold of 2.5 cm adopted in section 2.2, the resolution capability of SSH fields constructed from the interleaved tandem orbit is about 2.8° by 20 days in the subtropical band. The corresponding 90% quantile range is about 0.5 cm, which is well within the threshold criterion of 1.0 cm. In agreement with the conclusions of Greenslade et al. (1997), the spatial resolution of 2.8° is about a factor-of-2 improvement over the 5.5° spatial resolution capability of SSH fields constructed from a single altimeter in the T/P orbit. For the error thresholds adopted here, the smoothing would have to be increased to about 3.3° in the tropical band but could be reduced to about 2.2° within the subpolar band. Alternatively, the temporal smoothing in the subpolar band could be reduced to about 10 days with 2.8° spatial smoothing.

2.4. A Tandem T/P-Jason Sampling Pattern with 0.5° Offset

The root mean squared errors for the tandem T/P-Jason sampling pattern with 0.5° offset between the parallel ground tracks suggested by Leeuwenburgh and Stammer (2001) are shown in Figure 5 for three choices of smoothing parameters. While this tandem sampling pattern yields SSH fields with mapping errors smaller than those in Figure 1, the improvement is only modest compared with that obtained for the evenly spaced, interleaved sampling patterns considered in Figure 3. The closer offset of 0.5° between the T/P and Jason ground tracks leaves large diamond shaped regions unsampled. For 3° by 10-day smoothing (left panel of Figure 5), there are many regions with mapping errors larger than 4 cm. Errors in excess of 4 cm still exist when the temporal smoothing is increased to 20 days (middle panel of Figure 5). When the smoothing is increased to 5° (right panel of Figure 5), the mapping errors for the

0.5° offset tandem orbit decrease to less than 2.5 cm everywhere, but this is nearly a factor-of-2 larger than the mapping errors from the evenly spaced, interleaved ground track pattern.

The means and 90% quantile ranges of the mapping errors for the 0.5° offset tandem T/P-Jason sampling pattern are shown in Figure 6 as functions of spatial and temporal smoothing parameters. The improvements of the mean mapping errors relative to those from a single altimeter are evident from comparisons of the left panels of Figure 6 with the left panels of Figure 2; the mean mapping errors are about 25% smaller for the 0.5° offset tandem orbit. Comparison of the right panels of the two figures, however, reveals that, for small spatial smoothing, the 90% quantile ranges of the mapping errors are reduced only slightly for the 0.5° offset tandem orbit. The large spatial inhomogeneities of the mapping errors are readily apparent in all three panels of Figure 5.

For the mean error threshold of 2.5 cm adopted previously, the resolution capability of SSH fields constructed from the 0.5° offset tandem orbit is about 4.2° by 20 days in the subtropical band. The corresponding 90% quantile range is about 0.3 cm, which is well within the threshold criterion of 1.0 cm. The smoothing could be reduced to about 3.7° within the subpolar band but would have to be increased to about 4.6° in the subpolar band.

2.5. A Tandem Jason-ENVISAT Sampling Pattern

The European Space Agency is scheduled to launch the ENVISAT satellite in January 2002 as a successor to the ERS-1 and ERS-2 satellites. ENVISAT will be placed into the same orbit as the ERS satellites, with 98° inclination and 35-day exact repeat. Since ENVISAT will operate simultaneously with Jason-1, it is useful to explore the possibility of obtaining high-resolution SSH fields from this tandem altimeter dataset. This is complicated by the lack of coordination of the two orbit configurations (the different repeat periods and different orbit inclinations) and the fact that the orbit errors are expected to be a factor of 2 larger for ENVISAT than for Jason.

The root mean squared errors for the tandem Jason-ENVISAT sampling pattern are shown in Figure 7 for three choices of smoothing parameters for the case of ENVISAT and Jason orbit errors with standard deviations of 4 cm and 2 cm, respectively. For 3° by 10-day smoothing (left panel), the patches of large root mean squared errors are larger in magnitude and more extensive geographically than for the case of the interleaved, evenly spaced tandem T/P-Jason sampling pattern with 5-day offset (bottom left panel of Figure 3). These patches of large mapping errors migrate geographically for different estimation times in response to the complicated space-time sampling of the 35-day ENVISAT and 10-day Jason ground track patterns. When the smoothing is increased to 3° by 20 days, the Jason-ENVISAT mapping errors are reduced considerably (middle panel of Figure 7), but are still inhomogeneous, ranging from a low of about 1.5 cm to a high of about 3.5 cm. In comparison, the T/P-Jason mapping errors for 3° by 20-day smoothing are very nearly homogeneous with a value of about 2.25 cm in the subtropical band (bottom middle panel of Figure 3). Increasing the spatial smoothing to 5° (right panel of Figure 7) reduces the Jason-ENVISAT mapping errors to less than 2.5 cm everywhere.

The averages and 90% quantile ranges of the root mean squared errors for a tandem Jason-ENVISAT sampling pattern with ENVISAT and Jason orbit errors of 4 cm and 2 cm, respectively, are shown in Figure 8 as functions of spatial and temporal smoothing parameters. The structures of these RMSE plots are notably different from the RMSE plots considered previously for the single and tandem T/P and Jason sampling patterns. For a given degree of spatial smoothing, increasing the temporal smoothing is much more effective at reducing the mapping errors with the tandem Jason-ENVISAT data. This is because the close spacing of the ENVISAT ground tracks reduces the spatial resolution limitation that is inherent in the T/P and Jason sampling patterns, thus elevating the relative importance of the temporal resolution limitation of the long 35-day orbit repeat period.

In comparison with the results for the interleaved tandem T/P-Jason sampling pattern with evenly spaced ground tracks (Figure 4), another major difference in Figure 8 is the much larger 90% quantile

ranges for the tandem Jason-ENVISAT sampling pattern. This is a quantitative measure of the much greater inhomogeneity of RMSE noted previously from the example error maps in Figure 7; for small smoothing, the 90% quantile ranges are about a factor-of-2 larger for Jason-ENVISAT for the case of 4-cm ENVISAT orbit errors considered in Figure 8. The migration of the inhomogeneous mapping errors in space and time that is responsible for these larger 90% quantile ranges would contaminate wavenumber-frequency spectra of SSH variability in a very complicated manner. The energy level of these artifacts in SSH fields constructed from a tandem Jason-ENVISAT sampling pattern might obscure the spectral characteristics of SSH signals that are of interest (e.g., the Rossby wave dispersion application discussed below in section 3).

By the threshold mean error criterion of 2.5 cm, it is evident from Figure 8 that the resolution capability of the tandem Jason-ENVISAT sampling pattern for ENVISAT orbit errors of 4 cm is about 3.2° by 20 days in the subtropical latitude band. The corresponding 90% quantile range is about 0.8 cm, which is within the tolerance criterion of 1.0 cm but is about a factor of two larger than the 90% quantile ranges for the T/P and T/P-Jason sampling patterns considered above. This reflects the much greater spatial and temporal inhomogeneity of mapping errors in SSH fields constructed with the tandem Jason-ENVISAT sampling pattern. While a spatial resolution of 3.2° would be a significant improvement over the 4.2° by 20-day resolution capability of a tandem T/P-Jason sampling pattern with 0.5° offset, it falls short of the 2.8° by 20-day resolution capability of the evenly spaced, interleaved tandem T/P-Jason sampling pattern. The spatial resolution capability of the tandem Jason-ENVISAT sampling pattern improves to about 2.7° in the subpolar band and degrades to about 3.6° in the tropical band.

2.6. A Triplet T/P-Jason-ENVISAT Sampling Pattern

Continued operation of T/P after the launch of ENVISAT and the 6-month calibration and validation phase of Jason-1 would offer the opportunity for high-resolution mapping of SSH fields from the triplet T/P-Jason-ENVISAT sampling pattern. We consider here the case of ENVISAT in combination with the evenly spaced, interleaved tandem T/P-Jason sampling pattern.

The root mean squared errors for the triplet T/P-Jason-ENVISAT sampling pattern are shown in Figure 9 for three choices of smoothing parameters for the case of ENVISAT orbit errors with a standard deviation of 4 cm and T/P and Jason orbit errors with standard deviations of 2 cm. For 3° by 10-day smoothing (left panel), the mapping errors are somewhat smaller than those of the tandem T/P-Jason sampling pattern with interleaved, evenly spaced ground tracks and a 5-day offset between T/P and Jason (lower left panel of Figure 3). When the smoothing is increased to 3° by 20 days (middle panel of Figure 9), the average mapping error is somewhat smaller than that for the tandem T/P-Jason sampling pattern with the same smoothing applied. However, the mapping errors are much more inhomogeneous for the triplet sampling pattern, which could be problematic for some applications. These inhomogeneities are still evident when the smoothing is increased to 5° by 20 days (right panel of Figure 9).

The averages and 90% quantile ranges of the root mean squared errors for a triplet T/P-Jason-ENVISAT sampling pattern are shown in Figure 10 as functions of spatial and temporal smoothing parameters. As in Figure 8, the we have assumed that the ENVISAT orbit errors have a standard deviation of 4 cm and that the T/P and Jason orbit errors have standard deviations of 2 cm. While there is a reduction of the mean mapping error compared with the case of the tandem T/P-Jason sampling pattern with evenly spaced ground tracks shown in Figure 4, the improvement in resolution capability is less than 10%. Moreover, the 90% quantile range of the RMSE is much larger for the triplet sampling pattern than for the coordinated tandem T/P-Jason sampling pattern. This reflects the mismatch between the orbit configuration of ENIVSAT and the coordinated orbit configurations of T/P and Jason noted in section 2.5.

By the threshold mean error criterion adopted previously, the resolution capability of the triplet T/P-Jason-ENVISAT sampling pattern is about 2.5° by 20 days. However, it is apparent from Figure 10 that this degree of spatial smoothing does not satisfy the threshold criterion of 1.0 cm for RMSE

variability; for 2.5° by 20-day smoothing, the 90% quantile range of RMSE is about 1.5 cm for the triplet sampling pattern. The resolution capability of the T/P-Jason-ENVISAT sampling pattern thus depends critically on the precise value adopted for the tolerance for RMSE variability. For the value of 1.0 cm suggested previously, the resolution capability of the triplet sampling pattern is degraded to about 3°, which is worse than the 2.7° resolution of the tandem T/P-Jason sampling pattern and only slightly better than the tandem Jason-ENVISAT sampling pattern. Depending on the application, the inhomogeneity of the RMSE from the triplet sampling pattern may be problematic.

Regardless of the precise value adopted for the RMSE variability criterion, it is clear that the resolution capability of the triplet T/P-Jason-ENVISAT sampling pattern falls considerably short of the resolution that would be possible from a triplet sampling pattern with coordinated orbit configurations. For example, the resolution capability of SSH fields constructed from a triplet altimeter sampling pattern with the T/P 10-day exact-repeat orbit and evenly spaced ground tracks can be anticipated to be about 2° by 20 days.

2.7. Summary

For each of the altimeter sampling patterns considered here, the temporal smoothing required to map low-pass filtered SSH in the subtropical band with an uncertainty that has an average value of less than 2.5 cm is about 20 days. The spatial resolutions differ considerably for the various sampling patterns; SSH can be mapped with spatial resolutions of 5.5°, 2.8°, 4.2°, 3.2° and 2.5° for sampling patterns consisting, respectively, of a single altimeter in the T/P orbit, an evenly spaced interleaved tandem T/P-Jason sampling pattern, a 0.5° offset tandem T/P-Jason sampling pattern, a tandem Jason-ENVISAT sampling pattern, and a triplet T/P-Jason-ENVISAT sampling pattern. The latter two assume ENVISAT orbit errors with a standard deviation of 4 cm. Moreover, the 2.5° resolution capability of the triplet sampling pattern requires a very liberal RMSE variability criterion of 1.5 cm for the 90% quantile range of RMSE. For the 1.0 cm value that we feel is more appropriate for this criterion, the resolution capability of the triplet sampling pattern is degraded to about 3°. For all of these sampling patterns, the resolution capabilities are somewhat worse in the subtropical latitude band but improve somewhat in the subpolar band.

The values of 2.5 cm and 1.0 cm adopted here as threshold values of the average and 90% quantile range of root mean squared errors to assess the SSH mapping resolution capability of the various altimeter sampling patterns are obviously somewhat arbitrary. They are based on our subjective judgment of the amount of smoothing required to obtain usefully accurate SSH fields from T/P data. The key point, however, is that we have used a consistent set of criteria in evaluating the mapping resolution capabilities of all of the altimeter sampling patterns considered here. If different threshold values for the average and 90% quantile ranges were adopted, the conclusions about the precise values of the spatial and temporal resolution capability would differ somewhat. However, the relative accuracies of the various sampling patterns would not likely differ much from the values presented here. An interleaved tandem T/P-Jason sampling pattern with evenly spaced ground tracks would thus offer about a factor-of-2 improvement in the resolution capability of SSH fields relative to what can be obtained from a single altimeter in the T/P orbit configuration. Depending on the tolerance for inhomogeneity of the mapping errors, a triplet T/P-Jason-ENVISAT sampling pattern may offer a small additional improvement but the resulting resolution capability falls short of the factor-of-3 improvement that is expected from a triplet of altimeters in coordinated 10-day exact-repeat orbit configurations.

3. Rossby Wave Dispersion Characteristics

Of the three tandem altimeter sampling patterns considered in section 2, it has been shown that an interleaved tandem T/P-Jason sampling pattern with evenly spaced ground tracks would yield the greatest improvement of the resolution capability for mapping the SSH field. This attribute of the interleaved sampling pattern would have a beneficial impact on a wide range of scientific applications of altimeter data. One example is presented here.

Analysis of the longitude-time structure of SSH variability from the first 3 years of T/P data by Chelton and Schlax (1996) showed that westward propagation is nearly ubiquitous over the world ocean. A more recent global synthesis of westward propagating SSH signals from 7 years of T/P data confirms the results of the earlier analysis (Fu and Chelton, 2001). The propagation speeds decrease with increasing latitude in a manner that is qualitatively but not quantitatively consistent with the classical theory for oceanic Rossby waves. Westward phase speeds estimated from the T/P data are systematically higher than the phase speeds predicted from the classical theory. The discrepancies between the observations and the classical theory generally increase with increasing latitude, differing by more than a factor of two at 40° latitude (see Figure 5 of Chelton and Schlax, 1996, and Figure 14 of Fu and Chelton, 2001).

The apparent insufficiency of the classical theory has stimulated a great deal of interest in Rossby wave dynamics. Since Rossby waves are the mechanism by which the open ocean adjusts to wind stress, heat flux and eastern boundary forcing, it is important to understand the reason for the discrepancies between the observed and predicted westward phase speeds of oceanic Rossby waves. Ocean general circulation models that are currently under development for climate studies cannot be considered useful unless they accurately represent the observed Rossby wave speeds, thus correctly modeling the transient adjustment time of the ocean. An overview of theoretical attempts to account for the apparent Rossby wave speedup is given in section 3.4.5 of Fu and Chelton (2001). The most promising explanation to date appears to be that proposed by Killworth et al. (1997), who suggested that the speedup occurs because of the modification of free Rossby wave modes by vertically sheared mean currents.

The empirical and theoretical studies of Rossby wave propagation that have been conducted thus far have focused almost entirely on the long-wavelength, low frequency nondispersive regime. The adequacies or inadequacies of the various theories that have been proposed to explain the fast observed westward phase speeds are likely to become most apparent when the focus shifts to the full wavenumber-frequency spectral characteristics of the westward propagation. Spatial resolution is the most important limiting factor for wavenumber-frequency spectral analysis of SSH data from a single altimeter in the T/P orbit. The results of section 2.2 indicate that the resolution capability of SSH fields constructed from a single altimeter in the T/P orbit is about 5.5° in longitude and latitude by 20 days at middle and low latitudes; the spatial resolution capability improves slightly to about 4.5° in the subpolar latitudes.

Examples of wavenumber-frequency spectra of SSH computed along 24° latitude in each of the ocean basins from 6° by 60-day smoothed SSH fields are shown in Figure 11. The 6° spatial smoothing was adopted here as a slightly conservative approximation of the subtropical 5.5° resolution limitation deduced in section 2.2. The 60-day filter cutoff was chosen to eliminate any possibility of contamination of the SSH fields by tidal errors; the most energetic tidal signals all alias into periods shorter than about 60 days (Chelton et al., 2001). A 60-day period corresponds to a frequency of 0.016 cycles/day, which is higher than the maximum frequency displayed the figures. The solid vertical white line in each panel corresponds to the 6° zonal filter cutoff of the loess-smoothed SSH fields. The apparent decrease of the energy of SSH variability at larger negative zonal wavenumbers is due to attenuation of these short scales by the 6° zonal smoothing.

Over the range of wavenumbers that is resolved in SSH fields constructed from T/P data, the wavenumber-frequency spectral characteristics along 24° latitude exhibit a remarkable quality: the bands of energetic SSH variability fall very nearly along straight lines in wavenumber-frequency space. This indicates that the westward propagation of SSH signals is essentially nondispersive over the full range of wavenumbers resolved by the T/P sampling pattern. For comparison, the dispersion relations from the classical theory and the Killworth et al. (1997) shear-modified theory are shown in Figure 11 by the open and solid circles, respectively. It is clear from these plots that the wavenumbers and frequencies of energetic SSH variability are in much closer agreement with the Killworth et al. (1997) theory than with the classical theory. It is also apparent that a comprehensive test of the Killworth et al. (1997) theory will require knowledge of the spectral characteristics of SSH variability at larger negative wavenumbers; the

Killworth et al. (1997) theory becomes dispersive for the wavelengths shorter than the 6° of longitude that cannot be resolved in SSH fields constructed from the T/P sampling pattern. Moreover, the dispersion relations for the Killworth et al. (1997) theory and the classical theory become progressively more distinctive at these shorter wavelengths.

Assessment of the Killworth et al. (1997) theory, as well as of the other theories that have been proposed to explain the observed Rossby wave phase speeds, thus requires SSH fields with zonal spatial resolution higher than can presently be resolved from T/P data alone. The results of section 2.3 indicate that an interleaved tandem T/P-Jason mission with evenly spaced ground tracks would allow mapping of the SSH field with a zonal resolution of about 3° at middle and low latitudes. This would extend the wavenumber range of the spectra of SSH variability to the white vertical dashed lines in Figure 11. The extended range of the wavenumber-frequency spectral estimates would enable a quantitative test of the adequacy of the various theories for fast Rossby waves. If the Killworth et al. (1997) theory shown by the solid circles in Figure 11 is the mechanism for Rossby wave speedup, then the band of wavenumbers and frequencies of the most energetic SSH variability should flatten for zonal wavelengths shorter than the 6° limitation of SSH fields constructed from T/P data. This corresponds to zonal wavenumbers with negative values larger in magnitude than the filter cutoff wavenumber indicated by the vertical solid white lines in Figure 11.

4. Conclusions

The spatial and temporal resolution capabilities of SSH fields constructed from two potential tandem T/P-Jason orbit configurations have been quantified here by the mapping error estimates summarized in sections 2.3 and 2.4. While the 0.5° offset of the T/P and Jason ground tracks in the tandem mission suggested by Leeuwenburgh and Stammer (2001) would offer improvement over the resolution capability of SSH fields constructed from a single altimeter in the T/P orbit (an increase in midlatitude resolution from 5.5° to 4.2° of longitude and latitude), the improvement falls far short of the 2.8° resolution capability of an interleaved tandem orbit configuration with evenly spaced ground tracks. All other considerations aside, the interleaved tandem mission is far superior for global mapping of the SSH field.

The resolution capability of SSH fields constructed from the tandem Jason-ENVISAT sampling pattern has also been assessed in section 2.5. Because of the lack of coordination of the orbit configurations (66° inclination with 10-day exact repeat for Jason and 98° inclination with 35-day exact repeat for ENVISAT) and because of a factor-of-2 larger orbit errors for ENVISAT, the mapping resolution capability of the tandem dataset falls short of the 2.8° resolution obtainable from the tandem T/P-Jason sampling pattern with evenly spaced interleaved ground tracks. For ENVISAT orbit errors with a standard deviation of 4 cm, the resolution capability of the tandem Jason-ENVISAT sampling pattern would be about 3.2° in longitude and latitude.

After the launch of ENVISAT in January 2002, simultaneous operation with T/P and Jason-1 would yield an even higher SSH mapping resolution capability of about 2.5° by 20 days, assuming a liberal allowance of 1.5 cm for the 90% quantile range of RMSE variability. While this is an improvement over the 2.8° resolution capability of the tandem T/P-Jason sampling pattern, it falls short of the approximate 2° resolution capability that would be expected from a triplet altimeter sampling pattern from three altimeters in the 10-day T/P orbit repeat period with interleaved, evenly spaced ground tracks.

The scientific value of an interleaved tandem T/P-Jason sampling pattern was discussed in section 3 by summarizing a specific application that would benefit greatly from the doubling of the spatial resolution of the SSH field. The higher spatial resolution would allow wavenumber-frequency spectral analysis of the SSH fields at high wavenumbers where competing theories for Rossby wave dispersion differ most significantly. Since Rossby waves are the means by which the large-scale ocean circulation adjusts to atmospheric and eastern boundary forcing, a theoretical understanding of Rossby wave

dynamics is important to understanding ocean climate variability on time scales of the order of a month and longer.

References

Chelton, D.B., and M.G. Schlax, 1994: The resolution capability of an irregularly sampled dataset: with application to GEOSAT altimeter data. *J. Atmos. Ocean. Technol*., **11**, 534-550.

Chelton, D.B., and M.G. Schlax, 1996: Global observations of oceanic Rossby Waves. *Science*, **272**, 234-238.

Chelton, D.B., and M.G. Schlax, 2001: On the estimation of sea surface height and surface geostrophic velocity from a tandem TOPEX/POSEIDON and Jason-1 altimeter mission. *J. Geophys. Res*., submitted.

Chelton, D.B., J.C. Ries, B.J. Haines, L.-L. Fu and P.S. Callahan, 2001: Satellite altimetry. In *Satellite Altimetry and the Earth Sciences: A Handbook for Techniques and Applications*, L.-L. Fu and A. Cazenave, Eds., Academic Press, pp. 1-131.

Fu, L.-L., and D.B. Chelton, 2001: Large-scale ocean circulation. In Satellite *Altimetry and the Earth Sciences: A Handbook for Techniques and Applications*, L.-L. Fu and A. Cazenave, Eds., Academic Press, pp. 133-169.

Greenslade, D.J.M., D.B. Chelton and M.G. Schlax, 1997: The midlatitude resolution capability of sea level fields constructed from single and multiple satellite altimeter datasets. *J. Atmos. Ocean. Technol*., **14**, 849-870.

Killworth, P.D., D.B. Chelton and R.A. de Szoeke, 1997: The speed of observed and theoretical long extra-tropical planetary waves. *J. Phys. Oceanogr*., **27**, 1946-1966.

Leeuwenburgh, O., and D. Stammer, 2001: Uncertainties in altimetry-based velocity estimates. *J. Geophys. Res*., submitted.

Schlax, M.G., and D.B. Chelton, 1992: Frequency domain diagnostics for linear smoothers. *J. Amer. Stat. Assoc*., **87**, 1070-1081.

Schlax, M.G., D.B. Chelton and M.H. Freilich, 2001: Sampling errors in wind fields constructed from single and tandem scatterometer datasets. *J. Atmos. Ocean. Technol*., **18**, 1014-1036.

Stammer, D., and C. Dieterich, 1999: Space-borne measurements of the time-dependent geostrophic ocean flow field. *J. Atmos. Ocean. Technol*., **16**, 1198-1207.

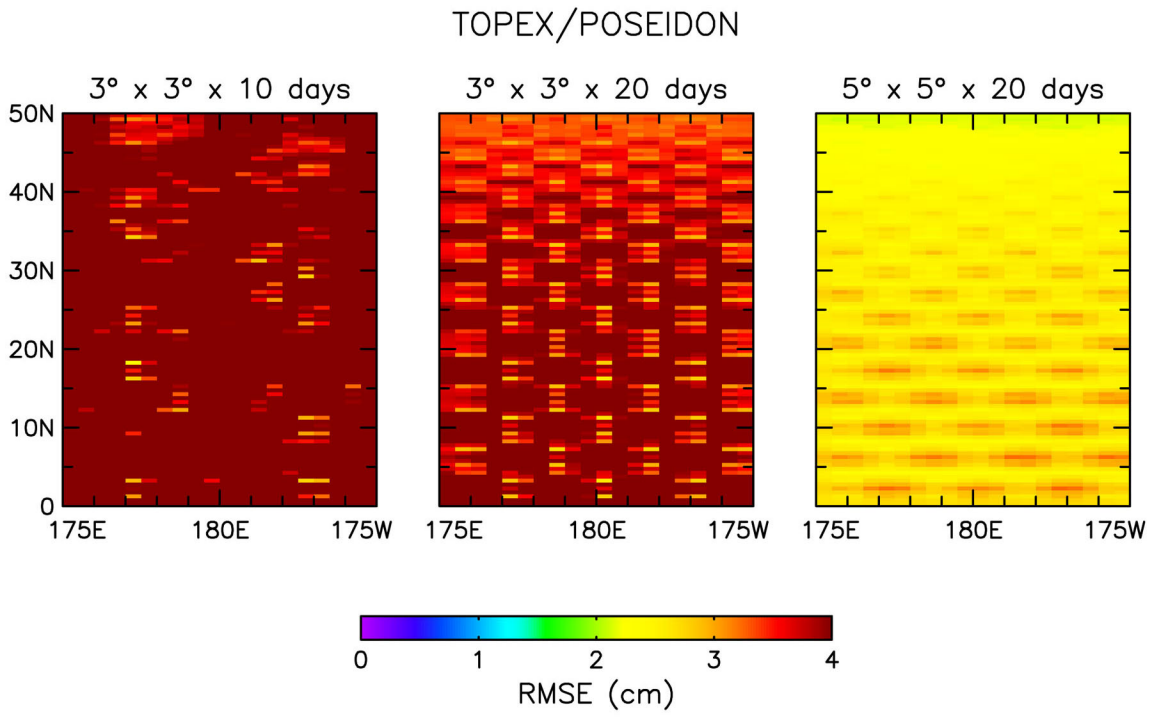

Figure 1. Mapping errors for a single altimeter in the T/P orbit for the zonal, meridional and temporal filter cutoff wavelengths and periods indicated at the top of each panel. The simulations are based on Gaussian autocorrelation functions with e-folding spatial and temporal scales of 50 km and 30 days and an SSH signal variance of 10 cm.

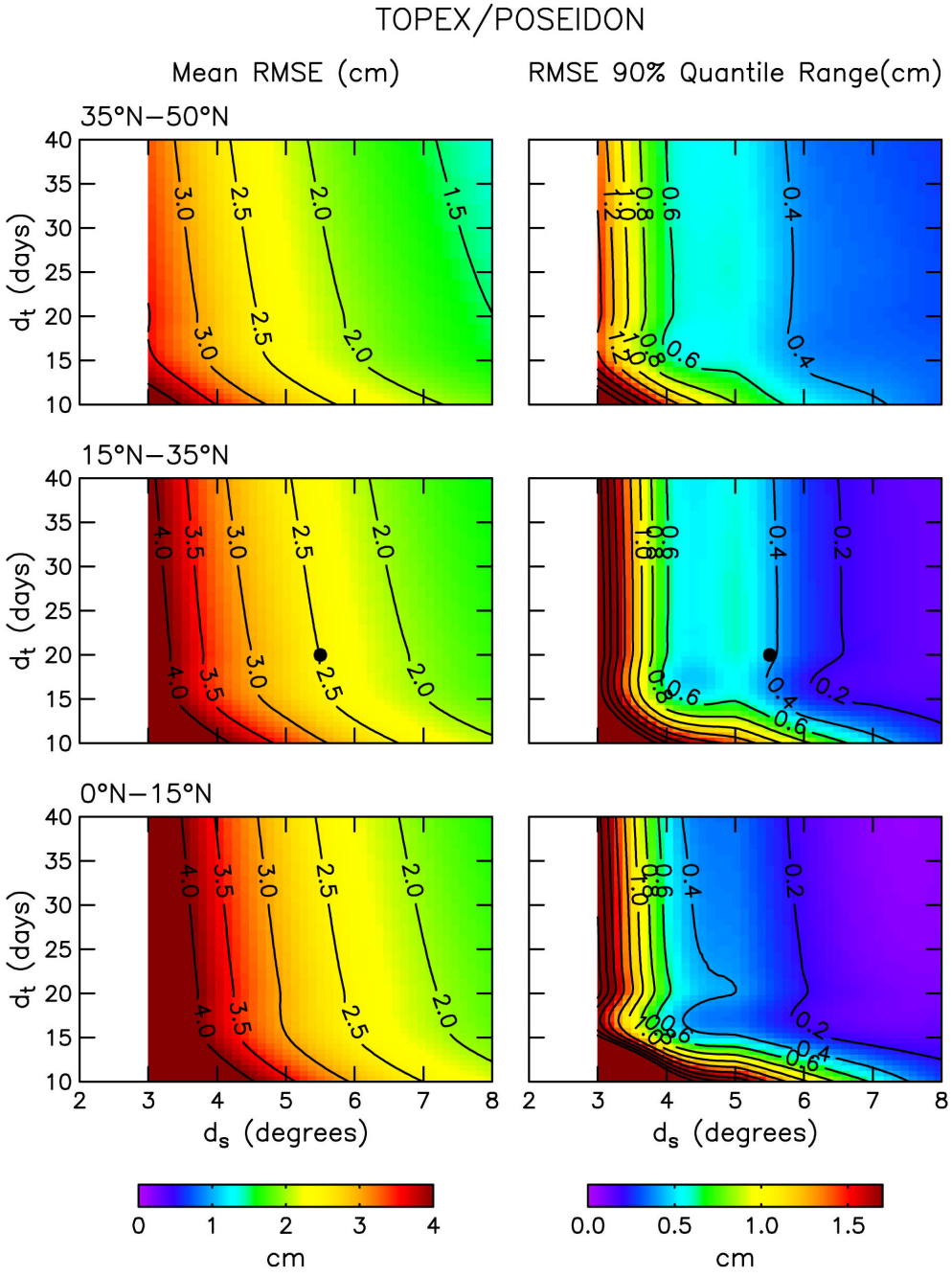

Figure 2. The averages (left panels) and 90% quantile ranges (right panels) of a histogram of the root mean squared errors for a single altimeter in the T/P orbit for SSH fields constructed with smoothing parameters that correspond to spatial filter cutoff wavelengths d_s ranging from 2° to 8° and temporal filter cutoff periods d_t ranging from 10 to 40 days. The mapping errors are not shown for d_s less than 3° because the coarse 2.834° ground track spacing of the T/P sampling pattern is unable to resolve such short scales. For clarity, the maximum contour displayed in the plots of 90% quantile range is 2 cm. Results are shown for three latitude bands: a subpolar band from 35°N to 50°N, a subtropical band from 15°N to 35°N and a tropical band from the equator to 15°N. The dots in the middle panels indicate the resolution capability in the subtropical band according to the criteria discussed in the text.

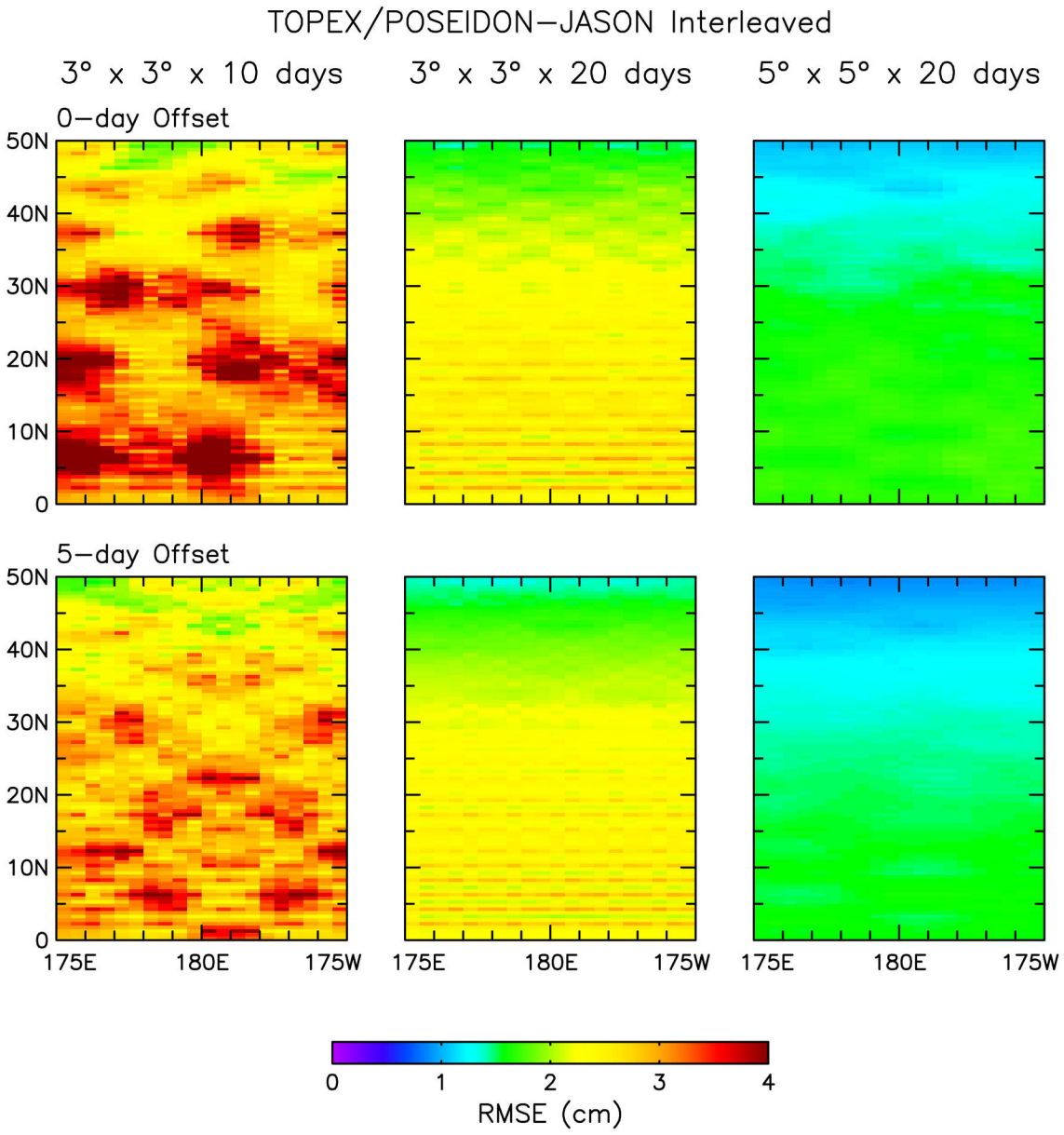

Figure 3. The same as Figure 1, except for SSH fields constructed from measurements from a tandem T/P-Jason sampling pattern with interleaved, evenly spaced ground tracks. The upper and lower panels correspond, respectively, to 0-day and 5-day offsets between neighboring T/P and Jason ground tracks.

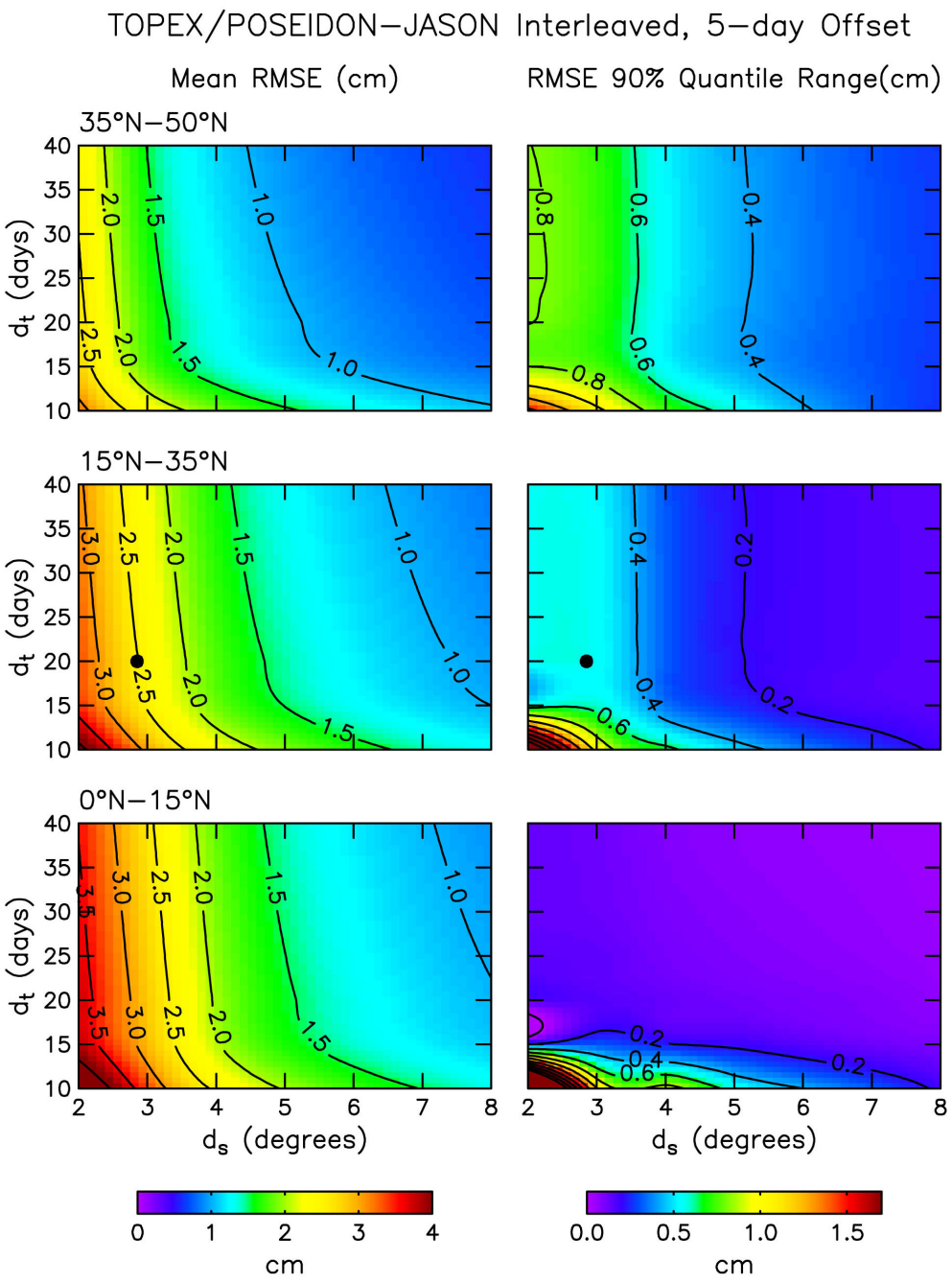

Figure 4. The same as Figure 2, except for SSH fields constructed from measurements from a tandem T/P-Jason sampling pattern with evenly spaced, interleaved ground tracks.

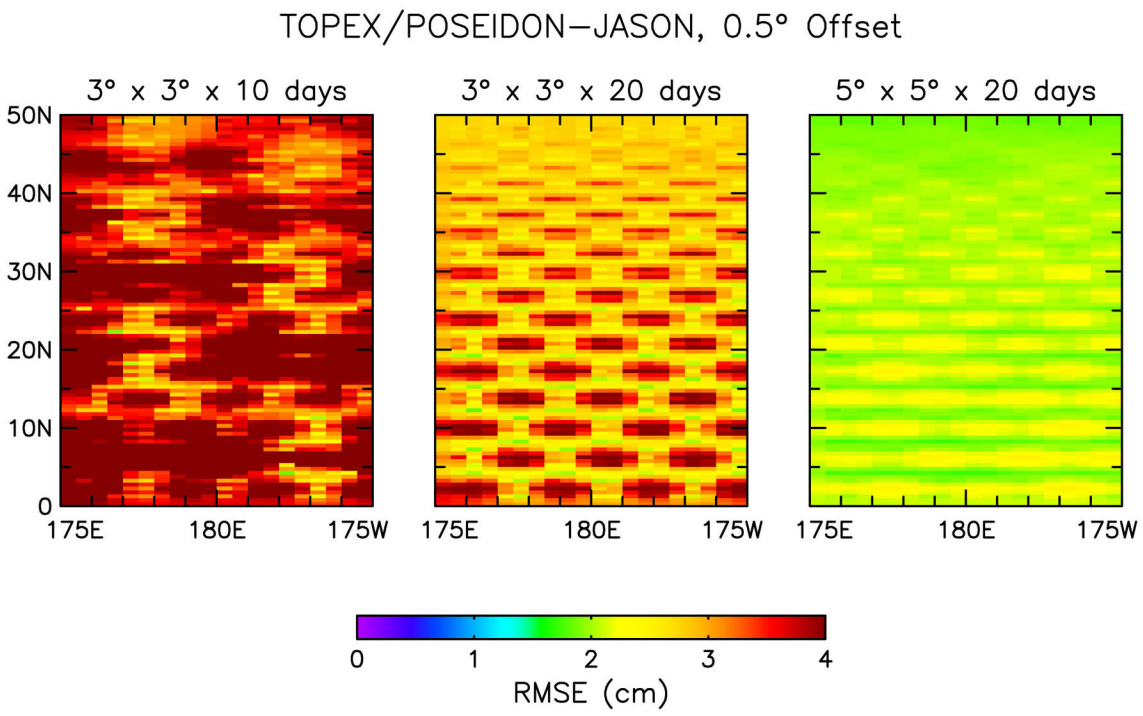

Figure 5. The same as Figures 1 and 3, except for SSH fields constructed from measurements from a tandem T/P-Jason sampling pattern with 0.5° offset between the parallel T/P and Jason ground tracks.

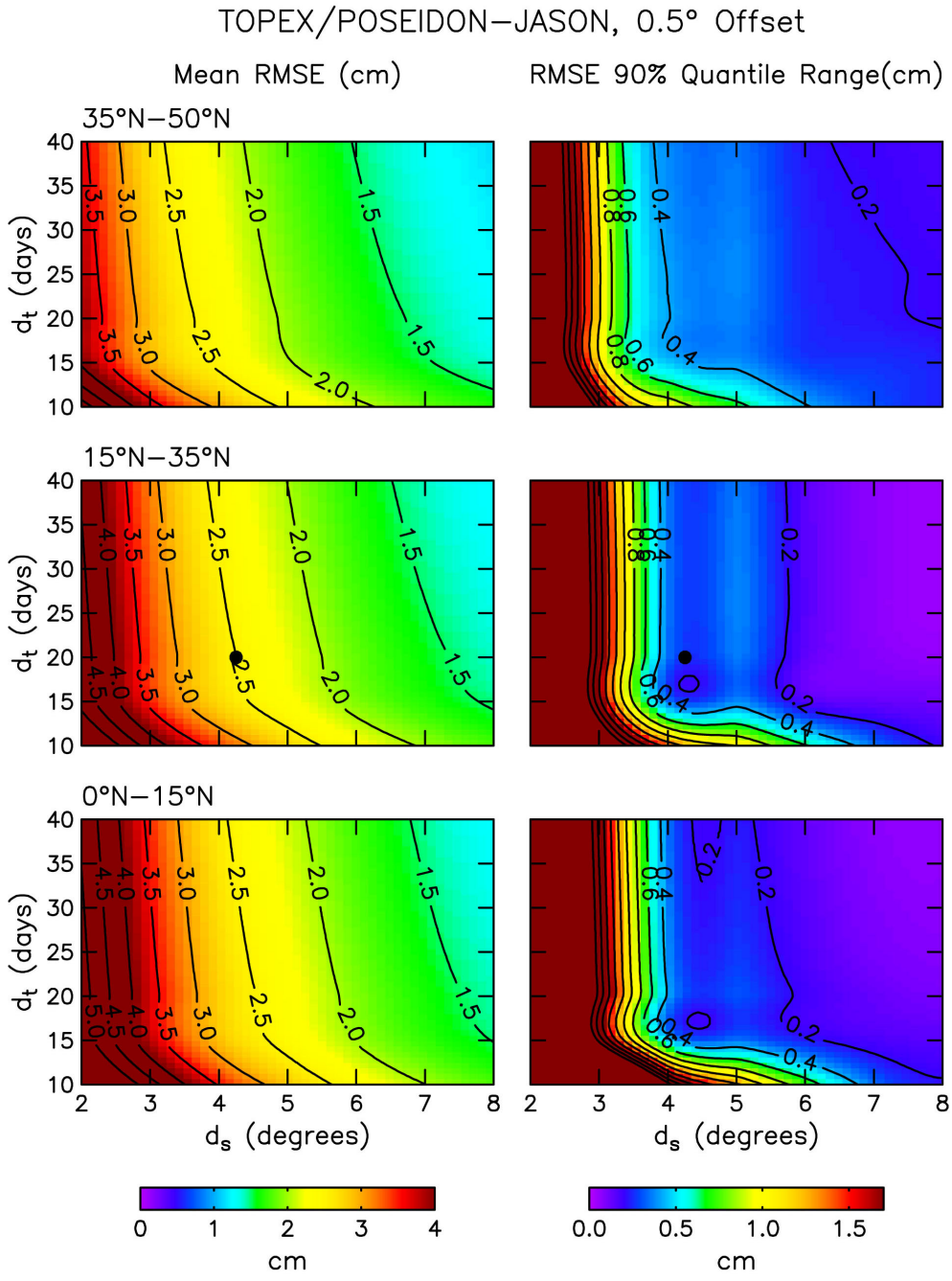

Figure 6. The same as Figures 2 and 4, except for SSH fields constructed from measurements from a tandem T/P-Jason sampling pattern with 0.5° offset between the parallel ground tracks.

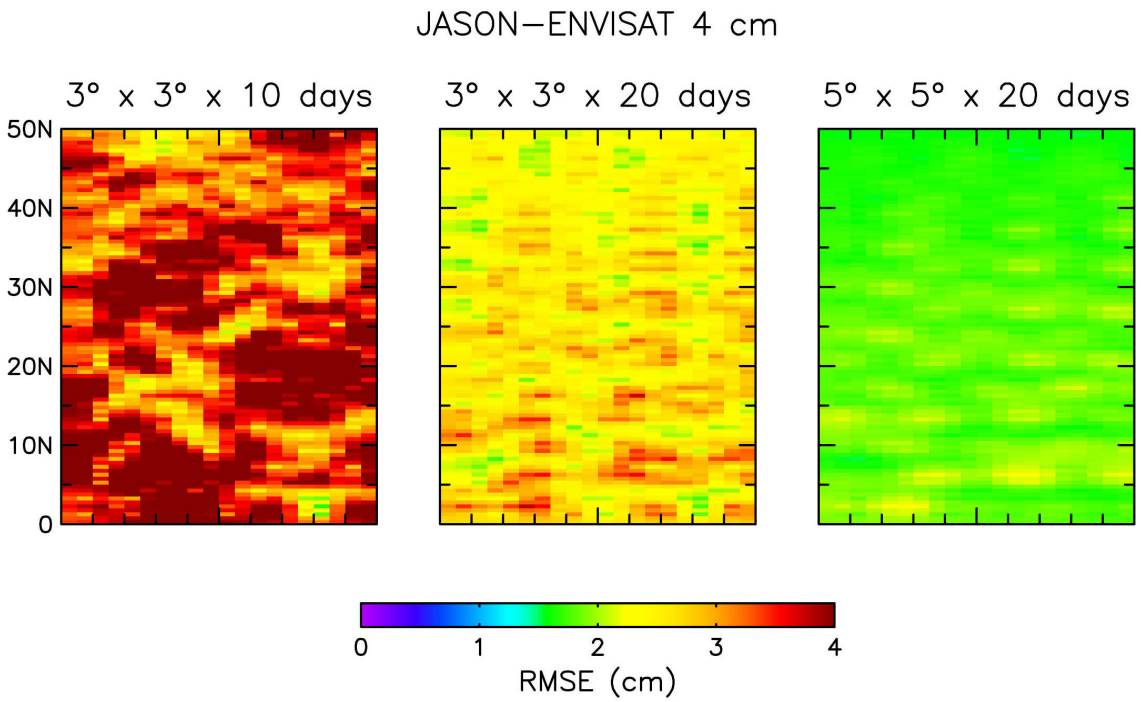

Figure 7. The same as Figures 1, 3 and 5, except for SSH fields constructed from measurements from a tandem Jason-ENVISAT sampling pattern. The ENVISAT and Jason orbit errors are assumed to have standard deviations of 4 cm and 2 cm, respectively.

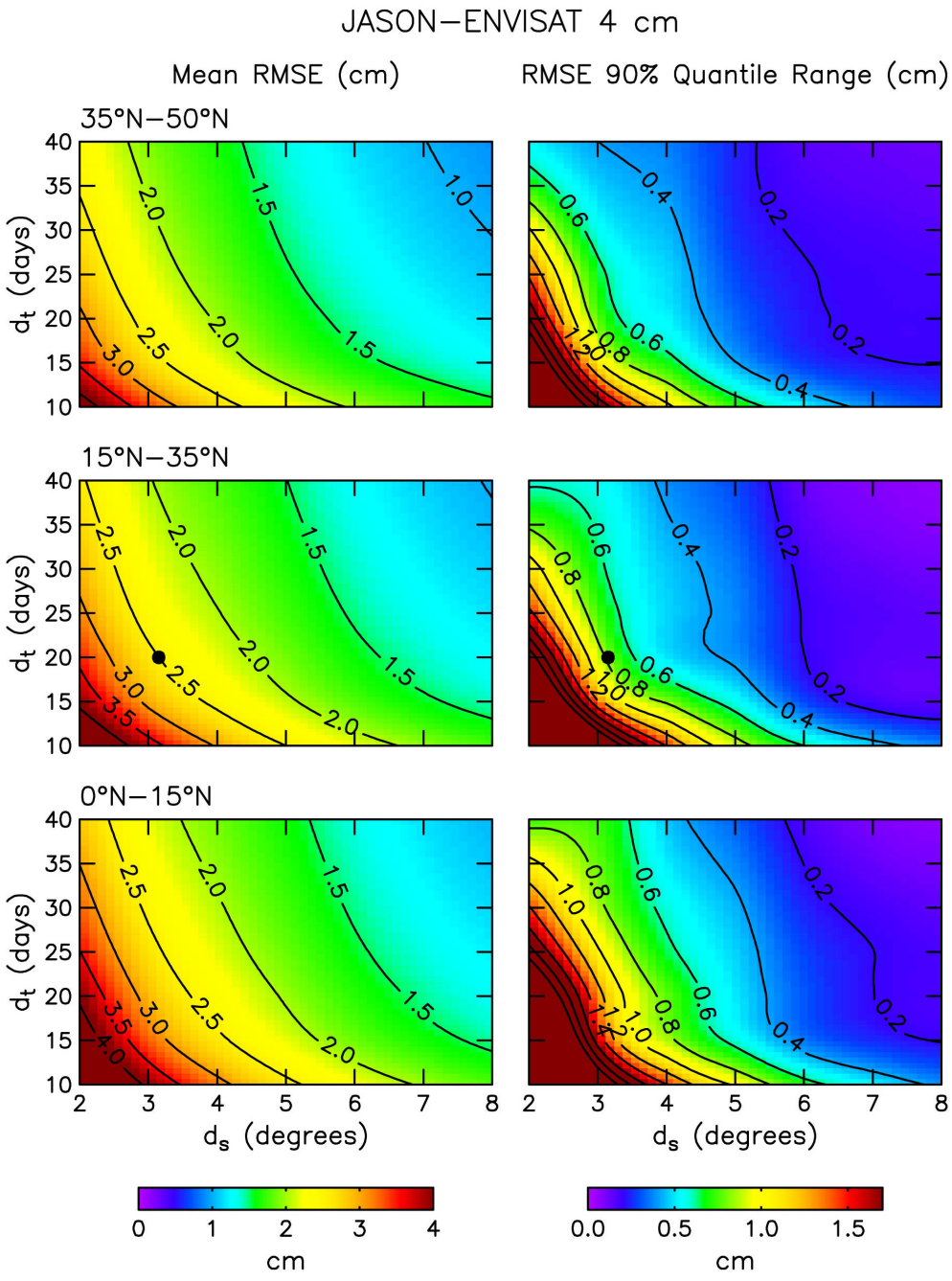

Figure 8. The same as Figures 2, 4 and 6, except for SSH fields constructed from measurements from a tandem Jason-ENVISAT sampling pattern. The ENVISAT and Jason orbit errors are assumed to have standard deviations of 4 cm and 2 cm, respectively.

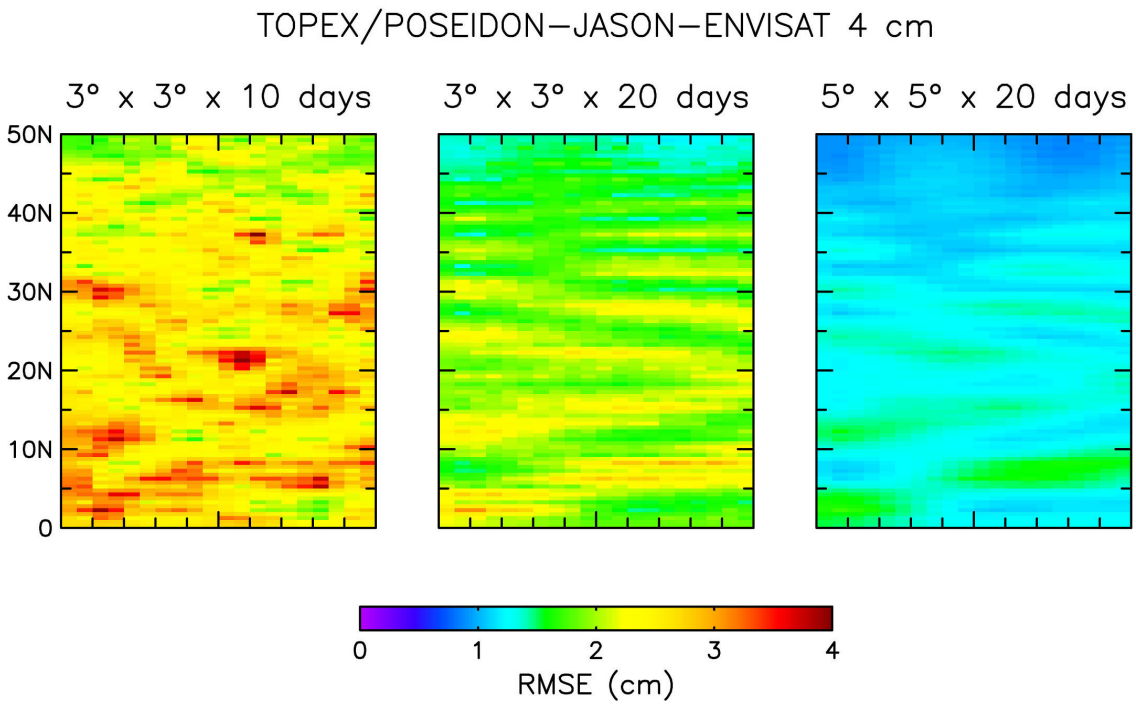

Figure 9. The same as Figures 1, 3, 5 and 7, except for SSH fields constructed from measurements from a triplet T/P-Jason-ENVISAT sampling pattern. The ENVISAT orbit errors are assumed to have a standard deviation of 4 cm and the T/P and Jason orbit errors are assumed to have standard deviations of 2 cm.

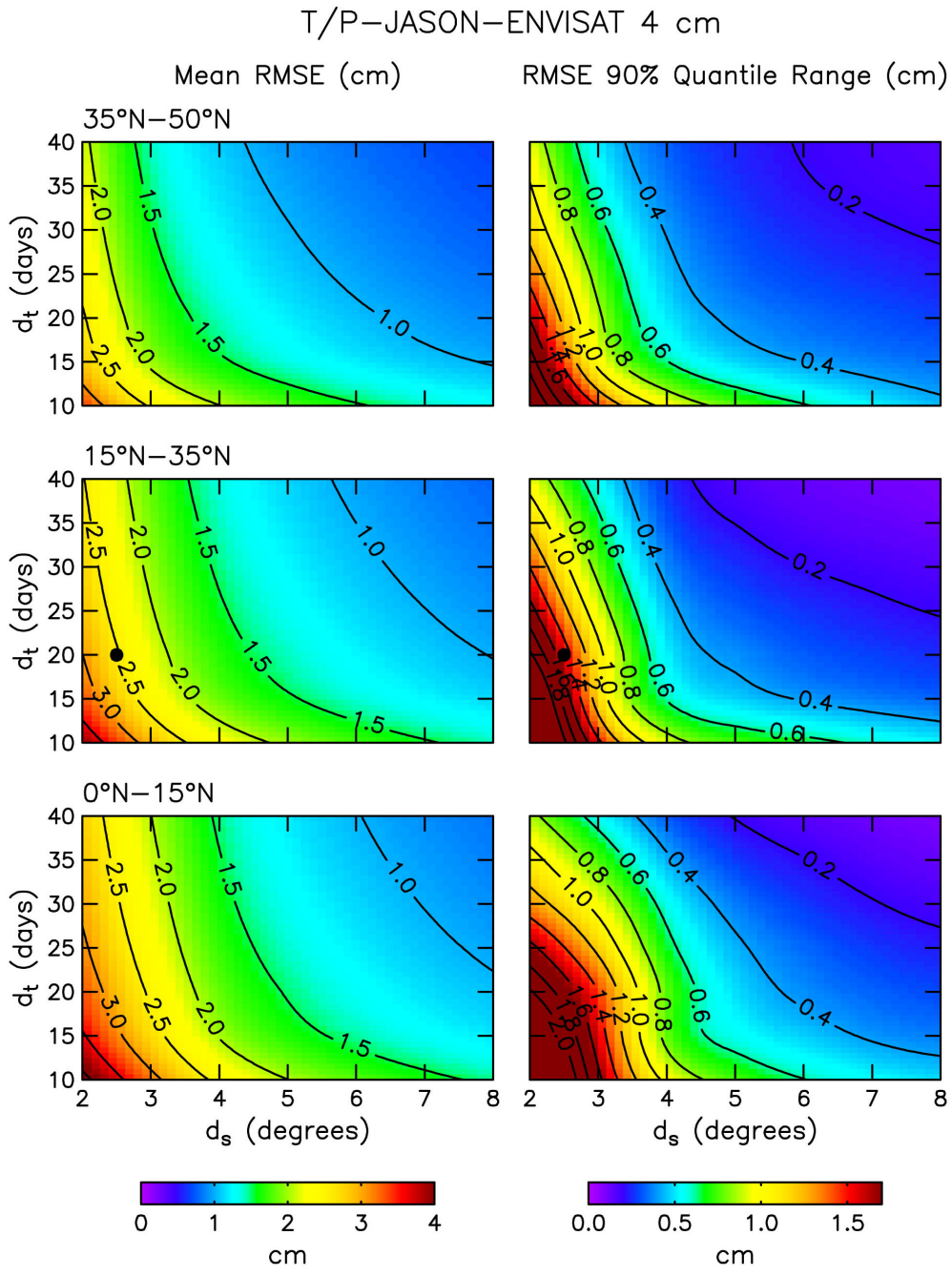

Figure 10. The same as Figures 2, 4, 6 and 8, except for SSH fields constructed from measurements from a triplet T/P-Jason-ENVISAT sampling pattern. The ENVISAT orbit errors are assumed to have a standard deviation of 4 cm and the T/P and Jason orbit errors are assumed to have standard deviations of 2 cm.

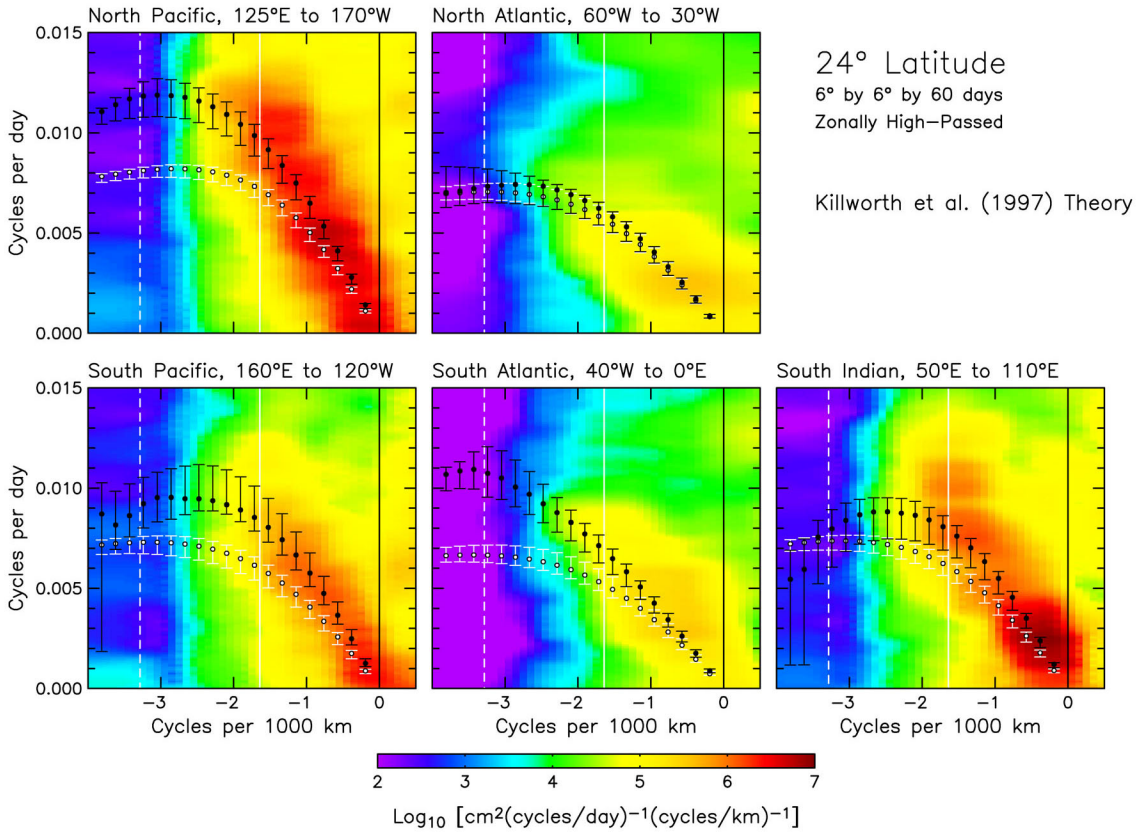

Figure 11. Wavenumber-frequency spectra computed from 7 years of T/P data along 24° latitude over the longitude ranges indicated at the top of each panel. Each spectral estimate was band averaged in space and time to obtain 18 degrees of freedom. The dispersion relation computed from the eigenvalue problems for the classical theory with zero mean background flow and the extended theory of Killworth et al. (1997) that includes the baroclinic background mean flow are shown by the open and solid circles, respectively. The error bars correspond to estimates of the 75% confidence intervals for the estimated dispersion relations.

A Comparison of Altimetric Methods for Estimating Surface Velocity

Olwijn Leeuwenburgh and Detlef Stammer
Scripps Institution of Oceanography, Mail Stop 0230
La Jolla, CA 92093

Abstract We simulate altimetric observations using the ouput of the 1/10 deg North Atlantic run of the Los Alamos POP model to investigate the uncertainties of surface geostrophic velocities estimated from three different methods utilizing conventional altimeters: along-track velocity estimation from two satellites in a parall-track configuration, cross-over analysis, and estimation of velocities from objectively mapped sea surface height fields. Part of the error budget can be attributed to particular limitations in each method associated with the spatial and/or temporal sampling characteristics. The addition of instrument noise and large scale along-track biases further highlights the sensitivity of each method to observation error. Velocity accuracies are comparable for the three methods based on assumed prior errors. However, at midlatitudes the parallel-track method leads to the best results with erros in the range of about 7 cm/s for both velocity components. This compares to about 10 cm/s for the U component based on OM and about 8-9 cm/s for the V component from the cross-over analysis. The cause for these increased uncertainties are fast motions in the ocean which are not captured properly at the cross-over points and which are filtered out by the OM procedure. However, the optimal choice for velocity determination depends strongly on the region and application of interest.

Introduction

In the past, estimates of the geostrophic surface flow field have been obtained from SSH measurements through two different methods: space-time objective mapping of SSH (e.g., *Ducet et al.*, 2000), and secondly, cross-track velocity estimation at the intersection of ascending and descending tracks (e.g., *Morrow et al.*, 1994). The uncertainty and resolution of maps obtained with the former approach have been discussed primarily in the context of the global resolution and mapping capabilities of single and multiple mission altimetry (*Greenslade et al.*, 1997; *Le Traon and Dibarboure*, 1999). Evaluation of velocities at cross-overs has been undertaken through fairly localized comparisons with moored current meters (e.g., *Strub et al*., 1997) and surface drifters (e.g., *Willebrand et al*., 1990). *Stammer and Dieterich* (1999) suggested a different method to obtain the surface flow field with high along-track resolution using SSH observations from two altimeters which are operated in tandem along parallel tracks. Such a configuration can be considered, for example, for a T/P-JASON tandem mission, or for multiple satellites as proposed for the WITTEX mission (*Raney and Porter*, 1999). The availability of a high-resolution data source, the 1/10 deg North Atlantic run of the Los Alamos POP model described by *Smith et al.* (2000), as well as the prospect of new technology aimed at improving our current knowledge of the surface flow field, calls for an evaluation of methods of velocity estimation and their performance in the presence of realistic observation errors.

Parallel-Track Methods

The approach taken here is identical to that of *Stammer and Dieterich* (1999) who presented a schematic of the construction of SSH slopes and subsequent calculation of velocities in two orthogonal directions using observations from two parallel tracks. Important characteristics of this method are that individual velocity components are estimated using two SSH samples located on separate parallel tracks. This may impact the uncertainty in velocity estimates in two ways: the spacing between SSH samples may be larger than the local scale of SSH variability, causing aliasing and underestimation of energy on small scales, and secondly, a very small spacing may cause an increase of sensitivity of the SSH slope to observation errors in the SSH samples. Figures 1 and 2 show that configurations with a track spacing larger than 0.75 deg are prone to errors of the first kind, leading to substantial underestimation of eddy kinetic energy, while those with a track spacing smaller than 0.5 deg are sensitive to errors of the second kind. An mportant benefit of the parallel-track method, besides its high density along-track sampling of

the flow field, is the fact that both components of the flow field are sampled instantaneously so that errors related to the temporal sampling can be neglected. For 4 cm instrument noise and a once-per-revolution 'orbit error' with 1 cm amplitude, velocity errors between 20 deg and 50 deg are smallest for track separations between 0.5 deg and 0.75 deg and are typically 7 cm/s in magnitude (Fig. 1). The geographical distribution of the error magnitudes (Fig. 2) shows that errors are larger in high energy regions due to the reduced spatial scales of variability. Errors are also increased near the equator due to the small value of f, and in the U component near the turning latitude due to the small sample distance. Both effects increase the sensitivity to noise.

Cross-over Analysis

At cross-over locations it is possible to estimate two components of the velocity vector, which subsequently can be rotated into a Cartesian frame of reference. The two components are not obtained simultaneously, but with a time lag which may be as large as half the repeat period. The resulting errors in the estimates of the two velocity components will therefore depend jointly on this time lag and on the time scale of ocean variability at the cross-over. To minimize these errors, we interpolate time series of both components to the mid-time between over flights. Here we investigate the 'interleaving-tracks' scenario for a T/P-JASON tandem mission, leading to a quadrupling of the number of cross-overs. The advantage of using cross-overs is that in estimating each velocity component, SSH observations from one single arc are used only, thus minimizing the effect of long-wavelength along-track errors and eliminating contributions of biases between two different tracks. From investigating the results for the case without observation error we find that significant errors in U and V arise due to the non-simultaneous measurement of the two components. As may be expected, this effect is largest in areas of high temporal variability, such as the Gulf Stream Extension, where errors may be as large as 20 to 25 cm/s (errors are a bit smaller in U). We find that introducing a time-lag between the two missions does not lead to an overall error reduction. Repeating these calculations for the GEOSAT and ERS configurations (single mission setup) shows that errors tend to be larger, especially in the V-component. This may be explained by the higher inclination of the orbits, as well as by the longer repeat periods and thus the increase in the maximum time lag between over flights at individual cross-overs. Our computations with observation error are all based on 4 cm random instrument noise. Velocities were estimated by determining the slope of a straight line fit to the along-track data. The length of this fit relates to the extent of smoothing. After testing several smoothing length scales, we decided to use a latitude-dependent length of the fit of the form $L=100+100 \cos(\text{lat} \cdot 90/30)$ km for 0 deg < lat < 30 deg N and L=100 km for lat >30 deg N. The final effect of adding random noise and applying smoothing is then to uniformly raise the uncertainty in each velocity component with 3 to 5 cm/s with respect to the no-noise case (Fig. 3). Errors in U and V are around 5 to 8 cm/s for the largest part of the North Atlantic with increased levels of error towards the equator where the geometry of the cross-over leads to a poor determination of the V-component and f is small, and within the Gulf Stream Extension and North Atlantic Current regions where time scales are short. The results are not very much worse than the idealized case without noise, implying that the largest error contribution is the non-simultaneous temporal sampling of the two velocity components.

Objective Mapping

This method was explored in much detail by *Le Traon and Dibarboure* (1999). They presented formal mapping errors in U and V as a percentage of local signal variance for a range of spatial scales, two different latitude bands, and a variety of mission combinations. As an addition to their experiments, and for direct comparison with the previous two methods we compute errors in U and V from the difference between the estimated and 'true' velocities. In order to give an estimate of the uncertainties in currently used products and approaches, we have largely followed the processing steps and parameter choices of *Ducet et al*. (2000). This involved latitude dependent along-track smoothing scales, subsampling intervals, and spatial and temporal correlation scales. Here we investigate the combination of T/P and JASON. *Le Traon and Dibarboure* (1999) concluded that a T/P-ERS combinations leads to comparable results.

We added 2 cm random noise to both the T/P and JASON samples. Different from *Ducet et al.* (2000) we selected from each quadrant the four data points nearest to the interpolation point, for both T/P and JASON separately. The results presented here were obtained by interpolating SSH to a 0.3 deg sub-grid of the model grid, from which we obtained velocities by taking centered differences (interpolating to finer grids tended to lead to an increased effect of mapping error when computing SSH gradients). Our results were more or less similar when noise-free data were used, suggesting that most of the velocity error originates from an inadequate data distribution or statistical model. Fig. 4 shows the resulting rms differences in U and V. The results are fairly similar in appearance to those from the previously discussed methods. Errors are significantly larger however for both the U and V components in the high energetic regions of the Gulf Stream Extension and North Atlantic Current. At low latitudes, the V component is retrieved with much greater accuracy than in the other two methods.

Summary and Conclusions

The goal of this paper is to evaluate the uncertainties associated with three methods to estimate the surface velocity from SSH measurements, notably cross-over analysis, parallel track methods, which have recently been proposed in the light of upcoming tandem missions, and objective mapping. Each of the methods was simulated using the output of a high resolution GCM model to which realistic errors were added. Fig. 5 compares the parallel-track, cross-over, and objective mapping methods as a function of latitude with errors in U and V averaged zonally over the width of the North Atlantic and for the error cases considered above. At latitudes between 10 deg and 55 deg the parallel-track and cross-over methods are able to retrieve the U component with an average error of 6 cm/s. At higher latitudes the parallel-track method does not do as well as the other two. At low latitudes errors in V are large for all methods, with objective mapping producing the smallest errors up to about 30 deg latitude. Between 30 deg and 53 deg the parallel track method has the smallest errors, with a typical average error of 7 cm/s between 30 deg and 40 deg as compared to 10 cm/s for the other two methods. Again, at higher latitudes, it's performance deteriorates. If one assumes a 3 cm rather than a 1 cm orbit error, errors for the parallel-track method are increased by about 1 or 2 cm/s in U and 4 cm/s in V at mid-latitudes. For all three methods errors increase strongly towards the equator due to the small value of the Coriolis parameter. At high latitudes the small track spacing in the parallel-track method and a large crossing angle in the cross-over method cause large errors in U. We find that for all three methods a significant fraction of resulting velocity errors can be related to spatial or temporal sampling problems. We conclude that it is important to consider these error sources when evaluating different methods of analysis and that neglect of these effects is likely to result in inaccurate estimates of uncertainties.

There are many scientific benefits from an enhanced velocity sampling, including, for the first time, complete velocity and energy statistics. Presently related studies are underway to try to utilize all available surface observations to construct surface flow fields. Those include surface drifters, ADCP and gridded SSH fields. However, in-situ data are sparse and a real success in measuring velocities with high space-time resolution can only come from space-based methods. Results will be essential for studies of the near-surface Ekman flow field, for studies of the wind work on the ocean and respective dissipative processes near the surface. More generally, a good understanding of the energetics of the ocean is still missing after many years of intense measurement campaigns including altimetric missions. Complete understanding of the surface flow field is essential here (see e.g. Wunsch, 2000).

In combination with a complete drifter coverage it can be expected that new insights about the Ekman layer in the ocean can be obtained that presently can only be obtained in limited form from ADCP measurements.

A complete understanding of velocity statistics is largely missing. We have no information about wavenumber spectra of velocity. Because of this we have no insight into the existence and evolution of turbulent processes (geostrophic turbulence), energy cascades, enstrophy cascades, barotropic inverse energy cascades, etc.

For many of the above mentioned applications continuous measurements of velocity are essential. Observations limited to cross-overs can often be too sparse to capture spatial structures, turning points, stream axes, etc. This can be essential for estimating Reynolds stresses - a rather noisy quantity that will require substantial filtering and averaging. Here it is doubtful that point measurements can help us obtain more insight. As has been seen even in numerical models, a good spatial coverage and spatial averaging is essential to obtain stable estimates of eneregy convergences.

At present, monitoring boundary currents and their kinetic energy is limited to cross-track velocities. From cross-over points we can get two components. With a parallel-track approach one may establish continuous monitoring across frontal structures that allow a full kinetic eneregy estimate, studies of isotropy, changes of the current axis, strength of transports, etc. This approach would especially be beneficiary to studies of boundary currents where most of the climate relevant ocean transports happen. A dedicated velocity mission will clearly be a quantum leap in advancing our observational understanding of the ocean.

Our conclusion that the parallel-track method would perform best with 0.5° to 0.75° track separation does not prevent it to be applied with an evenly interleaved configuration. Uncertainties increase for larger seperation but may still be smaller at midlatitudes than those resulting from the other two methods. The implementation of an interleaved configuration without any time offset, as recommended by the JASON Science Working Team, will allow a thorough intercomparison of this new method with the traditional methods under real conditions and will maximize the potential for new applications of altimetric data in studies of surface velocities.

Acknowledgments. We are grateful to Rick Smith for providing the model fields. Valuable discussions with Lee-Lueng Fu and Dudley Chelton are highly appreciated.

References

Ducet, N., P.Y. Le Traon and G. Reverdin, 2000: Global high resolution mapping of ocean circulation from TOPEX/POSEIDON and ERS-1/2. *J. Geophys. Res.*, **105**, 19,477-19,498.

Greenslade, D.J., D.B. Chelton and M.G. Schlax, 1997: The midlatitude resolution capability of sea level fields constructed from single and multiple satellite altimeter datasets. *J. Atmos. Oceanic Technol.*, **14**, 849-870.

Le Traon, P.Y., and G. Dibarboure, 1999: Mesoscale mapping capabilities of multiple-satellite altimeter missions. *J. Atmos. Oceanic Technol.*, **15**, 1208-1223.

Morrow, R., R. Coleman, J. Church and D. Chelton, 1994: Eddy momentum flux and its contribution to the Southern Ocean from Geosat altimetry. *J. Phys. Oceanogr.*, **24**, 2050-2071.

Raney, R.K., and D.L. Porter, 1999: WITTEX: A constellation of three small satellite radar altimeters. *Proceedings, Oceanobs99,* Saint-Raphael, France, 18-22 October.

Smith, R.D., M.E. Maltrud, F.O. Bryan and M.W. Hecht, 2000: Numerical simulation of the North Atlantic Ocean at 1/10 deg. *J. Phys. Oceanogr.*, **30**, 1532-1561.

Stammer, D., and C. Dieterich, 1999: Space-borne measurements of the time-dependent geostrophic ocean flow field. *J. Atmos. Oceanic Technol.*, **16**, 1198-1207.

Strub, P.T., T.K. Chereskin, P.P. Niiler, C. James and M.D. Levine, 1997: Altimeter-derived variability of surace velocities in the California Current System; 1. Evaluation of TOPEX altimeter velocity resolution. *J. Geophys. Res.*, **102**, 12,727-12,748.

Willebrand, J., R.H. Kaese, D. Stammer, H.-H. Hinrichsen and W. Krauss, 1990: Verification of Geosat sea surface topography in the Gulf Stream Extension with surface drifting buoys and hydrographic measurements. *J. Geophys. Res.,* **95**, 3007-3014.

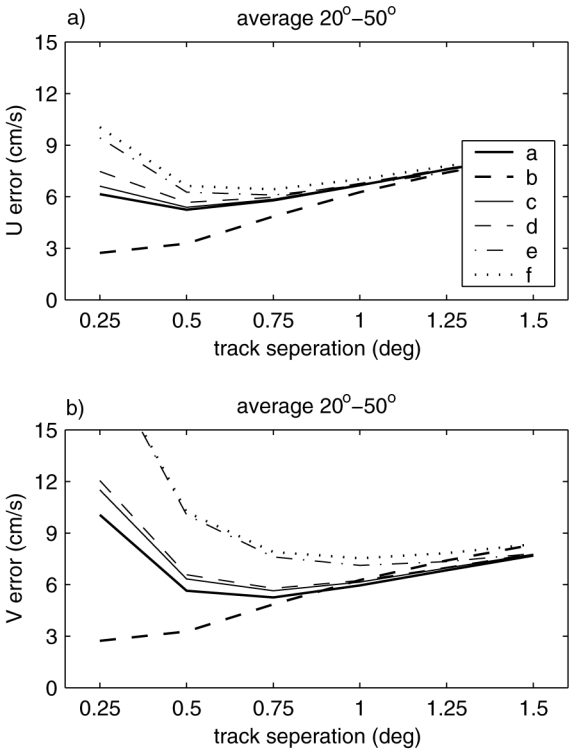

Figure 1. RMS errors in U and V between 20 deg N and 50 deg N as a function of track separation and error. The three components of the error budget represent noise, orbit error, and random bias added after along-track smoothing: a.(4,0,0) cm; a.(0,1,0) cm; c.(4,1,0) cm; d.(4,1,1) cm; e.(4,3,0) cm; f.(4,3,1) cm.

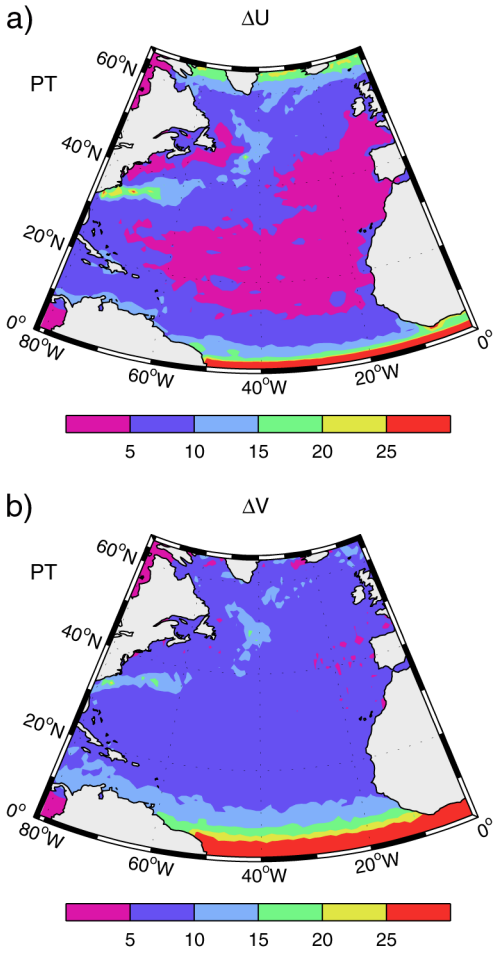

Figure 2. RMS errors in U and V for a track separation of 0.5 deg and with 4 cm noise and 1 cm orbit error.

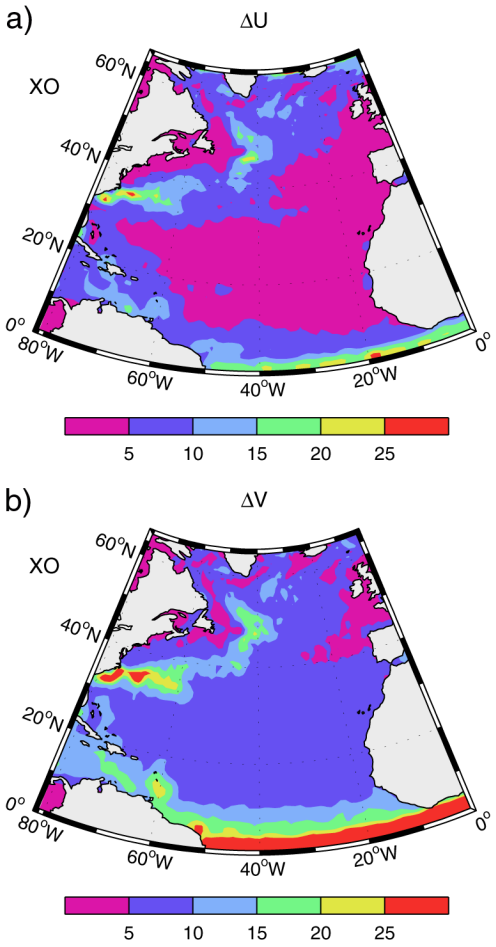

Figure 3. RMS errors in U and V for the cross-over method with 4 cm noise and a latitude-dependent smoothing length scale.

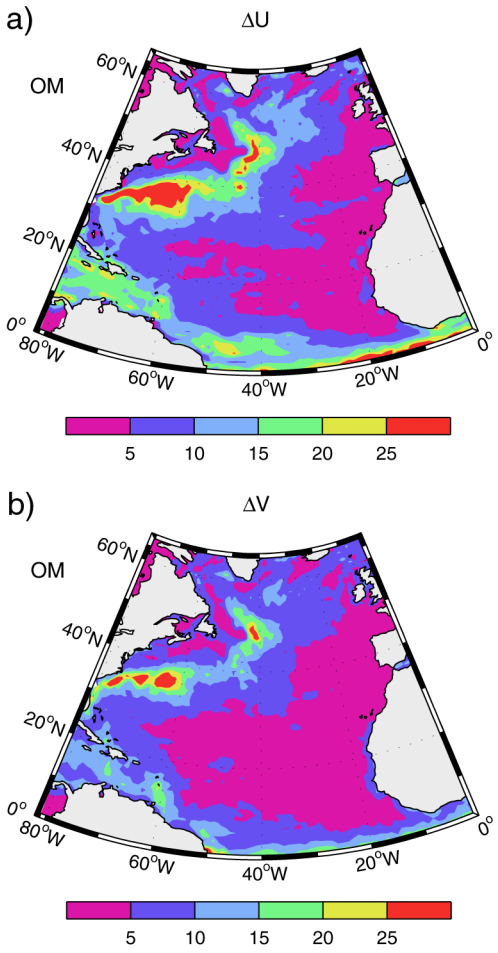

Figure 4. RMS errors in U and V for the objective mapping method with 2 cm and 3 cm noise in the data.

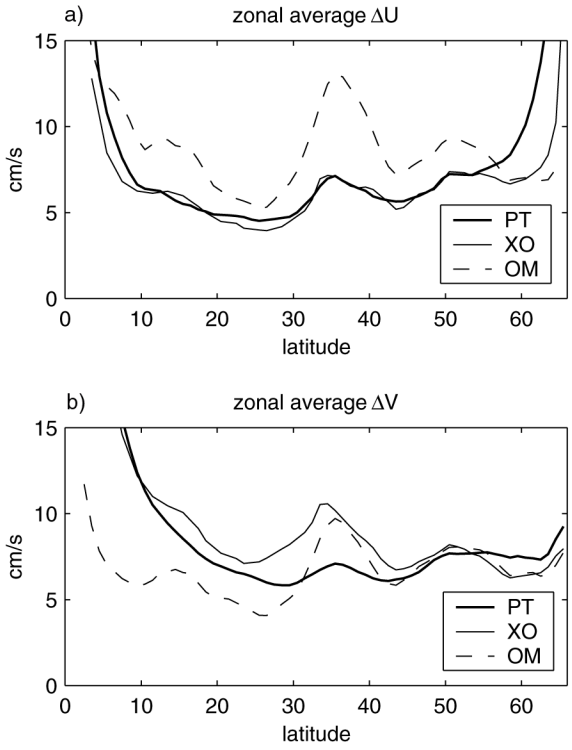

Figure 5. Zonal averages of RMS errors in U and V as a function of latitude for the parallel-track, cross-over and objective mapping methods.

On the Estimation of Surface Geostrophic Velocity from a Tandem TOPEX/POSEIDON and Jason-1 Altimeter Mission

Michael G. Schlax and Dudley B. Chelton
College of Oceanic and Atmospheric Sciences
104 Oceanography Administration Building
Oregon State University
Corvallis, OR 97331-5503

1. Introduction

An important application of satellite altimeter data is the estimation of the surface geostrophic velocity field. While geostrophic velocity can be computed from smoothed and gridded SSH fields (e.g., Qiu 1995), the spatial smoothing attenuates the mesoscale signals that are of interest in most applications of velocity estimates. Higher resolution estimates of geostrophic velocity can be obtained by the crossover method, which utilizes SSH data obtained from a satellite placed in an exact-repeat orbit to estimate geostrophic velocity at the intersections of ascending and descending ground tracks (Parke et al., 1987; Morrow et al., 1992; 1994). Besides the coarse distribution of the crossover points, a limitation of the crossover method is the time separation between ascending and descending ground track samples of the crossover location; temporal variability of the velocity field introduces errors in velocity estimates obtained from the nonsimultaneity of the crossovers.

In anticipation of a probable tandem TOPEX/POSEIDON-Jason altimeter mission with coordinated orbits, Stammer and Dieterich (1999) devised an alternative to the crossover method that would utilize SSH data obtained from closely spaced, parallel ground tracks sampled essentially simultaneously. This proposed parallel-track method estimates orthogonal components of geostrophic velocity from between-track differences of SSH. From simulations based on the characteristics of TOPEX/POSEIDON (T/P) measurement errors, the optimal tandem T/P-Jason mission for geostrophic velocity estimation is one for which the ground tracks are offset by a longitudinal shift of about 0.5° of longitude (Leeuwenburgh and Stammer, 2001). A closer track spacing amplifies the effects of measurement errors on estimates of the along-track component of geostrophic velocity and a wider track spacing increases sampling errors from unresolved mesoscale variability with spatial scales shorter than the track spacing.

The goal of this paper is to present analytical formulae for the estimation of error variances of the zonal and meridional components of geostrophic velocity from the crossover and parallel-track methods. Using these formulae, the precisions of the two methods are compared to determine whether one method is preferable to another for geostrophic velocity estimation. A second goal is to use the results of this analysis to assess the utility of crossover estimates of geostrophic velocity from a tandem T/P-Jason mission with evenly spaced, interleaved ground tracks.

2. Geostrophic Velocity Estimation

The SSH observations are assumed to be contaminated by random instrumental measurement errors and long-wavelength environmental measurement and orbit errors. The instrumental measurement errors are assumed to be uncorrelated with zero mean, variance σ^2_e, and independent of the long-wavelength measurement errors. The geostrophic velocity field that is of interest is assumed to be a realization of an isotropic stationary random process with zero mean, variance σ^2_s and temporal autocorrelation $\rho(\tau)$ as a function of lag τ. The process is further assumed to be uncorrelated with either of the measurement error processes.

It will be shown that long-wavelength measurement and orbit errors have negligible effect on crossover estimates of geostrophic velocity. However, this is the largest source of error in parallel track

estimates of geostrophic velocity. For a time separation of less than a few days between neighboring ground tracks, errors in the long-wavelength environmental corrections will be significantly correlated between neighboring tracks. Much of the environmental measurement error is thus eliminated when differencing SSH between two parallel tracks that are sampled simultaneously. The residual environmental measurement error in SSH differences between two parallel tracks is probably about 1 cm. Long-wavelength measurement error is therefore dominated by the orbit error which is random from track to track with an rms of 2–3 cm for T/P (Chelton et al., 2001). The orbit errors of Jason-1 are expected to be about the same. We assume that the long-wavelength errors have zero mean and variance σ^2_o and are uncorrelated between different ground tracks and different repeats of a given ground track. Residual long-wavelength measurement and orbit errors with standard deviations of 1, 2 and 3 cm are considered here to illustrate the sensitivity of the geostrophic velocity estimates to these errors.

The error variances calculated here for both the crossover method and the parallel track method consider only the effects of measurement errors. The total error also includes sampling errors from unresolved mesoscale variability. Inclusion of the sampling error contribution requires assumptions about the spatial scales of variability. This would considerably complicate the derivation of the analytical expressions (1) and (2) below. In the present study, we therefore consider only the effects of measurement errors. The errors presented here thus represent lower bounds for the mean squared errors of both methods.

2.1. Crossover Method

The crossover method provides an estimate of geostrophic velocity at the intersection of an ascending and a descending ground track by estimating the along-track slopes of SSH from each track. These slopes were estimated here from least-squares line fits to the along-track SSH data on either side of the crossover location. Cross-track geostrophic speeds were calculated from these along-track slopes by the geostrophic relation. The nonorthogonal cross-track geostrophic speeds at the crossovers were then converted to zonal and meridional velocity components. An advantage of the crossover method is that, since the basic geostrophic speed estimates are taken along-track, the long-wavelength measurement errors are essentially eliminated by the spatial high-pass filtering operation of the slope estimation.

Because the cross-track speeds from the ascending and descending crossovers are nonorthogonal and the angle between them changes with latitude, the geometric transformation to obtain zonal and meridional components results in latitudinally varying error variances arising from the presence of measurement errors in the SSH data (Morrow et al., 1994). Furthermore, at a given crossover, the ascending track is sampled at a different time from the descending track, so that the two cross-track speeds sample the time-varying flow field at different times. To obtain an instantaneous estimate of the velocity components, some interpolation in time is required. Finally, the analysis is restricted to the crossover locations, which, depending on the satellite orbit, may comprise a grid that is sparse relative to the mesoscale features of interest.

It is shown in Chelton and Schlax (2001) that the error variances of crossover estimates of the zonal and meridional geostrophic velocity components are

$$\sigma^2_{\hat{u}_c} = \frac{g^2}{f^2}\frac{6}{\cos^2\gamma}\frac{\sigma_e^2}{\Delta_x^2 M\left(M^2-1\right)} + \frac{\sigma_s^2}{\cos^2\gamma}\left[1-\rho(T)\right]\frac{\Delta_t}{2T} \qquad (1a)$$

and

$$\sigma^2_{\hat{v}_c} = \frac{g^2}{f^2}\frac{6}{\sin^2\gamma}\frac{\sigma_e^2}{\Delta_x^2 M\left(M^2-1\right)} + \frac{\sigma_s^2}{\sin^2\gamma}\left[1-\rho(T)\right]\frac{\Delta_t}{2T} \qquad (1b)$$

where g is the gravitational acceleration, f is the Coriolis parameter, T is the orbit repeat period (9.9156 days for T/P and Jason), Δ_x is the along-track distance between successive measurements of SSH, Δ_t is the time separation between ascending and descending ground tracks and γ is the azimuth of the ground tracks (defined to be half of the angle between ascending and descending ground tracks). These equations are based on cross-track speeds estimated by a least-squares fit of a line to $M_{1/2}$ points on either side of the crossover, using a total of $M = 2M_{1/2} + 1$ points. This least-squares procedure acts as a low-pass filter for cross-track geostrophic speeds; increasing the value of $M_{1/2}$ attenuates increasingly longer-scale along-track variations of cross-track speed. The wavelength in kilometers that corresponds to the half-power point of the filter transfer function is linearly related to $M_{1/2}$ (Chelton and Schlax, 2001).

The time separation between the ascending and descending tracks varies considerably with latitude but is constant for a given latitude. In deriving (1), it is assumed that the estimation time is the midpoint between the times of the ascending and descending tracks, and that zeroeth-order interpolation is used, i.e., the estimated cross-track speeds from the ascending and descending tracks are used directly to estimate the geostrophic velocity at the estimation time. This provides an upper bound on the effects of interpolation error on geostrophic velocity estimates; the usual linear interpolation (e.g., Morrow et al. 1994) or a more sophisticated interpolation scheme would result in smaller interpolation errors. However, use of one of these higher order interpolation methods considerably complicates the derivation of (1), so the present analysis considers only the effects of zeroeth-order interpolation. For analytical convenience, it has further been assumed that the autocorrelation function decreases linearly with increasing time lag. The results will show that the error variances are relatively insensitive to the interpolation errors, so this assumption is not a serious constraint.

The insensitivity of the crossover method to long-wavelength measurement errors is evidenced by the fact that neither (1a) nor (1b) depends on the orbit error standard deviation. Equations (1) further show that the variance of the crossover estimates is partitioned into separate contributions involving the measurement error (the first term in each equation) and the error due to temporal interpolation (the second terms). Since the measurement error is inversely related to the cube of M, significant gains in precision can be made with small increases in M. This improved precision is achieved at the expense of reduced spatial resolution of the speed estimates (i.e., larger filter cutoff wavelength). The interpolation error terms are independent of M and vary as expected, increasing with the signal variance and the time separation, and decreasing with increasing autocorrelation time scale. Both terms vary latitudinally as a result of the geometry of the ground tracks via factors involving the azimuth angle. Since only the instrumental measurement error is divided by the Coriolis parameter f, it dominates in the velocity component errors at low latitudes and for estimates with small along-track smoothing.

The latitudinal variations of the velocity component errors are shown in Figure 1 for four selected values of $M_{1/2}$. In all cases, the standard deviation of the instrument measurement errors is assumed to be 2 cm, a conservative approximation of the 1.7-cm instrument error of the T/P dual-frequency altimeter, and the variance of the geostrophic velocity signal of interest is assumed to be 50 cm^2/s^2. The latter is intended to be a characteristic value for the geostrophic velocity field. The four interpolation error scenarios shown in each panel correspond to autocorrelation values at lag T of 1.0, 0.75, 0.5 and 0.25. The case for which the autocorrelation at lag T is 1.0 is equivalent to a signal variance of zero, which corresponds to zero interpolation error, in which case all of the velocity component errors are due to instrumental measurement errors. The case of 0.5 is a typical value for the autocorrelation of sea-surface slopes (Stammer, 1997). The 0.75 and 0.25 cases are shown to illustrate the weak sensitivity of the interpolation errors to the autocorrelation time scale.

For the case of small along-track smoothing with $M_{1/2} = 2$ (Figure 1a), which corresponds to a wavelength filter cutoff of approximately 50 km, the errors in both components are very high, exceeding

8 cm/s at all but the highest latitudes where the error in the meridional velocity component estimate becomes as small as 6 cm/s. Because of the ground track geometry, the errors of this component are especially large, exceeding 20 cm/s for latitudes lower than 35°. It is easy to see that, even with instrumental measurement errors of only 2 cm, the crossover method is not capable of providing usefully precise velocity estimates with smoothing over such a short span of data. The effects of interpolation error are scarcely noticeable in Figure 1a.

Increasing the along-track smoothing to $M_{1/2} = 4$ (Figure 1b) filters the speeds more stringently (with a filter cutoff wavelength of about 100 km), with a strong decrease in the overall error owing to the inverse cubic dependence on M in the first terms of equations (1). The crossover estimates of geostrophic velocity become more precise but the errors still exceed 3 cm/s everywhere for the zonal component and are considerably larger for the meridional component, except at high latitudes where the crossover angle favors the estimation of the meridional component and amplifies the errors of the zonal component. The effects of the autocorrelation time scale on interpolation error are apparent with this degree of smoothing, but interpolation error still contributes only a minor amount to the total error variance of the geostrophic velocity estimates.

Figures 1c and 1d are cases where the spans of the least-squares fit lines reduce the measurement errors sufficiently so that measurement errors become secondary everywhere except at the lowest latitudes where the Coriolis parameter approaches zero. There is little difference between the errors of the crossover estimates of geostrophic velocity with these two different values of $M_{1/2}$ that correspond to filter wavelength cutoffs of 200 km and 300 km. This is because the total error is dominated by the interpolation error contribution, which is identically the same for all of the error estimates in Figure 1. The rapid latitudinal fluctuation of the interpolation errors with amplitudes of a few cm/s results from the latitudinal variation of the separation times between the ascending and descending ground tracks at the crossovers. The errors in the meridional velocity component are larger than those for the zonal component by several cm/s. The weak sensitivity to the signal autocorrelation time scale is evidenced by the small differences in the velocity component errors for the wide range of autocorrelation values shown.

It can be concluded from Figure 1 that measurement errors are the primary limiting factor for crossover estimates of geostrophic velocity with small along-track smoothing. For along-track smoothing with filter wavelength cutoff longer than about 200 km, the effects of measurement errors become negligible and the errors of the velocity components are dominated by the effects of interpolation error. An along-track smoothing corresponding to a filter cutoff wavelength in the range 100-200 km therefore seems most sensible. In regions of very energetic eddy variability (i.e., where the signal variance is larger), the increased signal-to-noise variance ratio might allow less along-track smoothing.

2.2. Parallel-Track Method

In the parallel-track method, orthogonal components of the geostrophic velocity are estimated as described by Stammer and Dieterich (1999) based on differences of SSH between two closely spaced ground tracks that are sampled essentially simultaneously. These differences are then converted to zonal and meridional components by a simple rotation of the coordinate system. The simultaneity of the SSH measurements obviates the need for the temporal interpolation that was shown in section 2.1 to be a major source of error in the crossover method. Another potential attraction of the parallel-track method is the possibility of obtaining geostrophic velocity estimates on a high resolution along-track grid, rather than just at the coarsely spaced crossovers. The extent to which this is advantageous depends on the degree of along-track smoothing that must be applied to mitigate the effects of measurement errors on the velocity estimates. The along-track smoothing and the filtering properties of the parallel track method are discussed below. It should also be noted that, except in the along-track direction, the resolution of velocity estimates provided by the parallel-track method is limited to the coarse resolution imposed by the T/P ground track spacing.

There are two significant drawbacks to the parallel track method. Firstly, long-wavelength measurement errors and orbit errors have a strong effect on the accuracy of geostrophic velocity estimates computed by differencing SSH between the parallel tracks. Secondly, the perpendicular distance between the parallel tracks decreases with increasing latitude, which amplifies the effects of long-wavelength measurement and orbit errors on the geostrophic velocity estimates as shown below.

It is shown in Chelton and Schlax (2001) that the error variances of parallel-track estimates of the zonal and meridional geostrophic velocity components are

$$\sigma^2_{\hat{u}_p} = \frac{2}{d'^2}\frac{g^2}{f^2}\frac{\sigma^2_e}{M} + \frac{2}{d'^2}\frac{g^2}{f^2}\sigma^2_o\left[1 - 2\cos(\pi/4 - \gamma)\sin(\pi/4 - \gamma)\right] \tag{2a}$$

and

$$\sigma^2_{\hat{v}_p} = \frac{2}{d'^2}\frac{g^2}{f^2}\frac{\sigma^2_e}{M} + \frac{2}{d'^2}\frac{g^2}{f^2}\sigma^2_o\left[1 + 2\cos(\pi/4 - \gamma)\sin(\pi/4 - \gamma)\right] \tag{2b}$$

In these equations, $d' = d/\cos(\pi/4)$ is the distance over which the SSH differences are formed, where $d = 111\delta\phi\cos\theta\cos\gamma$ is the perpendicular distance in km between the two parallel tracks at latitude θ for ground track azimuth γ. The factor M in the denominators of the first term in each equation is the number of points along track over which the SSH measurements are averaged prior to differencing (see below). The precision of the parallel-track method depends both on instrumental measurement errors (the first term on the right side of each equation) and on long-wavelength measurement and orbit errors (the second terms).

It is important to recognize that the differencing used to estimate the geostrophic speeds in the parallel-track method imposes an inherent filtering of the flow field that depends upon the differencing distance. The filter transfer function for velocities obtained by the differencing operation has a linear relation between the differencing distance and the filter cutoff wavelength (Chelton and Schlax, 2001). As a tradeoff between increased sensitivity to long-wavelength measurement and orbit errors from unresolved mesoscale variability when the track offset is small and increased sensitivity to sampling errors when the track offset is large, Leeuwenburgh and Stammer (2001) conclude that a track offset of 0.5° is the optimal track separation. The latitudinal variation of the filter wavelength cutoff is shown for this track spacing by the solid line in Figure 2. The filtering of the parallel-track method decreases from about 170 km near the equator to about 50 km at high latitudes. At the middle latitudes of the Gulf Stream and Kuroshio Extension where the eddy variability is most energetic in the northern hemisphere, the filtering imposed by a track offset of 0.5° is about 120 km.

In the initial formulation of the parallel track method by Stammer and Dieterich (1999), no provision was made for the mitigation of instrumental measurement errors; the between-track differences were made between pairs of single SSH measurements assuming that the measurements were error free. Without some sort of smoothing applied to the SSH data, the measurement error contributions to the geostrophic velocity component error variances [the first terms in equations (2)] would cause the parallel-track method to appear less precise than necessary, and hence appear at a disadvantage with respect to the crossover method. It is therefore necessary to apply some along-track filtering for the analysis presented here.

Leeuwenburgh and Stammer (2001) addressed the instrumental measurement error issue by smoothing the SSH data along-track prior to forming the parallel track estimates of geostrophic velocity from between-track differences of the noisy SSH measurements. They applied the latitudinally varying along-track smoothing with filter wavelength cutoff shown by the dashed line in Figure 2. This form of along-track smoothing is independent of the inherent filtering (solid line in Figure 2) imposed by the

perpendicular track spacing of the parallel ground tracks. Because of this mismatch between the filtering properties of the between-track differencing and the along-track smoothing, it is difficult to quantify the effective filtering of the analysis by Leeuwenburgh and Stammer (2001).

The ultimate goal of this analysis is to compare the error variances from the crossover and parallel-track methods. The filtering that each method imposes on the geostrophic velocity estimates should therefore be similar. The smoothing parameters of the two methods were selected so that, to the extent possible, they resolve the same spatial scales of the geostrophic velocity. The specifics of the filtering applied here are as follows. As discussed in section 2.1, the crossover method filters the underlying geostrophic flow field according to the distance over which the least-squares line fits are done. The filtering of the parallel-track method, on the other hand, is constrained by the nature of the orbit and varies with latitude since the perpendicular track separation decreases with increasing latitude. A value of $M_{1/2}$ for the crossover method was chosen so that, for a given latitude, the filter cutoff wavelength for the crossover method matched the filter cutoff wavelength for the parallel-track method. Because $M_{1/2}$ is an integer, it is not possible to match the filtering precisely for the two methods.

For the along-track smoothing in the parallel-track method, the SSH measurements were block averaged over the same $M = 2M_{1/2} + 1$ observations that were used in the least-squares line fits for the crossover estimates. The between-track SSH differences were formed from these block averages. A more sophisticated form of along-track smoothing could be used to filter the SSH data. However, the effects of other forms of filtering would be more difficult to incorporate in the analytical expressions (2) for the geostrophic velocity component error variances. The simple block average smoothing suffices for present purposes.

The filter wavelength cutoff of the above latitudinally varying filtering for the crossover method is shown by the dots in Figure 2. As the track separation decreases with increasing latitude, the value of $M_{1/2}$ decreases in integer steps from 7 at the lowest latitudes to a minimum accepted value of 2 at the high latitudes. For different values of the track offset, the half span $M_{1/2}$ would have to be modified.

The latitudinal variations of the errors of the velocity component estimates based on along-track smoothing applied as described above are shown for a longitudinal track separation of 0.5° by the dashed, heavy solid and dotted lines in Figure 3. These three curves correspond to long-wavelength measurement errors with standard deviations of 1, 2 and 3 cm/s, respectively, which illustrate the sensitivity of parallel track estimates of geostrophic velocity to long-wavelength measurement and orbit errors. In all of these plots, the increased errors at low latitudes are due to the $1/f$ dependence inherent in all geostrophic velocity estimates. The increased errors at latitudes higher than about 40° are due to the increased sensitivity to long-wavelength measurement and orbit errors as the ground track separation decreases with increasing latitude from the convergence of the parallel ground tracks.

It should be noted that the error estimates in Figure 3 are somewhat smaller than those presented by Leeuwenburgh and Stammer (2001) for equivalent values of the orbit error standard deviation. The primary reason for this is that Leeuwenburgh and Stammer (2001) calculated the mean squared error between the velocity component estimates and the numerical model output used in their simulation. Their empirical analysis thus included the effects of simulated measurement errors, as well as the effects of sampling errors from unresolved spatial scales of mesoscale variability that have not been considered here for the reasons discussed previously. The error estimates presented in Figure 3 are thus a lower bound on the mean squared error of parallel-track estimates of geostrophic velocity.

2.3. Comparison of the Two Techniques

For comparison with the errors of parallel track estimates of geostrophic velocity components, the latitudinal variations of the errors of crossover estimates are shown by the thin solid lines in Figure 3 for an instrumental measurement error standard deviation of 2 cm, a signal variance of 50 cm^2/s^2 and an autocorrelation at lag T of 0.5, which we believe provide a realistic assessment of the crossover method

for typical open-ocean conditions. The error variances are based on latitudinally varying $M_{1/2}$ selected to be consistent with the smoothing inherent in the parallel track method as described in section 2.2.

For orbit errors larger than 2 cm, the parallel track estimates of geostrophic velocity are less precise than the crossover estimates at all latitudes equatorward of 55°. For smaller orbit errors of 1-2 cm, the crossover and parallel-track methods for estimating the geostrophic flow field would achieve comparable precision over the latitude range from about 20° to 55°. At lower latitudes, the parallel track estimates of the zonal velocity component become more prone to orbit errors because of the track geometry; an orbit accuracy of 1 cm is required to match the precision of the crossover method. At latitudes higher than 55°, crossover estimates of the zonal component of geostrophic velocity become less precise than parallel track estimates, owing to the geometry of the converging ground tracks.

The errors presented here may be somewhat pessimistic. The use of more sophisticated temporal interpolation than the zeroeth-order interpolation considered here [e.g., the linear interpolation used by Morrow et al. (1992, 1994) and Leeuwenburgh and Stammer (2001)] would reduce the errors of the crossover method relative to the errors shown in Figure 3. It may also be beneficial to apply more efficient along-track slope estimation schemes such as weighted least-squares. Likewise, it might be possible to reduce the error variances of the parallel track method by applying orbit error reduction techniques such as those summarized by Tai (1989). It is difficult to imagine, however, that the residual long-wavelength measurement and orbit errors could be reduced to less than the 1-2 cm range of values for which the precisions of velocity estimates in Figure 3 are comparable for the crossover and parallel-track methods.

2.4. Summary

The crossover method has the advantages that the slope estimation removes long-wavelength errors, reduces the effects of other measurement errors by averaging, and provides a readily interpretable filtering of the cross-track speed field. The major drawback that is unique to the crossover method is the requirement that some temporal interpolation be performed in order to obtain simultaneous estimates of the cross-track speeds. The parallel-track method does not suffer from this limitation, but has the disadvantages that it is very sensitive to long-wavelength measurement and orbit errors and that the poleward convergence of the tracks necessarily imposes a latitudinally varying filter on the geostrophic flow field that is not adjustable. The $1/f$ dependence of the errors of geostrophic speed estimates poses a severe limitation for both the crossover and parallel-track methods at low latitudes; the amplification of geostrophic velocity errors towards the equator where $f = 0$ places a lower limit to the latitude where either method may be applied. At high latitudes, the increase of the ground track azimuth degrades the crossover estimates of zonal velocity, while poleward convergence of the ground tracks increases the error variances of both the zonal and meridional velocity estimates from the parallel-track method. Leeuwenburgh and Stammer (2001) also noted these features of the two methods.

The conclusions of Figure 3 indicate that the two methods are comparable at latitudes lower than about 55°, assuming residual long-wavelength measurement and orbit errors of 1-2 cm. Larger residual long-wavelength measurement and orbit errors would render the parallel track method less precise than the crossover method.

We emphasize again that the analysis presented here considers only the effects of measurement errors. The mean squared errors of both methods depend on the geostrophic velocity signal variance as well because of the effects of unresolved mesoscale variability on the slope estimates. The mean squared errors are therefore larger than the measurement error variances presented here. To a large extent, however, sampling errors are likely to have a comparable effect on both methods. The relative accuracies of the two methods may therefore be largely dominated by the different sensitivities to the various components of measurement errors. Given the dependencies on the signal variance, as well as the spatially variable filtering of both methods and the temporal interpolation required by the crossover method, it is to be expected that the relative performance of the methods will vary geographically. This is

borne out in the empirical simulation results of Leeuwenburgh and Stammer (2001). Overall, however, the conclusions of Leeuwenburgh and Stammer (2001) are consistent with the results presented here. For realistic residual long-wavelength measurement and orbit errors, the parallel track method offers no significant advantage in precision compared with crossover estimates of geostrophic velocity. Indeed, if residual long-wavelength measurement and orbit errors are larger than 2 cm, the parallel track method is somewhat less precise than the crossover method.

3. Estimating Eddy Kinetic Energy and Reynolds Stresses

Although the coarse grid of crossover points in the T/P sampling pattern is rather limiting, the crossover technique described in section 2.1 nonetheless provides useful estimates of the velocity variance, especially in the midlatitude regions of most energetic eddy variability. An example of the velocity variance ellipses formed from the variances of the two orthogonal velocity components and the cross covariance between the two components (Preisendorfer, 1988; Morrow et al., 1992; 1994) is shown in Figure 4a and the associated eddy kinetic energy is shown in Figure 4b. When multiplied by the water density, the variances and cross covariance have units of force per unit area and represent horizontal fluxes of momentum by the eddy field, the so-called eddy Reynolds stresses.

The cross-track velocity estimates from which the orthogonal velocity components were computed for the velocity variances in Figure 4 were estimated from 9 years of T/P data based on along-track slopes obtained from least squares fits with $M_{1/2} = 4$, which corresponds to a filter wavelength cutoff of approximately 100 km. This is analogous to the filtering properties of 50 km block averages. The energetic velocity variability in Figure 4 near the Gulf Stream is of particular interest. The anisotropy of the velocity variability (i.e., the elongation and orientation of the ellipses) is important to ocean dynamics. In baroclinically unstable flow regimes such as the Gulf Stream, eddies force the mean and slowly varying flow by a cross-stream convergence of alongstream momentum, thus accelerating the mean flow (Cronin, 1996; see also Figure 7.3.1 of Pedlosky, 1987). The convergence or divergence of eddy momentum flux can be determined from horizontal gradients of the Reynolds stresses. The coarse 2.834° staggered grid of crossover points from a single altimeter in the T/P orbit is severely restrictive in this regard (Figure 5a); the distribution of the crossover points is too coarse relative to the width of the Gulf Stream to obtain useful estimates of the eddy convergence of momentum.

A byproduct of the sampling pattern of an interleaved tandem T/P-Jason altimeter mission with evenly spaced ground tracks is a four-fold increase in the number of crossovers of ascending and descending ground tracks. Such a tandem mission would result in a staggered grid of crossover points with 1.417° longitudinal spacing (Figure 5b). This quadrupling of the number of crossover points would greatly enhance the ability to investigate eddy-mean flow interaction from altimeter data.

It is noteworthy that the sampling pattern of the tandem mission with 0.5° offset suggested by Leeuwenburgh and Stammer (2001) would not significantly improve studies of eddy-mean flow interaction. The method yields Reynolds stress estimates at closely spaced intervals along the centerline between the parallel tracks with inherent smoothing on the order of 100 km (see Figure 2). However, the orthogonal components of the Reynolds stress gradient field that effects the momentum flux in eddy-mean flow interaction cannot be estimated with the same high along-track resolution. The gradients can be estimated from Reynolds stresses at the midpoints between the crossovers of intersecting centerlines. These midpoints are separated by 1.417° of longitude, thus yielding estimates of Reynolds stress gradients with the same resolution obtainable from the single-satellite crossover method. Because of this lack of improvement in spatial resolution, combined with the fact that the parallel track estimates of geostrophic velocity offer no improvement in precision over the crossover method for realistic long-wavelength measurement and orbit errors, the parallel track method is no more useful than the crossover method for the investigation of eddy-mean flow interaction. Indeed, the parallel track method may be less useful if the residual long-wavelength measurement and orbit errors exceed 2 cm.

4. Conclusions

The precisions of geostrophic velocity estimates obtained from the crossover method introduced by Parke et al. (1987) and the parallel-track method introduced by Stammer and Dieterich (1999) were investigated from analytical formulae based on best estimates of the various components of altimeter measurement error. The results are generally consistent with the empirical analysis of simulated altimeter data by Leeuwenburgh and Stammer (2001) and show that no significant advantage of precision is obtained by the parallel-track method of geostrophic velocity estimation as compared to the crossover method. Indeed, if the long-wavelength measurement and orbit errors exceed 2 cm/s, the crossover method may provide more accurate estimates of geostrophic velocity. While the parallel-track method would provide velocity estimates at closely spaced points along the centerline between the two parallel tracks (albeit with an inherent spatial filtering as described in section 2.2), this sampling pattern offers no significant improvement of the resolution of horizontal gradients of the Reynolds stress field that are needed to estimate eddy momentum flux convergence and divergence.

References

Chelton, D.B., and M.G. Schlax, 2001: On the estimation of sea surface height and surface geostrophic velocity from a tandem TOPEX/POSEIDON and Jason-1 altimeter mission. *J. Geophys. Res*., submitted.

Chelton, D.B., J.C. Ries, B.J. Haines, L.-L. Fu and P.S. Callahan, 2001: Satellite altimetry. In *Satellite Altimetry and the Earth Sciences: A Handbook for Techniques and Applications*, L.-L. Fu and A. Cazenave, Eds., Academic Press, pp. 1-131.

Cronin, M., 1996: Eddy-mean flow interaction in the Gulf Stream at 68°W. Part II: Eddy forcing on the time-mean flow. *J. Phys. Oceanogr.*, **26**, 2132-2151.

Leeuwenburgh, O., and D. Stammer, 2001: Uncertainties in altimetry-based velocity estimates. *J. Geophys. Res*., submitted.

Lozier, M.S., W.B. Owens and R.G. Curry, 1995: The climatology of the North Atlantic. *Prog. Oceanogr*., **36**, 1-44.

Morrow, R., J. Church, R. Coleman, D. Chelton and N. White, 1992: Eddy momentum flux and its contribution to the Southern Ocean momentum balance. *Nature*, **357**, 482-484.

Morrow, R., R. Coleman, J. Church and D. Chelton, 1994: Surface eddy momentum flux and velocity variances in the Southern Ocean from Geosat altimetry. *J. Phys. Ocean*., **24**, 2050-2071.

Parke, M.E., R.L. Stewart, D.L. Farless and D.E. Cartwright, 1987: On the choice of orbits for an altimetric satellite to study ocean circulation and tides. *J. Geophys. Res*., **92**, 11,693-11,707.

Pedlosky, J., 1987: Geophysical Fluid Dynamics. Springer-Verlag, New York, 710 pp.

Preisendorfer, R.W., 1988: Principal Component Analysis in Meteorology and Oceanography, Elsevier, Amsterdam, 425pp.

Qiu, B., 1995: Variability and energetics of the Kuroshio Extension and its recirculation gyre from the first two-year TOPEX data. *J. Phys. Oceanogr.,* **25**, 1827-1842.

Stammer, D., 1997: Global characteristics of ocean variability estimated from regional TOPEX/Poseidon altimeter measurements. *J. Phys. Oceanogr*., **27**, 1743-1769.

Stammer, D., and C. Dieterich, 1999: Space-borne measurements of the time-dependent geostrophic ocean flow field. *J. Atmos. Oceanic Technol*., **16**, 1198-1207.

Tai, C.K., 1989: Accuracy assessment of widely used orbit error approximations in satellite altimetry. *J. Atmos. Oceanic Technol*., **6**, 147-150.

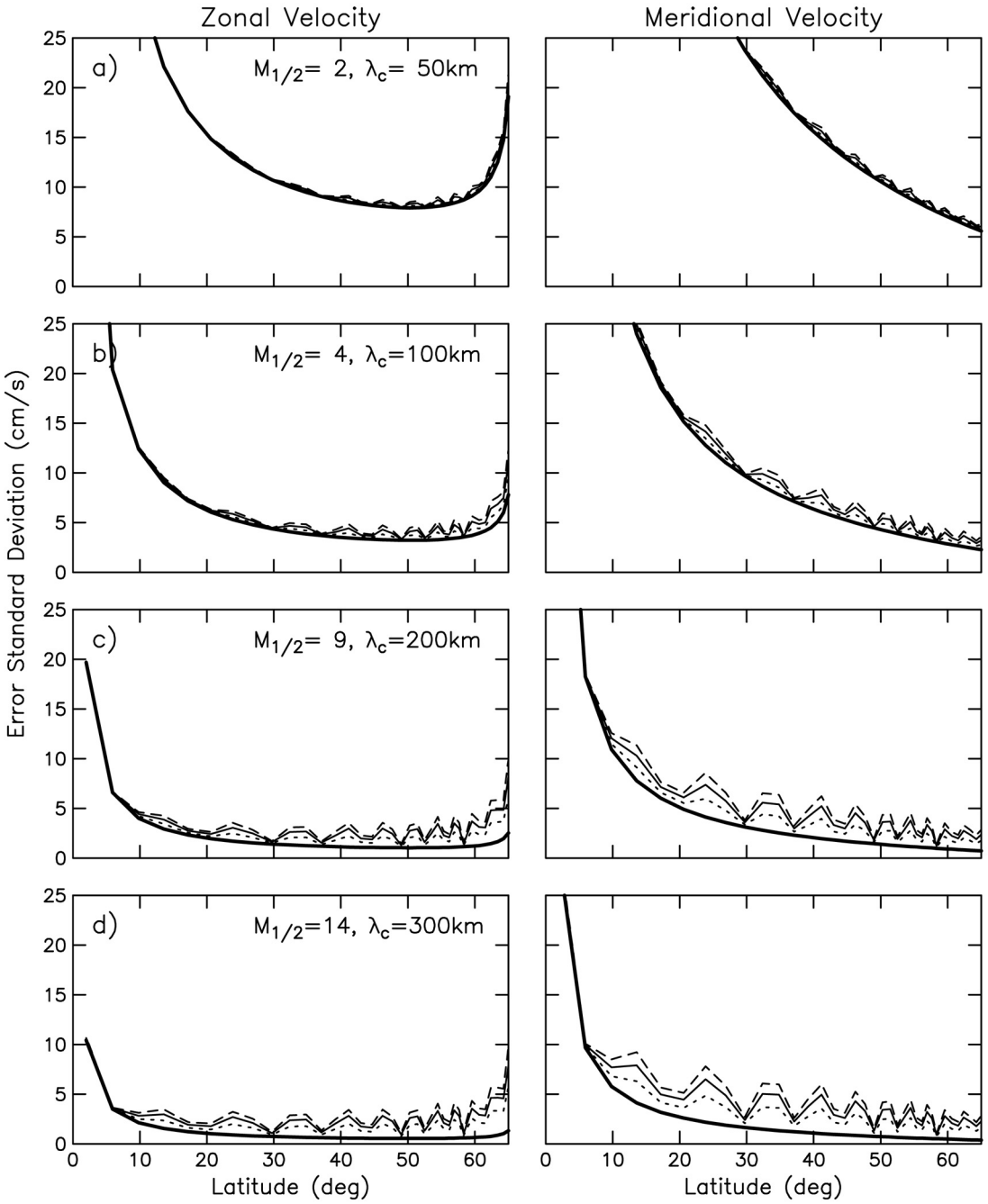

Figure 1. Latitudinal variations of the component error standard deviations of crossover estimates of geostrophic velocity for instrumental measurement errors with σ_e = 2 cm, geostrophic velocity signal variance σ^2_s = 50 cm^2/s^2 and signal autocorrelation functions $\rho(T)$ = 1.0, 0.75, 0.5 and 0.25 at lag T equal to the 9.9156-day T/P orbit repeat period (heavy solid, dotted, thin solid and dashed lines, respectively). Results are shown for along-track smoothing with half spans of a) $M_{1/2}$ = 2, corresponding to a filter wavelength cutoff of about 50 km; b) $M_{1/2}$ = 4, with a filter wavelength cutoff of about 100 km; c) $M_{1/2}$ = 9, with a filter wavelength cutoff of about 200 km; and d) $M_{1/2}$ = 14, with a filter wavelength cutoff of about 300 km.

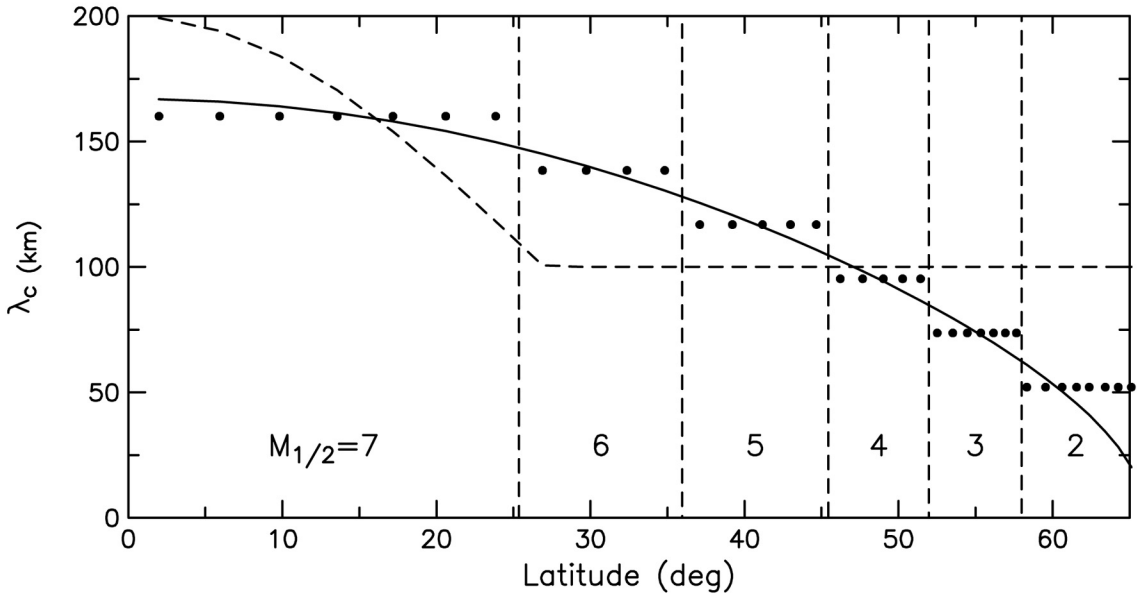

Figure 2. Latitudinal variations of the filter wavelength cutoffs in the parallel track estimates of geostrophic velocity components with a 0.5° offset between the parallel tracks. The solid line indicates the inherent filtering imposed by the latitudinal variation of the perpendicular separation between the parallel ground tracks. The dashed line indicates the filtering from the along-track smoothing applied by Leeuwenburgh and Stammer (2001) to reduce the effects of measurement errors. The dots indicate the filter wavelength cutoff associated with the values of $M_{1/2}$ (labelled near the bottom of the plot) chosen for the crossover method here in an effort to achieve similar filtering with the two velocity estimation methods.

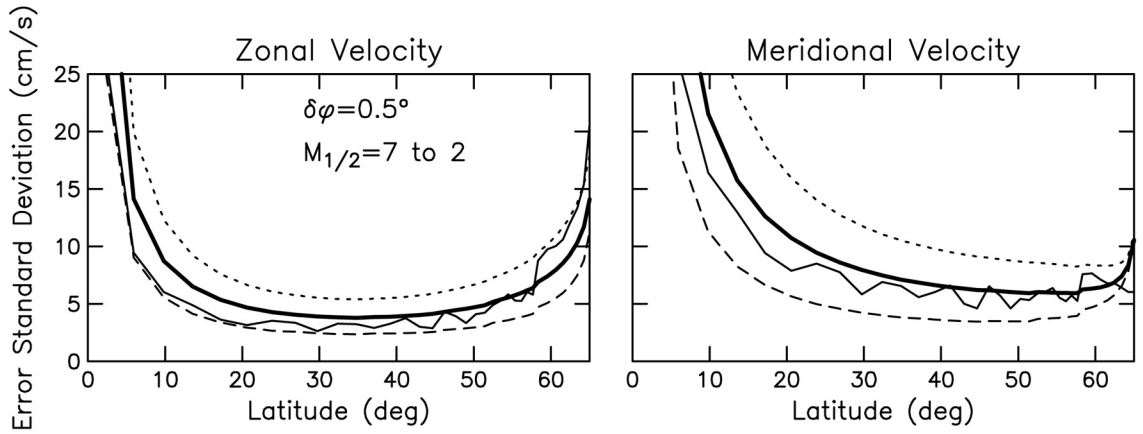

Figure 3. Comparison of the latitudinal variations of the component standard deviations estimated by the crossover method and the parallel track method for a parallel track offset of $\delta\phi = 0.5°$. The results are based on instrumental measurement errors with $\sigma_e = 2$ cm. The crossover estimates (thin solid lines) assume a geostrophic velocity signal variance of $\sigma^2_s = 50$ cm^2/s^2 and a signal autocorrelation function $\rho(T) = 0.5$ at lag T equal to the 9.9156-day T/P orbit repeat period. The parallel track estimates are based on long-wavelength measurement and orbit errors with $\sigma_o = 1$, 2 and 3 cm (dashed, heavy solid and dotted lines, respectively). Along-track smoothing was applied for both methods as described in the text.

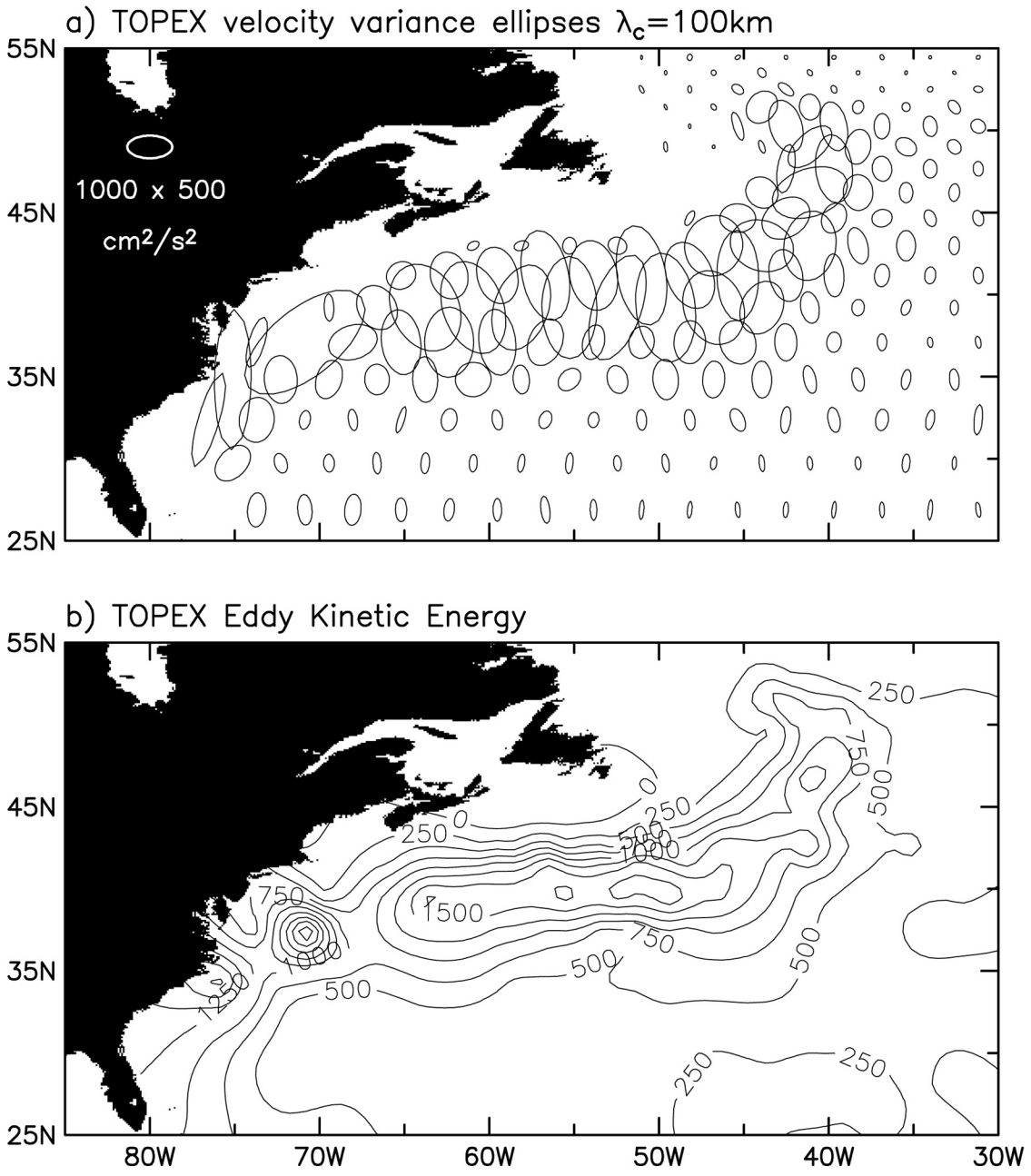

Figure 4. a) Velocity variance ellipses based on geostrophic velocity estimates computed by the crossover method from T/P data at the crossovers of ascending and descending ground tracks, and b) the associated eddy kinetic energy in cm^2/s^2.

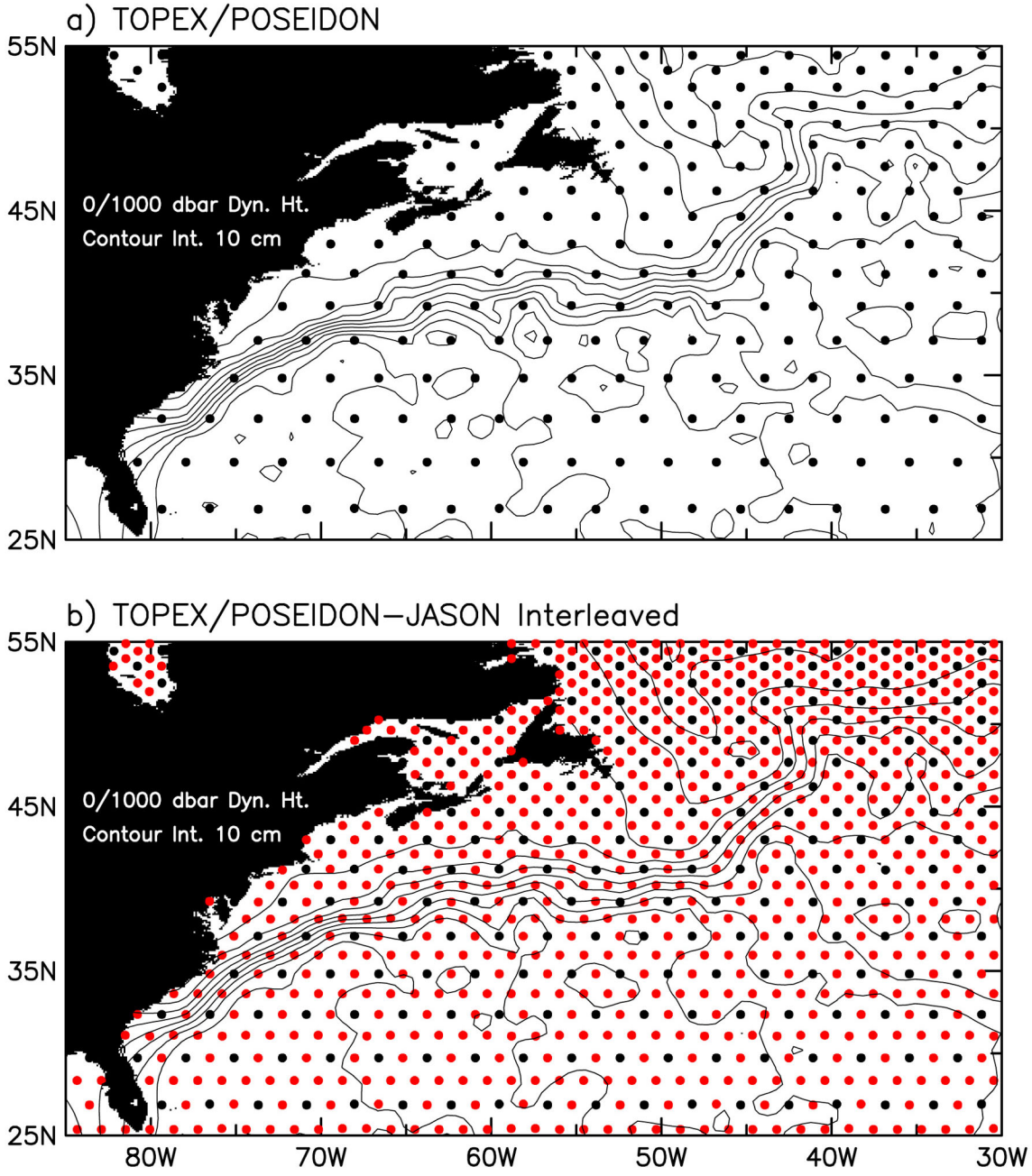

Figure 5. The locations of the crossovers of ascending and descending ground tracks from a) a single altimeter in the T/P orbit configuration, and b) an interleaved tandem orbit configuration with evenly spaced ground tracks. The red dots in b correspond to the additional crossover points afforded by the tandem mission. The contours in both panels represent the dynamic height of the sea surface relative to a reference level of 1000 dbar computed from the Lozier et al. (1995) hydrographic dataset.

Part 3

New Technologies for High-Resolution Measurements of Ocean Topography

WITTEX: An Innovative Multi-Satellite Radar Altimeter Constellation

A Summary Statement for the High-resolution Ocean Topography Science Working Group

R. Keith Raney and David L. Porter
Johns Hopkins University Applied Physics Laboratory
11100 Johns Hopkins Road, Laurel, MD 20723-6099, USA

Abstract WITTEX consists of multiple radar altimeters on individual satellites in the same orbit plane. Earth rotation separates their respective measurement tracks on the surface. In the monostatic version (co-located transmitter and receiver), each satellite generates one track, at nadir, as is standard in pulse-limited ocean altimetry. The nadir altimeters would have two frequencies (to mitigate ionospheric path delays) and a three-frequency radiometer (to estimate wet atmosphere propagation delays). Delay-Doppler techniques would be used to reduce each instrument's power and mass requirements, increase measurement precision, sharpen along-track resolution, and reduce the minimum stand-off distance from land. In the bistatic version (transmitter and receiver located respectively on neighboring satellites), an additional track would be generated at the midpoint on the surface between the satellites. Like nadir altimetry, the bistatic geometry supports natural measurements, in the sense that the sea surface heights are derived from the minimum of the waveform's range history. (This is in distinct contrast to the off-nadir geometry of a wide-swath altimeter, which is an un-natural measurement since surface heights must be extracted from a continuously increasing range history.) The bistatic altimeters need to have only one frequency. In general, a WITTEX-bistatic constellation of n satellites would generate 2n-1 surface tracks. All nadir and bistatic data will support wind speed, significant wave height, and sea surface height measurements with conventional algorithms and TOPEX-class accuracies. The co-planar satellites could be launched cost-effectively from one vehicle. Their sub-satellite tracks would be separated in proportion to their inter-satellite orbital spacing. At maximum latitudes their tracks coincide, so their respective height measurements can be cross-calibrated routinely. Data from a WITTEX constellation would support measurement of both components of the surface gradient, and would open a variety of beneficial solutions to the time/space sampling trade-off. In the future, in addition to a continuing altimeter in the Jason orbit, an operational WITTEX deployment is recommended. If nadir-viewing only, it would consist of five co-planar satellites in a Geosat orbit. These would produce five tracks at ~30 km separations at low latitudes. A WITTEX-bistatic configuration would maintain the same coverage with only three satellites. The cost of a WITTEX constellation, including all satellites, their altimeters, and their launch, is predicted to be less than the corresponding costs of TOPEX/Poseidon.

Introduction

Coordinated multiple nadir-sensing altimeters have long been acknowledged to offer the only way to achieve significant improvement in temporal and spatial topographic sampling of the global oceans, while simultaneously maintaining height accuracy (NASA, 1987; Rapley et al., 1990, Koblinsky et al., 1992; Fu et al., 1998; Greenslade et al., 1997; Jacobs et al., 1999; LeTraon and Dibarboure, 1999; Tapley et al., 1994; Stammer and Dieterich, 1999). In spite of their appealing and substantial science value, however, multiple satellite solutions have always been considered to be unrealistic, because their costs were perceived to be prohibitive (Fu et al., 1998; Koblinsky et al., 1992; NASA, 1999). The cost barrier can be substantially reduced, however, if the altimeters can be deployed simultaneously with only one launch vehicle, and if each individual satellite is sufficiently small and low cost. As outlined below, delay Doppler altimeters in a nadir-viewing WITTEX constellation should meet both conditions.

It is normally assumed that one altimeter generates height data along its track at nadir, so that "the number of altimeters" is equivalent to "number of tracks." However, there is a fundamental distinction to be made. The essential attribute for applications is the number of tracks along which accurate height measurements can be obtained, not the number of satellites. Mid-way between the nadir tracks from two altimeter satellites there is another track that could be generated, if the satellite pair was equipped with a bistatic radar. (In this context a bistatic radar is one in which the transmitter is on one satellite, and the receiver is on the other.) It can be shown that the measurement accuracies realized in the bistatic mode are

comparable to those in the nadir mode, to first order (Raney, 2001). If nadir and bistatic altimeters are combined, n satellites would generate 2n-1 measurement tracks on the surface. We denote such a constellation WITTEX-bistatic.

In the descriptions that follow, it is assumed that all WITTEX configurations would complement an ongoing TOPEX-class measurement series.

WITTEX

WITTEX is named in honor of Emil Witte who was the first to discover (1878) the geostrophic current equation. It also is an acronym for Water Inclination Topography and Technology Experiment. The two-dimensional geostrophic current can be derived if two orthogonal components of the surface height gradient can be observed hence WITTEX. To date, satellite radar altimeters have been able to measure only the along-track component. WITTEX would overcome that limitation with a constellation of three or more co-planar small-satellite radar altimeters (Fig 1). The satellites are spaced apart by several hundred kilometers. Their sub-satellite tracks are laterally separated because of the Earth's rotation. At a given latitude, measurements occur within minutes of each other, so that the cross-track surface gradient can be measured as well as the usual along-track gradient. Track separation may be adjusted during mission operations by selection and maintenance of the inter-satellite spacing. Thus, measurement of the two-dimensional surface gradient can be optimized during a single flight mission. The sea surface height (SSH) data are free of off-nadir errors, since all measurements enjoy the accuracy inherent to pulse-limited geometry. Since all WITTEX satellites are co-planar, their surface tracks coincide at their latitude extremes. Height data from all measurements should agree at these points; WITTEX constellations are self-calibrating.

A WITTEX constellation can be tuned to favor dense spatial coverage, relatively tight temporal coverage, or other priorities. A change from one scenario to another would require a few days. Using the Geosat 17-day orbit as a reference (~800 km altitude, 108-degree inclination, ~17-day repeat, and 160 km equatorial track separation), consider four three-satellite possibilities (Fig 2). One could also envisage operational five-track coverage (Fig. 3) which could be realized either by nadir instruments alone or by a bistatic configuration.

SCENARIO I, *High spatial resolution* (~200 km orbital spacing): Each triplet of sub-satellite orbit tracks would be 24 km wide, and span less than 1 minute. This arrangement would support measurement of both the along-track and the cross-track surface gradients at about the same resolution.

SCENARIO II, Uniformly dense spatial coverage (~900 km orbital spacing): Each triplet of tracks would have a time spread of about 4 minutes, and all adjacent tracks would be ~50 km apart at the equator. This spacing is nearly optimum for observing oceanic eddy fields and surface energy transport (Stammer and Dieterich, 1999).

SCENARIO III, *High temporal resolution* (~2600 km orbital spacing): This arrangement would place each succeeding altimeter's track on top of the spatially adjacent one. This would generate three- and six-day revisit cycles, in addition to the normal 17-day Geosat cycle. An alternative version of this scenario would space the satellites ~5200 km apart, resulting in effective six- and twelve-day repeat cycles within each 17-day base cycle. Frequent revisit is desirable to observe the evolution of large-scale features, such as El Niño.

SCENARIO IV, Site-specific coverage (controlled spacing): Given that one of the altimeters would be dedicated to a fixed exact-repeat mission, the others in the constellation could be moved as required upon command. This would allow a user to shift the altimeters' tracks to pass over an area of particular interest, which would have scientific, military or natural hazard applications. With two roaming satellites, any given site could be covered by both an ascending and a descending pass. This guarantees at least one

cross-over and more frequent coverage at the site of interest. Alternatively, the satellites could be timed to generate four cross-overs that would bracket the site. Finally, this scenario could be tuned to provide much-needed spatial data to upgrade existing bathymetric surveys.

SCENARIO V, an operational constellation of small, nadir-viewing satellites (~460 km orbital spacings). Five altimeters in a Geosat orbit would produce ~30 km inter-track spacing near the equator, and near-simultaneous coverage (<5 minutes time spread) by each set of five nadir tracks. The next adjacent set of five tracks would occur three days later (or earlier). This time/space coverage is nearly ideal for observation of mesoscale eddy fields (Jacobs et al., 1999), surface energy transport (Stammer and Dieterich, 1999), and geostrophic current vectors (Greenslade et al., 1997; Stammer and Dieterich, 1999), none of which can be observed directly by present means. This scenario provides better temporal and spatial coverage as well as greater on-orbit redundancy, at relatively small marginal cost over a constellation of fewer satellites.

WITTEX-Bistatic

The same track coverage portrayed in Fig. 1 could be generated by only two satellites if the center track were illuminated in a bistatic mode. A bistatic radar is one for which the transmitter and the receiver are located separately, in this case on different widely spaced satellites. The bistatic sea surface height measurement can be shown (Raney, 2001) to sustain accuracies comparable to those of the nadir mode. The bistatic measurement focuses on the specular point between the transmitter and the receiver. The specular point is located at the minimum radar range between the two satellites, and its forward reflection (towards the receiver) is very strong. Note that knowledge of the precise range or incident angle of the specular point is not required, since the sea surface height is contained in the minimum range observed in the reflected signal. The Doppler properties of reflections from the neighborhood of the specular point are equivalent to those at nadir, so that all advantages of the delay-Doppler paradigm (outlined in the following section) carry over to the bistatic case. In general, n satellites equipped with nadir and bistatic altimeters would generate 2n-1 accurate measurement tracks on the surface.

In the generalized WITTEX-bistatic configuration, each satellite would host three altimeters: one viewing nadir, and two others, each pointed at the nominal specular point corresponding to the fore and aft neighboring satellites in the constellation. (The end members would require only one bistatic instrument, but it should be cost effective to make all satellites identical. This would support partial on-orbit redundancy, and achieve maximum cost savings through duplicate satellite construction.) The nadir instruments would be as described below. The bistatic instuments would use only one frequency, and would not include radiometers. The necessary atmospheric and ionospheric path-length corrections to the bistatic legs could be interpolated from the nadir instruments, as there always would be sufficient data available from the nadir measurements. (Note that the greatest space and time separations between the bistatic and the nadir propagation paths would be half of the surface track spacing, and within a few minutes coincidence, respectively.) Further, each pair of satellites must communicate with each other, and maintain knowledge of their respective spacings to within a few centimeters. Whereas this is well within the state-of-the-art, it is a requirement in addition to those of a simpler WITTEX constellation. Clearly, each WITTEX-bistatic satellite would be somewhat larger and more complex than the smaller-better-cheaper nadir-sensing WITTEX birds.

Bistatic WITTEX constellations open new possibilities for on-orbit arrangements. We have considered one situation (Scenario VI) that is a step towards maximizing coverage from a multi-satellite configuration. If all specular points were used, including especially those between outlying spacecraft, then four satellites would be sufficient to generate nine (9) surface tracks. In a Geosat orbit, these would have equatorial spacings of only about 18 km. There are two primary down sides to this scenario. Two of the spacecraft would have to be host to three bistatic altimeters in addition to the nadir-viewing instrument. Also, several of the bistatic measurements would be at included angles considerably larger than sixty degrees, and hence their accuracies would be degraded. The most appealing bistatic

constellations are those in which only nearest-neighbor specular points are used, as illustrated by the next scenario.

SCENARIO VII, three-satellite WITTEX-bistatic (~920 km orbital spacings). Instead of five nadir-sensing altimeters, consider three bistatic (and nadir) altimeter satellites in a Geosat orbit. These would produce the same coverage as Scenario V (Fig. 3), namely, ~30 km inter-track spacing near the equator, and near-simultaneous coverage. Note that the interpolations required for bistatic path length corrections would need to span only 30 km.

Implementation

One vehicle can launch multiple satellites efficiently into the same orbit plane, if the satellites are sufficiently small. Fortunately, the delay Doppler radar altimeter (DDA) leads to a smaller instrument, and therefore a smaller satellite, than would be possible with the conventional radar altimeter paradigm (Raney, 1998). In addition, altimetry performance is improved. Although the DDA technique requires much less transmitted power, it yields more precise measurements than a conventional radar altimeter even though it has a much smaller along-track footprint (Jensen and Raney, 1998), and it can operate more reliably up to the shoreline. The delay Doppler technique has been proven in airborne demonstrations, supported by NASA's Instrument Incubator Program.

The waveform-generation algorithms of an orbital version would be similar to those of TOPEX, augmented by the delay Doppler paradigm. The waveform data volume from each altimeter will be on the order of twice that of TOPEX; the high-resolution waveforms will be generated at a 27 Hz rate, corresponding to resolved footprints of 250 m in the along-track direction. Waveforms averaged at a 1-Hz rate would have along-track resolution of 6.75 km, regardless of SWH. These waveforms have been shown (by simulation) to have comparable accuracy and approximately half the variance of the corresponding TOPEX 1-Hz SSH, wind speed (WS), and significant wave height (SWH) measurements.

The Earth's equatorial rotation rate of ~450 m/s, combined with a track-repeat tolerance of ~1 km, translates into an along-orbit relative position control requirement of only ~9 km for the nadir WITTEX configurations. Relative spacecraft spacings must be known to centimeters for accurate height measurements from the WITTEX-bistatic array. As is true for all WITTEX scenarios, their respective height measurements coincide at the latitude extremes. This provides a robust basis for cross-satellite relative calibration.

Each WITTEX nadir altimeter has two frequencies and an on-board water vapor radiometer (WVR), similar to the TOPEX design. The bistatic radars need have only one frequency. The DDA approach, combined with recent advances in spacecraft technology, leads to substantial miniaturization for either the nadir or the bistatic altimeters. The mass of each nadir WITTEX satellite is predicted to be less than 100 kg. This is about one-third that of Geosat Follow-On. The nominal mass objective for each WITTEX-bistatic satellite is less than 200 kg.

The cost estimated for either a five-satellite WITTEX-monostatic constellation or a three-satellite WITTEX-bistatic constellation (including their payloads and launch into a Geosat orbit) is less than the counterpart costs for TOPEX/Poseidon. Although there are only three satellites in the bistatic configuration of Scenario VII, each is more complicated than the nadir-viewing WITTEX spacecraft. Nevertheless, the total cost of the bistatic version could well be substantially less than that of a five-track nadir WITTEX configuration. WITTEX-monostatic would require five two-frequency altimeters with WVRs, as opposed to WITTEX-bistatic, which would require only three two-frequency altimeters with WVRs. In addition, two bistatic single-frequency altimeters would be required, augmented by inter-satellite communications and distance measurements. The operational costs of WITTEX-bistatic should be less. For example, precision orbit determination would be required for only three satellites, rather than five.

WITTEX-Wide

WITTEX-Wide would be a constellation of three co-planar radar satellites, except that the center satellite (DD2 in Fig 1) would be a DDA and a wide-swath altimeter (Rodriguez et al., 2001), rather than a nadir-sensing instrument alone. From a TOPEX-class orbit, the JPL multi-beam altimeter concept would generate SSH data at ~15-km postings across a swath approximately ±100-km centered on nadir. In the WITTEX-Wide concept, two co-planar altimeters (DD1 and DD3), one leading and one trailing the wide-swath altimeter, would create parallel tracks to each side of the swath's center line. If DD1 and DD3 were separated from the wide-swath altimeter by about 1200 km along their orbit, the resulting cross-track nadir spacings would be about 75 km at the equator. The set of three satellites in such a WITTEX-Wide constellation would pass each observation neighborhood within five minutes of each other.

Although appealing in principle, a wide-swath altimeter has several disadvantages that have to be overcome before it might live up to its promise. These disadvantages include: (*i*) a large sensitivity to errors in satellite roll knowledge, (*ii*) an inherent inability to measure SWH off-nadir, (*iii*) an inherent dependence on extrapolations (and, at low wind speeds, sensitivity to the relative direction of wave propagation) for off-nadir em-bias corrections, (*iv*) a lack of direct measurements to correct for wet atmosphere delays in the off-nadir channels, (*v*) a lag of many days before cross-track and along-track height measurements can be reconciled at their intersections, (*vi*) a progressive trend toward parallel tracks as the measurement latitude approaches the plane of inclination, thus frustrating the roll correction algorithm, (*vii*) a necessity to develop and qualify new analysis algorithms, and (*viii*) a relatively costly approach that may not readily be configured to support operational reliability and on-orbit redundancy.

WITTEX-Wide could help to offset many of these disadvantages. Inherently accurate pulse-limited heights from "the outrigger" altimeters would provide continuous roll- and path-length-corrected height data that could be used as reference profiles to reduce systematic errors from the wide-swath off-nadir measurements. However, these benefits, like the effectiveness of the wide-swath correction algorithm itself, decrease monotonically (to zero) as latitude increases towards the altimeters' inclination.

On Natural Height Measurements

The great virtue of a pulse-limited radar altimeter is that the measurement objective, sea surface height, is measured directly (subject of course to path length corrections and precision orbit determination). That is, the radar range of interest is the minimum range observed in the ensemble of signals reflected beck to the radar. There is no need to establish the precise neighborhood giving rise to the reflection, nor to the angle of incidence relative to the radar. Nadir is by definition the closest point to the altimeter, and any change in sea surface height is manifest as a corresponding change in the minimum range to that point. This may be denoted a *natural measurement*.

The same virtue carries over to bistatic measurements of sea surface height. That is, the radar range of interest is the minimum range observed in the ensemble of reflected signals available to the radar. Just as in nadir altimetry, for bistatic height measurements there is no need to establish the precise neighborhood giving rise to the reflection, nor to the angles of incidence or reflection relative to the radars. The specular point is by definition at the minimum reflected range between the two satellites, and any change in sea surface height is manifest as a corresponding change in the minimum range of all rays reflected from the neighborhood of that point. Thus, a WITTEX-bistatic height is also a *natural measurement*.

The situation is very different for any scheme that would attempt to measure sea surface height through backscatter gathered in a side-looking geometry. The wide swath altimeter is one example of such a geometry. In the side-looking case, extraction of sea surface height from radar range data requires that the angle from the radar to the ocean's surface be known, indeed, very well known. Radar range

increases monotonically with time, and with incident angle. There is no minimum in the range data that would firmly establish the height measurement point. If very accurate sea surface heights are required, then extremely accurate knowledge is required of the incident angle at the point of measurement. Height measurements in a side-looking geometry is by definition a problem in triangulation, rather than a minimum distance along a straight line. Triangulation introduces new uncertainties, and these induce new sources of sea surface height error. We consider triangulation to be an *un-natural measurement* if accuracy is required.

Being an un-natural measurement, wide swath altimetry starts with a fundamental disadvantage. This disadvantage can never be fully overcome. As acknowledged by its most ardent proponents (Rodriguez et al., 2001), there is no way to meet the angle knowledge requirement by direct means. The tolerances fall approximately two orders of magnitude beyond current hardware capabilities. Thus, the implied systematic errors in off-nadir height measurements must be met by indirect methods. Those methods include extensive temporal and spatial averaging. This averaging in effect is a low-pass filter. The end product of height fields may well have data postings at relatively close spacings and reduced variance, but only those signals that pass through the averaging filter will be portrayed.

Conclusions

At present there are no means in place to observe vector velocity fields over the oceans. A WITTEX constellation would be the first and perhaps the only feasible means to meet this requirement. Estimates of kinetic energy, Reynolds stresses, mean and meandering flows of the world's oceans would become a routine observation. These estimates would contribute to accurate modeling of CO_2 atmosphere-ocean exchange as well as the long-term modeling of large-scale dynamic effects such as El Niño.

Mesoscale ocean phenomenon (~50-100 km) are both spawned by and can drive the mean flow. Oceanic rings, western boundary current meanders, and deep ocean eddies are important in modifying not only the dominant flow over much of the ocean but in affecting the geochemical, chemical and biological oceanography. Eddy fields transport, entrap, and disperse chemicals, dissolved substances, nutrients, small organisms and particulate matter, and are central to the oceanic energy exchange processes.

The WITTEX concept, either the nadir-viewing WITTEX-monostatic or WITTEX-bistatic, is an elegant response to these and other long-standing needs in precision oceanic altimetry. In contrast to other means of generating coverage, it is inherently accurate, and self-calibrating. WITTEX offers a flexible, capable, unique, and cost-effective approach that would significantly advance the state-of-the-art of satellite radar altimetry.

Ten years from now we could be poised to implement a nearly ideal yet affordable multiple satellite solution in response to the altimetric requirements delineated by the oceanographic and geodetic science communities. In subsequent decades, the paradigm for operational ocean topographic measurements should be radar satellite constellations.

References

Fu, L.-L., C. Wunsch, R. Cheney, and C. Koblinsky, 1998: Measuring ocean topography for understanding and predicting climate change. (Response to NASA Request for Information).

Greenslade, D.J.M., D.B. Chelton, and M.G. Schlax, 1997: The mid-latitude resolution capability of sea level fields constructed from single and multiple altimeter data sets. *J. Atmos. Oceanic Technol*., **14**(8): 849-870.

Jacobs, G.A. et al., 1999: Navy Altimeter Data Requirements. NRL/FR/7320--99-9696, Naval Research Laboratory, Stennis Space Center, Mississippi.

Jensen, J.R. and R.K. Raney, 1998: Delay Doppler radar altimeter: better measurement precision. Proceedings IEEE Geoscience and Remote Sensing Symposium IGARSS'98. IEEE, Seattle, WA, pp. 2011-2013.

Koblinsky, C., P. Gaspar, and G. Lagerloef, 1992: The future of spaceborne altimetry: oceans and climate change. Joint Oceanographic Institutions, Inc, Washington, DC.

LeTraon, P.Y. and G. Dibarboure, 1999: Mesoscale mapping capabilities of multiple-satellite altimeter missions. *J. Atmos. Oceanic Technol.*, **16**, 1208-1223.

NASA, 1987: Altimetric System, Earth Observing System Panel Report, Vol. IIh, Washington, D.C.

NASA, 1999: Report of the Workshop on NASA Earth Science Enterprise Post-2000 Missions, NASA, Washington, DC.

Raney, R.K., 1998: The delay Doppler radar altimeter. *IEEE Transactions on Geoscience and Remote Sensing*, **36**(5): 1578-1588.

Raney, R.K., 2001: Bistatic WITTEX Altimetry. SRO-01-05, Johns Hopkins University Applied Physics Laboratory.

Rapley, C.G., H.D. Griffiths, and P.A.M. Berry, 1990: Proceedings of the Consultative Meeting on Imaging Altimeter Requirements and Techniques. University College London, London, England.

Rodriguez, E., B.D. Pollard, and J.M. Martin, 2001: Wide-swath altimetry using radar interferometry. *IEEE Transactions on Geoscience and Remote Sensing*, (to appear).

Stammer, D. and C. Dieterich, 1999: Space-borne measurements of the time-dependent geostrophic ocean flow field. *J. Atmos. Oceanic Technol.*, **16**, 1198-1207.

Tapley, B. et al., 1994: Report of the Altimeter Study Group to NASA Headquarters and the EOS Payload Panel. The Earth Observer, Vol. 7(No. 1).

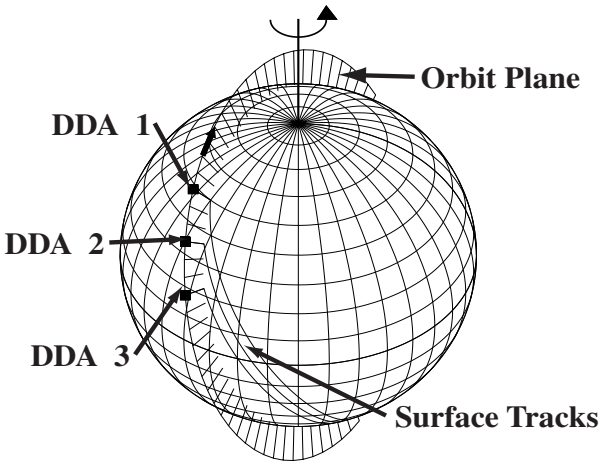

Figure 1. Three-satellite nadir-viewing WITTEX Constellation.

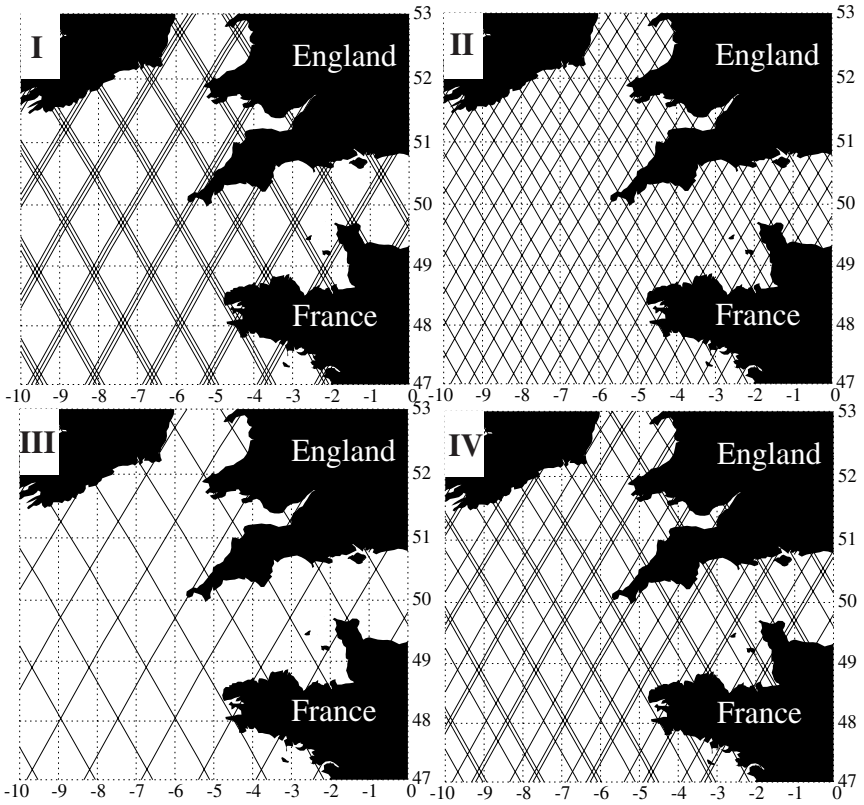

Figure 2. Four three-satellite nadir-viewing WITTEX scenarios.

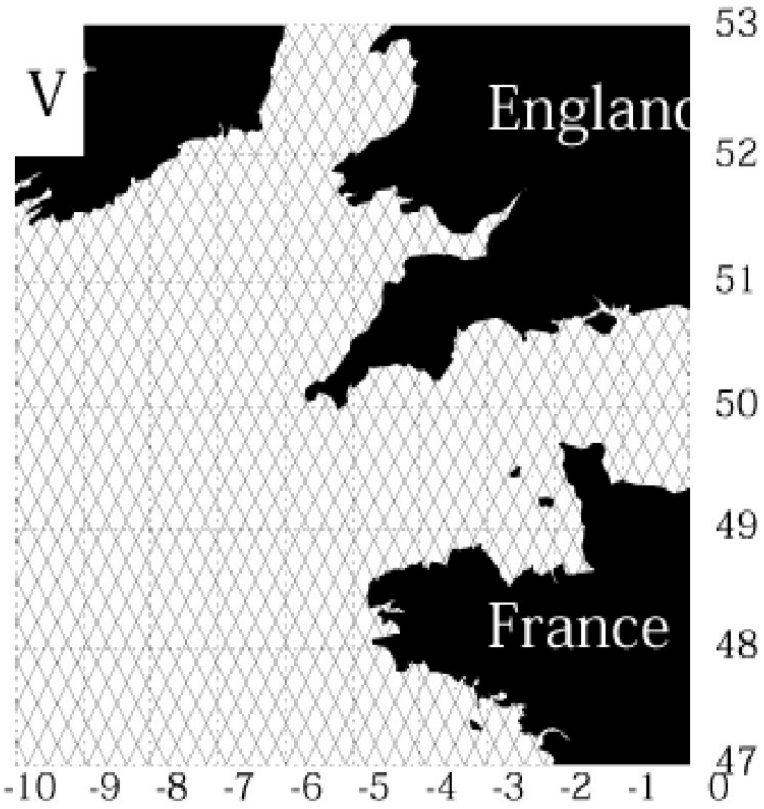

Figure 3. An operational five-track pattern from Geosat orbit.

Status of Ka-Band Altimetry Studies

Patrick Vincent and Eric Thouvenot
CNES
18, Avenue Edouard-Belin
31401 Toulouse Cedex, France

Abstract. Ka-band altimetry has been proposed by Verron et al. (2001) to complement the altimetry reference missions of the Jason class. The goal of this paper is to provide information on the so-called "AltiKa" proposal in terms of science requirements, responsive technical specifications, and a priori performances. Besides the fact that the feasibility of embarking an AltiKa payload on a microsatellite has already been assessed, there is also the information that a small launcher may have the capability of launching several microsatellites simultaneously (up to three) in a number of configurations that may be adapted to the space time requirements of high resolution altimetry.

1. Introduction

The development of altimetry has been steady and the benefits outstanding. There has been a quasi-continuous series of missions, starting with GEOSAT (1985), and then ERS-1/2 (1991 and 1995), and TOPEX-POSEIDON (1992). These will continue into the next century with Jason-1 and ENVISAT, that are respectively scheduled for launch in 2001.

More generally, the heritage of past and current oceanographic space missions has paved the way for the incremental implementation of the space component of the Global Ocean Observing System. Because they have already demonstrated their "pre-operational" maturity, in terms of end-to-end performances, value to users and affordability, altimeter and scatterometer missions are the first immediate candidates for operational transition. Short-term decisions are therefore required to secure continuity and enhancement of the current altimeter and scatterometer systems in the GODAE (Global Ocean Data Assimilation Experiment) timeframe and beyond.

In the short term, the future looks secure with a two-satellite altimeter system being maintained for the next five years with Jason-1 and ENVISAT. It is foreseen that the combined use of their data with measurements from independent gravity missions such as CHAMP (2000), GRACE (2001) and possibly GOCE (2004) will be another breakthrough. It should enable absolute estimates of ocean currents, to be obtained by subtracting an independent estimate of the geoid from individual altimeter height measurements.

A first firm decision is however needed in the very short term to secure continuity through Jason-2 measurements in the GODAE window. Further decisions will be needed to maintain a multi-satellite system providing the required accuracy, coverage and sampling beyond the GODAE window, after the end of life of ENVISAT. Such a system should provide an affordable service equivalent to one Jason-class mission and one or two medium accuracy missions of the ENVISAT class. Several options need to be evaluated, taking into account results of R & D and demonstration missions aimed at validating new candidate observing techniques.

The goal of this paper is then to provide the reader with the status of Ka-band altimetry, considering the embarkment of the system on a microsatellite platform.

2. The AltiKa proposal: about science objectives

The science objectives of the AltiKa mission are described in Verron et al. (2001) and in Remy et al. (1999) in very details.

Hereafter, we only recall those of the objectives that most impact the design of the altimeter instrument and the payload.

2.1. Ocean mesoscale variability

Based on the need to resolve the mesoscale variations and to study the effect of these fluctuations on the energetics of the mean circulation, the spatial and temporal resolution required is set by the need to directly observe the mesoscale variability to a degree that allows, in conjunction with assimilative numerical models, a proper description of the oceanic eddy field and the interactions of this field with the mean field.

In 1999, G. Mitchum et al. summarized some of the requirements for a well adapted sea-surface height system: The section below partly derives from Mitchum et al.'s statements concerning space altimetry. The constraint concerning the spatial and temporal resolution of a sea-surface height system means that we must be able to resolve signals that occur at spatial scales on the order of several oceanic Rossby radii, and on time scales of days to weeks, which cannot presently be done with a single altimeter. The important question is how many altimeters must be available at any given time, and what orbits should these satellites occupy? Jacobs et al. (1999) have estimated that three altimeters are needed to directly observe the mesoscale variations without additional statistical or dynamical model input. If assimilative models are used, however, two satellites may be adequate. In a different set of simulations, Le Traon and Dibarboure (1999) conclude that most of the improvement in reproducing the mesoscale variability is obtained in going from a single altimeter to two flying simultaneously. Adding additional altimeters improves the results, but to a lesser degree.

It is clear that at least two altimeters are required, and that additional altimeter would still improve the science return, but the optimal number is still under study.

Other ocean topics may also add spatial and temporal requirements that will impact the number of altimeters needed to get high space-time resolution.

2.2. Contribution in coastal altimetry and continental waters

The initial single satellite AltiKa proposal did not have the goal to answer the space-time requirements corresponding to a fully adapted sampling of the coastal dynamical features. We'll come to the possibility of flying a multisatellite AltiKa constellation in the conclusion.

However, coastal altimetry has been a driver to derive new instrumental spcecifications to answer new performance requirements both in terms of noise and along-track space resolution.

At the same time, we also considered how a new altimetry system may answer requirements dealing with the observation of continental waters (lakes, reservoirs, rivers) such as the requirements listed in the HYDRASAT proposal. Once again, besides the time sampling issue, we looked at the orbit pattern that may be useful to have in complement of Jason to sample the major continental water areas; we also tried to focus on space resolution requirements avoiding to design an instrument that would be specific to the altimetry of lakes and rivers keeping in mind that the main driver is ocean altimetry.

Some main technical features of the Ka-band altimeter that is part of the AltiKa payload are directly derived from the coastal and continental water requirements : they are described in more details in sections 3 and 4.

2.3. Ice sheet ice monitoring

As the AltiKa payload has been foreseen to also continue the ERS/ENVISAT series of altimeter measurement of ice sheets, we also considered some basic features of ice altimetry that may impact the technical specifications of AltiKa.

The monitoring of the ice-sheet height over Antarctica and Greenland is of primary importance for climate studies. However, one of the major limitations of the ice sheet mass balance study, is presently the poor knowledge of the radar wave penetration within the snowpack, in Ku-band for the ERS1/2 altimeters. The induced volume echo is of the same magnitude as the surface echo, yielding to a critical situation: The induced effect is twofold: it directly acts on the surface elevation accuracy and, due to the temporal change in the snow characteristics from daily to yearly scales, it produces a long term analysis error that can hide the long term trend.

Then, the objective was to try speciying the altimeter so that penetration effects would be minimized with respect to Ku-band altimetry.

3. Ka-band payload characteristics

3.1. General requirements and proposed payload

The above objectives were translated into some main features of the Ka-band payload:

- get an altimeter instrument whose range noise performance may be so that the recovery of the ocean short wavelength features is improved,
- get an altimeter instrument with an improved space resolution along-track and a better performance when approaching or leaving coastal boundaries,
- get an altimeter instrument that will minimize the penetration effects over media such as continental ice,
- embark an orbitography system that will ensure a high level of accuracy in terms of orbitography and that will ease the connection of historical altimetry series within a common well surveyed geodetic reference frame,
- embark a microwave radiometer that will help correcting altimeter measurements for wet troposphere effects.

To answer the previous requirements, it is proposed to compose an AltiKa payload with:

- A single frequency Ka-band (35 GHz) altimeter instrument (see Phalippou et al. (2000) for details)
- A two-frequency radiometer,
- A DORIS receiver,
- A passive laser retroreflector array.

3.2. Summary of some characterisitics of the Ka-band altimeter

From the above requirements, we derived altimeter instrument specifications that are compared with the POSEIDON-2 specifications in the table below:

	AltiKa	POSEIDON2
Altitude	500 to 800 km	1340 km
Inclination	~98°	66°
Lifetime	2 years (objective : 3 years)	5 years
Frequency	35.75 GHz	13.65 GHz
Bandwidth	480 MHz	320 MHz
PRF	4000 Hz	~2000 Hz
Signal to noise ratio	> 10dB	> 10dB
Spectral analysis	128 gates	128 gates
Integration duration	25 to 50 ms	50 ms
Mass	<20 kg	70 kg (C+Ku)
Consumption	< 50 W	78 W (C+Ku)

To comment the above table, we can add the following:

- At Ka-band, the ionosphere effects are much lower than at Ku-band and maybe considered as negligible, except for some exceptional ionospheric situations (in the latter cases, the embarkment of DORIS may provide a backup solution to retrieve the ionospheric correction). This is one reason for the choice of such a frequency band for a single frequency altimeter.
- The decorrelation time of sea echoes at Ka-band is shorter than at Ku-band. This gives the possibility to significantly increase the number of independent echoes per second compared with Ku-band altimeters. The instrument is designed for a high Pulse Repetition Frequency (PRF) around 4000 Hz.
- The antenna beamwidth is smaller for the Ka-band altimeter than for Ku-band POSEIDON 2. This gives a Brown echo which is sharper than the echo obtained with altimeters such as POSEIDON 2; the echo power is also lower due to larger gain variation in the pulse limited footprint.
- The 480 MHz bandwidth that may be used at Ka-band will provide a high vertical resolution (0.3 m) which is improved with respect of all flying altimeters (including Jason and ENVISAT)
- It is known that Ka-band EM waves are sensitive to rain. In addition to attenuation effects, perturbation of echoes by rain has to be analyzed in terms of the retrieval of the 3 geophysical parameters to be estimated from waveforms (to be discussed in a decicated section).

3.3. About the dual frequency radiometer

The selection of the radiometer type has been driven by:

- The basic science requirement, that is to perform the measurements necessary to get the wet troposphere correction with a sufficient accuracy;
- The willingness to embark the AltiKa payload on a microsatellite, which requires a compact and simple instrument.

Frequencies have been selected to be optimal for the case of a dual frequency radiometer, that is 23.8/36.5 GHz. A three-frequency radiometer would be more difficult to embark because the lowest frequency (19 GHz) would impact the system on the microwave and antenna point of views. In addition, it is possible to overcome this drawback by adapting a wet troposphere retrieval algorithm incorporating

the relationship between the wind and the altimeter backscatter coefficient (for instance, such a solution is used for the ENVISAT altimetry).

The 23.8 GHz frequency will use the full width of the allocated bandwidth, that is 400 MHz. Concerning the 36.5 GHz frequency, the fact that it is near from the altimeter frequency does not allow the use of the whole allocated bandwidth which is 1 GHz. In addition, the accuracy of the wet tropospheric correction does not much depend on this bandwidth. Then, it is envisaged to use a 400 to 700 MHz bandwidth with a high probability to select a 400 MHz band (so that the high frequency of the radiometer is centered at 36.8 GHz).

After comparing the known radiometer concepts, we selected a so-called "Total Power" radiometer which has the most simple architecture and that also provides the best radiometric sensitivity. The counterpart is the necessary frequent radiometric calibrations because of the high sensitivity to the gain variations.

3.4. An integrated Altimeter + Radiometer instrument

One of the initial requirements to design the AltiKa payload was that it should be possible to embark it on a microsatellite and that it could also be provided as a whole to become a passenger on an apportunity platform.

This has lead us to define an integrated instrument that allows for interface optimization and reduction of the number of units (boxes) . Indeed, the integrated instrument is composed of:

- One microwave unit that gathers all microwave functions of the altimeter and the radiometer, including the calibration functions of the radiometer and the sources of the antenna.
- One processing unit that gathers all functions dedicated to the altimeter and radiometer processing, as well to a global management unit.

4. Performances and impact on some science objectives

4.1. Minimizing the range noise of the altimeter measurement

The Ka-band (35 GHz) is more interesting than the Ku-band for the altimeter since it improves the link budget and allows larger bandwidth (up to 500 MHz) and pulse repetition frequency (4 kHz).

The selected 480 MHz bandwidth provides a 0.3 m vertical resolution.

Due to the smaller antenna beamwidth, the Brown echo has a sharper shape in Ka-band than that what is obtained with conventional altimeters in Ku/C-band (e.g. POSEIDON 2).

The proposed architecture for the Ka-band altimeter is based on the classical deramp technique for pulse compression and it takes benefits of French experiences from the realisations of POSEIDON 1 & 2. A wide band chirp (~480 MHz) of about 107 µs duration is emitted. The digital processing includes the real time FFT, echo integration and radiometer processing (power averaging). The main limitation of Ka-band is the non-operationality for rain rate higher than several mm/h (5 to 10% of time for AltiKa depending on the geographic area).

Range noise comparison with POSEIDON 2 altimeter shows that AltiKa will provide excellent performances (see Figure 1).

Since no ionospheric correction is required for AltiKa (DORIS might indeed provide a correction in extreme, rare ionospheric conditions), the expected improvement is close to a factor of 3 (for example, 1-s range noise at 2-m SWH would be less than 0.8 cm for AltiKa vs 2.2 cm for POSEIDON 2).

4.2. Space resolution improvement wrt classical Ku-band altimetry

This very good range performance will be associated with reduced footprints and better coastal performance as well.

Performance for coastal applications depends:
(i) on waveform / footprint relationship
(ii) on antenna diagram / footprint relationship (to obtain attenuation of land contribution to echo
(iii) on tracking performance for complex (coastal or in-land) echoes.

AltiKa characteristics have been optimized for these 3 issues:
- AltiKa is close to a beam limited altimeter: there is no 'plateau' in the echo, since it strongly attenuates shortly after leading edge due to the small antenna aperture. This will greatly reduce the pollution of 'land gates' into 'ocean gates'.
- Tracking loops were designed at the same time as SIRAL/CRYOSAT altimeter for which continuous tracking in ocean/land/ice conditions is required. Thus, AltiKa is supposed to provide data in most coastal zones and in-land water areas. Moreover, in case of loss of track, acquisition/locking phase is required to be shorter than 500 ms, allowing a quick return to nominal tracking conditions (about 3 km along track).

	Leading edge (2-m SWH)	128-gate echo (2-m SWH)	Footprint diameter at 3-dB attenuation
POSEIDON2 (Ku-band)	5.3	19.1	19.5
POSEIDON2 (C-band)	5.3	19.1	49.5
AltiKa (800 km)	4.1	12.7	7.2
AltiKa (500 km)	3.4	10.3	4.6

Footprint diameter for different criteria (values given for a 75-cm antenna for AltiKa)

These values will be associated with small footprints for the radiometer as well since altimeter and radiometer will share the same antenna. In addition to the altitude reduction, which is the main contributor to the radiometer footprint reduction, it may also be noticed that the absence of an additional 19-GHz channel to the radiometer is also an advantage since this low frequency would give the largest footprint.

This is why it is expected that AltiKa will give useful data as close as 5 km from a majority of coastal areas. Associated with a shorter data cycle (probably 500 ms instead of 1 s), it will probably represent a major improvement in mesoscale and coastal applications of radar altimetry.

4.3. Minimizing penetration effects over continental ice

An empirical analysis of the temporal variability of the satellite radar altimetric observation demonstrates that the Ku-band radar penetration above the dry snowpack of Antarctica is between 5 m in the interior to 14 m at a lower altitude, before decreasing due to wetness near the coast. The absorption coefficient of dry snow being 0.05 m^{-1}, it induces a scattering coefficient comprised between 0.05 and 0.16 m^{-1}, depending on ice the grain size which varies from 0.2 to 3 mm.

In Ka-band, Mie scattering can be assumed, then the scattering coefficient is inversely proportional to the radar wavelength at a power 4. From Ku to Ka bands, the scattering coefficient will increase by a

factor 55: the volume scattering will then be clearly dominant over the surface scattering. Inversely, the radar wave extinction will also increase to values comprised between 2.75 and 8.75 m^{-1}, leading to a penetration depth over snow surface between 0.3 and 0.1 m. The altimetric observation and height restitution will thus correspond to a thin subsurface layer. The accuracy will then be considerably improved.

Moreover, ice grain size, that is one of the pertinent climatological snow parameters, could be directly derived from Ka-band scattering coefficient, which is not possible from present day Ku measurements that also highly depend on surface roughness.

However, the major benefit will lie in the reduction of the induced long term bias due to the temporal change in the snowpack surface. Indeed, a strong temporal variability of the altimetric observations over Antarctica ice sheet has been recently exhibited with the help of the ERS-1 three day orbit mission. These temporal variations are linked to meteorological events and consequently play a role on a large band of the temporal spectrum, from few hours to few decades. They are due to changes in surface roughness induced by change in wind, which modifies the echo surface part and then, both the waveform shape and the elevation recovery. Even with a dedicated correction, the residual correction yields to a raw noise estimate of 10 cm.

4.4. Propagation losses

4.4.1. Attenuation effects. It is known that propagation of EHF waves through the troposphere may suffer from severe attenuation due to the interaction of the electromagnetic wave with the atmospheric contents. As far as the Ka-band altimeter is concerned, current requirement is that the instrument provides nominal performance 90% of time, with an objective as high as 95%. An extensive study has been made to analyze the contributions from:

(i) gazes: attenuation is calculated for oxygen and water vapour. Even if the allocated frequency range is nearly ideally chosen with respect to the water propagation spectral window, strong attenuation may result from moderate to high humidity contents. Values may vary from 0.4 to 2.1 dB when humidity varies from 7.5 to 50 g/m3.

(ii) clouds: 7 types of clouds are taken into account for the propagation models. Attenuation is estimated from their liquid vapour contents and depths. As expected, cumulus and cumulonimbus are generally the main contributor (0.2 to 0.7 dB) to the total loss, and sometimes stratocumulus (0.05 to 0.2 dB).

(iii) rain: attenuation by rain, and possibly snow, is computed from rain rate and rainfall thickness.

Other possible contributors (ice, fog) have been shown to have no significant influence (order of 0.1 dB for the fog).

As far as rain is concerned, maximum precipitation rates are known as less than 1.5 mm/hr everywhere (95% through time) or even 1.0 mm/hr (90% through time) over ocean and polar areas, except in a region off the Philippines islands for which previous figures have to be doubled. Following accepted statistical distributions, one can associate some classical layering distributions with the previous rates. Then, total attenuation due to rain may be computed. Results show that attenuation is lower than 1.8 dB (95%) or even 1.2 dB (90%). Given these figures, we can conclude that:

- Case 1: no rain or very low rain rates, then a nominal functioning of AltiKa is ensured,
- Case 2: rain rates greater than 1.5 mm/h, then altimeter measurements will be degraded or even not acquired for the largest rain rates,
- Case 3: moderate rain rates less than 1.5 mm/h, then the echoes will have to be corrected using a specific algorithm modeling the perturbation of the echoes by rain cells.

To refine the previous statements, 7 years of TMR data from TOPEX/POSEIDON have been used to check some seasonal effects and to analyze the effect of local time which may be an important parameter to select in the case of a sun-synchronous orbit for AltiKa. Translation of TMR measurements into rain attenuation has been performed using dedicated algorithms and results have been mapped versus location, local time, month in the year, and on a multi-year time scale. On the one hand, the study has confirmed that Ka-band data availability will be greater than 90% over the world ocean and even greater than 95% for some areas such as the North Atlantic. On the other hand, it appeared that local times from 6 am to 12 am, and from 6 pm to 12 pm are the worst cases for rain, which may provide a «light» constraint for the optimization of the link budget of the instrument and select the most adequate local time for a sun-synchronous orbit.

4.4.2. Impact of rain cells on waveform analysis. The following considerations are derived from Tournadre (1999):

Approximations made in previous studies to estimate the effect of rain cells on Ku-band altimeter waveforms are no longer valid; a second new method has thus been developed based on the true integration of rain attenuation.

It may be shown that the difference between the two methods is significant even for low rain rates (few tenths of mm/hr). The method can be used to compute the altimeter waveform for any rain field. It shows that a precise retrieval of altimetric parameters (significant wave height, wind speed and sea surface topography) will require to take into account corrections for rain cell perturbations even for low rain rates.

The sensitivity of Ka band measurements to rain may also lead to a way of estimating very light rainfall over the oceans, for which we dramatically lack of information and which could lead to a great improvement of our knowledge of the oceanic rain climatology.

4.5. Anticipated radiometer performances

The following figures present the major elements of the radiometer performance budget:

- resolution : about 0.3 K for the 23.8 GHz frequency, and 0.4 K for the 37 GHz frequency
- sensitivity : better than 1K
- accuracy : better than 3K (worst case estimate).

5. Conclusion: Status of the Ka-band altimetry studies

The Ka-band altimetry concept that is proposed exhibits enhanced performances in terms of vertical resolution, time decorrelation of echoes, space resolution, range noise. In addition, an adapted tracker algorithm has already been designed to perform near-continuous altimetric tracking above all surfaces, which is especially important when approaching or leaving coasts. Also, it appears that, even if Ka-band measurements are more sensitive to rain than Ku-band measurements, rain does not prevent from acquiring a fairly high percentage of measurements (objective is up to 95%) except for strong rain rates : nevertheless, the development of new algorithms taking into account rain perturbations of the altimeter echoes is necessary and presently under study.

Of course, even if not presented in this note, the presence of the DORIS system and of a laser retroreflector array in the AltiKa package ensures that the classically required orbitography performances will be reached and that the AltiKa altimeter series may be linked to TOPEX/POSEIDON, Jason and ENVISAT series in a well monitored geodetic reference frame.

Preliminary studies have shown that a microsatellite platform such as the MYRIADE series under development at CNES is well suited to embark the AltiKa payload. A recent study has been performed considering a classical sun-synchronous 35 day ENVISAT-type orbit (6 am ascending node) at an altitude of 800 km and a 98 degree inclination, also requiring a +/- 1km repeatability for the ground track. The main issues relating with the accommodation of the AltiKa payload on the microsatellite platform have been analyzed: mass, power, pointing, fields of view of the various instruments, TM/TC rate, thermal and electromagnetic environment, etc. A detailed report is still under writing at the present time, the conclusion of it being that AltiKa is a valid candidate for the embarkment on such a microsatellite.

During the same study, a very preliminary analysis of possibly launching several (up to 3) AltiKa microsatellites with the same small launcher has been performed. (See Figure 3 for an example of accommodation of three AltiKa microsatellites inside a DNEPR fairing.) The feasibility of such an approach has been assessed for two configurations: one is to have 3 satellites flying in the same orbit plane with a 120 degree lag in terms of position on the orbit (classical constellation type), the second one being to have the 3 satellites flying on different orbit planes that would be separated up to 0.24 degree corresponding to one third of the typical 35 day ground track spacing (formation flying). These 2 configurations may of course answer differently space time requirements of high resolution ocean altimetry and maybe inputs for ocean simulation to illustrate their relative interest in terms of science return.

It shall be noticed that the technical studies that are referred to are preliminary ; they need to be consolidated by more detailed analysis including the possibility of considering other microsatellite platforms and launchers. However, the results that are presented demonstrate the potential of Ka-band altimetry both in technical and performances aspects, validating the AltiKa concept for a high performance continuation of ENVISAT altimetry and to potentially contribute in high resolution altimetry.

Finally, it may be stressed that the Ka-band altimeter payload defined above may be embarked as a passenger of opportunity missions as a complement to existing altimeters such as the POSEIDON ones : we would then get multi-frequency measurements that may be of much use for all applications mentioned above.

6. References

Jacobs et al., 1999: Navy altimeter data requirements, Technical Report, Naval Research Laboratory, Stennis Space Center, MS 39529-5004.

Le Traon, P.Y. and G. Dibarboure, 1999: Mesoscale mapping capabilities from multiple altimeter missions. *J. Atm. Ocean. Tech.*, **16**, 1208-1223.

Mitchum G. et al., 1999: The future of sea-surface height observations, OCEANOBS99, Saint-Raphael.

Phalippou L., E. Caubet and E. Thouvenot, 2000: A Ka-band altimeter for future altimetry missions, IGARSS'2000,

Rémy F., B. Legresy and P. Vincent, 1999: New scientific opportunities from Ka-band altimetry. IGARSS'99, Hamburg, Germany.

Tournadre J., 1999: Estimation of rain fall from Ka-band altimeter data. IGARSS'99, Hamburg, Germany.

Verron J., P. Bahurel and P. Vincent, 2001: AltiKa: Etude de la circulation océanique mésoéchelle par altimétrie en bande Ka sur microsatellite. Research proposal to CNES.

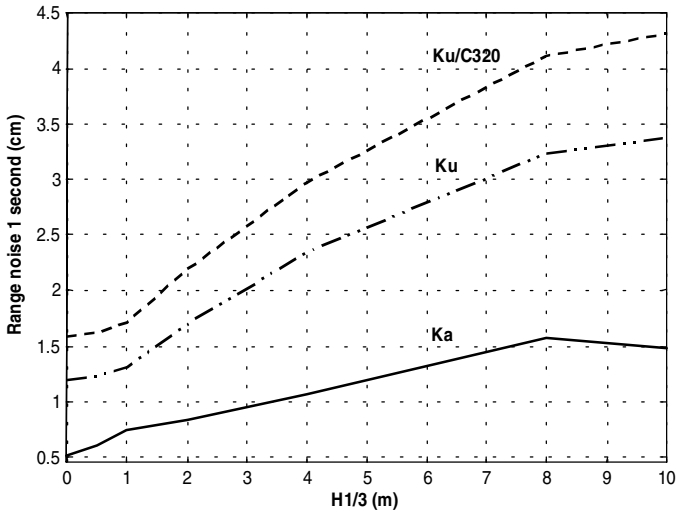

Figure 1. Comparison of AltiKa (at 800 km) and POSEIDON 2 (at 1340 km) performance.

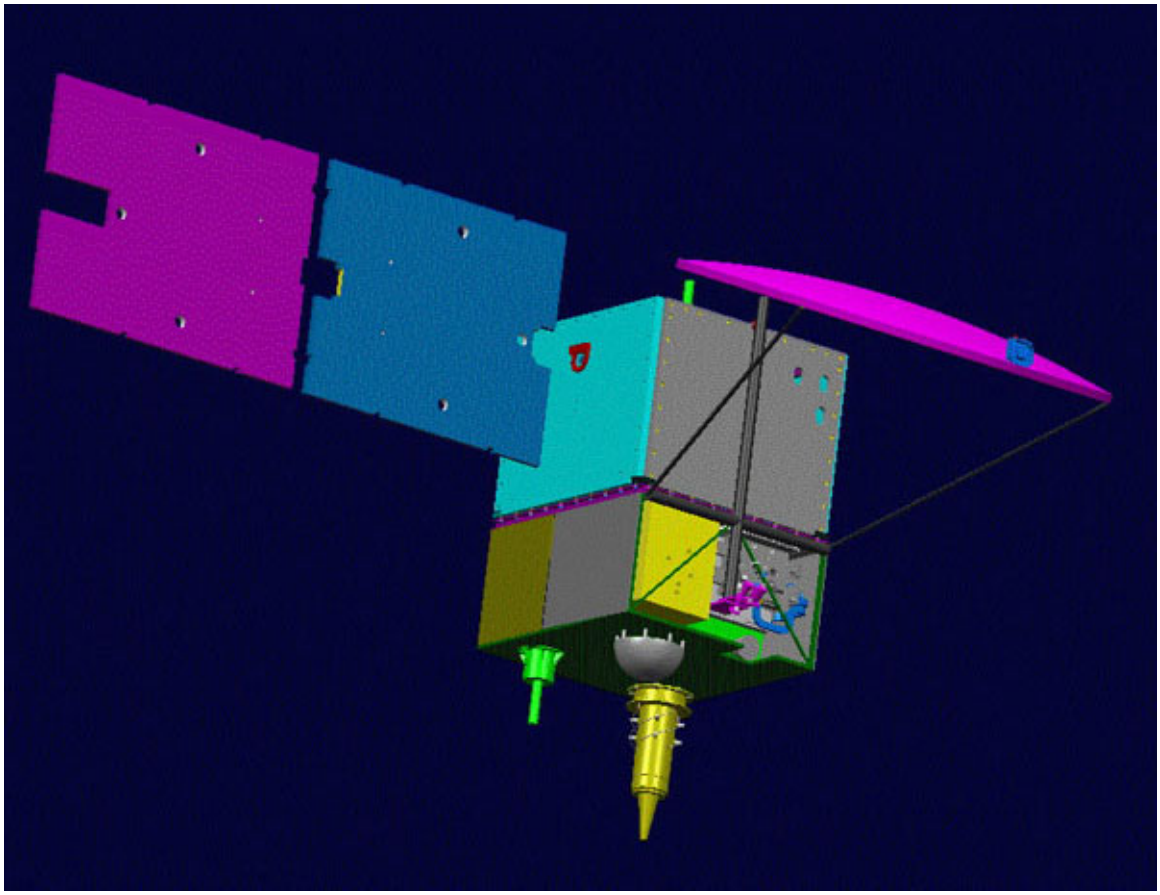

Figure 2. Artist view of the AltiKa micro-satellite.

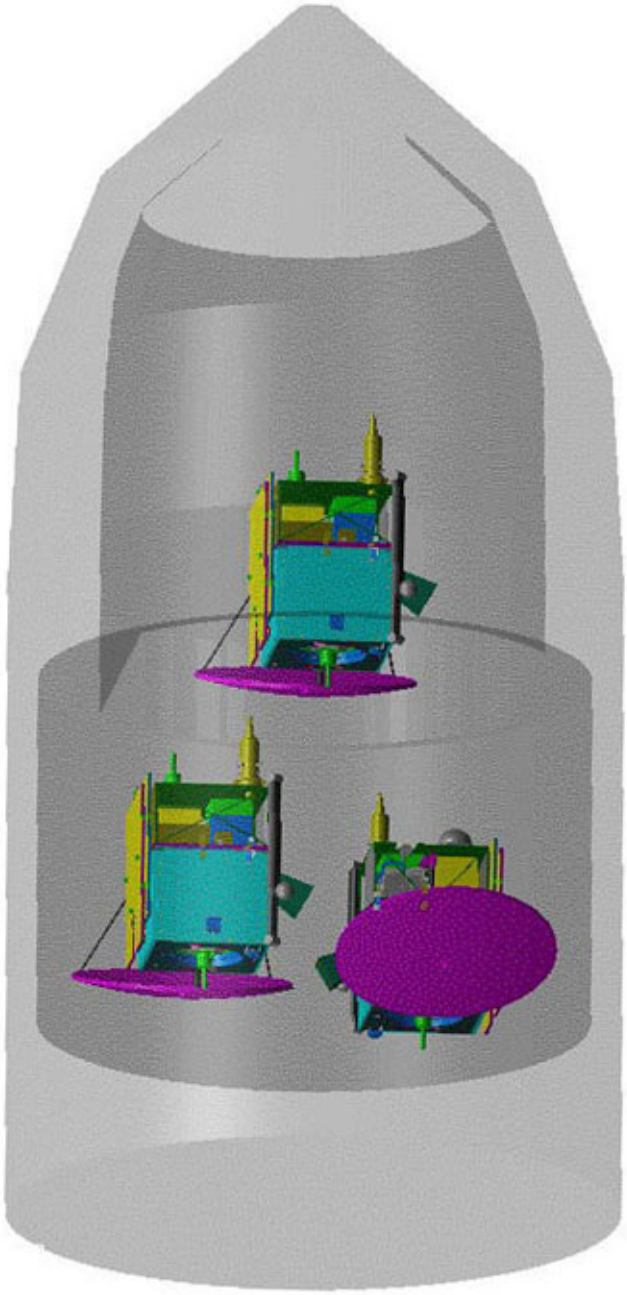

Figure 3. Example of accommodation of three AltiKa microsatellites inside a DNEPR fairing.

The Measurement Capabilities of Wide-Swath Ocean Altimeters

Ernesto Rodriguez and Brian D. Pollard
Jet Propulsion Laboratory
California Institute of Technology
Pasadena, CA 91109

Introduction

The High-resolution Ocean Topography Science Working Group (HOTSWG) meeting held in Washington D.C. in April of 2001 examined the capabilities of various instruments for meeting future science needs for high resolution ocean topography.

Among the instruments considered was the Wide-Swath Ocean Altimeter (WSOA), an interferometric radar capable of providing ocean topography over 200 km swaths. The design presented during the April '01 HOTSWG meeting was a design which had been proposed by JPL for inclusion as a demonstration mission together with the proposed Jason-2 mission. Due to limitations in the Jason bus, the instrument shown did not represent the ultimate potential of the technique for future missions, such as the NPOESS platform. In addition, it was repeatedly stated during the meeting that, even for a demonstration mission, it would be highly desirable if the random height errors could be reduced.

In this chapter, we review the WSOA system concept and capabilities, and address the concerns of the HOTSWG. In addition to issues identified by the HOTSWG, E. Walsh (private communication) has brought up a concern which he thinks limits the accuracy of any off-nadir height measurement instrument. Since the answer to his concern highlights the difference between the WSOA and more conventional altimeters, we think it is useful to present the resolution to the HOTSWG.

This chapter is divided as follows:

- **Overview of the WSOA Instrument:** In this section, we review the WSOA system concept, its predicted perfomance integrated with the Jason-2 altimeter.
- **Design Improvements to the Jason-2 WSOA Demonstration Mission:** After the April '01 meeting we reexamined the WSOA design and found improvements in the processing techniques and the mode of operation which can be accommodated with the Jason-2 bus. These improvements help to significantly reduce the random measurement noise.
- **Potential Design Changes for Future Missions:** This section addresses design changes which could be made with the current technology, but require the use of a different platform to fly the WSOA instrument. In this section, we show that, with currently available radar and interferometric mast technology, and with a platform capable of handling the products and moments of inertia of the WSOA instrument, single pass height performance accuracy comparable to nadir altimeters can be achieved over the entire swath. The performance improves even further if it is taken into account that the WSOA will revisit most points on the surface at least twice within a 10 day cycle.
- **Is Off-nadir Altimetry Inherently Limited?** This section addresses concerns raised by E. Walsh, and shows that the WSOA concept is qualitatively and quantitatively different from traditional altimetry.

The WSOA Measurement Concept

In order to map ocean mesoscale phenomena adequately, it is necessary to be able to resolve phenomena which are on the order of the Rossby radius of deformation (a conservative value would be on

the order of 30km) and have a typical lifetime on the order of a month. It is not possible to reconcile both of these requirements with a single nadir looking altimeter: the TOPEX altimeter has a repeat cycle of 10 days, but an equatorial separation of 300 km. Given a sufficient number of satellites, it is possible to meet these requirements, but at the cost of coordinating and launching multiple platforms, as well as cross-calibrating different systematic errors due to orbit and instrument biases.

The Wide Swath Ocean Altimeter (WSOA) concept is an attempt to meet the requirements using a single platform. The WSOA consists of a suite of instruments: a conventional nadir altimeter (Ku and C-band nadir altimeters, 3-frequency radiometer, and GPS receiver) supplemented by a Ku-band radar interferometer [Rodriguez and Martin, 1992] [Rodriguez et al., 2001]. Figure 1 shows a diagram of the integrated instrument. The nadir altimeter is used for high precision basin scale measurements, for the estimation of ionospheric and tropospheric delays, and for the calibration of the interferometer.

The radar interferometer illuminates 100 km swaths on either side of the nadir track using right and left-looking beams. The intrinsic cross-track resolution varies from approximately 670 m in the near range to about 100 m in the far range. The along-track resolution is given by the azimuth beamwidth, and is approximately 13.5 km. In order to have spatially uniform resolution cells, and to reduce random measurement error, the final measurements are averaged to 15 km resolution cells.

The 200 km swath enables the WSOA to achieve near global coverage with a single instrument. Figure 2 shows a comparison of the coverage obtained by two TOPEX-like altimeters, separated at the equator by 150 km, and the coverage obtained by a single WSOA. The height field shown is from the Los Alamos National Laboratory 0.1 degree eddy-resolving circulation model. The WSOA results shown are the products of a measurement simulator which includes random and systematic measurement errors.

Another advantage of the 200 km swath is that, in contrast with a nadir looking altimeter, a typical point on the ocean surface will be imaged at least twice within a 10-day repeat period, and often more frequently. Figure 3 shows the number of times the North Atlantic is imaged by the instrument. The multiple looks at the same point can be used to improve temporal sampling, but, perhaps more importantly, to reduce random measurement errors by averaging, optimal interpolation, or assimilation. Typically, one observes that the effective random measurement error is reduced by a factor of $1/\sqrt{2}$, or better.

The high accuracy requirements for ocean topography measurements implies that the measurement error budget must be thoroughly understood. The errors for interferometric measurements and for the WSOA in particular are described in detail in [Rodriguez and Martin, 1992] [Rodriguez et al., 2001], so we limit ourselves here to a brief statement of results. The WSOA errors can be derived into three components: random errors, media errors, and platform roll errors. The random error contribution depends on the system signal to noise ratio (SNR), on the length of the interferometric baseline, and on the processing used. At the HOTSWG meeting, we presented the random height error coresponding to an implementation of WSOA designed to fit on the Jason platform constraints, which limit the baseline length to 6.4 m. The predicted performance is shown in the second column of Table 1a. We have subsequently refined our operational mode and processing algorithms, so that the single pass random height accuracy has improved significantly. These results are presented in the next section. During the HOTSWG meeting we also showed that, after mosaicking the data over one cycle, and applying the cross-over calibration described below, the mosaicked data root mean squared error dropped to 3.2 cm. Since the mosaicking algorithm is linear, we expect that the performance using the improved WSOA described in section 3, will improve linearly with the improved random noise performance. This remark applies as well to the estimation of geostrophic velocity.

The WSOA interferometer does not directly measure tropospheric, ionospheric, and EM bias corrections, but uses the corrections from the nadir altimeter. Spatial variability of the ionosphere, troposphere, wave and wind fields over the scales of the swath will induce residual height errors. To

quantify these residual errors, we use the TOPEX along-track measurements of these quantities to estimate spatial variability of the corrections. Since these errors have a latitudinal dependence, we subdivide the data into 10 degree latitude bands. The result for the total (tropospheric, ionospheric, and EM bias) error for the global average, and the worst and best latitude bands is presented in Figure 4.

Finally, the lack of knowledge in the spacecraft roll angle induces height errors. In order to remove these errors, we have deviced a calibration scheme which uses ascending and descending WSOA data at cross-over regions to estimate and remove the roll errors (see Figure 5). In order to validate the accuracy of the calibration technique, we have performed a simulation using one year of LANL circulation model data and a set of spacecraft roll characteristics for the Jason platform provided to us by CNES/Alcatel. An example of the resulting corrected height fields is shown in Figure 2b. As mentioned above, the total height root mean squared error, including random and roll errors, is 3.2 cm.

One of the principal advantages of the WSOA measurements is that one can obtain the two-dimensional sea surface, rather than just the traditional along-track profiles measured by nadir altimeters. The availability of a two-dimensional height field allows the calculation of surface topography derivatives in the zonal and meridional directions. This means that it is possible to estimate the full **vector** geostrophic velocity everywhere WSOA measurements are available, rather than the single component of the velocity measured by a nadir altimeter. Figure 6a shows an example for the magnitude of the two-dimensional geostrophic velocity for the topography presented in Figure 2b. The results of the LANL based simultaion show that the root mean squared error for the U and V components of the geostrophic velocity for the mosaicked data is 4.7 cm/s and 5.9 cm/s, respectively. One can then use the time series of vector velocities to obtain estimates for the Reynolds stresses sampled at high resolution (Figure 6c). Similarly, the Laplacian of the height field can be used to estimate the geostrophic relative vorticity (Figure 6b). The accuracy for these derived fields has been obtained using simple mosaicking, which is a simplistic model for the optimal estrimation for these quantities. The estimation accuracies using more sophisticated techniques is currently under investigation.

Design Improvements to the Jason-2 WSOA Demonstration Mission

The measured interferometric phase is noisy because the two interferometric channels are not perfectly correlated. In the design presented at the April '01 HOTSWG, the following were the sources of signal decorrelation:

- Thermal noise.
- Geometric decorrelation: this is due to the fact that at boresight, the surface will speckle slightly differently for each receiver channel.
- Angular decorrelation: this is due to the fact that iso-phase lines are not aligned with iso-range lines.
- Misregistration: for the simple design, the returns were not completely aligned on the ground away from the center of the swath.

As an example of the relative contribution of each source of decorrelation, Figure 7 shows the different contributions for the design presented at the April '01 HOTSWG meeting.

After some thought, we have realized that, for a minor computational penalty on the on-board processor, it is possible to eliminate two of the sources of decorrelation: the geometric and misregistration correlations.

In addition to improving phase noise, it is possible to reduce height noise by making the measured interferometric phase difference more sensitive to height variations. This can be accomplished by extending the interferometric baseline. However, it can also be accomplished by transmitting from both interferometric antennas, as described below.

The following subsections describe how these sources of error can be incorporated into the WSOA design, the penalties incurred in doing so, and the gains in performance.

Improving Channel Co-Registration

Due to the fact that the two interferometric receivers are separated by the interferometric baseline, signals from the same point on the ground will arrive at different times at the receivers. It is possible to add a single delay between the channels so that the signals are corregistered for a given incidence angle. However, residual misregistration will still occur away from the selected direction.

In order to perform channel registration, conventional synthetic aperture radars (SAR) use an interpolation algorithm using a finite interpolation kernel. However, in order to preserve phase accuracy, the kernel length is not small, and the procedure is computationally expensive.

The WSOA is a real aperture radar, and we show in Appendix A that in this case the interpolation of the two channels can be performed add a small computational cost using the chirp-z or chirp scaling algorithm [Rabiner, et al., 1969] [Raney, et al., 1994] . In contrast to conventional SAR's, the co-registration during range compression does not disturb subsequent synthetic aperture image formation.

As shown in Appendix A, the computational cost of using chirp-scaling for co-registration is small and can be easily incorporated into the current WSOA design.

The Wavenumber Shift for WSOA

The source of geometric decorrelation is the fact that the interferometric phase is not constant for all the scatterers within a given resolution cell. This variation in the interferometric phase causes the total interferometric contribution from that cell to add slightly incoherently, thus reducing the signal correlation.

Gatelli et al. [1994] had an insight: suppose that one were dealing with monochromatic signals, and chose the wavelengths of the two channels to be such that the projected wavevectors on the ground are identical for both channels. In this case, the interferometric phase would be constant for all scatterers in the resolution cell, and the returns would add coherently.

When dealing with a finite bandwidth signal, things are a bit more complicated, but Gatelli et al. [1994] provide a solution: take the signal from both channels and shift the spectra in such a way that the appropriate wavelengths are multiplied together so that the phase variation over the resolution cell is canceled. This spectral shift means that noise is now brought into the processing bandwidth. In order to remove this additional noise, Gatelli et al. propose to use a low-pass filter so that only the parts of the spectra which overlap contribute to the interferometric return. The penalty for this low-pass filter is a loss in resolution, but this loss is usually small and acceptable.

The wave-number shift proposed by Gatelli et al. [1994] applies to SAR's, where the angular variation of the resolution cell in the azimuth direction is very small, so that iso-range and iso-phase lines can be consireded to be aligned. However, this situation no longer applies for the WSOA: since it is a real aperture system, significant deviations can occur between these two sets of lines. Viewed in another way, this is equivalent to saying in the monochromatic case that two wavelengths can be found to cancel the interferometric phase for one given azimuth direction, but not for all.

In Appendix B, we show the effects of implementing the wave-number shift for WSOA: the geometric correlation term can be made to disappear, but the angular correlation term remains. Nevertheless, the performance gains are still significant enough to warrant the inclusion of this algorithm in the WSOA on-board operation.

The operations involved in implementing the wave-number shift consist of shifting the spectrum of the two signals after range compression by multiplying both with a phase ramp in time, followed by FIR filtering of the signals. The spectral shift can be combined with the last step of the chirp-scaling algorithm, which also involves multiplying each signal sample with a complex number, so that no computational penalty is involved. There is a computational penalty involved in FIR filtering the signals, but for small filter kernels, as will be the case for WSOA, the number of computations is small compared to performing the range compression.

A study of the modifications required show that the on-board processor already prototyped for WSOA is capable of accommodating both chirp scaling and the wavenumber shift.

Ping-Pong Interferometric Operation for WSOA

If one transmit out of one antenna and receives in both, the interferometric phase difference will be given by

$$\Phi = 2kr_1 - k(r_1 + r_2) = k(r_1 + r_2) \approx kB\sin\theta$$

However, if it were possible to transmit and receive out of one antenna, followed by transmitting and receiving out of the other one (which is called ping-pong mode in conventional interferometry), the interferometric phase would be

$$\Phi = 2kr_1 - 2kr_2 \approx 2kB\sin\theta$$

i.e. operating in ping-pong mode results in obtaining an effective baseline which is twice as long as the physical baseline.

All things remaining the same, one could think of implementing ping-pong mode by alternating the antenna used for transmit with every pulse. However, this simple approach will not work: it is well known that for distributed scatterers, such as the ocean surface, pulses which are separated by more than one-half an antenna length are not correlated. Therefore, in order to implement ping-pong mode one must transmit bursts of pairs of pulses, with the pulse separation being such that the two pulses are correlated and fit in the same return window.

In order to do this and retain constant average power, the pulse length of the two pulses must be halved, leading to a decrease in the signal-to-noise ratio (SNR). However, it can be shown that the height noise is proportional to the square root of the SNR, while the proportional to the inverse baseline length so that roughly a factor of $\sqrt{2}$ performance gain can be achieved.

An additional concern when using close pulse pairs for ping-pong mode is that the range ambiguities will increase, degrading performance. Similarly, one must be careful to chose the pulse repetition frequency and the pulse spacing so that both returns fit with the return window without interference, and there is no interference with the nadir altimeter.

A detailed calculation shows that for the proposed WSOA system, a pulse spacing can be found such that the range ambiguities from the second pulse does not significantly increase the range ambiguity level: in practice, the range ambiguity is always dominated by the 0th, opposite side ambiguity. Further reduction of ambiguity contamination can be achieved by using opposite direction chirps for each pulse. Similarly, a PRF can be found such that ping-pong operation can occur simultaneously with the nadir altimeter.

The real cost of using ping-pong mode is the increased load on the on-board processor. One can show that a pulse length can be used such that half the range samples are required for the compression of each channel. However, using ping-pong mode introduces an additional calibration error on the transmit channel which canceled out in "standard" operation. This additional transmit phase imbalance can be calibrated using the null-baseline interferogram, but at the cost of roughly doubling the required number of range compressions. This will increase the processor power requirements, but we estimate that this mode could be demonstrated in the Jason-2 mission as an experimental mode.

Performance Improvements

We have taken into account the changes proposed above and calculated the expected performance for instantaneous mapping for an interferometric baseline of 6.4 m, assuming a single-transmit chirp length of 90 μsec, and a ping-pong chirp length of 45 μsec. The ocean σ_0 was assumed to be in the 95% percentile (only 5% darker ocean conditions), in order to be conservative. The results for standard operation with and without chirp-scaling and wavenumber-shifts are presented in Table 1a. Similar results for ping-pong operation are presented in Table 1b.

Notice that a performance gain from 30% to 50% can be achieved by using these improved processing and operating techniques. It should also be emphasized that these results are for the instantaneous performance of the interferometer. Due to the wide-swath capabilities, all imaged points will be revisited from 2 to 4 times within 10 days, so that additional gains in performance can be expected. As presented in the HOTSWG meeting, using optimal interpolation or simple averaging can significantly reduce the error estimated over a repeat cycle.

Potential Design Changes for Future Missions

The Proteus bus puts limitations on the performance of the WSOA which might be alleviated if another bus were used. The foremost restriction is imposed due to the fact that the Proteus bus yaw steers, so that the WSOA can only be fully operational for part of the mission. The temporal coverage characteristics were already presented at the HOTSWG meeting, and are the main reason for which the WSOA/Jason-2 combination can only be regarded as a demonstration mission. This restriction can be alleviated by using a platform which has solar panels with two degrees of freedom, or if a sun-synchronous orbit is deemed acceptable.

The greatest additional restrictions for the WSOA on Jason-2 are placed by the attitude control system. Bus characteristics place restrictions on the moments and products of inertia which can be accommodated, and also on the lowest allowable frequency. The net result of these restrictions is that the interferometric baseline length must be shorter than the limits set by the current state of the art in rigid deployable masts. Preliminary studies at A.E.C. Able have shown that 10 m masts are well within the limits of feasibility and would be able to meet the stability requirements set by WSOA.

Using the parameters for the previous section, but allowing the baseline to be 10 m long, the expected performance is presented in Table 2a and Table 2b.

An additional limitation, at least at the current time, is the amount of power available from the bus. If the duty cycle were allowed to be doubled by doubling the PRF, while maintaining the same peak power and a 6.4m baseline, the performance shown in Table 3a and Table 3b.

Finally, if one both doubles the duty cycle and increases the baseline length to 10 m, one obtains the performance shown in Tables 4a and 4b.

In summary, given a platform with greater capability for tolerating higher moments and products of inertia, or having higher average power capabilities, the performance of the WSOA can rival that of a conventional altimeter without requiring any improvements in currently available technology. Studies at

JPL have shown that there currently exist platforms which could provide a suitable environment to the WSOA. Some of the platforms have been examined for the Ocean Observer Mission studied by IPO.

Is Off-Nadir Altimetry Inherently Limited?

In a private communication, E. Walsh has raised the concern that the angular variations in the backscatter cross section, σ_0, induce unacceptably large errors on the WSOA estimated heights. In this section we address these errors (leaving mathematical details for an appendix) and show that they are a minor contributor to the WSOA error budget.

The main source for Walsh's concern is due to a misunderstanding of the algorithms which are used to estimate the surface height for coherent interferometers, such as WSOA. In an previous design for a non-coherent interferometer [Bush, et al., 1984] [Parsons and Walsh, 1989], the height had been estimated by tracking the centroid of the waveform formed by the power interference pattern. In this case, the height estimation algorithms are analogous to the height estimation algorithms for conventional altimetry: a single height estimate is obtained by tracking a "waveform" consisting of many range samples. The typical size of the waveform in range is 245 m, for the example chosen by Walsh. This corresponds to a ground resolution of about 3 km. As Walsh correctly points out, the angular variations subtended by such an area will cause a significant shift of the waveform centroid. Using this technique, one would obtain height errors which are meter level, which are unacceptable for WSOA science applications.

Coherent interferometers [Rodríguez and Martin, 1992], on the other hand, do not use waveform tracking to obtain a height estimate. Rather, since the complex samples are returned, it is possible to assign an interferometric phase to each range sample, rather to many range samples. This interferometric phase, together with the radar range (which is not estimated, but rather set by the clock accuracy of the system, and the corresponding time tagging of each range sample), can be converted to an estimate of the surface height, following the algorithm described in [Rodríguez and Martin, 1992].

The angular variation of the backscatter cross section will also result in height biases for a coherent interferometer. However, the range of incidence angles will correspond in this case to the angles subtended by the imaged pixel, rather than by the angles subtended by the interferometric lobe. The ratio of these angles is equal to the ratio of the radar intrinsic range resolution to the range subtended by the interferometric lobe, $7.5/245 \approx 0.03$ so that intuitively one expects the effects to be two orders of magnitude smaller than the biases for the incoherent interferometer case.

Appendix C derives the exact value for the biases, and confirming the intuitive argument outlined above. Using formulas derived in that appendix and the WSOA values for the range resolution and the platform height h, following Table 5 shows the expected height biases as a function of wind speed. As can be seen from this table, the expected errors due to the angular variation of the cross section are very small compared to the other contributors to the WSOA error budget, and can therefore be neglected.

Appendix A: Resampling Using the Chirp-Z Transform

If uniform and identical sampling is used for both radar channels, the imaged pixels on the ground will fail to line up exactly due to the slightly different viewing geometry for each channel.
The range difference between the channels is two given by

$$\Delta r \approx B \sin\theta_0 + B \frac{\cos\theta_0}{\tan\theta_0} \frac{\delta r}{r_0} \qquad (1)$$

where B is the interferometric baseline, θ_0 is the angle to a reference point, r_0 is the range to that point, and δr is the range relative to the reference range, and the expansion has been taken to the center of the swath.

Assuming that the first channel is sampled as $r_1 = r_0 + \delta r$, the second channel must be sampled at the ranges

$$r_2 = r_0 + B\sin\theta_0 + (1+\zeta)\delta r$$

where $\zeta = B\cos\theta_0 / (r_0 \tan\theta_0)$. Assuming that constant timing differences are taken care of by suitably choosing the range compression function, the co-registration problem is reduced to sampling the second channel at $(1+\zeta)\delta r$ if the first channel is sampled at δr. This can be accomplished by using the chirp-scaling algorithm [Rabiner, et al., 1969] [Raney, et al., 1994]. The details are given in the following paragraphs.

Assume the transmit signal is given by

$$S(t) = A(t)e^{i\alpha t^2}e^{i\omega_0 t} \qquad 2)$$

In terms of the system bandwidth Δf and the chirp duration T, $\alpha = \Delta f/(2T)$. The received signal from a point target after down-conversion is given by (after removing the shift to the center pixel)

$$S(t) = A(t-\tau_0)e^{i\alpha(t-\tau_0)^2}e^{-2ik_0 r_2}$$

$$\tau_0 = \frac{2}{c}(r_2 - r_0 - B\sin\theta_0)$$

where k_0 is the center frequency wavenumber, r_2 is the second channel range to the point target.

We proceed to apply the chirp scaling algorithm by multiplying the signal prior to range compression by the quadratic phase factor $\exp[i\beta t^2]$ ($\beta = \alpha\zeta$). Range compression and resampling are achieved by convolving the signal with the reference function $\exp[-i(\alpha+\beta)t^2]$, so that the range compressed signal can be written as

$$S(t) = e^{-2ik_0 r_2}\int d\tau \;\; A(\tau-\tau_0)e^{i\alpha(\tau-\tau_0)^2}e^{i\beta\tau^2}e^{-i(\alpha+\beta)(\tau-t)^2} \qquad (3)$$

Defining the point target response as

$$x(t) = \int d\eta \;\; A(\eta)\exp[2i\alpha\eta t] \qquad (4)$$

the return signal can be written after some rearrangement of terms as

$$S(t) = e^{-2ik_0 r_2} e^{-i\alpha(1+\zeta)t^2} e^{i\alpha\tau_0^2} \exp\left[2i\alpha\tau_0\left((1+\zeta)t - \tau_0\right)\right] \chi\left((1+\zeta)t - \tau_0\right) \qquad (5)$$

If $\beta = 0$ (i.e., no chirp scaling), the result at would be

$$S(t') = e^{-2ik_0 r_2} e^{-i\alpha t'^2} e^{i\alpha\tau_0^2} \exp\left[2i\alpha\tau_0(t' - \tau_0)\right] \chi(t' - \tau_0) \qquad (6)$$

If we set $t' = (1+\zeta)t$ (i.e., the correctly resampled signal), we see that the only difference between equations (5) and (6), is a phase factor $e^{-i\beta t^2(1+\zeta)}$ which can be removed after range compression by post-multiplying the signal.

Notice that, in terms of computation, the chirp scaling algorithm does not increase the number of operations during range compression: it merely changes the reference function, which involves no additional computation. The additional computation occurs in the pre- and post-multiplication of the signal by the appropriate chirp functions. This involves merely N complex multiplications, where N is the number of signal samples, while the range compression involves two 5NlogN Fourier transforms and N complex multiplications, so that the resampling is computationally cheap compared to the range compression.

Appendix B: The Wave-Number Shift for WSOA

Given maximum likelihood estimation, the interferometric phase standard deviation, σ_0, is given by

$$\sigma_\Phi = \frac{1}{\sqrt{2N_L}} \frac{\sqrt{1-\gamma^2}}{\gamma} \qquad (7)$$

where γ is the correlation coefficient between the two interferometric channels:

$$\gamma = \frac{\left|\left\langle v^{(1)} v^{(2)*} \right\rangle\right|}{\sqrt{\left\langle v^{(1)} v^{(1)*} \right\rangle \left\langle v^{(2)} v^{(2)*} \right\rangle}} \qquad (8)$$

and $\langle\ \rangle$ denotes ensemble averaging over speckle realizations. The random height error is due to errors in the estimation of interferometric phase, and is given by [Rodriguez and Martin, 1992]

$$\delta h = \frac{r_0 \tan\theta_0}{kB} \sigma_\Phi$$

where r_0 is the range from the platform to the surface, θ_0 is the look angle, k is the electromagnetic wavenumber, and B is the length of the interferometric baseline.

Equation (7) shows that the phase standard deviation can be predicted if the correlation coefficient can be modeled. The return signals after range compression co-registration can be modeled as

$$v^{(1)}(t) = A\int dS \;\; \chi\left(t - 2r_1/c - \Delta\right) G(\phi)s(r,\phi)e^{-2ikr_1} + n_1 \tag{9}$$

$$v^{(2)}(t) = A\int dS \;\; \chi_r\left(t - 2r_2/c - \Delta\right) G(\phi)s(r',\phi)e^{-2ikr_2} + n_2 \tag{10}$$

where A is a constant which depends weakly on range; Δ is a delay introduced to coregister the two channels; χ_r is the system range point target response; ϕ is the azimuth angle coordinate (any point in the surface plane can be defined by its ground range ρ and its azimuth angle ϕ); $G(\phi)$ is the system antenna pattern, which is assumed to be much broader in the range direction than the system range resolution, so that only its azimuth variation must be included; r_1 and r_2 represent the range from the reference and secondary antennas to a point on the surface; n_1 and n_2 represent the thermal noise in channels 1 and 2, respectively, and are assumed to be uncorrelated white noise processes with variance N; and, finally, $s(r',\phi)$ represents the rough surface brightness which is assumed to satisfy

$$\langle s(\mathrm{r})s^*(\mathrm{r}')\rangle = \delta(\mathrm{r} - \mathrm{r}')\sigma_0 \tag{11}$$

where σ_0 is the normalized radar cross section. Equation (11) is consistent with the deep phase approximation in rough surface scattering [Tsang, et al., 1985], which applies when the surface rms roughness is large compared to the wavelength. That approximation is valid for all the systems studied. Notice that we assume that the radar cross section is constant over the radar resolution cell (see Appendix C for a relaxation of this assumption).

To study the effects of the spectral shift algorithm, we introduce the Fourier transform of the range ptr

$$\chi(t) = \frac{1}{2\pi}\int d\omega \;\; e^{i\omega t}W(\omega) \tag{12}$$

and rewrite the equations for the return signal (neglecting for the moment the thermal noise contributions) to obtain

$$v^{(i)}(t) = A\frac{1}{2\pi}\int d\omega \;\; e^{i\omega(t-\Delta)}W(\omega)$$
$$\int dS \;\; e^{-2i\omega r_1/c}G(\phi)s(r,\phi)e^{-2ikr_1} \qquad (13)$$

$$v^{(2)}(t) = A\frac{1}{2\pi}\int d\omega \;\; e^{i\omega(t+\Delta)}W(\omega)$$
$$\int dS \;\; e^{-2i\omega r_2/c}G(\phi)s(r,\phi)e^{-2ikr_2} \qquad (14)$$

The first step of the wavenumber shift algorithm starts by multiplying both of the interferometric signals in the time domain by a phase factor equivalent to the interferometric phase relative to a reference track. Over a localized region, this is equivalent to multiplying by a constant phase factor, and one which varies linearly in time. For our purposes, we will neglect the constant phase term and assume that the first signal is multiplied by a phase factor $\exp[iwt]$, while the second is multiplied by the complex conjugate. The result of multiplying by a phase ramp in the time domain will be to shift the spectrum in the frequency domain. We will choose w to maximize the spectral overlap of wavenumber components over the pixel. After shifting the spectra, both signal are low-passed filter with an FIR filter whose frequency response we will denote by $H(\omega)$. The filter characteristics will be chosen below to reduce the noise introduced by the frequency shift.

After both of these operations, the return signals can be written as

$$v^{(1)}(t) = A\frac{1}{2\pi}\int d\omega \;\; e^{i\omega(t-\Delta)}W(\omega - w)H(\omega)$$
$$\int dS\, e^{-2i(\omega-w)r_1/c}G(\phi)s(r,\phi)e^{-2ikr_1} \qquad (15)$$

$$v^{(2)}(t) = A\frac{1}{2\pi}\int d\omega \;\; e^{i\omega(t+\Delta)}W(\omega + w)H(\omega)$$
$$\int dS\, e^{-2i(\omega+w)r_2/c}G(\phi)s(r,\phi)e^{-2ikr_2} \qquad (16)$$

In order to calculate the interferometric correlation, one must evaluate the expectation value of the channel cross-product:

$$\left\langle v^{(1)}(t)v^{(2)*}(t)\right\rangle = |A|^2\left(\frac{1}{2\pi}\right)^2\int d\omega_1\int d\omega_2 \;\; e^{i(\omega_1-\omega_2)t}e^{i(\omega_1+\omega_2)\Delta}$$
$$W(\omega_1 - w)W^*(\omega_2 + w)H(\omega_1)H^*(\omega_2)F(\omega_1,\omega_2) \qquad (17)$$

where the last function is defined as

$$F(\omega_1,\omega_2)=\sigma_0\int dS\;\; e^{-2i(k_1r_1-k_2\,r_2)}e^{2iw(r_1+r_2)/\;c}G^2(\phi) \tag{18}$$

and $k_i\equiv k+\omega_i/\;\;c$. Notice that equation (11) was used to reduce the double spatial integral to a single integral.

To proceed further, we notice that we can approximate

$$\begin{aligned} r_1-r_2 &\approx B\left[-\sin\theta+\sin\theta(1-\cos\phi)\right] \\ &\approx B\left[-\sin\theta+\sin\theta\frac{\phi^2}{2}\right] \end{aligned} \tag{19}$$

where we have made use of the fact that the azimuth beamwidth of a typical system is much smaller than 1. Expanding about r_0 and $\theta_0=\arccos(H/\;\;r_0)$, this can be further approximated as

$$r_1-r_2\approx B\left[-\sin\theta_0+\sin\theta_0\,\frac{\phi^2}{2}-\cos\theta_0\cos\theta_0\frac{\delta\rho}{r_0}\right] \tag{20}$$

where $\delta\rho=\delta r/\sin\theta_0$ is the deviation in ground range of the surface point from r_0, and terms of order $\left(R/\;\;(\sin\theta_0 r_0)\right)^2$, where R is the system range resolution, have been neglected.

After making the previous approximation and assuming that we are dealing with a narrow-band system so that , one can evaluate the integral to obtain

$$\begin{aligned} F(\overline{\omega},\Delta\omega)=\frac{\rho_0\sigma_0}{2\sin\theta_0}\,e^{2ikB\sin\theta_0}e^{2i\overline{\omega}/cB\sin\theta_0}e^{-2i\Delta\omega r_0/c}e^{4i\omega r_0/c} \\ \frac{c}{2}\,2\pi\delta\left(\Delta\omega-2w-\frac{ckB\cos\theta_0}{r_0\tan\theta_0}\right) \\ \int d\phi\;\; e^{-ikB\sin\theta_0\phi^2}G^2(\phi) \end{aligned} \tag{21}$$

where $\Delta\omega=\omega_1-\omega_2$ and $\overline{\omega}=1/2(\omega_1+\omega_2)$.

Notice that if one chooses the spectral shift

$$\omega=-\frac{c}{2}\,\frac{kB\cos\theta_0}{r_0\tan\theta_0} \tag{22)}$$

the phase is constant over the range resolution cell, for a given azimuth, and it is not hard to convince ones self that the is just the shift in frequency required by geometry so that the projected wavenumber on the ground is the same for both channels. After making this choice for the spectral shift one has that the cross-channel product expectation function can be written as

$$\left\langle v^{(1)}(t)v^{(2)*}(t)\right\rangle = |A|^2 \left(\frac{1}{2\pi}\right)\frac{\rho_0\sigma_0}{\sin\theta_0}\frac{c}{2}e^{2ikB\sin\theta_0}e^{4iwr_0/c}$$
$$\int d\omega\ \ e^{2i\omega(-B\sin\theta_0/c-\Delta)}W(\omega-w)W^*(\omega+w)\left|H(\omega)\right|^2$$
$$\int d\phi\ \ e^{-ikB\sin\theta_0\phi^2}G^2(\phi) \qquad 23)$$

Notice that if the coregistration delay Δ is chosen appropriately, the phase term disappears in the first integral. Furthermore, if one chooses $H(\omega)$ to be centered at zero frequency and with a spectral width of $\Delta f - w/\pi$, where Δf is the bandwidth of W, then only the parts of the signal which correlate on the ground contribute to the return, and no additional noise is brought in due to the spectral shift.
Using the previous results, we obtain the following expression for the complex correlation coefficient

$$\frac{\left|\left\langle v^{(1)}v^{(2)*}\right\rangle\right|}{\sqrt{\left\langle v^{(1)}v^{(1)*}\right\rangle\left\langle v^{(2)}v^{(2)*}\right\rangle}} = \gamma_\phi\gamma_N = \gamma \qquad (24)$$

and the angular (γ_ϕ), and noise (γ_N) correlation factors are given by

$$\gamma_N = \frac{1}{1+SNR^{-1}} \qquad (25)$$

$$\gamma_\phi = \frac{\int_{-\pi}^{+\pi} d\phi\ \ \exp\left[-ikB\sin\theta_0\frac{\phi^2}{2}\right]G^2(\phi)}{\int d\phi\ \ G^2(\phi)} \qquad (26)$$

where SNR is the system signal-to-noise ratio.

The result obtained for the correlation function share the angular and noise correlation functions with the results previously presented at the HOTSWG, but the introduction of co-registration and spectral domain shifts have done away with the misregistration and geometric decorrelation terms. The noise decorrelation term, γ_N, is common to the cross-correlation of any two signals with additive uncorrelated white noise. The fact that the angular correlation term cannot be made to disappear like the geometric correlation term is due to the fact that iso-phase difference contours are hyperbolas, whereas iso-range contours are circles, so that the projected wavelengths can only be made to coincide along one given azimuth direction.

Appendix C: Mathematical Details of σ_0 Angular Variations

The interferometric signal can be modeled as

$$\langle v_1 v_2^* \rangle = A \int dx \;\; e^{-i\Phi(x)} \sigma_0(x) \chi(x - x_0) \tag{27}$$

where v_i is the coherent signal in channel i, A is a constant which is not important for the following discussion, x is the cross-track distance from the interferometer ground track, $\Phi(x)$ is the interferometric phase difference, which is given by

$$\Phi = kB\sin\theta = kB\frac{x}{r} = kB\frac{x}{\sqrt{h^2 + x^2}} \tag{28}$$

where $k = 2\pi/\lambda$ is the EM wavenumber ($\lambda \approx 2.5$ cm for WSOA), B is the baseline length (7 m for WSOA), θ is the look angle, r is the range, and h is the height above the ocean (1336 km for WSOA).

Following Walsh (and geometric optics), I will take the angular variation of σ_0 to be given by

$$\sigma_0 = ae^{-\theta^2/s^2} \tag{29}$$

where a is a constant independent of look angle, and s^2 is the mean squared slope, which, following Walsh, we will assume to be related to the 10 m wind speed, U_{10}, as follows

$$s^2 = 0.018U_{10}^{1/2} \tag{30}$$

where U_{10} is measured in meters/second.

Finally, $\chi(x)$ is the system range point target response (ptr) as a function of the cross-track distance, and x_0 is the pixel center location. In order to simplify the algebra in the following discussion, I will assume that the ptr can be represented as a Gaussian, as follows

$$\chi(x) = \exp\left(-4(\ln 2)\frac{x^2}{X^2}\right) \tag{31}$$

where X represents the half-power ground resolution (i.e.; $\chi(X/2) = 1/2$), and is related to the system range resolution R by the equation $X = R/\sin\theta$. For WSOA, the system range resolution R is 7.5 m, which corresponds to a bandwidth of 20 MHz.

In order to proceed, we note that for the system parameters used for WSOA, the phase and cross section variations over a pixel are small, so that one is justified in expanding the integral in equation (27) about x_0. Keeping up to first order terms in the Taylor expansion, one readily shows that

$$\Phi \approx kB\sin\theta_0 + \kappa\eta \tag{32}$$

where $\sin\theta_0 = x_0 / \sqrt{h^2 + x_0^2} = x_0 / r_0$, $\eta = x - x_0$, and the cross-track interferometric fringe wavenumber κ is given by

$$\kappa = \frac{kB}{r_0}\cos^2\theta_0 \tag{33}$$

Similarly, one can show that σ_0 can be expanded as

$$\sigma_0(\theta) \approx \sigma_0(\theta_0)\left[1 + \beta\eta\right] \tag{34}$$

where β is given by

$$\beta = -\frac{2\theta_0}{s^2}\frac{\cos\theta_0}{r_0} \tag{35}$$

Introducing these approximations, equation (27) can be written as

$$\left\langle v_1 v_2^* \right\rangle = A e^{-i\Phi(\theta_0)}\sigma_0(\theta_0)\int d\eta\ e^{-i\kappa\eta}(1+\beta\eta)\chi(\eta) \tag{36}$$

The integral can be evaluated by using the following trick

$$\int d\eta\ e^{-i\kappa\eta}(1+\beta\eta)\chi(\eta) = \left(1 + i\beta\frac{\partial}{\partial\kappa}\right)\int d\eta\ e^{-i\kappa\eta}\chi(\eta) \tag{37}$$

and noticing that the integral in the right hand side of equation (37) is just the Fourier transform of the ptr, which I will denote by $\tilde{\chi}(\kappa)$. The interferometric return can then be written as

$$\left\langle v_1 v_2^* \right\rangle = A e^{-i\Phi(\theta_0)}\sigma_0(\theta_0)\tilde{\chi}(\kappa)\left(1 + i\beta\frac{\tilde{\chi}'(\kappa)}{\tilde{\chi}(\kappa)}\right) \tag{38}$$

where $\tilde{\chi}'(\kappa) = \partial\tilde{\chi}(\kappa)/\partial\kappa$. With the exception of the expression contained in the last parenthesis of equation (38), this equation represents the expected interferometric return when there is no angular variation of the backscatter cross section. Therefore, all phase (and consequently, height) errors will be introduced by the expression contained in the last parenthesis. In general, the term proportional to β will be much smaller than 1 (as can be verified by inserting an expression for the ptr), and one may approximate

$$\left(1 + i\beta\frac{\tilde{\chi}'(\kappa)}{\tilde{\chi}(\kappa)}\right) \approx \exp\left[\, i\beta\frac{\tilde{\chi}'(\kappa)}{\tilde{\chi}(\kappa)}\,\right] \equiv \exp\left[-i\,\delta\Phi\right] \tag{39}$$

where $\delta\Phi$ is the phase error induced by changes in the cross section as a function of incidence angle. Using equations (31), (33), (35), and the fact that the Fourier transform of a Gaussian is itself a Gaussian, one can show that the phase error as a function of incidence angle is given by the following expression

$$\delta\Phi = -\frac{R^2}{r_0^2}\frac{1}{4\ln 2}\frac{kB\cos\theta_0}{\tan^2\theta_0}\frac{\theta_0}{s^2} \tag{40}$$

In order to translate this phase error into a height error, we recall that the two are related by the following equation

$$\delta h = \frac{r_0\tan\theta_0}{kB}\delta\Phi \tag{41}$$

Using equation (40), this can be written as

$$\delta h = -\frac{R^2}{r_0}\frac{1}{4\ln 2}\frac{\cos\theta_0}{\tan\theta_0}\frac{\theta_0}{s^2} \tag{42}$$

For the range of incidence angles used by WSOA ($\theta_0 < 4°$), one can approximate $\tan\theta_0 \approx \theta_0$ and $\cos\theta_0 \approx 1$, so that the final expression for the height error is given by

$$\delta h = -\frac{R^2}{h}\frac{1}{4\ln 2}\frac{1}{0.018U_{10}^{1/2}} \tag{43}$$

where I have replaced the mean squared slope by its wind speed dependent equivalent, as given in equation (30).

Acknowledgements. We would like to thank Ed Walsh for expressing his concern and quantifying the errors for the incoherent interferometer case. We would also like to thank E. Thouvenot (CNES) and his colleagues in CNES and Alcatel for helping us to characterize the Proteus bus roll spectrum.

References

Bush, G.B., E.B. Dobson, R. Matyskiela, C.C. Kilgus, and E.G. Walsh, 1984: An Analysis of a satellite multibeam altimeter. *Marine Geodesy*, **8**(1-4), 345-384.

Gatelli, F., A. Monti-Guarnieri, F. Parizzi, P. Pasquali, C. Prati, F. and Rocca, 1994: The wavenumber shift in SAR interferometry. *IEEE Trans. Geoscience & Rem. Sens*., **32**(4) 855-865.

Parsons, C.L., and E.J. Walsh, 1989: Off-nadir radar altimetry. *IEEE Trans. Geoscience and Rem. Sens*., **27**(2), 215-224.

Rabiner, L., R. Schaffer, and C. Rader, 1969: The chirp-z transform and its applications. *Bell Syst. Tech. J*., **48**, 1249-1292.

Raney, R.K., H. Runge, R. Bamler, I. Cumming, and F. Wong, 1994: Precision SAR processing using chirp scaling. *IEEE Trans. Geoscience and Rem. Sens*., **32**, 786-789.

Rodríguez, E., and J.M. Martin, 1992: Theory and design of interferometric synthetic aperture radars. *IEEE Proc.-F Radar and Signal Proc*., **139**(2), 147-159.
Rodriguez, E., B.D. Pollard, and J.M. Martin, 2001: Wide-Swath Ocean Altimetry using radar interferometry. *IEEE Trans. Geoscience & Rem. Sens*., in press.
Tsang, L., J.A. Kong, and R.T. Shin, 1985: Theory of Microwave Remote Sensing. Wiley-Interscience, New York.

Cell Center (km)	Height Error (cm)	Height Error Spectral Shift (cm)
22.1	5.2	3.9
36.4	4.7	3.6
50.7	4.5	3.5
65.0	4.6	3.8
79.2	5.2	4.3
93.5	6.5	5.4

Table 1a: 6.4 m Baseline Height Noise Performance for Single-Transmit Operation

Cell Center (km)	Height Error (cm)	Height Error Spectral Shift (cm)
22.1	5.6	4.1
36.4	4.3	3.3
50.7	3.7	2.9
65.0	3.5	2.8
79.2	3.9	3.1
93.5	4.8	3.9

Table 1b: 6.4 m Baseline Height Noise Performance for Ping-Pong Operation

Cell Center (km)	Height Error (cm)	Height Error Spectral Shift (cm)
22.1	4.4	3.1
36.4	3.7	2.7
50.7	3.4	2.5
65.0	3.3	2.6
79.2	3.8	2.9
93.5	4.6	3.6

Table 2a: 10 m Baseline Height Noise Performance for Single-Transmit Operation

Cell Center (km)	Height Error (cm)	Height Error Spectral Shift (cm)
22.1	5.2	3.3
36.4	3.6	2.6
50.7	3.0	2.2
65.0	2.7	2.1
79.2	2.9	2.2
93.5	3.5	2.6

Table 2b: 10 m Baseline Height Noise Performance for Ping-Pong Operation

Cell Center (km)	Height Error (cm)	Height Error Spectral Shift (cm)
22.1	3.7	2.8
36.4	3.3	2.5
50.7	3.2	2.5
65.0	3.2	2.7
79.2	3.7	3.0
93.5	4.6	3.8

Table 3a: 6.4 m Baseline, Double Duty Cycle, Height Noise Performance for Single-Transmit Operation

Cell Center (km)	Height Error (cm)	Height Error Spectral Shift (cm)
22.1	4.0	2.9
36.4	3.0	2.3
50.7	2.6	2.0
63.0	2.4	2.0
79.2	2.7	2.2
93.5	3.4	2.7

Table 3b: 6.4 m Baseline, Double Duty Cycle, Height Noise Performance Ping-Pong Operation

Cell Center (km)	Height Error (cm)	Height Error Spectral Shift (cm)
22.1	3.1	2.2
36.4	2.6	1.9
50.7	2.4	1.7
65.0	2.3	1.8
79.2	2.7	2.0
93.5	3.3	2.5

Table 4a: 10 m Baseline, Double Duty Cycle, Height Noise Performance for Single-Transmit Operation

Cell Center (km)	Height Error (cm)	Height Error Spectral Shift (cm)
22.1	3.6	2.3
36.4	2.6	1.8
50.7	2.1	1.5
65.0	1.9	1.5
79.2	2.1	1.5
93.5	2.5	1.8

Table 4b: 10 m Baseline, Double Duty Cycle, Height Noise Performance for Ping-Pong Operation

U_{10} (m/s)	Height Error (cm)
1	0.08
7	0.03
10	0.03
15	0.02

Table 5: Height error due to brightness variations, as a function of wind speed.

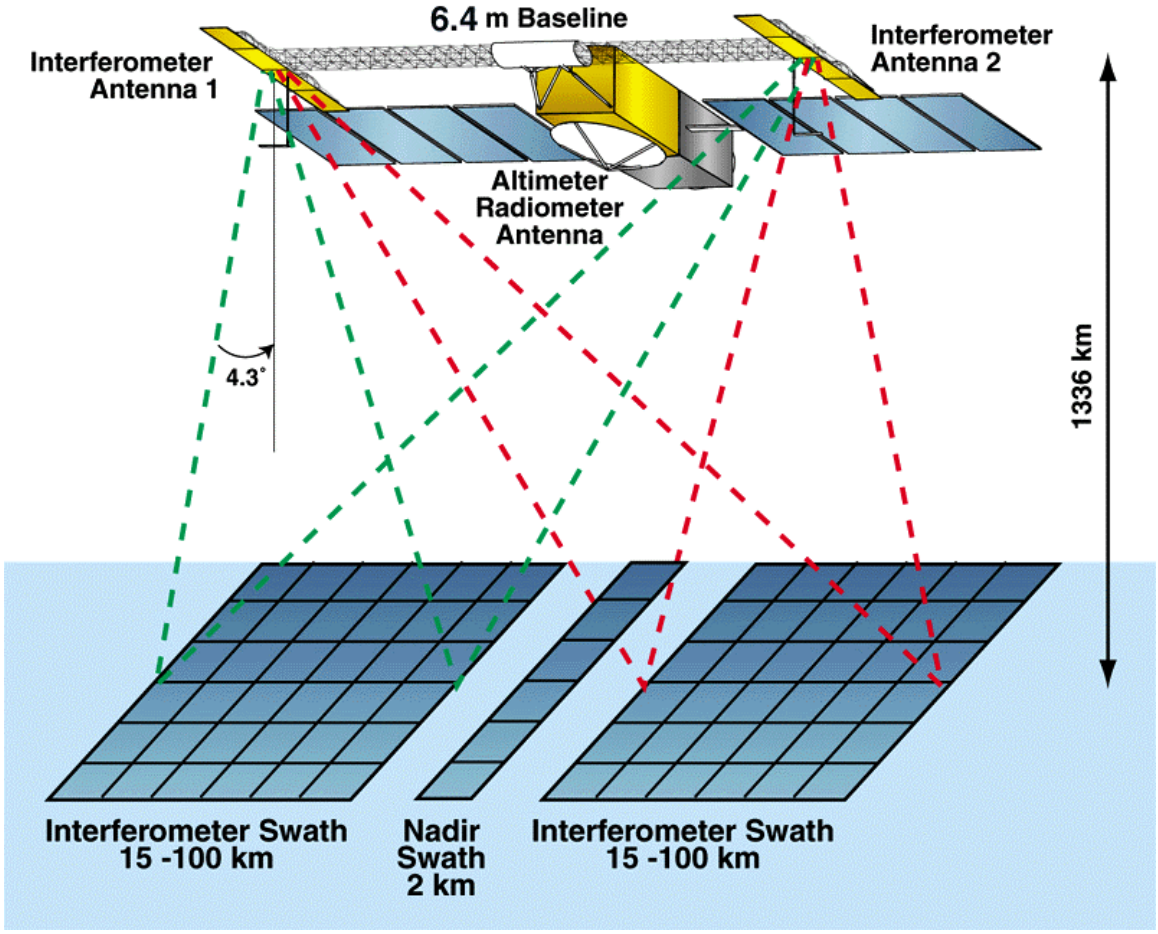

Figure 1. Wide Swath Ocean Altimeter measurement concept. TheWSOA is shown here integrated with the Jason Altimeter and the Proteus bus.

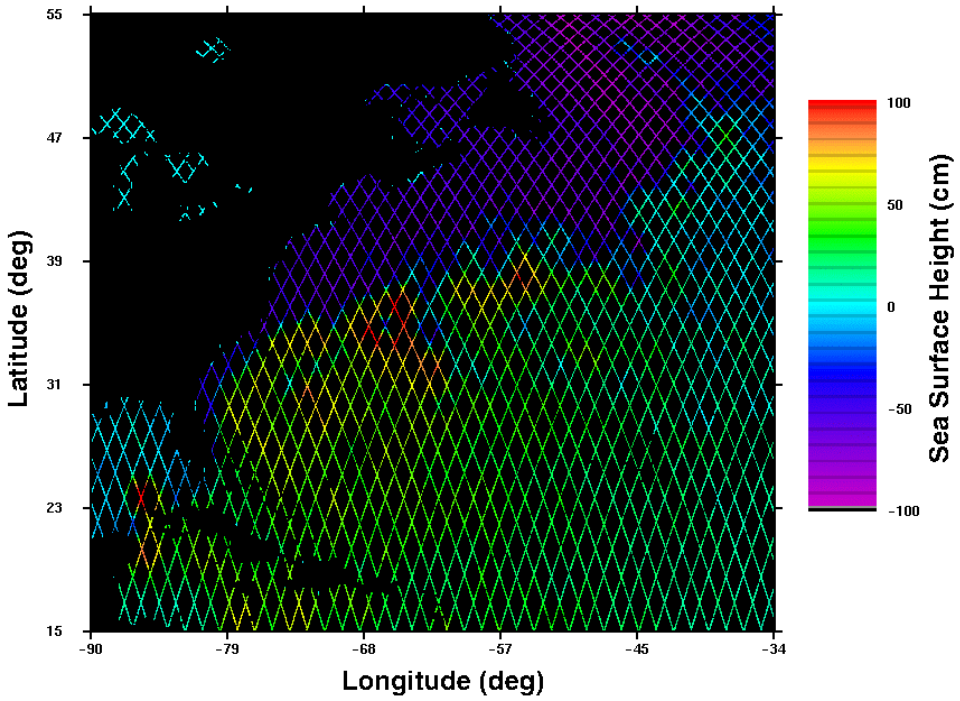

Figure 2a. Example coverage of the North Atlantic for two TOPEX class altimeters flying in formation with an equatorial separation of 150 km.

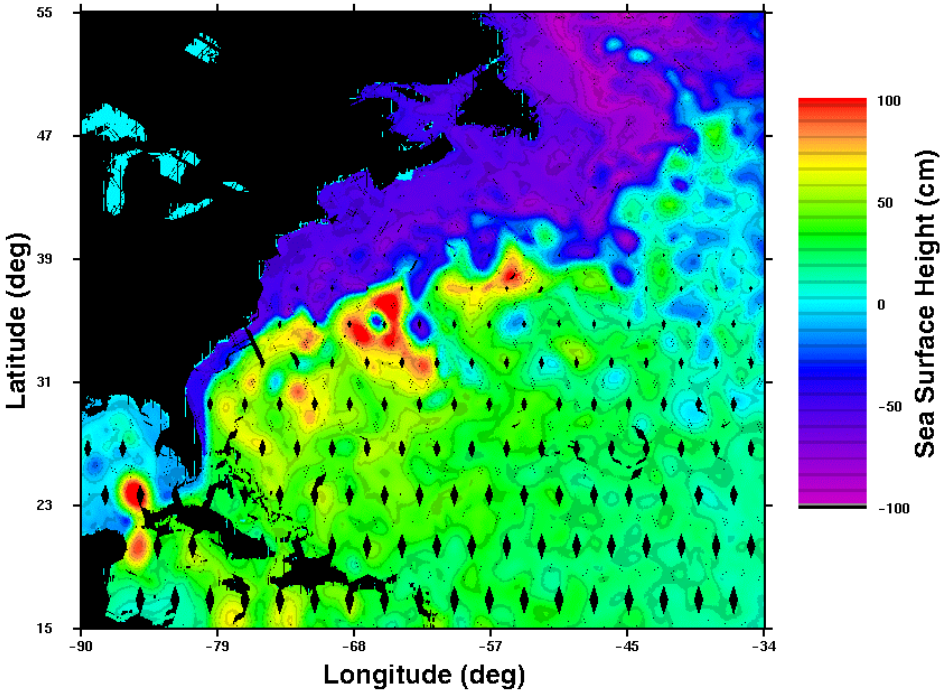

Figure 2b. Simulated estimated heights by a single WSOA in a TOPEX orbit. The height field shown includes measurement noise and residual calibration errors.

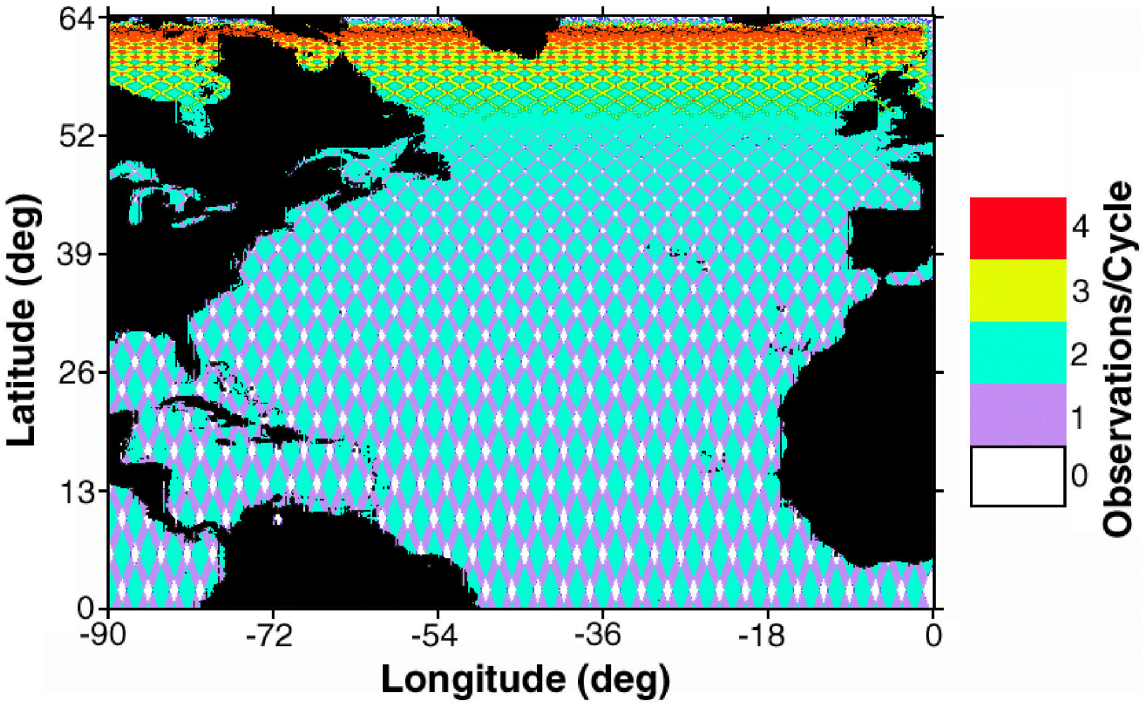

Figure 3. Number of times each surface point is mapped by WSOA during a 10 day repeat cycle. Unlike conventional altimeters, most points in the ocean are mapped at least twice, and often more frequently.

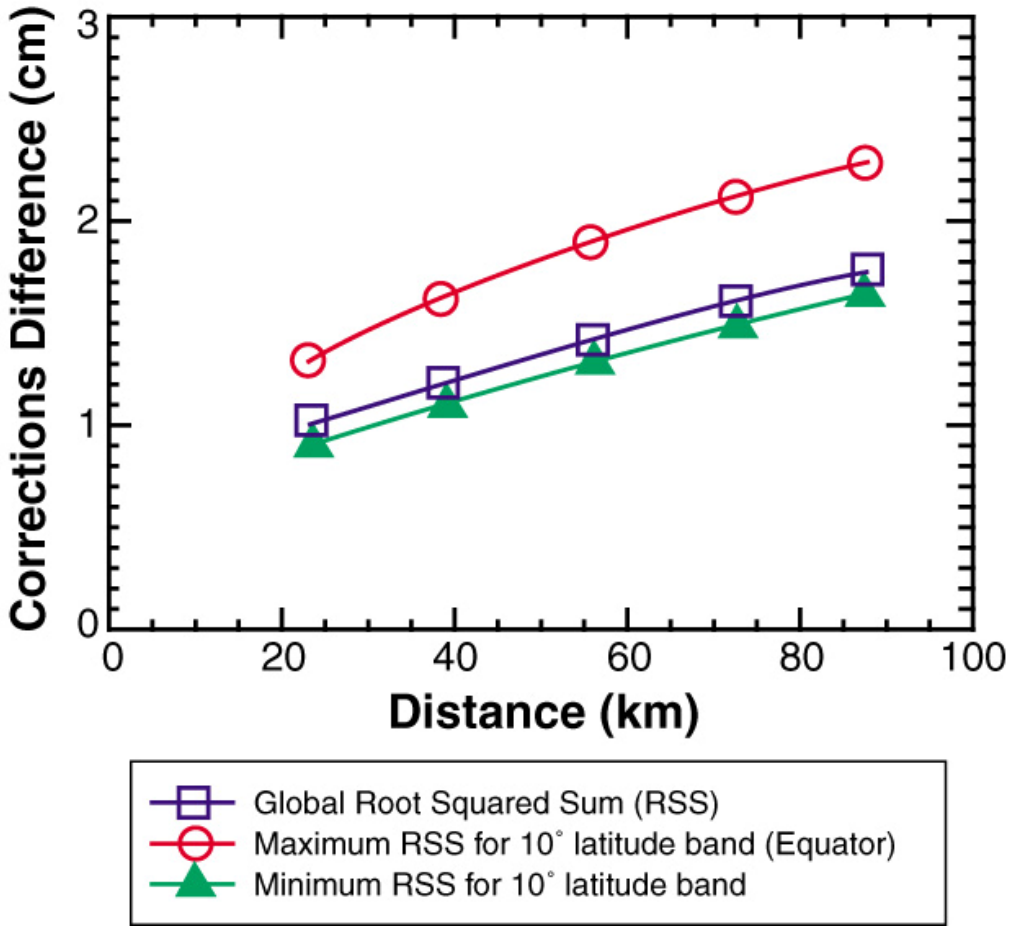

Figure 4. Contribution of tropospheric, ionospheric, and EM bias error sources as a function of distance from the satellite nadir track. The estimates were derived from TOPEX measurements.

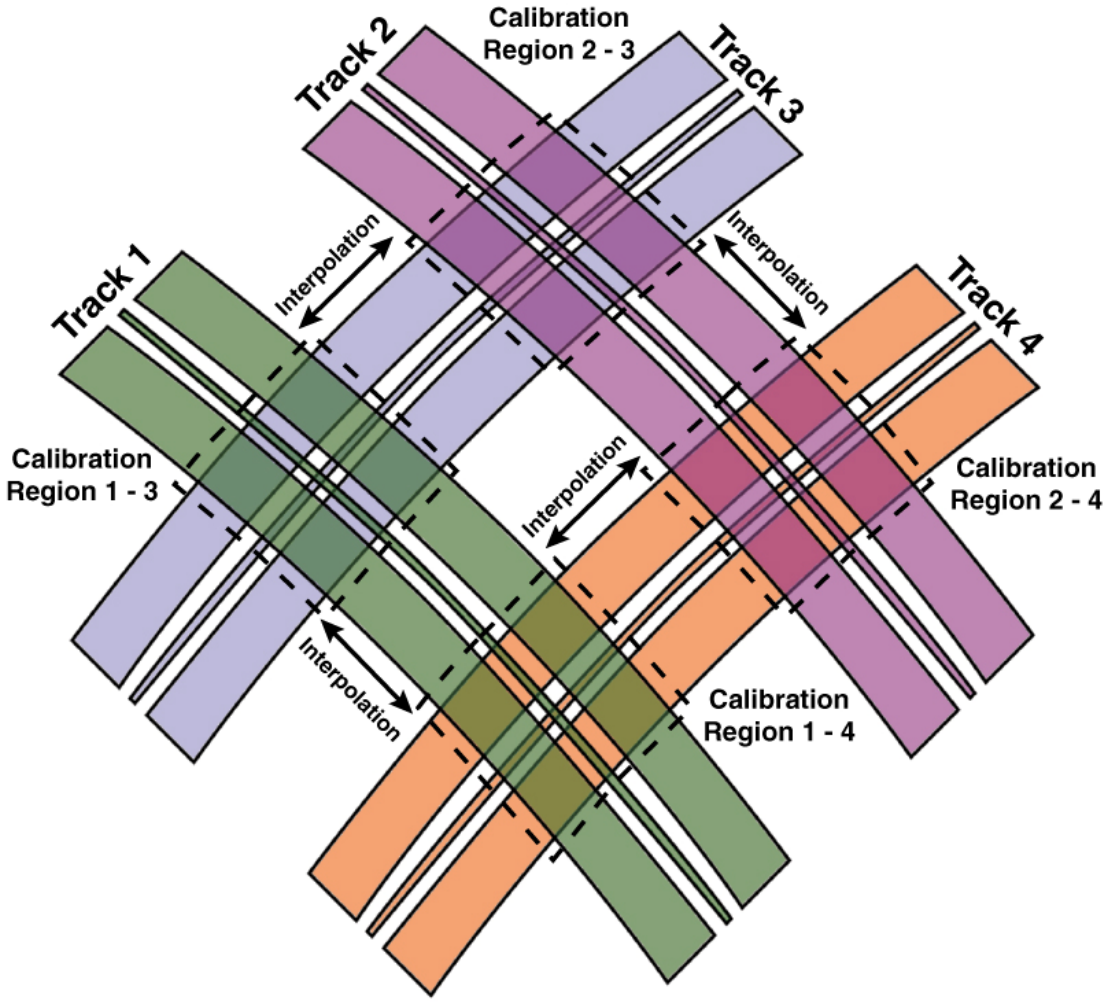

Figure 5. Schematic of the proposed calibration scheme for removing spacecraft roll errors using interferometer and altimeter cross-overs. Assuming four passes, there will be four cross-over regions where the spacecraft roll can be estimated. The estimates of roll are then interpolated between cross-over regions.

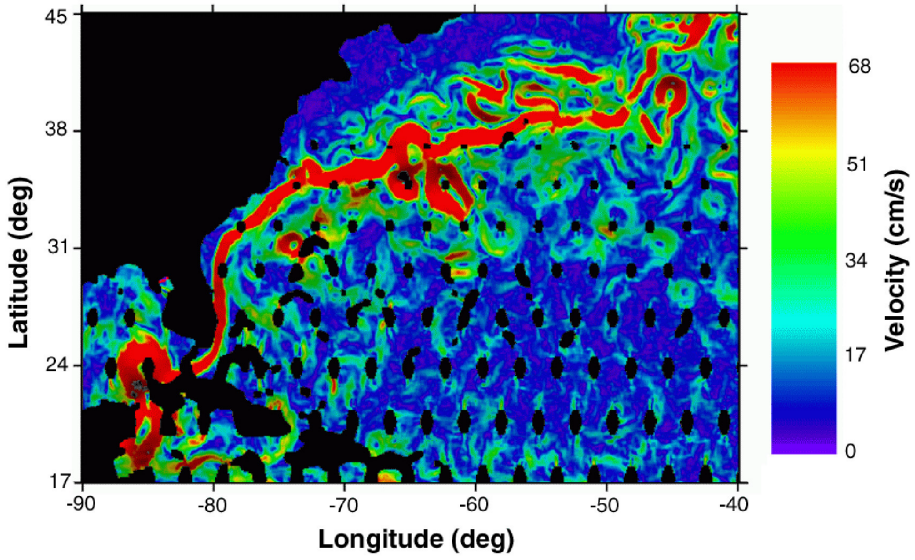

Figure 6a. Magnitude of the geostrophic velocity estimated from the WSOA height simulation results shown in Figure 2a.

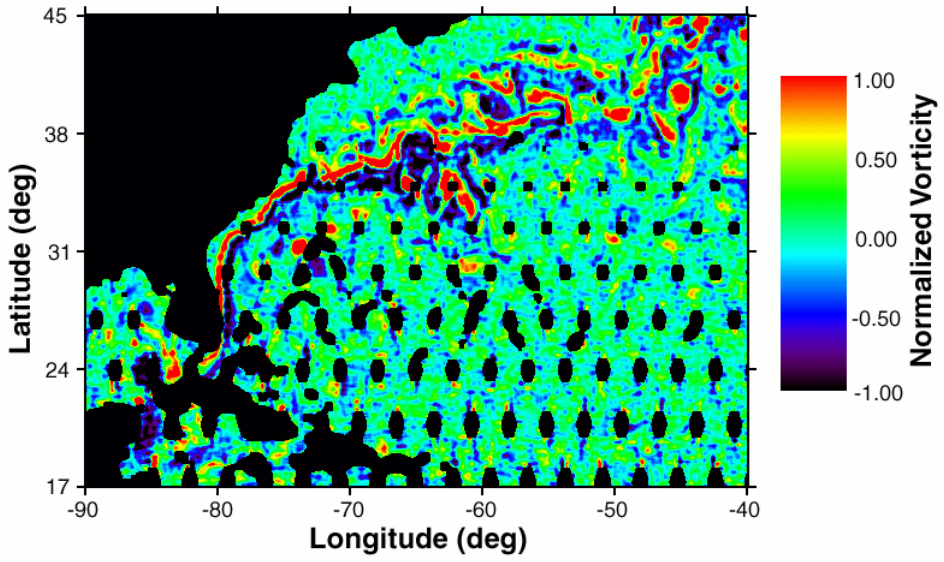

Figure 6b. Relative vorticity estimated from the WSOA height simulation results shown in Figure 2a.

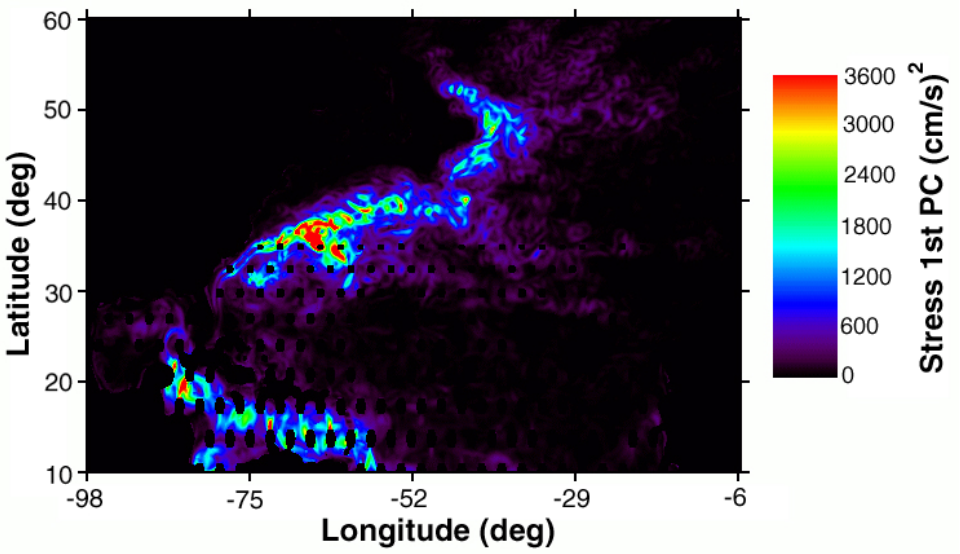

Figure 6c. Principal component of the Reynolds stress tensor, derived from a six month WSOA simulation of the North Atlantic, based on the LANL North Atlantic eddy resolving model.

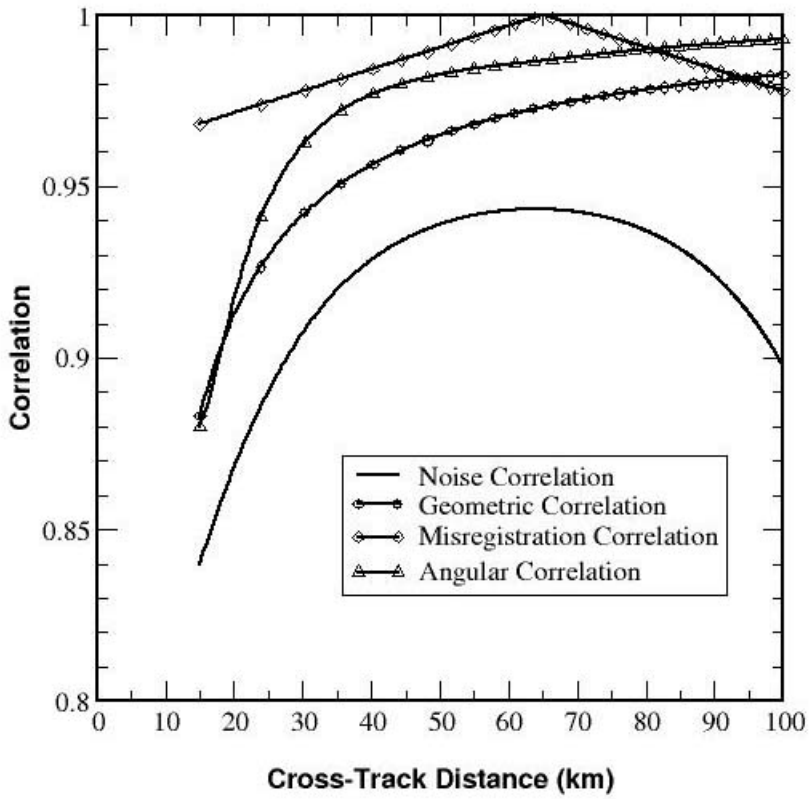

Figure 7. Components of the total correlation between the two interferometric channels assuming the simplest onboard processing. Using the more sophisticated algorithms described in the text, the misregistration and geometric correlations can be neglected. The total correlation is the product of all correlations, and determines the instrument height noise.

High-Resolution Ocean Topography from GPS Reflections

Cinzia Zuffada
Jet Propulsion Laboratory
California Institute of Technology
Pasadena, California 91109

This note is based on the presentation on March 28, 2001 at the High-resolution Ocean Topography (HOT) Science Working Group (SWG) meeting. In this note we describe the salient features of the GPS reflection technique and discuss the altimetry application. Next, we summarize the history of GPS reflection development at JPL and the preliminary findings. We then illustrate what is required in terms of a GPS-reflections receiving system to make these measurements in a realistic space scenario. Last, we outline another application of the technique for coastal monitoring using fixed GPS receivers.

1. Motivation and Scientific Potential

The Global Positioning System (GPS), which was first conceived and built for the purpose of navigation, has been utilized in the last decade to study the Earth's interior, surface and environment in ways that far exceed anyone's original imagination. Scientific applications of the GPS include measuring seismic tectonic motions, Earth orientation and polar motion, gravimetry, neutral atmospheric temperature and water vapor profiling, and ionospheric electron density profiling and global monitoring. All of these applications have been well proven and provide new ways to enhance our knowledge about the Earth and its environment. The advantage of GPS is twofold: the transmitted signal is global and is there at all times and in all weather conditions and the receiver technology is rather inexpensive, compared to alternative remote sensing systems. More recent and less developed applications explore the possibility to utilize the GPS signals scattered off the ocean and sensed by an air- or spaceborne receiver in a bistatic radar geometry, as a means of doing altimetry and scatterometry (Garrison et al., 1998; Lin et al., 1999; Lowe et al., 2000; Zuffada and Elfouhaily, 2000; Zuffada et al., 2000; Treuhaft et al., 2001).

Currently, the constellation of 24 GPS transmitters broadcasts at two frequencies in the L-band (~ 1.2 and 1.5 GHz). Both carriers are modulated by one or two pseudo-random noise codes, which result in periodic sequences of positive and negative pulses, each unique to a given transmitter. The codes are referred to as Coarse Acquisition (C/A) and Precision (P). Upon impinging on the ocean surface, the signal is reflected (actually scattered off) primarily in the specular (forward) direction, in an amount dependent on surface roughness and angle of incidence. An airborne (or spaceborne) receiver, connected to a down-looking GPS antenna whose axis is ideally located in the specular direction, could collect such scattered signal. When considering the 24 transmitters and one such receiver a multistatic radar system is obtained, in principle capable of intercepting bounces from several areas of the ocean simultaneously, as illustrated in Fig.1. By analogy to traditional altimetry, the bistatic GPS reflected signal can be analyzed to derive the important descriptors of the ocean surface; i.e. ocean height and surface wind vector.

Traditional altimetry, such as on Topex/Poseidon, is limited to looking in the (nominal) nadir direction and obtaining one height observation at a time below the altimeter, following very nearly repeatable tracks passing over the same point every ten days. The track separation varies, being largest at the equator where it is about 300 km. By contrast, a GPS receiver in low-Earth orbit (LEO) with an antenna pointed toward the Earth's surface can, in principle, track about 10 GPS reflections simultaneously, therefore providing a coverage that is an order of magnitude denser than nadir-viewing altimeters. As seen in Fig. 2, the reflection ground tracks of a satellite at the altitude of 400 km would cover the Earth nearly uniformly in just 1 day, with across track separation at most about 75 km. Based on the GPS orbit repeatability, in any given cell of the Earth's surface of size 50 km^2, there would be about 12 reflection measurements in 10 days, randomly occurring within the cell. The average of such measurements could produce the reading for the given cell size in the 10 days period. Such dense coverage can be translated into a higher temporal and spatial resolution than TOPEX/Poseidon, therefore

possibly indicating the ability to recover certain ocean topography features or processes that are precluded with traditional altimeters.

It is anticipated that the GPS altimetry will improve our current capability in two important ways:

- High-resolution Ocean Topography

These include the measurements of mesoscale eddies which play an important role in the transport of momentum, heat, salt, nutrients, and other chemical properties of the ocean. Mesoscale eddies are ocean features analogous to atmospheric storms, which result in sea-height changes above the mean (peaks and valleys) of about 10 cm on spatial scales between ~10-100 km with temporal evolution of ~ 1 week to 1 month.

- Improved Temporal Resolution Through Rapid Coverage

Another possible application of very rapid coverage of the ocean is the monitoring of fast moving barotropic waves that propagate across ocean basins too quickly to be seen by the TOPEX/Poseidon 10-day repeat cycle.

2. Direct and Reflected GPS Signals

The process of acquiring the received signal consists of performing a cross-correlation between the incoming sequence and a replica of the transmitted signal, shifted in time and frequency to account for the proper propagation delay and Doppler. The output of the correlator is maximized in time when the incoming sequence and the appropriate replica are perfectly aligned. Additionally, for a direct signal the correlator is non zero when the alignment is within +/- 1 code chip away from perfect and has a symmetric shape around the maximum. (The chip is the rate of probable occurrence of code transition, and is 1.023 MHz and 10.23 MHz, for C/A and P codes, respectively. Hence, the chip duration over which the correlator output is non zero is the reciprocal of this rate.) By contrast the correlator output for the reflected signal is non zero over a period of several code chips and is not symmetric about its maximum. Therefore the reflected signal can be distinguished from the direct one based on its shape, as evidenced in Fig. 3; furthermore we will describe how the shape is affected by the state of the ocean surface in a manner that allows us to extract the ocean properties from it.

The areas of the ocean surface contributing to the reflected signal vary as a function of time according to the advancement of the wave front. For the sake of illustration let's define the plane of incidence as that containing transmitter, receiver and specular reflection point (chosen as the origin), i.e. the plane of Fig. 4. This plane is perpendicular to the mean ocean plane and is a plane of symmetry for the reflection. The shortest reflection path connects transmitter and receiver via the specular reflection point and hence its contribution is received at the earliest times. The contributions from the surrounding area in the ocean are received later on. Specifically, the points on the ocean plane contained in an elliptical annulus of progressively increasing axes (major axis in the plane of incidence) and center (also in the plane of incidence) moving towards the transmitter give rise to scattered fields which are received at the same time. The size of the annuli and their ellipticity is determined by the receiver altitude and reflection geometry; the higher the elevation angle, the more circular the annuli become. In general it can be observed that the ocean surface is sampled along preferential directions, according to the reflection geometry. Hence, the received signal senses different areas on the ocean as time goes by, thus affecting the resolution (see Zuffada and Elfouhaily, 2000).

3. Altimetry Measurement

Assuming that a receiver is connected to both an upward looking and a down looking antenna, it will be able to acquire a direct signal followed in time by a reflected one (see Fig. 3). The delay between

the arrival of the peak of the direct signal and the contribution from the specular reflection point on the leading edge of the reflected waveform (usually not corresponding to the peak) is the quantity of interest for altimetry measurements. Such delay can be converted into path difference (reflected minus direct) by multiplication with the speed of light. From precise knowledge of the positions of transmitter and receiver and with an *apriori* estimate of the sea surface topography such path difference can be expressed in terms of the surface altitude below the receiver and the elevation angle. A retrieval scheme can be set up to solve for these parameters, accounting for various sources of error such as transmitter and receiver clocks, the ionosphere and the neutral atmosphere.

4. Resolution

The cross correlation is equivalent to an integration over a time consistent with the coherence of the phenomena being observed. This in turn depends on the size of the target contributing to the scattering, i.e. the larger the area the shorter the coherence time. Since the GPS reflection measurement samples progressively increasing areas over the ocean, one must establish what area is sufficient to acquire the needed signal. For altimetry measurements it is important to collect the contribution from the point of specular reflection, which occurs one code chip following onset of non zero correlator output. This corresponds to an area over the ocean referred to as the first iso-range ellipse (see Fig. 4), implying that all the points contribute to the received signal with relative delay of no more that one code chip away from the minimum value. The size of this footprint depends on the receiver altitude (airborne or spaceborne) and on the reflection geometry ranging from a few square km to tens of square km.

The coherence time for the ocean at L-band ranges from a fraction of 1 msec to 10 msec, thus implying that one received waveform is generated at the corresponding rate. Because the signal level is very weak, many responses need to be combined to boost the signal and reduce the variance, thereby improving accuracy. To determine the measurement resolution one must examine the footprint behavior in the amount of time over which an incoherent average is performed. Such time is of order 1 to 10 seconds, depending on roughness conditions and needed accuracy. During this time the footprint will have moved by an amount determined by the receiver velocity along track, typically of order 1 to 10 km (see Zuffada et al., 2000).

5. Accuracy

The altimetry measurement accuracy depends on how precisely the peak of the direct signal and the contribution from the specular reflection point on the reflected signal can be located in time. In essence, the limiting factors are the transmitted power levels, the scattering cross section coefficients at L-band, the receiver integration time, the receiving antenna gain and the number of incoherently averaged samples. The first four parameters contribute to the accuracy of the single sample waveform, while the fifth compensates for the sample-to-sample variability. The integration done in the receiver is equivalent to performing a spatial filtering with selectivity chosen by the designer, normally to be maximum at the specular reflection point, and tapering off away from it past the area of the first iso-range. The antenna gain can be chosen so that an additional spatial filtering is performed. These features also allow for a reduction of the effective footprint.

Once the average signal to noise ratio (snr) has been achieved through incoherent averaging, a prediction of the accuracy formal error can be obtained by performing a covariance analysis where the problem parameter is the relative delay error and the operator is the bistatic radar - forward scattering integral representing the cross correlation output. Hence, the initial choice of antenna gain will impact the final accuracy through the incoherent averaging process. The higher the gain the higher the snr at the expense of increased complexity and size and reduced beamwidth.

Based on the available GPS transmitted power and typical values of coherent integration times, we can determine the antenna gain necessary to achieve a desired target snr per single measurement. This target value is chosen so that we optimize the antenna requirements in terms of size/costs and we project

an accuracy sufficient for eddy resolution in 10 days with a given constellation of receivers. Naturally, to obtain the same height accuracy, one can increase the single measurement snr and decrease either the time or the number of satellites in the constellation. At the altitude of 400 km we found the target gain to be 30 dB, corresponding to an accuracy of 10 cm/4 sec of the averaged altimetry measurement. To increase the accuracy over this value many measurements need to be combined to define one average altimetry measurement in a given ocean cell size. A possible scenario is illustrated in the last section leading to resulting constellation sizes required for eddy resolution (see Zuffada et al., 2000).

6. Roadmap to GPS Altimetry

6.1. Fixed Location GPS Receiver for Coastal Monitoring

One of the severe limitations for the conventional radar altimetry is that it loses lock when approaching the coastline, thus leaving an area of 2~3 footprints (about 20 km) without reliable measurements. The GPS signal could be exploited for this application by installing fixed receivers along the coast at some altitude (for example 200 m) and spaced by about 20 km. This could be a simple experimental set-up: the receiver is not moving, the signal level is always adequate and the local coverage would be very dense over the period of time of a day or so. With this geometry the low elevation reflections over the ocean would be tracked. Because the ocean appears smoother at low elevations, it is likely that the reflections would have a coherent component, absent in the more general case instead, practically achieving the condition of reflection from a perfectly conducting plane, where coherent reflection rather than scattering is expected. In this case one can track the phase of the GPS signal, thus increasing the accuracy dramatically. This concept has been tested in an experiment at Crater Lake, which yielded very accurate height determination with rms errors of 2 cm in 1 sec (see Treuhaft et al., 2001), as illustrated in Fig. 5. This is very encouraging. A further demonstration of such a fixed location GPS receiver at the Harvest platform is undergoing.

6.2. Moving GPS Receivers for Ocean Altimetry

In the last few years the Jet Propulsion Laboratory has been active in the development of the GPS-altimetry measurement technology within the funded GOALS Instrument Incubator Task. Initial development of data processing algorithm for ocean science applications has been funded through the NASA Research and Analysis program. Within the currently funded projects, JPL is pursuing investigations to (a) understand the impact of the fundamental ocean processes on the measured GPS-reflected waveform, (b) assess the measurement accuracy for general experimental conditions and system parameters and (c) feed this knowledge into the design of the next generation of JPL GPS receivers to process reflections.

At the beginning of this effort JPL obtained the first GPS reflected signal from space, by examining a calibration signal collected by the SIR-C flying on the Space Shuttle, whose antenna happens to have the right bandwidth for capturing the GPS L2 signal. Additional data was collected from a CESSNA airplane flying over the ocean west of Santa Barbara, CA in the first altimetry experiment carrying instrumentation to acquire and record raw GPS signals. The data was processed and a preliminary height accuracy of 9 cm in 5 minutes was demonstrated.

The work on GPS reflection technology development at JPL is founded on the considerable heritage of advanced GPS receivers developed at JPL. These began with the Rogue and TurboRogue geodetic ground receivers in the 1980s, and were followed by the TurboRogue Space Receiver (TRSR), which is now flying on GPS/MET as well as (in somewhat upgraded form) on the Danish Ørsted and South African Sunsat missions. The BlackJack represents a major redesign of the TurboRogue carried out over the past four years, intended primarily for flight applications. The first BlackJack recently flew on the space shuttle as part of the Shuttle Radar Topographic Mapper (SRTM), and several versions have been delivered for flight on a diversity of upcoming NASA and international missions. These include

Jason-1, ICESat, the Vegetation Canopy Lidar (VCL), the German CHAMP, the Argentine SAC-C, and the Australian FEDSAT missions.

7. Roadmap to an Eddy-Resolving Mapping Capability

The global coverage of the GPS signal makes it particularly appealing for possible sampling of mesoscale eddies, whose spatial features smaller than 50 km and temporal variability of the order of several days make them elusive to the currently existing altimetry systems. We have already pointed out that one single receiver at 400 Km altitude connected to a suitable receiving antenna system, would result in reflection ground tracks covering the Earth nearly uniformly in just one day, with across track separation at most about 75 km (see Fig. 2). Based on the GPS orbit repeatability, in any given cell of the Earth's surface of size 50 km^2, there would be about 1.12 4-sec reflection measurements in one day, or 12 in 10 days, randomly occurring within the cell, thus reducing the effective cross track separation progressively as the cell is being populated. Due to the randomness of the errors and the independent measurements, an improvement in the accuracy according to the square root of the number of measurements is obtained. Based on this it is shown that already a constellation of two receiving satellites would achieve a height accuracy of 6 cm in 10 days in a 50 km^2 cell, while a constellation of eight satellites would accomplish the same thing in a 25 km^2 cell instead, showing the system scalability (see Zuffada et al., 2000). It is noted that another way of improving the accuracy consists of increasing the number of available reflections by increasing the number of transmitters. This is of practical interest since a European GPS constellation is planned to be deployed in the near future. The frequencies of operation and signal characteristics will be very similar to the existing US constellation so that the same acquisition and processing algorithms and hardware will be useful to process the wealth of available reflections.

References

Garrison, J.L., S.G. Katzberg, and M.I. Hill, 1998: Effect of sea roughness on bistatically scattered range coded signals from the Global Positioning System. *Geophys. Res. Lett*. **25**, 2257-2260.

Lin, B, S.J. Katzberg, J.L. Garrison, and B. Wielicki, 1999: The relationship between the GPS signals reflected from sea surface and the surface winds: Modeling results and comparisons with aircraft measurements. *J. Geophys. Res*. **104**, 20,713-20,727.

Lowe, S.T., J.L. Labrecque, C. Zuffada, L.J. Romans, L. Young and G.A. Hajj, 2001: First Spaceborne Observation of an Earth-Reflected GPS Signal. *Radio Science* (accepted for publication).

Zuffada, C., and T. Elfouhaily, 2000: Determining wind speed and direction with ocean reflected GPS signals. In *Proc. Sixth Int. Conf. Remote Sens. Marine Coast. Environ.*, Vol. II, Charleston, SC, pp. 429-435.

Zuffada, C., S. Lowe, G. Hajj, L. Young, Y. Chao, 2000: GPS bistatic altimetry: a tool for studying ocean mesoscale features. Presented at AGU 2000 Fall Meeting, San Francisco, CA (invited).

Treuhaft, R., S. Lowe, C. Zuffada, and Y. Chao, 2001: 2-Cm GPS Altimetry Over Crater Lake. *Geophys. Res. Lett*., (accepted for publication).

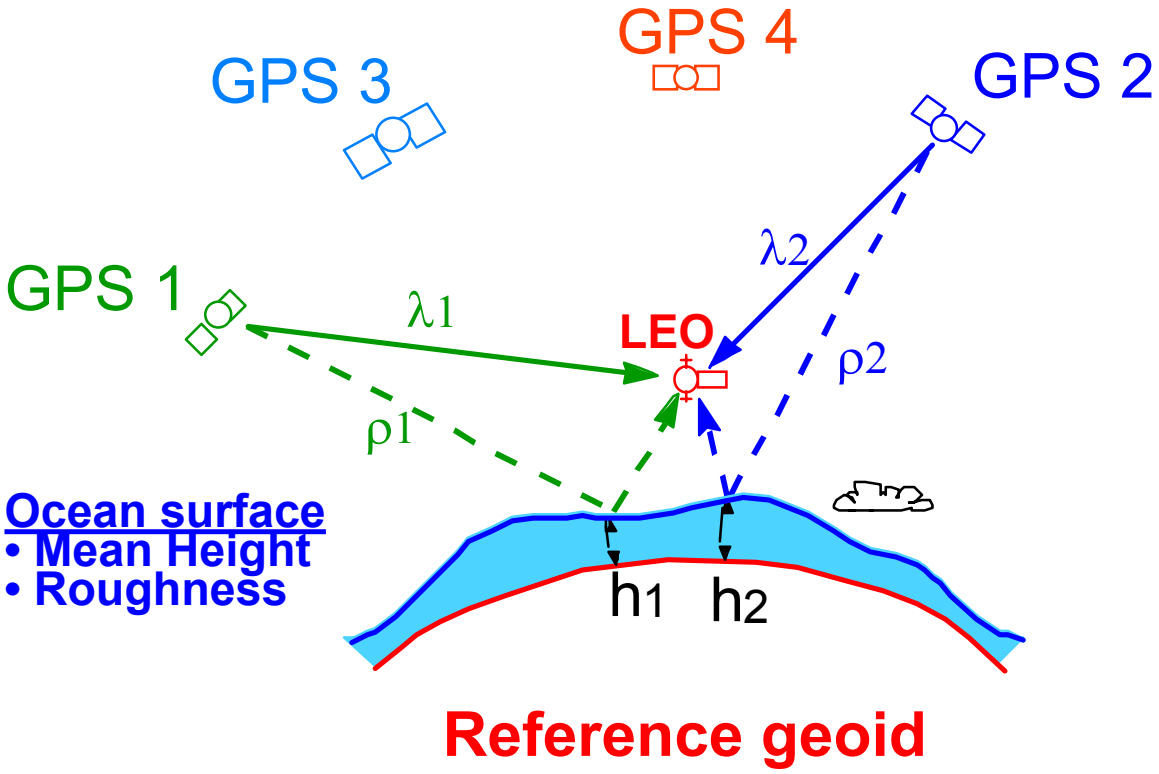

Figure 1. Bistatic GPS measurement concept.

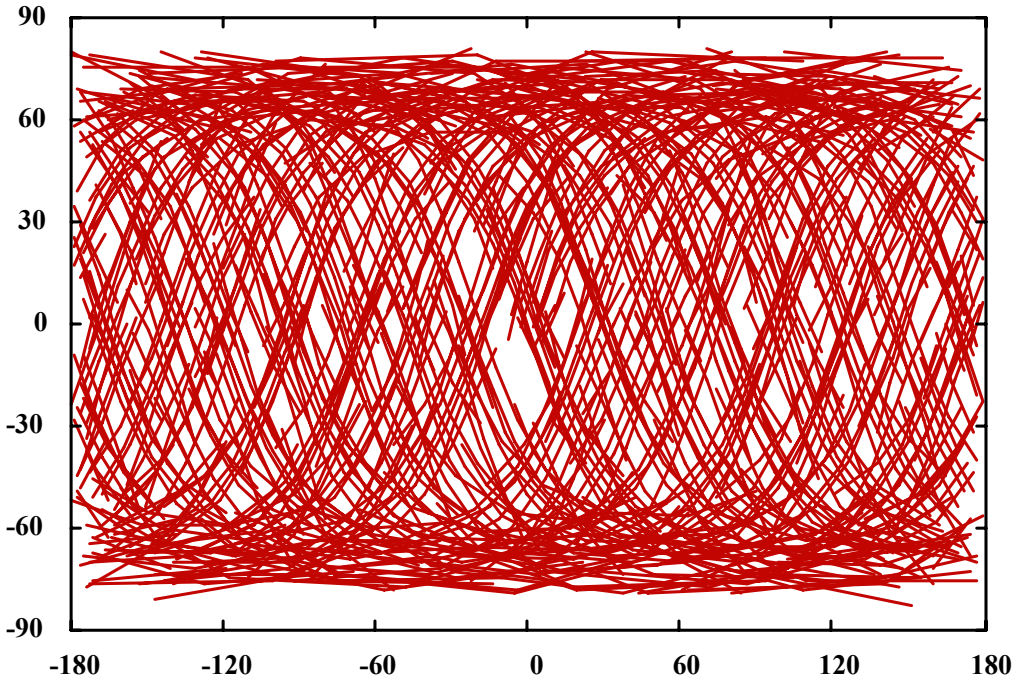

Figure 2. Reflection ground tracks corresponding to one day coverage from all transmitters and one single receiver at 400 km.

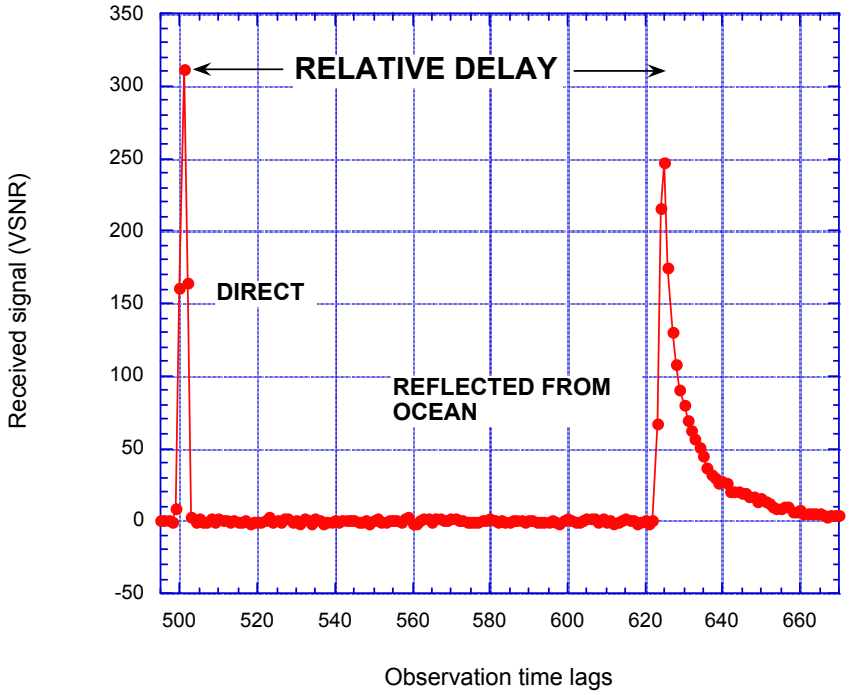

Figure 3. Direct and reflected GPS signal collected from receiver on board airplane.

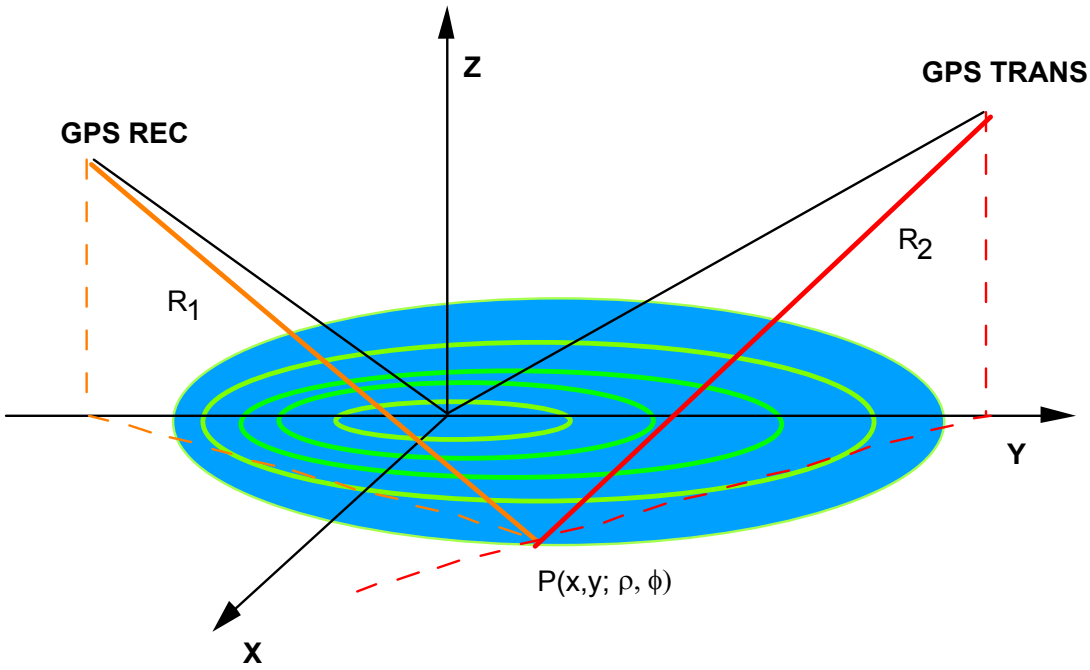

Figure 4. Plane of incidence (YZ), iso-range ellipses and general scattering point.

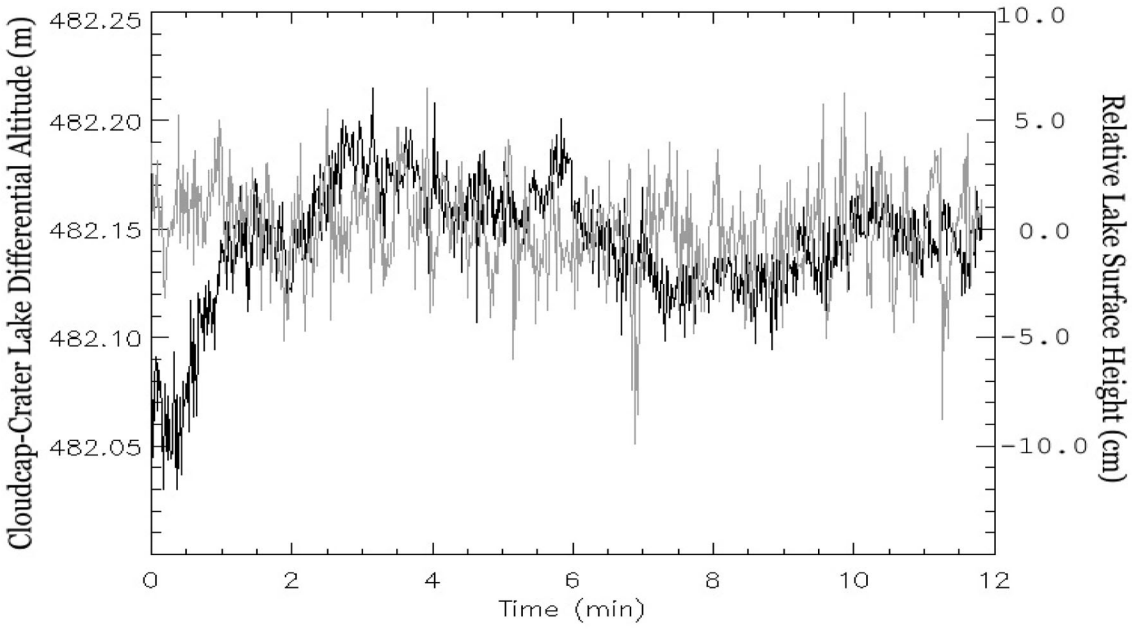

Figure 5. Height of lake surface determined as height of GPS receiver at fixed site above body of water.